

AN AUTOMOTIVE AIR CONDITIONING COMPRESSOR ELECTRIC MOTOR DRIVE

Teză destinată obținerii
titlului științific de doctor inginer
la
Universitatea "Politehnica" din Timișoara
în domeniul INGINERIE ELECTRICĂ
de către

Ing. Anamaria UNGUREAN (MUNTEANU)

Conducător științific: prof.univ.dr.ing. Ion BOLDEA
Referenți științifici: prof.univ.dr.ing. Mircea RĂDULESCU
prof.univ.dr.ing. Iulian BIROU
conf.univ.dr.ing. Lucian TUTELEA

Ziua susținerii tezei: 27.09.2012

Seriile Teze de doctorat ale UPT sunt:

- | | |
|------------------------|---|
| 1. Automatică | 7. Inginerie Electronică și Telecomunicații |
| 2. Chimie | 8. Inginerie Industrială |
| 3. Energetică | 9. Inginerie Mecanică |
| 4. Ingineria Chimică | 10. Știința Calculatoarelor |
| 5. Inginerie Civilă | 11. Știința și Ingineria Materialelor |
| 6. Inginerie Electrică | |

Universitatea „Politehnica” din Timișoara a inițiat seriile de mai sus în scopul diseminării expertizei, cunoștințelor și rezultatelor cercetărilor întreprinse în cadrul școlii doctorale a universității. Seriile conțin, potrivit H.B.Ex.S Nr. 14 / 14.07.2006, tezele de doctorat susținute în universitate începând cu 1 octombrie 2006.

Copyright © Editura Politehnica – Timișoara, 2006

Această publicație este supusă prevederilor legii dreptului de autor. Multiplicarea acestei publicații, în mod integral sau în parte, traducerea, tipărirea, reutilizarea ilustrațiilor, expunerea, radiodifuzarea, reproducerea pe microfilme sau în orice altă formă este permisă numai cu respectarea prevederilor Legii române a dreptului de autor în vigoare și permisiunea pentru utilizare obținută în scris din partea Universității „Politehnica” din Timișoara. Toate încălcările acestor drepturi vor fi penalizate potrivit Legii române a drepturilor de autor.

România, 300159 Timișoara, Bd. Republicii 9,
tel. 0256 403823, fax. 0256 403221
e-mail: editura@edipol.upt.ro

Preface

The thesis represents an approach to the design and control of permanent magnet synchronous motors fed with rectangular current, as part of dedicated automotive electric drives. The present thesis includes the electromagnetic design for a 6 slots/ 8 poles 3 phase permanent magnet synchronous actuator with surface permanent magnets, an optimization design stage based on a modified Hooke-Jeeves method followed by FEM inspection. Furthermore, because the cogging torque and total torque ripples are not satisfactory, a FEM embedded hybrid design procedure is defined, that uses FEM calculated values and under-relaxation coefficients to go back and correct the geometrical/electromagnetic variables that have major impact upon the aforementioned characteristics. A new sensorless control strategy, based on six-step commutation and trapezoidal current command is proposed. The necessary information is obtained by processing only the current and voltage measurements data from the d.c. link.

Both motor design and control strategy conception, as integrated part of the automotive air conditioning compressor electric drive chosen as case study, must comply with specific requirements: low cost, compact size, high efficiency and practical implementation.

Acknowledgements

"The Ph.D. thesis was partially supported by the strategic grant POSDRU/88/1.5/S/50783 (2009) within the Sectoral Operational Programme Human Resources Development, Romania, co-financed by the European Social Fund – Investing in People".

First of all I wish to express my gratitude to my supervisor Prof. Ion Boldea for giving me the chance to be part of his research team, for his guidance, support and fruitful ideas, that made this work possible. Secondly, I would like to thank Assoc. Prof. Tutelea Lucian who also had a major contribution to my engineering education.

I also wish to thank Prof. Frede Blaabjerg for his support during the three months PhD internship at Aalborg University, Denmark.

Many thanks to all my colleagues from the Power Electronics and Motion Control research team.

Most of all, I want to express my love and appreciation for my family and my husband, Ciprian; without their encouragement and understanding, this period would have been much harder.

Timișoara, September 2012

Anamaria Ungurean (Munteanu)

Ungurean (Munteanu), Anamaria

An Automotive Air Conditioning Compressor Electric Motor Drive

Teze de doctorat ale UPT, Seria 6, Nr.30 , Editura Politehnica, 2012, 188 pagini, 100 figuri, 18 tabele.

ISSN: 1842-7022

ISBN: 978-606-554-524-3

Keywords: automotive, compressor, surface permanent magnet synchronous motor (SPMSM), concentrated (non-overlapped) windings, cogging torque, finite element method, sensorless control, starting method

Abstract

The present thesis wishes to offer a possible solution for the automotive air conditioning compressor electric motor drive. The low cost, high efficiency, compact size and practical implementation constraints are considered for the two major research direction that arise- motor design and control strategy. The thesis includes the design methodology for a 6 slots/ 8 poles 3 phase permanent magnet synchronous actuator with surface permanent magnets. Classic electromagnetic design is followed by the optimization design stage based on a modified Hooke-Jeeves method and FEM inspection. Furthermore, because the cogging torque and total torque ripples are not satisfactory, a FEM embedded hybrid design procedure is defined, that uses FEM calculated values and under-relaxation coefficients to go back and correct the geometrical/ electromagnetic variables that have major impact upon the aforementioned characteristics. A new sensorless control strategy, based on six-step commutation and trapezoidal current command is proposed. The necessary information is obtained by processing only the current and voltage measurements data from the d.c. link. The proposed method is conceived to comply with the air conditioning compressor drive requirements, but may be applied to other systems with similar characteristics.

Table of contents

Preface	3
Acknowledgement	4
Abstract	4
Table of contents	5
Motivation.....	8
Objectives of the thesis	9
Outline of the thesis	10
Nomenclature	11
List of figures and tables	17
CHAPTER 1	
The Automotive Air Conditioning System And Its Characteristics	20
Abstract	20
1.1. Introduction	20
1.2. The air conditioning system - a trip through time.....	24
1.3. Automotive air conditioning system – today	26
1.3.1. System typical structure.....	26
1.3.2. Principle of operation	27
1.4. The compressor	31
1.4.1. Types of compressors	31
1.4.2. The reciprocating piston type compressor	34
1.4.3. The four-cylinder radial type compressor	35
1.4.4. The six-cylinder axial type compressor	35
1.5. Typical drive system for the air conditioning compressor.....	36
1.6. The electrically driven compressor	37
1.7. Requirements for the compressor electric drive	40
1.8. Conclusions	42
References
CHAPTER 2	
6 Slot/8 Pole Synchronous Machine: Analytical Design for a Surface	
Permanent Magnet Motor	46
Abstract.....	46
2.1. Introduction	46
2.2. PM rotors variety	46
2.3. Concentrated winding stator	48
2.4. Preliminary analytical design	51

2.4.1. Topology quality factors	51
2.4.2. Active material selection	52
2.4.2.1. Stator and rotor core.....	52
2.4.2.2. Permanent magnets	53
2.4.3. Design theme	55
2.4.4. Electric and magnetic loadings	55
2.4.5. Some dimensioning guidelines	56
2.4.6. Technological constraints	56
2.4.7. Dimensioning methodology.....	57
2.5. Active materials weights and costs	66
2.6. Thermal verification	67
2.7. Conclusion	68
References	69
CHAPTER 3	
6 Slot/8 Pole Synchronous Machine: Optimal Design for a Surface	
Permanent Magnet Motor	72
Abstract.....	72
3.1. Introduction	72
3.2. The modified Hooke Jeeves optimization method	75
3.3. Optimization results	78
3.4. Conclusions.....	83
References	83
CHAPTER 4	
6 Slot/8 Pole Synchronous Machine: FE Analysis and Embedded FEM for	
direct optimization.....	86
Abstract.....	86
4.1. Introduction	86
4.2. FE analysis of 6/8 SPMSM with trapezoidal current control	87
4.2.1. FE software	87
4.2.2. FE model.....	87
4.2.3. Field distribution	89
4.2.3.1 No-load field distribution	89
4.2.3.2 Field distribution under load	92
4.2.4. No-load phase flux linkage and back-EMF.....	94
4.2.5. Cogging (zero-current) torque calculation	96
4.2.5. Electromagnetic torque calculation	97
4.3. FEM embedded hybrid design methodology.....	98
4.3.1. Cogging torque mitigation	99
4.3.2. Electromagnetic torque optimization.....	101
4.3.3. Stator Notches	102
4.4. Conclusions.....	104
References	104
CHAPTER 5 Suitable control strategies	
107	
Abstract.....	107
5.1. Introduction	107

5.1.1. Scalar (V/f) control of PMSM	108
5.1.2. Vector control of PMSM	110
5.1.3. DTFC of PMSM	111
5.1.4. Rectangular current control of PMSM	111
5.2. Sinusoidal control	112
5.3. Rectangular control	120
5.3.1 Six-step commutation pattern	120
5.3.2 Position information for six-step commutation	121
5.3.3 Novel approach to ZCD determination	121
5.3.4. Proposed sensorless speed control strategy	125
5.3.5. The alignment stage	125
5.3.6 Start-up procedure	127
5.3.7. I-f to sensorless control switching	129
5.3.8. Speed sensorless control	131
5.3.9. Preliminary experimental results	132
5.4. Conclusions	135
References	135
CHAPTER 6 The Experimental Test Platform	140
Abstract	140
6.1. SPMSM prototype	140
6.2. IM loading machine	141
6.3. ABB ACS 600	141
6.4. Incremental encoder	142
6.5. The Supply system	142
6.5.1. Lead-acid automotive batteries	143
6.5.1. Three phase inverter	143
6.6. Sensor box	144
6.7. DS1103	145
6.8. Software	145
6.9. Conclusions	146
References	146
CHAPTER 7 Conclusions and Contributions	147
7.1. Conclusions	147
7.2. Contributions	148
7.3. Future work	148
Appendix	149
Summary in Romanian	179
Author's papers related to the PhD thesis	184
Author's CV	185

Motivation

Going from point A to point B by car, is not anymore just a transportation act, but a driving experience. The automotive industry equips the modern vehicle with an increasing number of electronic and electric devices, in order to enable that "experience", to comply with new required functionalities or general/specific regulations. But the increasing power demand on the vehicle does not come without complementary concerns regarding energy generation, efficient power utilization, or pollution. Giving the economic circumstances, there is a constant interest on how to reduce fuel consumption and benefit from all the secondary advantages this measure could inoculate.

Dedicated electric drives have made their way through, not only for hybrid or electric cars, but also for traditional ones. This is due to the high efficiency, better control, fuel reduction and low maintenance they bring along.

However, equally important constraints are imposed by industrial specificities. Low cost, high efficiency, compact size and practicality are the guidelines to be respected for any research activity carried out in this domain

Motor design and motor control strategy conception are now challenged to align to these requirements simultaneously and come up with useful and practical solutions.

Since the air conditioning system is the largest auxiliary consumer on the vehicle, its dedicated electric drive will be the target.

The electric motor will be designed in respect to modern engineering practice, while the control strategy tries to offer a motion-sensorless solution.

Objectives

The major objectives of the thesis are:

- to offer a comprehensive overview of the automotive air conditioning system characteristics;
- to identify advantages and requirements for the dedicated automotive air conditioning compressor electric drive
- to choose the right topology for the electric motor needed in the application
- the implementation of the electromagnetic design for a fractional slot concentrated winding permanent magnet synchronous machine case study: a surface permanent magnet synchronous motor with 8 rotor poles and 6 stator slots, with low cogging torque, fed with trapezoidal currents;
- the optimization stage of the prior obtained topology in order to reduce initial cost
- FEM inspection and validation of the resulted prototype
- Methods to mitigate cogging torque amplitude while maintaining the total torque capability
- to propose a new sensorless control method for the SPMSM motor drive system, that should meet all constraints imposed by the application specificities;
- using a safe starting strategy under heavy load torque, called I-f control, with seamless transition to the proposed method;
- experimental validations using advanced laboratory equipments are expected;

Outline of the thesis

The thesis is organized in 7 chapters following the above presented objectives:

The *first* chapter starts by pointing out the acting directions for an efficient power generation and „wise“ energy utilisation on the modern car. Using dedicated electric drives is one of the way, so the air conditioning system, as major auxilliary consumer is targeted. Finally, characteristics and special requirements for the electrically driven compressor are highlited. The *second* chapter presents a synthesis of fractional slot concentrated winding permanent magnet synchronous machines. The suitable topology is derived rationally and the electromagnetic, „classic“ design stage for the 6slot/8poles surface mounted permanent magnet actuator with concentrated windings case study is described. Chapter *three* presents an optimization mechanism, based on a modified Hooke-Jeeves method that aims to take the prioir designed prototype and reduce its initial cost. Chapter *four* deals with the FEM inspection stage, as part of the engineering practice for modern electric machinery design. The large cogging torque amplitude is revealed this way, so the necessity to reduce it arrises. The chapter proposes a new hibrid design methodology, that uses calculated FEM values and under-relaxation coefficients to go back in the analytic/optimal design and modify the geometrical characteristics that may contribute in cogging torque mitigation. On the same time, attention is paid on the total torque the machine has to deliver. Chapter *five* investigates possible control solutions for the given prototype, whose back-emf shape is neighter sinusoidal, neighter trapezoidal. A speed vector control is developed, but making use of an encoder. The strategy is used to determine the prototype’s torque capability and efficiency. Since it would be less expensive to implement a rectangular/trapeziudal current based control, a novel snesorless cpeed control strategy based on six-step commutation that only uses d.c. link measurement is proposed. In chapter *six* the test platform (from UPT) used for the experimental work is briefly described, while chapter *seven* summarizes the work and the conclusions, original contributions and future perspectives.

Nomenclature

Abbreviations

2D	Two-dimensional;
A/C	Air conditioning;
CFC	Chlorofluorocarbon compounds ("Freon");
CFC12(R12)	Dichlorodifluoromethane refrigerant;
CO ₂	Carbon dioxide;
d.c.	Direct current;
DSP	Digital signal processor;
EMF	Electromotive force;
EV	Electric vehicle;
FE	Finite elements;
FEA	Finite elements analysis;
FEM	Finite elements method;
GCD	Greatest common divisor;
HEV	Hybrid electric vehicle;
HFC134a (R134a)	Tetrafluoroethane refrigerant;
HVAC	Heating, Ventilation and Air-Conditioning;
ICE	Internal combustion engine;
IM	Induction machine;
LCM	Least common multiple;
LPF	Low-pass filter;
MMF	Magneto-motive force;
NdFeB	Neodymium Iron Boron – alloy;
No _x	Nitric oxides;
PI	Proportional-Integral controller;
PM	Permanent magnet;
PWM	Pulse width modulation;
PMSM	Permanent magnet synchronous motor;
SPMSM	Surface Permanent magnet synchronous motor;

Symbols

A_{frame}	Motor frame area	m^2
A_g	Airgap area	m^2
A_s	Slot area	m^2
a	Number of parallel current paths	-
B	Magnetic flux density	T
B_g	Air-gap flux density	T
B_r	Remanence or remanent magnetic flux density	T
B_{st}	Stator tooth magnetic flux density	T
B_{ys}	Stator yoke magnetic flux density	T
B_{yr}	Rotor yoke magnetic flux density	T
B_r	Remanence or remanent magnetic flux density	T
C_a	Specific price additional laminations cost	USD/kg
C_{lam}	Specific price for laminations	USD/kg
C_{pe}	Specific price for power electronics	USD/VA
C_{Co}	Specific price for cooper	USD/kg
C_{PM}	Specific price for PMs	USD/kg
$C_{p_winding}$	Penalty cost for stator overtemperature	USD
C_{p_PM}	Penalty cost for PM demagnetization	USD
C_i	Initial cost	USD
C_e	Energy losses cost	USD
C_p	Penalty cost	USD
C_ϕ	Flux concentration factor	-
d_1	Shoe depth	m
d_2	Wedge depth	m
d_s	Total slot depth	m
D_{si}	Stator inner diameter	m
D_{so}	Stator outer diameter	m
e_a, e_b, e_c	Back-EMF of stator phases a, b, and c	V
e_{max}	peak back-emf	V
f	Frequency	Hz
f_e	Electric frequency	Hz

f_{isp}	Specific tangential force	N/m ²
g	Air-gap length, radial	m
g_c	Effective airgap length (Carter coefficient calculation)	m
h_{PM}	PM height	m
H	Magnetic field intensity	A/m
H_c	Coercivity or coercive field strength	A/m
i_a, i_b, i_c	Currents of stator phases a, b, and c	A
i_{dc}	DC current	A
I_{ph}	Phase current	A
I_s	Slot peak current	A
J	Inertia of the motor shaft and the load system	kg·m ²
j_{Co}	Current density	A/m ²
k_1, k_2	Under-relaxation (correction) coefficients	-
k_c	Carter coefficient	-
$k_{cogging}$	Cogging torque factor	-
k_{cp}	Slot filling factor	-
k_d	Distribution factor	-
k_f	cooling factor	-
k_e	Coil span factor	-
k_{ml}	Magnet leakage factor	-
k_p	Coil span factor	-
$k_{quality}$	Global topology factor	-
k_{st}	Stack filling factor	-
k_w	Winding factor	-
l_{stack}	Stack length	m
l_{turn}	Coil turn length	m
L_e	End turn inductance	H
L_g	Airgap inductance	H
L_{ph}	Phase inductance	H
L_s	Slot leakage inductance	H
m_{Cu}	Weight of copper	kg
m_{PM}	Weight of permanent magnets	kg
m_{Fe}	Weight of total iron laminations	kg

14 Nomenclature

m_{rFe}	Weight of rotor core	kg
m_{sFe}	Weight of stator core	kg
n_s	Number of turns per phase	-
N_{ph}	Phase number	-
N_{PM}	Number of rotor poles	-
N_s	Number of stator slots	-
N_{sm}	Number of slots/pole	-
N_{sp}	Number of slots/phase	-
N_{ssp}	Number of slots/pole/phase	-
n_b	Mechanical rated (base) speed	rpm
P_c	Permeance coefficient	-
ρ_e	Energy cost	USD/kWh
ρ_f	Power factor	-
P_r	Copper (resistive) losses	W
P_{cl}	Iron losses	W
P_n	Rated power	W
P_s	Supplementary loss (due to friction)	W
q_s	Slot heat density	W/m ²
q_{st}	Stator heat density	W/m ²
R_e	End turn resistance	Ω
R_{ph}	Phase resistance	Ω
R_s	Slot resistance	Ω
R_{ri}	Rotor inner radius	m
R_{ro}	Rotor outer radius	m
T_e	Electromagnetic torque	Nm
$t_{operating}$	Operating time	years of use
T_{PM}	PM temperature	$^{\circ}\text{C}$
T_{PMad}	Maximum admissible PM temperature	$^{\circ}\text{C}$
T_w	Winding temperature	$^{\circ}\text{C}$
T_{wad}	Maximum admissible winding temperature	$^{\circ}\text{C}$
V_{st}	stator steel volume	m ³
w_{bi}	Stator back-iron width (yoke width)	m
w_s	Stator slot width (slot mouth)	m

W_{sb}	Stator bottom slot width	m
W_{si}	Stator slot width inside shoe	m
W_{tb}	Stator tooth width	m
W_t	Stator tooth width at airgap (shoe width)	m

Greek letters

a_{cp}	Coil-pole ratio	-
a_m	Magnet fraction	-
a_s	Slot fraction inside shoe	-
a_t	Heat transfer coefficient	W/m ² ·°C
ε	Coil span angle	rad
η	Efficiency	%
λ	Permeance factor	-
λ_{PM}	Flux linkage due to permanent magnet	Wb
Φ_g	Air-gap flux created by permanent magnets	Wb
Φ_{PM_0}	No load total PM flux	Wb
Φ_{PM_demag}	Total PM flux at maximum demagnetization current	Wb
γ_{Co}	Copper mass density	kg/m ³
γ_{Fe}	Iron mass density	kg/m ³
γ_{PM}	PM mass density	kg/m ³
ρ_{Co}	Copper resistivity	Ωm
μ	Permeability	H/m
μ_r	Relative permeability	-
μ_0	Permeability of air (vacuum, $4 \cdot \pi \cdot 10^{-7}$)	H/m
τ_c	Coil pitch	m
τ_p	Pole pitch	m
τ_s	Slot pitch	m
ω_e	Electrical angular speed	rad/s
ω_m	Mechanical angular speed	rad/s
θ_e	Electrical rotor angle coordinate (position)	rad
θ_m	Mechanical rotor angle coordinate (position)	rad
θ_p	Angular pole pitch	rad

16 Nomenclature

θ_s	Angular slot pitch	rad
θ_{se}	Angular slot-pole pitch	rad
ψ	Flux linkage	Wb
$\psi_{a_r}, \psi_{b_r}, \psi_c$	Total flux linkage of stator phases a, b, and c	Wb

Subscripts

$a;b;c$	Stator a,b,c phases;
avg	Average value;
m	Mechanical quantity;
req	Required value;
s	Stator quantity;
r	Rotor quantity;

Superscripts

*	Reference quantity;
^	Estimated quantity;

List of figures and tables

Nr. crt	Figure no.	Figure title	page
1	Figure 1.1.	Electric and electronic device systems on the modern cars [1.1]	20
2	Figure 1.2.	Electric power demand [1.2]	21
3	Figure 1.3.	Hybrid car operating principle [1.4]	22
4	Figure 1.4.	Early automobiles [1.10]	24
5	Figure 1.5.	Air conditioning system components on a car [1.11]	27
6	Figure 1.6.	Pressure/temperature curve R134a [1.7]	28
7	Figure 1.7.	Ideal vapour compression cycle [1.7]	29
8	Figure 1.8.	Automotive air conditioning system – operation diagram	30
9	Figure 1.9.	Reciprocating Piston Fixed Displacement Compressor [1.14]	32
10	Figure 1.10.	Trough vane Compressor [1.15]	33
11	Figure 1.11.	Scroll type Compressor [1.16]	33
12	Figure 1.12.	Operating cycles for a reciprocating compressor [1.14]	34
13	Figure 1.13.	Through view for a four-cylinder radial type compressor [1.14]	35
14	Figure 1.14.	Through view for a six-cylinder axial type compressor [1.14]	36
15	Figure 1.15.	Typical belt drive systems for the air conditioning compressor [1.19]	37
16	Figure 1.16.	Impact on fuel consumption – comparative study [1.21]	38
17	Figure 1.17.	Air-conditioning system diagram (with electric driven compressor) [1.20]	39
18	Figure 1.18.	Section through Delphi Electric Compressor: 1 - Scroll Compressor, 2 - Permanent Magnet Motor 3 - Inverter and Integrated Electronics [1.22]	39
19	Figure 1.19.	Semi-integrated packaging configuration for the compressor drive [1.23]	40
20	Figure 1.20.	Clutch cycle time for Ford Escort	41
21	Figure 2.1.	Typical PM rotor topologies: a) Surface PM (SPM) synchronous machine. (b) Surface inset PM (SIPM) synchronous machine. (c) Interior PM (IPM) synchronous machine. (d) Interior PM synchronous machine with circumferential orientation [2.6]	47
22	Figure 2.2.	B-H curve for SURA M800-50A	52
23	Figure 2.3.	Specific total losses versus frequency at 1.5 T (peak).	53
24	Figure 2.4.	Specific total losses versus peak flux density at 400 Hz.	53
25	Figure 2.5.	Demagnetization curves for NdFeB family	54
26	Figure 2.6.	Cross-section of a surface permanent magnet synchronous motor	58
27	Figure 2.7.	Stator slot geometry	59
28	Figure 2.8.	Rotor configuration	60
29	Figure 3.1.	Optimal design flow chart [3.1]	73
30	Figure 3.2.	Search and gradient movement considering a 2d optimization problem [3.1]	78
31	Figure 3.3.	Geometrical variable variation (inner and outer stator diameter and stack length)	79
32	Figure 3.4.	Geometrical variable variation (airgap, slot opening and tooth neck and wedge heights)	79
33	Figure 3.5.	Geometrical variable variation (slot depth, slot width and PM height)	79
34	Figure 3.6.	Objective function variation	80

18 List of figures and tables

35	Figure 3.7.	Rated efficiency variation	80
36	Figure 3.8.	Losses (copper and iron) variation	80
37	Figure 3.9.	Mass evolution (PM and total)	81
38	Figure 4.1.	Detail on finite elements mesh and material definition	88
39	Figure 4.2.	Winding schematic	89
40	Figure 4.3.	Flux line pattern for no-load, d -axis alignment	90
41	Figure 4.4.	Flux density distribution for no load, d -axis alignment	90
42	Figure 4.5.	Airgap flux density for no-load, d -axis alignment	91
43	Figure 4.6.	Flux line pattern for no-load, q -axis alignment	91
44	Figure 4.7.	Flux density distribution for no load, q -axis alignment	92
45	Figure 4.8.	Airgap flux density for no-load, q -axis alignment	92
46	Figure 4.9.	Flux line pattern for rated load condition and d -axis alignment	93
47	Figure 4.10.	Flux density distribution for rated load condition and d -axis alignment	93
48	Figure 4.11.	Airgap flux density distribution for rated load condition and d -axis alignment	94
49	Figure 4.12.	FEM-calculated no-load phase flux linkages	94
50	Figure 4.13.	FEM-calculated phase back-EMF constant k_E versus rotor angular mechanical position	95
51	Figure 4.14.	Cogging torque variation for the given SPMSM prototype	96
52	Figure 4.15.	Phase current variation versus rotor mechanical position	97
53	Figure 4.16.	Electromagnetic torque versus rotor mechanical position	98
54	Figure 4.17.	Cogging torque (a) and back-emf constant (b) for minimum slot opening	100
55	Figure 4.18.	Electromagnetic torque variation versus rotor mechanical angle	101
56	Figure 4.19.	Resulted cogging torque after FEM induced corrections	102
57	Figure 4.20.	Cogging torque comparison: initial, optimized and with notches	103
58	Figure 4.21.	"Final" electromagnetic torque	103
59	Figure 5.1.	Full positioning system – control structure [5.2]	108
60	Figure 5.2.	V/f (scalar) control for PM - SM with torque angle increment [5.3]	108
61	Figure 5.3.	V/f control system with two stabilizing loops control [5.4]	109
62	Figure 5.4.	Basic speed vector control of PM – SM: 1 - with motion sensor, 2 - sensorless [5.3]	110
63	Figure 5.5.	Direct torque and flux control (DTFC) of PM - SMs: 1 - with motion sensor, 2 - sensorless [5.3]	111
64	Figure 5.6.	Rectangular current control of BLDC [5.3]	112
65	Figure 5.7.	Speed vector control with encoder – general overview	112
66	Figure 5.8.	Torque command(estimated) for 3000 [rpm]	113
67	Figure 5.9.	Input and output powers	114
68	Figure 5.10.	Battery current and voltage variations	114
69	Figure 5.11.	dq currents and voltages	115
70	Figure 5.12.	Efficiency as function of speed and torque	115
71	Figure 5.13.	No-load start-up to 1000 [rpm] (speed and torque variation)	117
72	Figure 5.14.	No-load start-up to 2000 [rpm] (speed and torque variation)	117
73	Figure 5.15.	No-load start-up to 3000 [rpm] (speed and torque variation)	118
74	Figure 5.16.	3000 [rpm] operation with 3 [Nm] loading and unloading perturbation (speed and torque variation)	118
75	Figure 5.17.	Battery current and voltage variation for 3000 rpm operation with load perturbation	119
76	Figure 5.18.	Current circulation (sector 1) and equivalent circuits for: a.) on-time; b.) off-time [5.3]	122
77	Figure 5.19.	Battery (d.c.) current (experimental)	122
78	Figure 5.20.	Sector variation determined from encoder and from the	123

		battery current information (experimental)	
79	Figure 5.21.	Battery voltage waveform	124
80	Figure 5.22	Sinusoidal (a.) and trapezoidal (b.) phase bmf variation in respect to the rotor electrical position and corresponding phase currents	124
81	Figure 5.23.	Sensorless control strategy – principle schematic	125
82	Figure 5.24.	Rotor position (one pole-pair) during two sectors	126
83	Figure 5.25.	Motor start-up to -400 rpm: a). without alignment procedure and b). with alignment procedure (experimental)	127
84	Figure 5.26.	I-f starting principle	128
85	Figure 5.27.	Commutation during start-up	128
86	Figure 5.28.	Battery voltage variation (experimental) (a) and ZCD points(b)	129
87	Figure 5.29	Correction algorithm	130
88	Figure 5.30.	Synchronized motor after correction implementation (experimental)	131
89	Figure 5.31.	Speed errors for 800 rpm operation	132
90	Figure 5.32.	a)Start-up at 400 rpm, 0.6Nm load; b) zoom-in for a)	133
91	Figure 5.33.	Speed step response – 400-800-1200 rpm	133
92	Figure 5.34.	Speed response for “stronger” back-emf compensaion	134
93	Figure 5.35.	3Nm load perturbation for 800 rpm operation	135
94	Figure 6.1.	SPMSM prototype and IM loading machine on the test-bench	140
95	Figure 6.2.	ABB ACS 600 frequency converter	142
96	Figure 6.3.	Series connected lead-acid Bosch automotive batteries	143
97	Figure 6.4.	BPI inverter with custom build interface board and optic connection PCB	144
98	Figure 6.5.	Sensors box	144
99	Figure 6.6.	DS1103 PPC Controller Board [6.4]	145
100	Figure 6.7.	Control Desk interface	146

Nr. crt	Table no.	Table title	page
1	Table 1.1.	Automotive electric power requirements, an example [1.12]	23
2	Table 1.2.	Comparison between R12 and R134a refrigerant properties	28
4	Table 1.3.	Typical Performance Specifications for R134 air conditioning system	41
5	Table 2.1.	Winding factors for concentrated windings	50
6	Table 2.2.	Material properties for iron core laminations	52
7	Table 2.3.	Material properties for NdFeB family	53
8	Table 2.4.	Additional material properties for NdFeB 31/25	54
9	Table 2.5.	Dimensions and properties of the designed SPMSM	68
10	Table 2.6.	Machine parameters (analytical calculation)	68
11	Table 3.1.	Dimensions and properties of the designed SPMSM	82
12	Table 3.2	Machine parameters (analytical calculation)	82
13	Table 5.1.	Acquisition data for generator mode experiments	116
14	Table 5.2.	Soft switching six-step commutation table	120
15	Table 6.1.	Some SPMSM parameters	141
16	Table 6.2.	IM parameters	141
17	Table 6.3.	Incremental encoder characteristics [2]	142
18	Table 6.4.	Battery characteristics	143

CHAPTER 1

The Automotive Air Conditioning System And Its Characteristics

Abstract

This chapter offers a comprehensive overview of the automotive air conditioning system, its characteristics and requirements. A brief introduction regarding the numerous electric and electronic devices mounted on the modern automobile is realized in section 1 and the reason for choosing the climate control system as point of interest is given. A hystorical journey to the beginnings of the automotive air conditioning technology is realized in section 2 while the typical system structure is depicted in section 3. The heart component – the compressor – is analysed in section 4 and 5, while section 6 concentrates on the electrically driven compressor, its advantages, requirements and specific characteristics.

1.1. Introduction

The car of the present days, it's not only a comfortable mean of transportation, but also a specialized assemble that makes driving more entertaining



Figure 1.1. Electric and electronic device systems on the modern cars [1.1]

and easier. The automotive industry has equipped the modern car with devices that assist the driver in difficult manoeuvres, offer guidance in finding a specified location, ensure a comfortable and entertaining climate indoors, make fuel consumption more efficient and contribute for low-level CO₂ emissions

Figure 1.1. offers an overview of the electric/electronic gadgets mounted on the present "smart cars" [1.1].

It is needless to mention that each new functionality implemented on the car comes to enlarge the power demand. According to studies and forecasts carried out by Delphi Automotive Systems, the electric power demand will continue to increase (see Figure 1.2), especially if we are considering hybrid automobiles that use an electric motor for propulsion (referred in the graph under „with propulsion”).

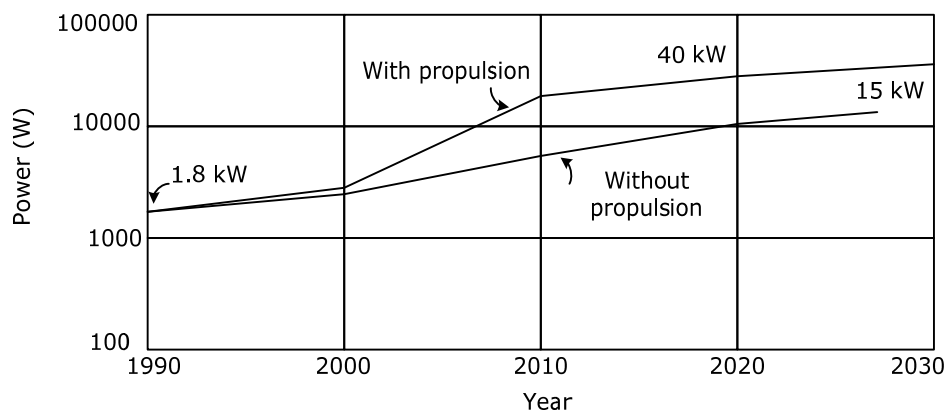


Figure 1.2. Electric power demand [1.2]

Since approximately 26.6% of the energy consumption worldwide is due to transportation (common and individual), it is more than evident that diligent efforts are carried out in order to come up with new solutions and assure an efficient power management. Traditional power sources predicted levels, polluting regulations and new technologies for regenerable power supplies have determined the evolution trend in the automotive industry. Three main directions are to be identified: electric cars, hybrid cars and several innovative systems for the so-called „traditional” cars.

Electric cars produce no tailpipe emissions, reduce our dependency on oil, and are cheaper to operate. Of course, the process of producing the electricity moves the emissions further upstream to the utility company’s smokestack—but even dirty electricity used in electric cars usually reduces our collective carbon footprint [1.4]. The car’s autonomy is around 100km (instead of about at least 500 km for traditional cars, depending on the fuel tank capacity), but the cost of utilization is almost six times lower if we are considering only „fuel expenses”. Furthermore, regular replacement of different filters and other maintenance operations required for internal combustion engine equipped cars are now eliminated. There is still the „refilling” problem left; at the gas station it takes only a few minutes, while recharging your car from the home electricity socket may take up to 8 hours. Research is carried out in order to obtain fast-charging stations, but the lack of such „electric power points” wide infrastructure makes the electric car not suitable for long distance transportation, for now. The almost zero CO₂ and NO_x emissions and no phonic pollution (a newly introduced defilement category) along

with the low operating costs are surely the attributes that will propel this type of car in the top of the future means of individual transportation. Still, because of the disadvantages mentioned before (even though they will be overcome by future engineering research), this solution falls outside the interest field, for the given research theme.

Hybrid cars, also referred as HEVs in the literature, introduce supplementary an electric motor for propulsion and an additional rechargeable battery pack. The operating principle is depicted in Figure 1.3 [1.4]. This new configuration can reduce fuel consumption by almost 50% and it is becoming more and more popular. Yet, another improved solution is trying to make its way on the car market – the „plug-in hybrid car” – which offers the possibility to recharge the additional batteries as in EVs (electric vehicles).

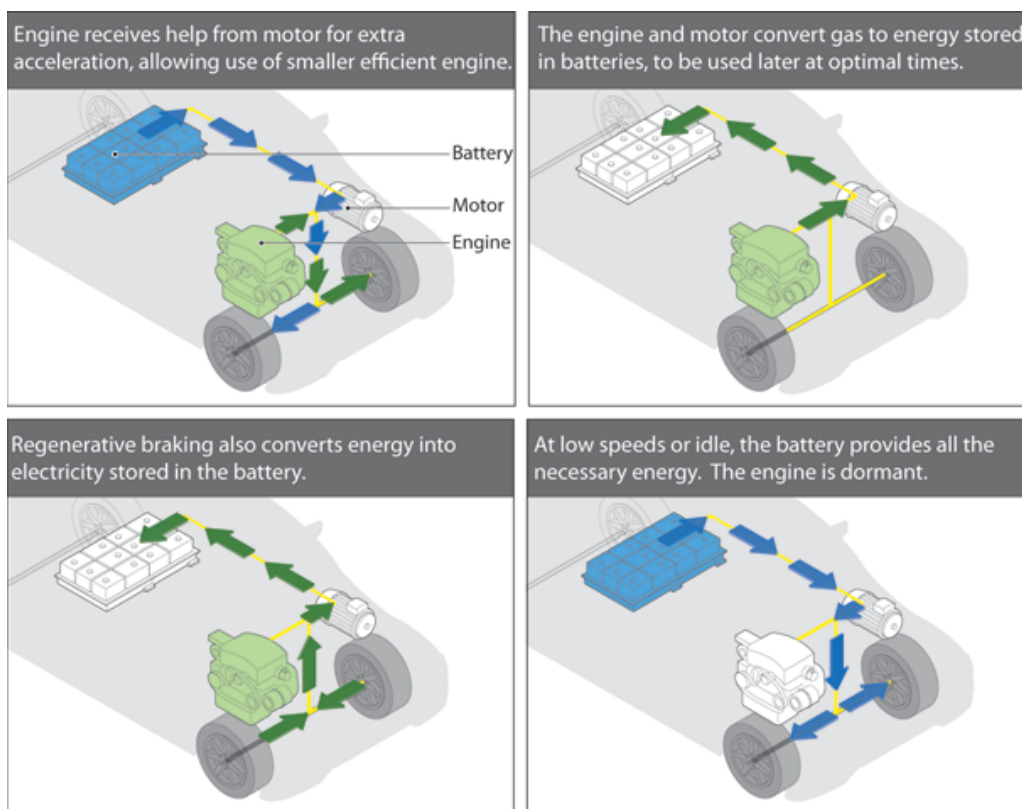


Figure 1.3. Hybrid car operating principle [1.4]

So hybrid vehicles have enabled us to make a huge step when it comes to fuel expenses reduction. The question that arises immediately is if we can push that 50% limit of savings even further.

There has already been noticed the advanced tendencies of car electrification, having into consideration not only the numerous electric devices but also the will to replace mechanical/hydraulic drives with electric ones in order to fulfil certain functionalities.

The reasons that govern these changes are related to the resulting high performance offered by electric systems instead of the traditional ones. Just as the lightning comes before thunder, the electrical system assures a shorter time response over the mechanical one. This becomes essential for safety applications – active or passive. Furthermore, the longer life-time guarantee and the higher efficiency are only some of the important “changing factors”.

An example for some of the electric power demanders on the modern car is given in Table 1.1 [1.12].

Electric Loads	Peak Power (kW)	Average Power (kW)
Electric vehicle/ hybrid electric vehicle propulsion	30–100	10–30
Fuel-cell electric vehicle air compressor	12	8
Active suspension	12	0.36
Integrated starter generator	4 - 8	2 - 4
Electric AC compressor	4.0	1.0
Variable engine valve	3.2	1.0
Heated catalytic converter	3.0	0.1
Heated windscreen	2.5	0.25
Electric power steering	1.5	0.1
Engine cooling fan (ICE)	0.8	0.4
Engine coolant pump (ICE)	0.5	0.4

Table.1.1. Automotive electric power requirements, an example [1.12]

It is important to specify that “auxiliary consumers” are considered the ones that have no implication in vehicle traction and/or propulsion, which, after all, is the main functionality the car is accomplishing as mean of personal transportation.

Since the modern car becomes a more and more intricate assemble with numerous auxiliary consumers, there has been a continuous interest in what can be synthetically called “automotive electric power and energy generation and management”. Alternative fuels are obtained, new technologies are implemented for the future batteries, a two-voltage-level power bus system is considered for the car and new optimization algorithms to efficiently use the limited available power are implemented.

So, on one part there are the power generators (improved, but with limitations) and on the other part, the increasing number of energy consumers, that require different power levels, at different moments of time, in accordance to their operating cycle. In between the two, the “power management” comes to deal with the power circulation in the automobile. The constraints in automotive electric power management systems are imposed by several key factors, including the following [1.12]:

- dynamic resource allocation requirement;
- practical component constraints;
- uninterruptible power availability requirement;
- power quality requirement;
- system stability requirement; and
- fault diagnosis and prognosis requirement.

The actual research will concentrate on the second factor afore mentioned. Components in vehicle power systems usually have practical limitations and impose constraints to the optimisation of power and energy management algorithms. A battery – the most common energy storage device in vehicles – has a limited power and energy capacity and, more importantly, a life cycle and sensitivity to temperature. Electric machines are used in vehicle drivetrains both as motors and generators. The power output and efficiency of these electric machines are not fixed but are functions of machine speed, torque and temperature. These limitations and constraints have a direct impact on the optimisation of the power management system.

So, one of the key for a successful power management should be to analyse better all the auxiliary systems that make use of electric drives and try to rise their efficiency and contribute this way, eventually, to another supplementary fuel reduction. This activity will have a positive impact on all types of vehicles, from traditional to HEV and electric; no matter which solution will be chosen in the future for propulsion/traction, additional consumers will continue to be present.

Before jumping courageously to analyse this electric-gadget-thicket, having in mind only our “noble purpose”, one should take into account objective limitations. The effort will be concentrated only on the air conditioning system, which is blamed to consume from 5% up to 10% of the total fuel [1.3], [1.5] for traditional cars. Consequently, the research will be focused to improve one of the largest auxiliary power consumers to be found on the automobile.

1.2. The air conditioning system - a trip through time

After the invention of the automobile has surpassed the horse drawn carriage and open cabin spaces were replaced by closed cabin spaces, the first heating, cooling and ventilating systems were introduced in order to meet customer expectations. Heating clay bricks placed inside the vehicle or simple fuel burners to



Figure 1.4. Early automobiles [1.10]

add heat to the vehicle's interior were the first attempt for the „warming functionality“. Ventilation inside the vehicle was achieved through opening or tilting windows or the windscreen; vents were added to doors and bulkhead to improve air circulation panels were the equivalent to our modern air ducts. Air flow was difficult to control because it was dependent upon the vehicle speed and sometimes would allow dirty, humid air which contained fumes to enter the interior from the engine compartment. Cooling could be as simple as having a block of ice inside the vehicle and allowing it to melt! Eventually a number of design problems were overcome, these included air vents at the base of the windscreen for natural flow ventilation and electric motors to increase the flow at low speeds. Eventually heat exchangers were introduced which used either the heat from the exhaust system or water from the cooling system as a source, to heat the inside of the vehicle cabin. Early cabin cooling systems were aftermarket sourced and worked on evaporative cooling. They consisted of a box or cylinder fitted to the window of the vehicle. The intake of the unit would allow air to enter from outside and travel through a water soaked wire mesh grille and excelsior cone inside the unit. The water would evaporate due to absorbing the heat in the air and travel through the outlet of the unit which acted as a feed to the inside of the vehicle.

The water was held in a reservoir inside the unit and had to be topped up to keep the cone wet otherwise the unit would not operate. The air entering the vehicle would be cool if the relative humidity of the air entering the unit was low. If the relative humidity of the air was high then the water could not evaporate. When the unit was working effectively it would deliver cool saturated water vapour to the inside of the vehicle which raised the humidity levels. These units were only really effective in countries with very low humidity [1.7].

The first mechanical automotive A/C system which worked on a closed cycle was introduced by Packard in 1939. The system used a compressor, condenser, receiver drier and evaporator (fitted inside the boot/trunk) to operate the system. The only system control was a blower switch. Packard marketing campaign included: 'Forget the heat this summer in the only air-conditioned car in the world.' The system took up half of the entire trunk space, was not very efficient, and had no thermostat (the compressor operated continuously with no clutch) or independent shut-off mechanism (it was necessary to have the belt removed to disengage the system during the winter months). The option was discontinued after 1941.

Over the period 1940–41 a number of manufacturers made vehicles with A/C systems but these were in small volume and not designed for the masses. It wasn't until after World War II that Cadillac advertised a new feature for the A/C system that located the A/C controls on the rear parcel shelf, which meant that the driver had to climb into the back seat to switch the system off. This was still better than reaching under the bonnet/hood to remove the drive belt.

Installing optional Airtemp air conditioning units to its Imperials in 1953, Chrysler beat Cadillac, Buick and Oldsmobile which added air conditioning as an option in the 1953 model year.

Airtemp was more sophisticated and efficient than the complicated rival air conditioners of 1953. It recirculated, rather than merely cooled, the air inside the vehicle, and it was also the highest capacity unit available on an automobile. It was also simple to operate, with a single switch on the dashboard marked with low, medium, and high positions, which the driver selected as desired. The system was capable of cooling a Chrysler from 48 degrees to 29 degrees in about two minutes, and of completely eliminating humidity, dust, pollen and tobacco smoke at the same

time. Since it relied on fresh air, and drew in sixty percent more of it than any contemporary system, Airtemp avoided the staleness associated with automotive air conditioning at the time. It was silent and unobtrusive. Instead of plastic tubes mounted on the package shelf as on GM and on other cars, small ducts directed cool air toward the ceiling of the car where it filtered down around the passengers instead of blowing directly on them, a feature that modern cars have lost [1.8].

In 1954–55 Nash-Kelvinator introduced air-conditioning for the mass market. It was an A/C unit that was compact and affordable with controls on the dash and an electric clutch [1.7]. Entirely incorporated within the engine bay, the combined heating and cooling system had cold air for passengers enter through dash-mounted vents. Nash's exclusive "remarkable advance" was not only the "sophisticated" unified system, but also its \$345 price that beat all other systems [1.8].

Automatic climate control was introduced by General Motors, who has made a front mounted air conditioning system optional in 1954 on Pontiacs, with a straight-eight engine that added separate controls and air distribution.

Ever since, the number of cars to have air-conditioning systems has continuously increased up to the point when this feature became standard equipment for all new built automobiles.

1.3. Automotive air conditioning system – today

1.3.1. System typical structure

An air-conditioner is a generic term for a unit which maintains air within a given space at a comfortable temperature and humidity. To achieve this, an air-conditioning unit must have a heater, cooler, moisture controller and a ventilator.

The principle of an HVAC (Heating, Ventilation and Air-Conditioning) system:

- heater – adding heat by transferring it;
- cooler – removing heat by transferring it;
- humidity – removing or adding moisture;
- purification – by filtration;
- ventilation – air movement through the vehicle.

The HVAC system creates a comfort zone for the occupants which can be adjusted within a range. The system must provide a way of controlling the climate inside the vehicle which is generally referred to as 'climate control'. An overview of the HVAC system from an automobile is presented in Figure 1.5. The basic elements have each a specific functionality, as follows [1.13]:

- *the compressor*: commonly referred to as the heart of the system, the compressor is usually a belt driven pump that is fastened to the engine; it is responsible for compressing and transferring refrigerant gas.
- *the condenser*: is designed to radiate heat; its location is usually in front of the radiator, but in some cases, due to aerodynamic improvements to the body of a vehicle, its location may differ. Condensers must have good air flow anytime the system is in operation.
- *the evaporator*: located inside the vehicle, it serves as the heat absorption component, still providing several functions; its primary duty is to remove heat from the inside of your vehicle and a secondary benefit is dehumidification. As warmer air travels through the aluminum fins of the cooler evaporator coil, the

moisture contained in the air condenses on its surface; dust and pollen passing through, stick to its wet surfaces and drain off to the outside.

- *the expansion valve*: controlling the evaporator temperature can be accomplished by controlling refrigerant pressure and flow into it with different types of devices; the thermal expansion valve, also known as TXV can sense both temperature and pressure, and is very efficient in fulfilling its functionality.
- *the receiver/dryer*: this device is present only in systems that have a thermal expansion valve; the primary function of the receiver-drier is to separate gas and liquid, the secondary purpose is to remove moisture and filter out dirt
- *the blower*: must assure the good air flow, necessary for the condenser to fulfil its functionality

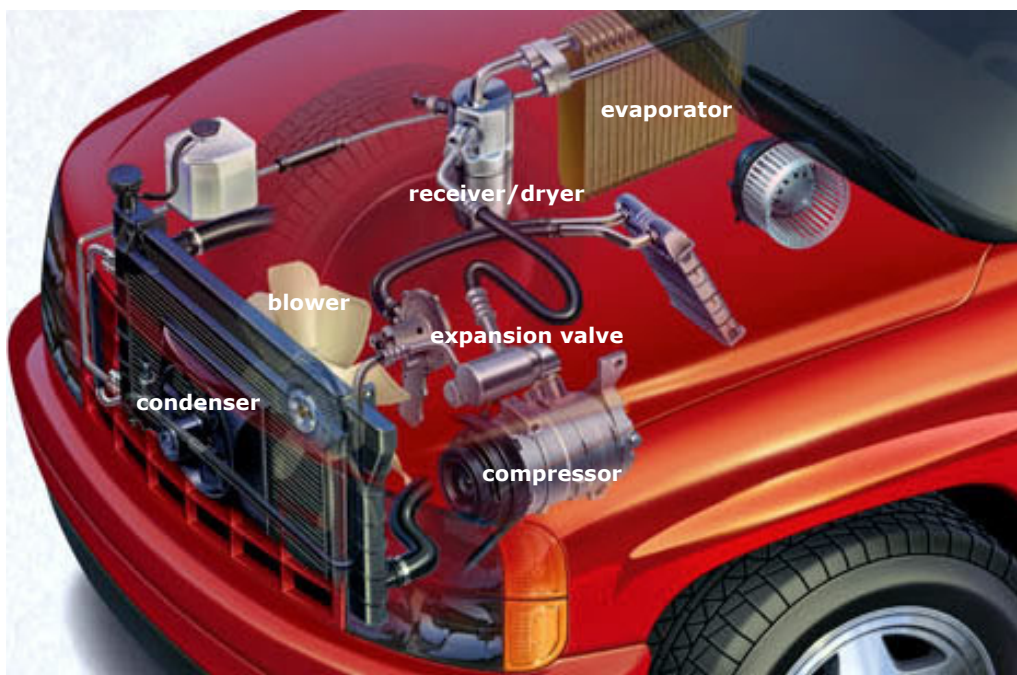


Figure 1.5. Air conditioning system components on a car [1.11]

1.3.2. Principle of operation

The vehicle's climate-control system provides for the following:

- a comfortable climate for all passengers,
- an environment calculated to minimize driver stress and fatigue,
- filters to remove particulate matter (pollen, dust) and even odours from the air,
- good visibility through all windows, and windshield.

The "vital" (working) fluid for the system is the refrigerant. An ideal refrigerant would have the following properties:

1. Zero ozone depleting potential and zero global warming potential,
2. Low boiling point,

3. High critical pressure and temperature point,
4. Miscible with oil and remain chemically stable,
5. Non-toxic, non-flammable,
6. Non-corrosive to metal, rubber, plastics,
7. Cheap to produce, use and dispose.

Widely used refrigerants are CFC12 – dichlorodifluoromethane (also known as R12) and HFC134a – tetrafluoroethane (also known as R134a). Their properties are compared in Table 1.2.

R12	R134a
It is miscible with mineral oils.	It is only miscible with synthetic polyalkylglycol (PAG) lubricants, not with mineral oils.
It does not attack metals or rubber.	It does not attack metals, but attacks certain plastics, so only use special seals
It is not explosive.	It is explosive and inflammable
It is odourless (in concentrations of less than 20%).	It is odourless.
It is not toxic (except in contact with naked flames or hot surfaces).	It is not toxic in low concentrations.
It readily absorbs moisture.	It readily absorbs moisture.
It is an environmentally harmful CFC gas (containing chlorine which destroys the atmospheric ozone layer).	It does not deplete the ozone
It is heavier than air when gaseous, hence the danger of suffocation	It is heavier than air when gaseous, hence the danger of suffocation near the ground.

Table.1.2. Comparison between R12 and R134a refrigerant properties

The graph in Figure 1.6 shows the pressure/temperature curve for refrigerant R134a. The graph shows the refrigerant to be in a gaseous/vapour state

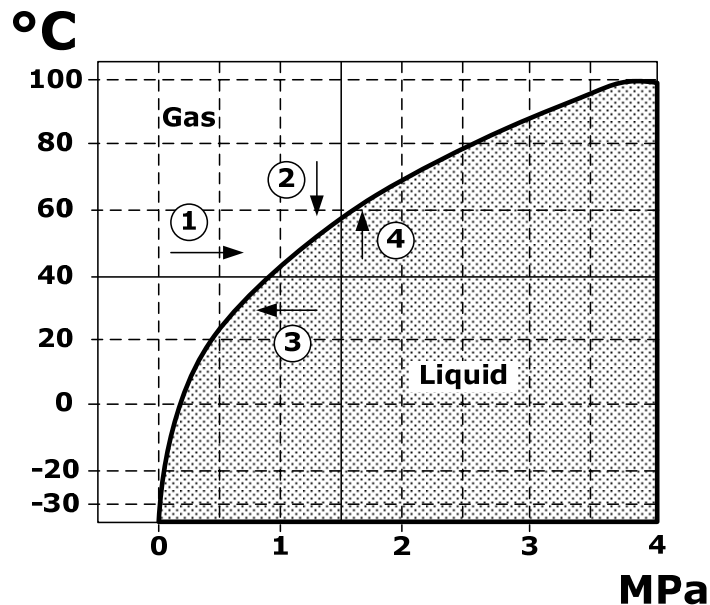


Figure 1.6. Pressure/temperature curve R134a [1.7]

above the curve and in a liquid state below the curve. The curve represents the boiling point of the refrigerant under varying pressure and temperature relationships. The following states are to be identified:

- (1) - The refrigerant is in a gaseous/vapour state and if the temperature is kept constant and the pressure is increased then the refrigerant will condense into a liquid.
- (2) - If the pressure is kept constant and the temperature is reduced then the refrigerant can be condensed into a liquid.
- (3) - If the temperature is kept constant and the pressure is reduced then the refrigerant will evaporate into liquid/vapour.
- (4) - If the pressure is kept constant and the temperature is increased then the refrigerant will evaporate into liquid/vapour.

The A/C system is designed to manipulate these relationships to enable the refrigerant to transfer heat from the cabin space. Currently the most common cycle used in automotive applications is the vapour compression cycle for R12 and R134a closed systems.

In Figure 1.7, the pressure/enthalpy diagram shows the beginning of the cycle as the refrigerant enters the compressor as a 'saturated vapour' at point **1**. The refrigerant is compressed adiabatically (the compressor is 100% efficient and no heat is removed by the process) and becomes a 'superheated vapour' due to the increase in pressure, temperature and enthalpy as shown by point **2**. The refrigerant by this point is above the temperature of the outside air. The refrigerant leaves the

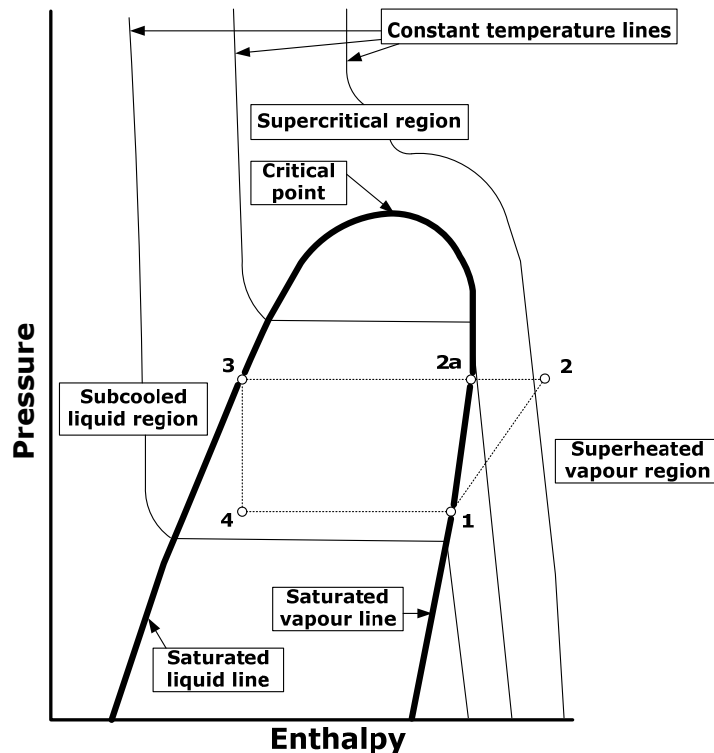


Figure 1.7. Ideal vapour compression cycle [1.7]

compressor and enters the condenser (heat exchanger). The condenser allows the heat to transfer to the outside air effectively removing enough heat to change into a saturated vapour from a superheated vapour point **2a**. This has lowered the temperature of the refrigerant. Now the refrigerant is a 'saturated vapour' the pressure and temperature are kept constant but heat is still being removed and only the enthalpy continues to decrease. The vapour begins to condense to liquid (latent heat of condensation). Condensation continues until all the vapour is a 'saturated liquid' point **3**. The refrigerant leaves the condenser as a saturated liquid and travels to an expansion valve or fixed orifice tube. The refrigerant now undergoes an 'isenthalpic' expansion process (constant enthalpy). The process significantly reduces the temperature and pressure of the refrigerant while the enthalpy remains the same.

The refrigerant flows through the evaporator which acts as a heat exchanger that transfers heat from the air flowing through its fins to the refrigerant flowing through its coils. The refrigerant absorbs the heat increasing in enthalpy while the temperature and pressure remain the same. The liquid refrigerant vaporises until it becomes a 'saturated vapour'. The saturated vapour then travels to the compressor to start the cycle again. A small amount of liquid refrigerant (flash gas) vaporises during expansion but most of the refrigerant is liquid at a temperature lower than that of the outside air (air inside the vehicle or entering the vehicle) point **4**.

The air-conditioning system (with R134a) works on a continuous cycle (see Figure 1.8). The compressor receives low pressure heat laden refrigerant vapour from the evaporator. The compressor pressurises the refrigerant from 0.2MPa to approximately 1.47MPa depending on system demand. This increases the temperature from approximately 0 to 80°C. At this temperature and pressure the refrigerant is above its boiling point of approximately 57°C. The compressor discharges superheated refrigerant vapour to the condenser. The refrigerant flows into the condenser. In the condenser the high pressure vapour condenses into a

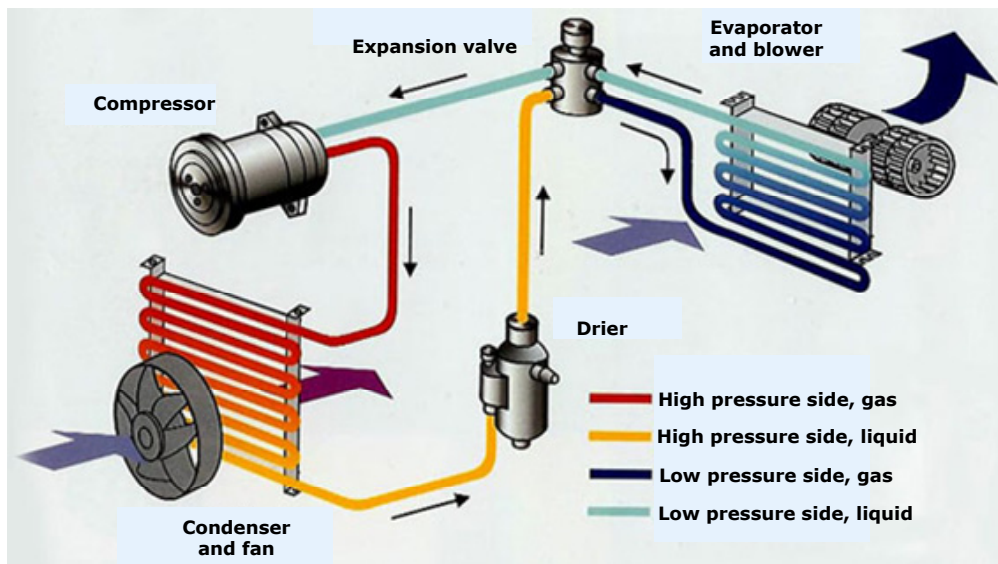


Figure 1.8. Automotive air conditioning system – operation diagram

high pressure liquid. This is achieved by reducing the temperature from, for example, 80°C to below 57°C which is the refrigerant's boiling point. This is achieved by forcing air over the surface of the condenser enabling heat to transfer from the refrigerant to the outside air thus reducing its temperature (sub-cooled). Only refrigerant in the form of a high pressure sub-cooled liquid leaves the bottom of the condenser outlet.

The sub-cooled liquid refrigerant flows into the receiver drier which stores, dries and filters the liquid refrigerant. The sub-cooled liquid refrigerant then flows from the receiver drier to the expansion valve which then changes the refrigerant into low pressure, low temperature liquid/vapour. This is achieved by lowering the pressure using a variable orifice. The orifice has high pressure one side (from the receiver drier) and low pressure the other (evaporator and compressor) and allows a small quantity of refrigerant to flow through it. The sudden drop in pressure and temperature causes some of the refrigerant to vaporise which is called a flash gas. The low pressure low temperature liquid/vapour then flows to the evaporator where the heat is transferred from its surface to the refrigerant through vaporisation. The heat comes from either inside (recycled air) or outside (fresh intake of air) the vehicle and is blown over the evaporator's surface. Once the refrigerant has completely vaporised and reached its saturation point it should still be able to carry more heat. The refrigerant continues to flow through the remainder of the evaporator coils absorbing more heat and becoming slightly superheated. The low pressure low temperature slightly superheated vapour refrigerant flows to the compressor and the cycle repeats itself.

1.4. The compressor

Considered the „heart component“ of the air conditioning system, the compressor is vital for the systems' operation. The function of the compressor is to compress and circulate superheated refrigerant vapour around a closed loop system, as it was explained in the previous section. Compressors vary in design, size, weight, rotational speed and direction as well as displacement. Some compressors are variable displacement and some are fixed. They can be mechanically or electrically driven.

In order to fulfil its functionality in the system the compressor and its drive use 80% of the energy required to operate the air-conditioning system. This means that the compressor drive used in the system will basically determine the overall efficiency of the system. This is particularly important for fuel economy and pollution. This is also the reason why the point of interest for this research is located here.

1.4.1. Types of compressors

Basically, three types of compressors can be identified:

➤ ***piston (reciprocating)***

The reciprocating piston compressor is the most widely used. The basic design (see Figure 1.9) consists of a piston in a cylinder with pressure actuated check valves to control suction and discharge flow through the cylinder. Standard

practice is to have the piston driven by a rod passing through a packing case to seal against pressure leaks. With this double acting design, gas can be compressed on both sides of the piston. The basic design is more than a hundred years old, and is well developed. The throughput and loading can be adjusted by speed variation, addition of clearance to the cylinders, deactivating cylinders to reduce displacement or active control of valve closing, which effectively gives variable control of displacement. Efficiencies of this type of compressor can be more than 85 percentages for conversion of horsepower input to pressure rise.

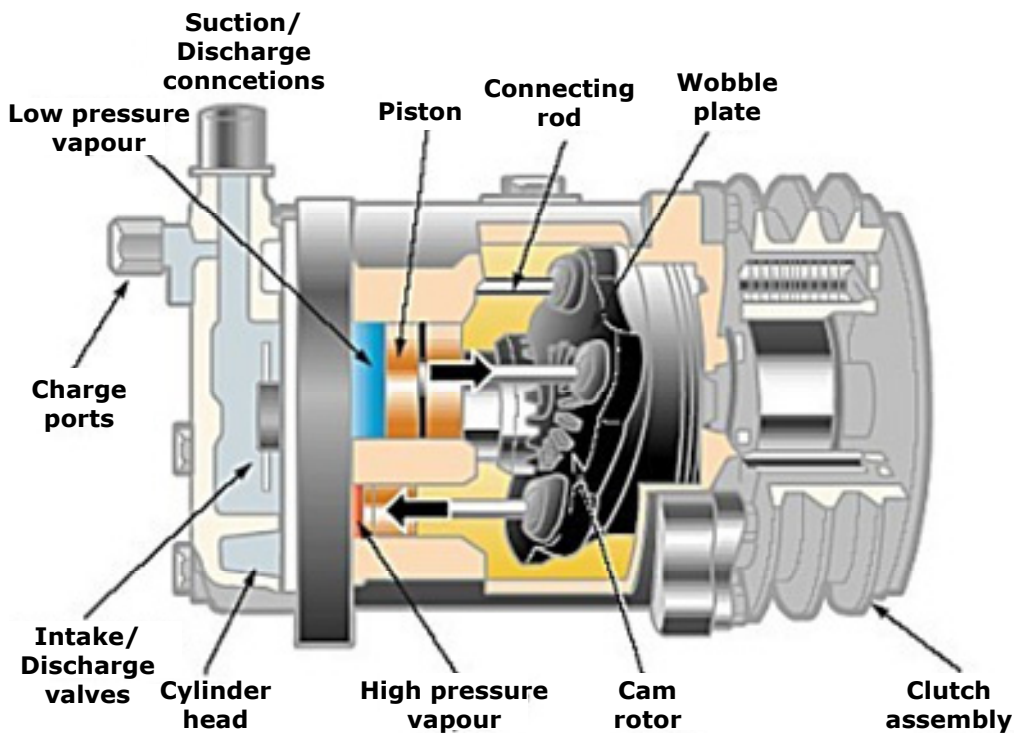


Figure 1.9. Reciprocating Piston Fixed Displacement Compressor [1.14]

➤ **vane**

A vane compressor (see Figure 1.10) consists of a cylindrical chamber with a rotating paddle wheel type drum mounted off centre in the chamber. As the drum rotates, the sliding paddle wheel vanes section off volumes, which decrease in volume as they move toward discharge. A suction port is machined into the area where the chambers have the highest volume, and a discharge port is located where the chambers have the smallest volume. Gas enters at the higher volume and is compressed and discharged at the minimum volume. This type of compressor will tolerate more dirt than a reciprocating unit. They came in two variants: through vane and eccentric vane.

➤ **scroll (rotary)**

The scroll compressor (see Figure 1.11) consists of two helices with one lying within the other. They are both mounted in a cylindrical housing. One helix is

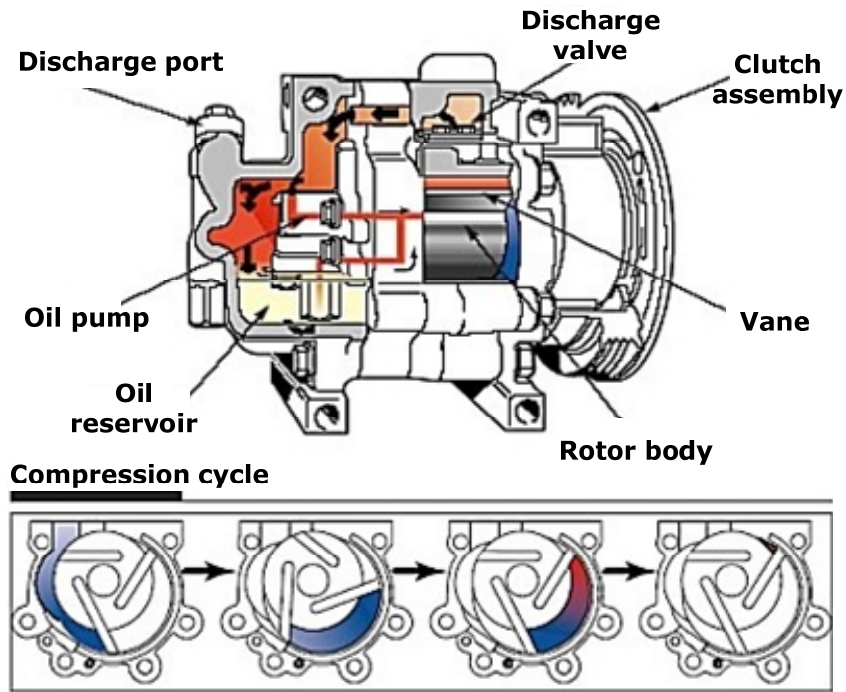


Figure 1.10. Trough vane Compressor [1.15]

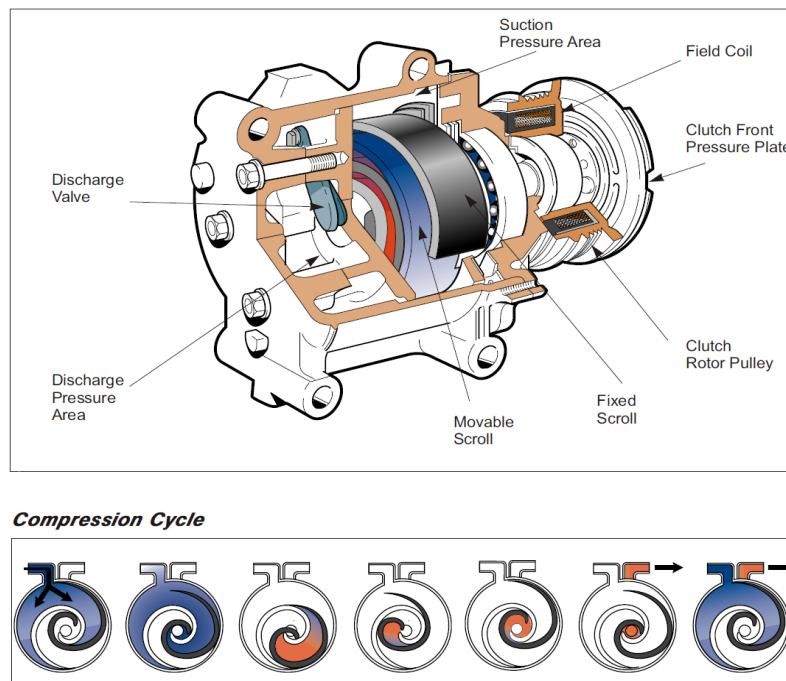


Figure 1.11. Scroll type Compressor [1.16]

fixed and the other is attached to the drive shaft of the compressor. The driven helix does not rotate itself but does orbit the other helix. The two helices through movement create crescent-shaped compression chambers. This compressor also requires oil injection for sealing and cooling. It is designed for high pressure ratios but is usually limited to discharge pressures below 1.82 MPa.

The most common types of compressors used for automotive air conditioning purposes are:

- Two cylinder reciprocating piston type
- Four cylinder RADIAL type
- Six cylinder AXIAL type

1.4.2. The reciprocating piston type compressor

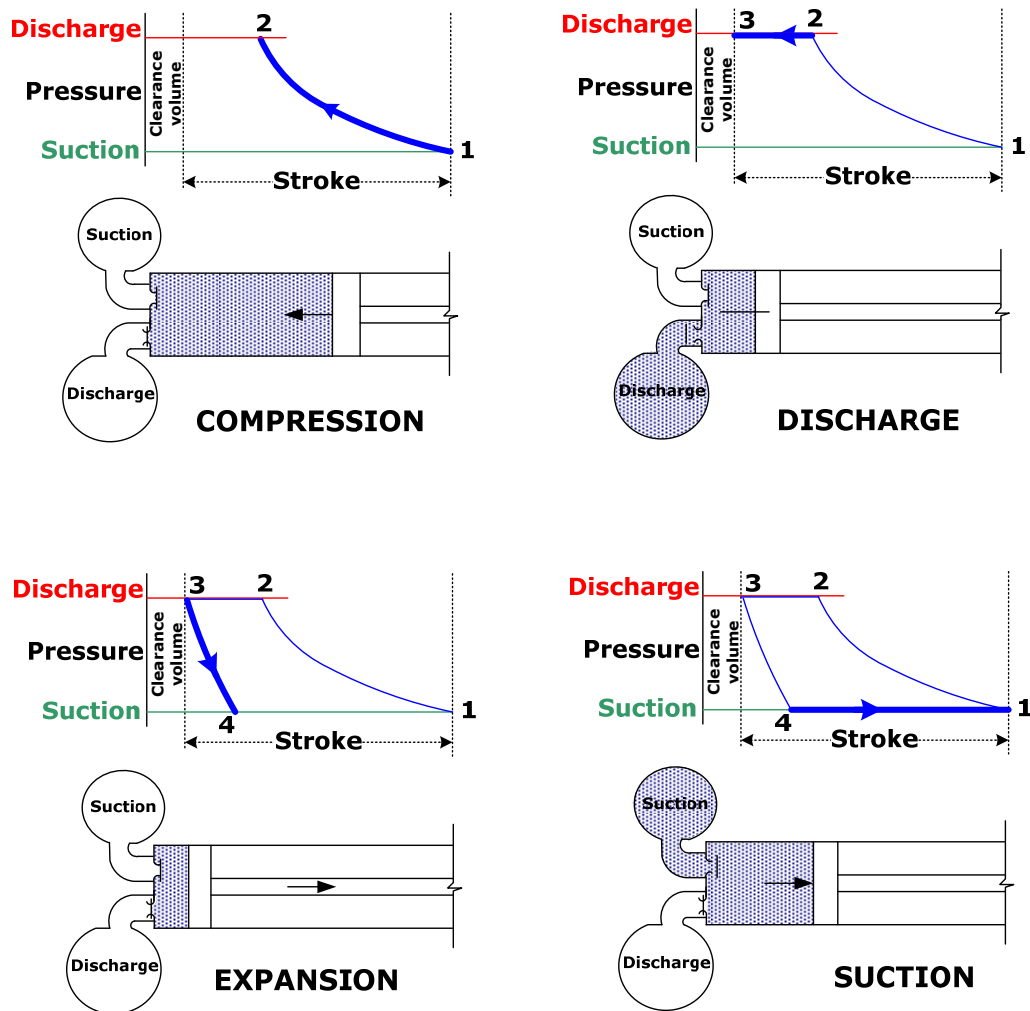


Figure 1.12. Operating cycles for a reciprocating compressor [1.14]

In a reciprocating compressor, the process follows four main events – compression, discharge, re-expansion and intake. The first two are accomplished as the piston moves forward, reducing cylinder volume, while the second takes place as the piston moves back down the cylinder (see Figure 1.12).

If we assume starting the cycle with the compressor at the bottom of its stroke, with maximum cylinder volume. The cylinder is full of gas at suction pressure, and both suction and discharge valves are closed by gas pressure. As the piston moves forward, the cylinder volume decreases and pressure rises. When the cylinder pressure rises slightly above discharge pressure, the discharge valve opens and gas is pushed into the discharge piping for the rest of the stroke. At top centre, the discharge valve closes. As there must be clearance between the piston face and cylinder head to prevent parts hitting each other, some volume of gas is trapped in the cylinder at discharge pressure. As the piston moves back down the cylinder, this gas re-expands until it reaches suction pressure. At this point, the suction valve opens and a fresh charge of gas flows into the cylinder for the remainder of the stroke.

1.4.3. The four-cylinder radial type compressor

The four-cylinder radial compressor (see Figure 1.13) positions four pistons at right angles to each other. The pistons are driven by a central shaft connected to the engine by the electric clutch assembly and V-belt. The radial compact design of the compressor is very popular on the vehicles of today.

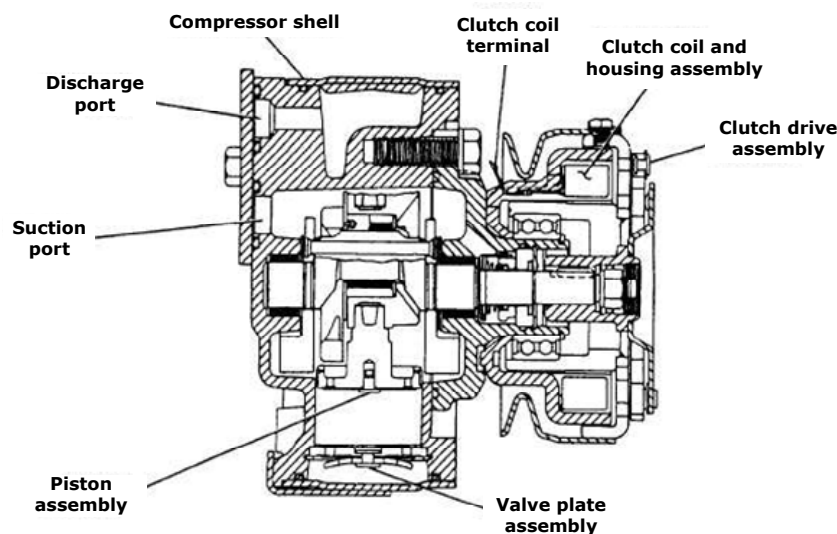


Figure 1.13. Through view for a four-cylinder radial type compressor [1.14]

1.4.4. The six-cylinder axial type compressor

This design uses three double-ended pistons driven by a wobble plate (see Figure 1.14). The three cylinders effectively produce a six-cylinder compressor. As the shaft rotates, the wobble plate displaces the pistons perpendicular to the shaft.

Piston drive balls are used to cut down friction between the wobble plate and pistons. Piston rings, also, are used to aid in sealing.

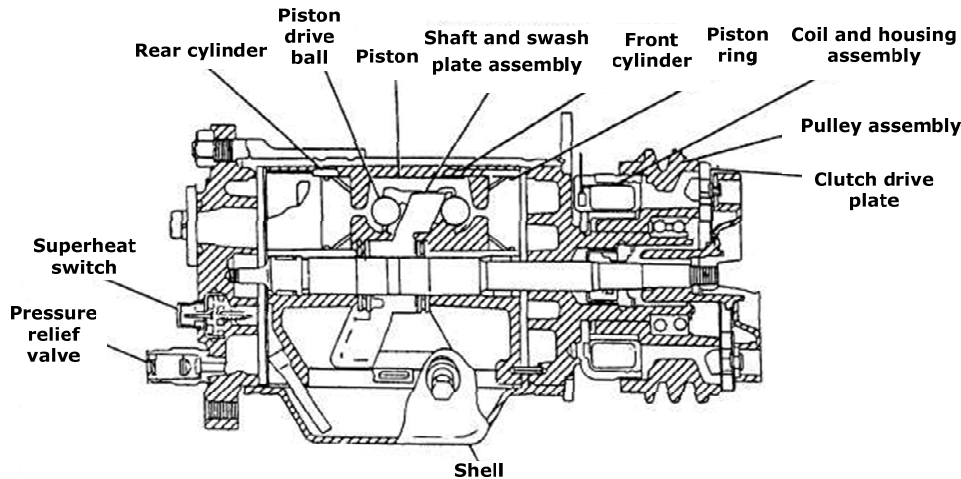


Figure 1.14. Through view for a six-cylinder axial type compressor [1.14]

1.5. Typical drive system for the air conditioning compressor

For „traditional“ configurations, the compressor is driven by the engine crankshaft via a pulley system (see Figure 1.15). The pulley system provides permanent drive to the multi groove drive belt. This means once the engine is started the multi groove drive belt pulley is rotating. There is an air gap between the multi groove drive belt pulley and the drive plate. When the engine is running the compressor is stationary until the A/C button is selected.

The clutch is designed to connect the rotor pulley to the compressor input shaft when the field coil is energized (A/C button on) and transmit the power from the engine crankshaft to the compressor by means of a drive belt. When the clutch is not engaged the compressor shaft does not rotate and refrigerant does not circulate. The field coil is actually an electromagnet, once energized it draws the pressure plate towards it, locking the rotor pulley and the pressure plate together causing the compressor internals to turn, creating pressure and circulating refrigerant.

However, if the air conditioning system is driven this way, some major disadvantages can be identified. The compressor will run with a constant speed, established by the engine crankshaft, not by actual compressor requirements; it is not only the optimal functionality issue involved, but also the lower efficiency that a constant speed control drive has over the variable speed one. On the other hand, every driver has noticed that the car has less power when the climate control system is switched on (apart from the fact that fuel consumption increases); the power required for operating the compressor is taken from the car's engine, affecting this way its performance. Last, but not least, several mechanical coupling related issues can be mentioned, since belts or pulleys need to be replaced after a certain number of kilometres (OEM specific).

So, additional operating costs are added; on one hand by the low efficien-

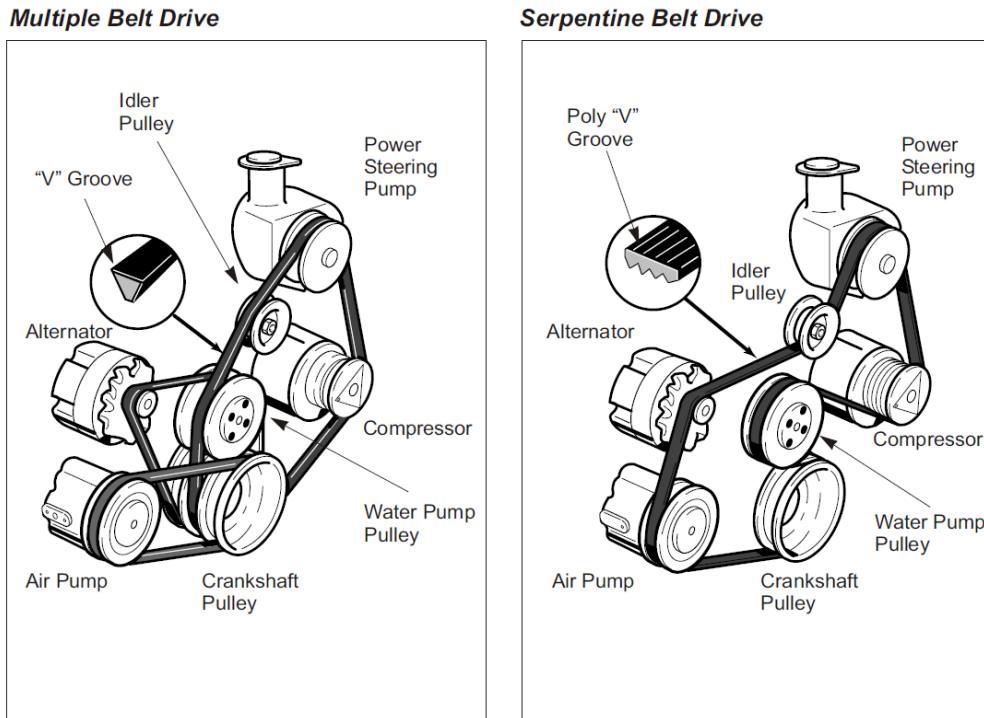


Figure 1.15. Typical belt drive systems for the air conditioning compressor [1.19]

cy the system actually has (the best systems designed do not go over 70%), contributing this way to the increase in fuel consumption, and maintenance costs on the other hand.

Partly, these disadvantages can be overcome by the electric drive system designed for air conditioning compressor. Even though the solution is more suitable for HEVs or electric cars, its implementation on a „traditional“ car brings numerous improvements.

1.6. The electrically driven compressor

The electrically driven compressor has been introduced by hybrid cars like Toyota Prius, Ford Fusion/Mercury Milan, Toyota Camry/Highlander, Lexus GS 450h, Hyundai Sonata, Chevrolet Silverado/Tahoe/Suburban (and their GMC friends) or Cadillac Escalade (and the list may continue).

It is proven [1.20] that the electric-drive implementation comes along with the following advantages:

- mechanical simplifications
- notable energy consumption reduction
- better control
- partial air conditioning operation with ICE off

The mechanical simplification are due to the absence of the driving belts system that was connected to the engine.

Regarding the fuel economy, the figures differ from one study to another. Still, according to Toyota&Denso studies [1.21] the impact on fuel consumption reduction by using an electric drive for the air conditioning compressor is massive, especially for urban driving mode (see Figure 1.16). Nevertheless, the electric driven compressor can reduce an electric hybrid's range by 18-30% depending on the environmental conditions, and even more if the solution should be implemented on traditional cars.

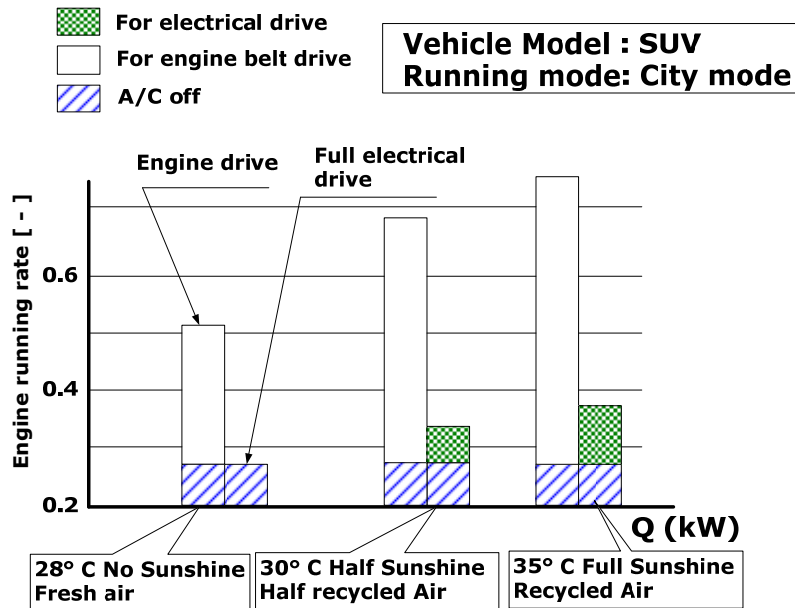


Figure 1.16. Impact on fuel consumption – comparative study [1.21]

The system is no longer using power from the internal combustion engine, and this assures not only partial functionality when the latter is off, but also independent and variable speed control, that should optimize the operating cycles of the compressor according to the specific requirements.

The compressor is now driven by an electric motor (see the general schematic of the whole air conditioning system in Figure 1.17).

Since volume is a key constraint for the automotive industry, the latest ideas, solutions and prototypes are concerned on delivering compact and (semi-) integrated systems.

In Figure 1.18 a Delphi prototype (still under development) is presented. The family of scroll compressors is driven by 315 volt brushless electric motors. Scroll displacements are 28 and 38 cc, for cooling capacities of 5.6 and 7.1 kW respectively. The motors are cooled using the low temperature refrigerant vapour from the evaporator with a resultant motor efficiency of 94%. The inverter is cooled by conduction from the same refrigerant and it too has efficiency in the 94 to 98% range [1.22]. However, the solution considered has some disadvantages if it were to be actually implemented and mounted on the car. Despite the high efficiency that is claimed, the cooling power is rather suitable for large automobiles and the 315 Volts that should supply the motor via the inverter, only introduces additional concerns for the d.c. bus.

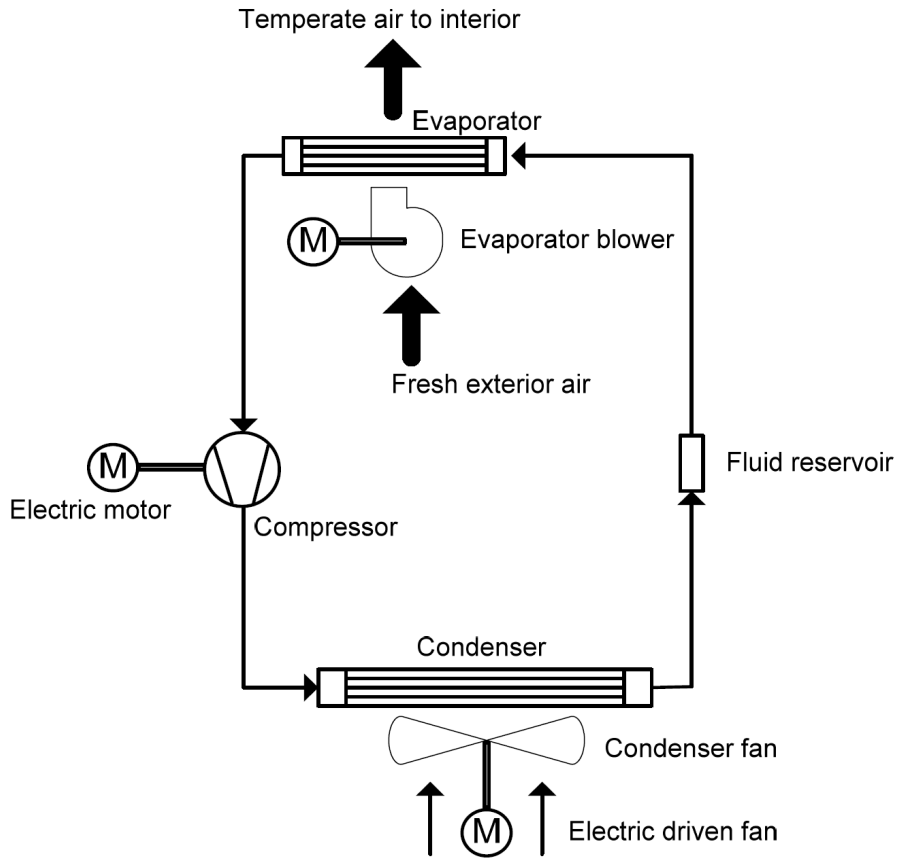


Figure 1.17. Air-conditioning system diagram (with electric driven compressor) [1.20]

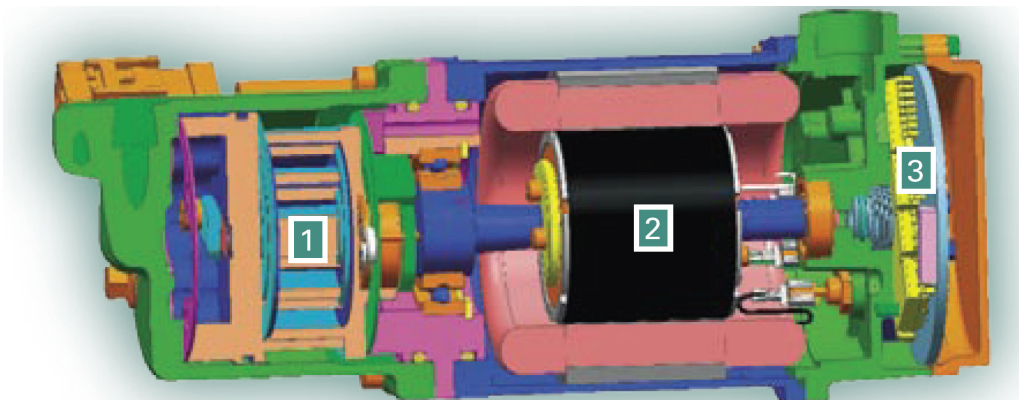


Figure 1.18. Section through Delphi Electric Compressor: 1 - Scroll Compressor, 2 - Permanent Magnet Motor 3 - Inverter and Integrated Electronics [1.22]

Another compact solution (prototype/under development) is presented in [1.23](see Figure1.19). This time the voltage supply level is set to 42V (which complies with automotive (future) regulations/standards).

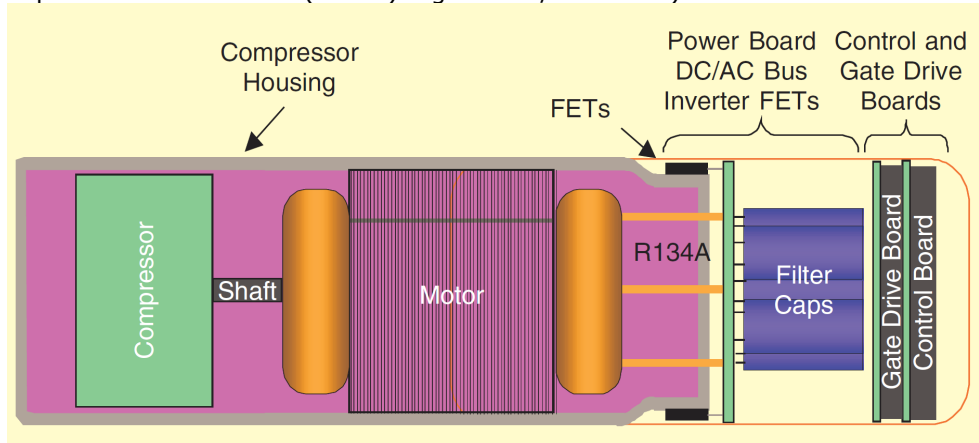


Figure 1.19. Semi-integrated packaging configuration for the compressor drive [1.23]

The 4.15 kW power considered for the permanent magnet motor, is more appropriate, but the general 85% efficiency (and 88% - peak) claimed, can still be improved.

However, a continuous interest on the automotive air conditioning system has led to numerous research activities [1.24 - 1.48]; from better system and process characterization and simulation, to parameter identification or actual control solutions for the driving electric motor.

Delphi, Visteon and Denso are only some of the companies that are studding and building prototypes for the electric driven compressor that should be found on future car. Compact size, high efficiency and cost are equally important constraints along with other specific automotive regulations. Continuous and extensive research activities to find the best solution are carried out.

Of course, there are several aspects involved, but the present thesis will concentrate on the electric motor and the control strategy needed for the electrically driven compressor.

1.7. Requirements for the compressor electric drive

Typical performance specifications of the air conditioning system (with R134 refrigerant) are presented in Table 1.3 (the values that are presented are not standard and may vary from one manufacturer to another).

Like almost all electric actuators involved in automotive applications, the electric motor that will drive the compressor will be a permanent magnet one (compact size, high torque density and low mentainance attributes keep these types of motors in the front line, even though the price for permanent magnets has exploded).

If medium-sized cars are taken into consideration, the motor should be able to deliver 2.5 kW and around 3Nm torque. The rated speed should be the maximum operating speed of the compressor and the d.c. supply voltage should take into account the 42 V, in order to comply with automotive regulations.

Regarding drive dynamics, the system is characterized by a low time constant, since it finally needs to regulate temperature variation. However, it is considered that the motor that drives the compressor should start in approximately

Typical Performance Specifications		
Parameter	Range	Stability
Compressor Chamber Temperature	Ambient + (-15°)C to 121°C	± 9 °C
Compressor Speed	400 to 6000 RPM	± 5 %
Discharge Pressure	1.135 MPa – 34.37 MPa	± 0.12 Mpa
Suction Pressure	0 MPa – 0.79 MPa	± 0.1 Mpa
Liquid Temperature	15.5 °C – 99 °C	± 5 °C
Evaporator Core Air Flow	1.41 m ³ /min – 42.47 m ³ /min	± 1%
Condenser Air Flow	14.15 m ³ /min – 141.6 m ³ /min	± 1%
Condenser Room Temperature	4.5 °C – 60 °C	± 5 °C
Evaporator Room Temperature	-9 °C – 60 °C	± 5 °C
Evaporator Room Dew Point	2 °C – 57.2 °C	± 5 °C
Glycol Flow	0 l/min – 45.43 l/min	± (0.7 ÷ 2.8) l/min
Glycol Temperature	15.5 °C – 110 °C	± 5 °C

Table 1.3 Typical Performance Specifications for R134 air conditioning system

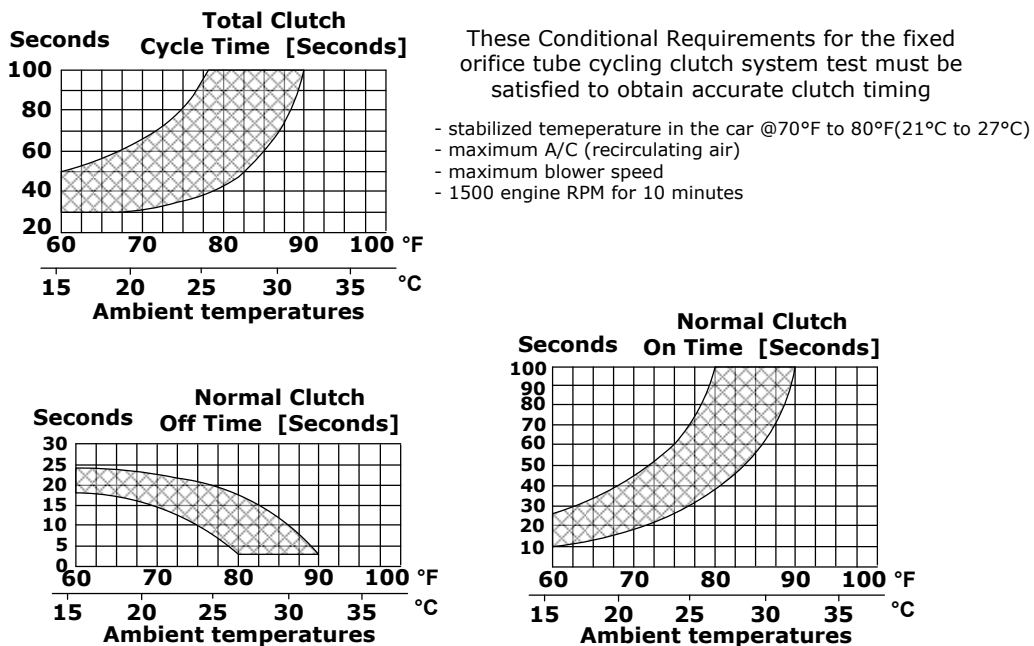


Figure 1.20. Clutch cycle time for Ford Escort

1 second, if minimum speed is demanded.

The compressor operating cycle is different from one air-conditioning system to another. Take for example the graphics in Figure 1.20. They present the operating cycle timings of the clutch (the device that engages the compressor activity in "classic" systems) in a fixed tube orifice system, on a Ford Escort. The operating (cycle) time is substantially influenced by ambient temperature and if the temperature is below 30°C, the compressor is not run continuously. Depending on environmental conditions, the operating cycling imposes a certain ratio between

“on” and “off” timings. This only means that for a given time interval the motor that drives the compressor will have to start and stop several times, operating and standstill occurs for few seconds. This characteristic only means that the motor will have to run intermittently if low temperatures are already achieved in the cabin, while continuously operation is required for intense heated environment.

On the other hand, the motor has to permanently operate under load condition. The load torque is generally speed-proportional, but depending on compressor specificities it might have a quadratic variation with speed.

The control strategy designed for the air conditioning compressor drive application has consequently to deliver accurate speed control (5% allowable steady-state speed error), under permanent speed-proportional load conditions, with slow dynamics, characterized by few seconds operating cycles. Once cooling was partially achieved, or the temperature is below a certain specified limit, the motor driving cycle is intermittent, and several starting and stopping operation are required for a given interval of let's say 3 minutes. Successful starting must be assured every time.

1.8. Conclusions

In this Chapter, the modern vehicle was subjected to a “radiographic examination” to prove the high number of electric and electronic devices that equip today's automobile. This only means that the vehicle installed power is continuously increasing, leading to power generation issues and wise energy management challenges.

Complying with this energy concern trend and taking into account specific competencies, the driving direction considered appropriate is to take existing drive systems that are already electric, or might be replaced by electric ones and try to increase efficiency and power levels. The reasons for choosing the automotive air conditioning compressor system are given. From historical evolution until actual drive requirements, the chapter tries to cover just about all important details related to this application.

References

- [1.1] <http://pattensauto.com/services/computer>
- [1.2] Lisa Eccles, David Morrison, “Advanced electrical components and systems will help determine whether fuel-saving hybrids can merge into the automotive mainstream”, 2001, <http://electronicdesign.com/article/articles/hybrid-electric-vehicles-propel-us-toward-an-80-mp>
- [1.3] http://delphi.com/news/pressReleases/pr_2012_04_25_004/
- [1.4] <http://www.hybridcars.com>
- [1.5] R. Farrington and J. Rugh, „Impact of Vehicle Air-Conditioning on Fuel Economy, Tailpipe Emissions, and Electric Vehicle Range”, presented at the Earth Technologies Forum Washington, D.C. October 31, 2000
- [1.6] Dietrich Kuhlitz, “Bosch Automotive – A Product History”, Journal of Bosch History”, Supplement 2
- [1.7] Steven Daly, „Automotive Air Conditioning and Climate Control Systems”, Elsevier Ltd, UK, 2006
- [1.8] http://en.wikipedia.org/wiki/Automobile_air_conditioning

- [1.9] http://www.automobilemag.com/features/news/1007_automotive_air_conditioning_history/
- [1.10] http://www.ehow.com/facts_7190262_history-air-conditioning-cars.html
- [1.11] http://www.climatictesting.com/Automotive_AC_System_Calorimeter.htm
- [1.12] John Shen, Abul Masrur, Vijay K. Garg and John Monroe, "Automotive Electric Power and Energy Management – A System Approach", Business Briefing: Global Automotive Manufacturing & Technology, 2003
- [1.13] Chris Bede, "Automotive Air Conditioning Systems", SmartTrac Computer Systems Inc., 2005
- [1.14] Mike Stubblefield, John H. Haynes, "The Haynes Repair Manual for automotive heating and air conditioning systems", Haynes Publications, Inc., California, USA, 2000
- [1.15] George McKinney, "Theory and Application Of Reciprocating Compressors", PDHengineer.com, Course N^o M-3030,
- [1.16] "Scroll Compressors - High Efficiency Compression for Commercial and Industrial Applications", Carrier Corporation Syracuse, New York, October 2004
- [1.17] SD Compressor - Service Manual, Sanden technical documentation for R134a air conditioning systems
- [1.18] Paul C. Hanlon (editor), "Compressor Handbook", McGraw-Hill, 2001
- [1.19] Ariazone – "Automotive Air Conditioning Training Manual", 2006
- [1.20] D. Iles, "Automotive Permanent Magnet Actuation Technologies", PhD Thesis, Politehnica University from Timisoara, 2005
- [1.21] Eugene Talley, "Hybrid Air Conditioning Systems Overview", Proceedings of Spring 2011 ICAIA Conference, 2011, pp. 1–68
- [1.22] "Air Conditioning Compressors", Delphi Thermal Systems, 2006
- [1.23] Malakondaiah Naidu, Thomas W. Nehl, Suresh Gopalakrishnan, Lukas Würth, "A semi-integrated, sensorless PM brushless drive for a 42-V automotive HVAC compressor", IEEE Industry Application magazine, July/August, 2005, pp. 20–28
- [1.24] Changqing Tian, Xianting Li, Xinjiang Yang, " Numerical analysis of evaporator frosting in automotive air-conditioning system with a variable-displacement compressor", Elsevier – Science Direct, Applied Energy, No. 82, 2005, pp. 1–22
- [1.25] Deng Shiming, Li Zheng, Qu Minglu, "Indoor thermal comfort characteristics under the control of a direct expansion air conditioning unit having a variable-speed compressor and a supply air fan", Elsevier – Science Direct, Applied Thermal Engineering, No. 29, 2009, pp. 2187–2193
- [1.26] Hu Huang, Qihe Li, Dongxue Yuan, Zhenchun Qin, Zhongbin Zhang, "An experimental study on variable air volume operation of ducted air-conditioning with digital scroll compressor and conventional scroll compressor", Elsevier – Science Direct, Applied Thermal Engineering, No. 28, 2008, pp. 761–766
- [1.27] Changqing Tian, Hongbo Xu, Liqin Zhang, Xianting Li "Experimental investigation on the characteristics of variable displacement swash plate compressor", Elsevier – Science Direct, Applied Thermal Engineering, No. 29, 2009, pp. 2824–2831
- [1.28] Cristian Cuevas, Jean Lebrun, Vincent Lemort, Eric Winandy, "Characterization of a scroll compressor under extended operating conditions", Elsevier – Science Direct, Applied Thermal Engineering, No. 30, 2010, pp. 605–615

- [1.29]** Hamid Khayyama, Abbas Z. Kouzani, Eric J. Hu, Saeid Nahavandi, "Coordinated energy management of vehicle air conditioning system", Elsevier – Science Direct, Applied Thermal Engineering, No. 31, 2011, pp. 750–764
- [1.30]** Hamid Khayyama, Saeid Nahavandi, Eric Hub, Abbas Kouzani, Ashley Chonka, Jemal Abawajy, Vincenzo Marano, Sam Davis, "Intelligent energy management control of vehicle air conditioning via look-ahead system", Elsevier – Science Direct, Applied Thermal Engineering, No. 31, 2011, pp. 3147–3160
- [1.31]** Hamid Khayyama, Jemal Abawajy, Reza N. Jazar, "Intelligent energy management control of vehicle air conditioning system coupled with engine", Elsevier – Science Direct, Applied Thermal Engineering, No. 48, 2012, pp. 211–224
- [1.32]** Khaled S. AlQdah, "Performance and Evaluation of Aqua Ammonia Auto Air Conditioner System Using ExhaustWaste Energy", Elsevier – Science Direct, Energy Procedia, No. 6, 2011, pp. 467–476
- [1.33]** Yuan Mao Huang, Sheng-An Yang, "A measurement method for air pressures in compressor vane segments", Elsevier – Science Direct, Measurement, No. 41, 2008, pp. 835–841
- [1.34]** Luca Cecchinato, "Part load efficiency of packaged air-cooled water chillers with inverter driven scroll compressors", Elsevier – Science Direct, Energy Conversion and Management, No. 51, 2010, pp. 1500–1509
- [1.35]** Cristian Cuevas, Nestor Fonseca, Vincent Lemort, "Automotive electric scroll compressor: Testing and modeling", Elsevier – Science Direct, International Journal of Refrigeration, No. 35, 2012, pp. 841 – 849
- [1.36]** Orhan Ekren, Mehmet Akif Ezan, Aytunc Erek, "Experimental assessment of energy storage via variable speed compressor", Elsevier – Science Direct, International Journal of Refrigeration, No. 34, 2011, pp. 1424 – 1435
- [1.37]** Sepehr Sanaye, Masoud Dehghandokht, Hassan Mohammadbeigi, Salman Bahrami, "Modeling of rotary vane compressor applying artificial neural network", Elsevier – Science Direct, International Journal of Refrigeration, No. 34, 2011, pp. 764 – 772
- [1.38]** Orhan Ekren, Savas Sahin, Yalcin Isler, "Comparison of different controllers for variable speed compressor and electronic expansion valve", Elsevier – Science Direct, International Journal of Refrigeration, No. 33, 2010, pp. 1161 – 1168
- [1.39]** Alpaslan Alkan, Murat Hosoz, "Comparative performance of an automotive air conditioning system using fixed and variable capacity compressors", Elsevier – Science Direct, International Journal of Refrigeration, No. 33, 2010, pp. 487 – 495
- [1.40]** Xudong Wang, Yunho Hwangb, Reinhard Radermacher, "Two-stage heat pump system with vapor-injected scroll compressor using R410A as a refrigerant", Elsevier – Science Direct, International Journal of Refrigeration, No. 32, 2009, pp. 1442 – 1451
- [1.41]** Michele Albieri, Alessandro Beghi, Cristian Bodo, Luca Cecchinato, "Advanced control systems for single compressor chiller units", Elsevier – Science Direct, International Journal of Refrigeration, No. 32, 2009, pp. 1068 – 1076
- [1.42]** Yiming Chen, Shiming Deng, Xiangguo Xu, Mingyin Chan, "A study on the operational stability of a refrigeration system having a variable speed

- compressor", Elsevier - Science Direct, International Journal of Refrigeration, No. 31, 2008, pp. 1368 - 1374
- [1.43]** Qi Qi, Shiming Deng, "Multivariable control-oriented modeling of a direct expansion (DX) air conditioning (A/C) system", Elsevier - Science Direct, International Journal of Refrigeration, No. 31, 2008, pp. 841 - 841
- [1.44]** Cristian Cuevas, Eric Winandy, Jean Lebrun, "Testing and modelling of an automotive wobble plate compressor", Elsevier - Science Direct, International Journal of Refrigeration, No. 31, 2008, pp. 423 - 431
- [1.45]** Sung Chul Kim, Jong Phil Won, Min Soo Kim, "Effects of operating parameters on the performance of a CO₂ air conditioning system for vehicles", Elsevier - Science Direct, Applied Thermal Engineering, No. 29, 2009, pp. 2408-2416
- [1.46]** Shujun Wang, Junjie Gu, Tim Dickson, Jennifer Dexter, Ian McGregor, "Vapor quality and performance of an automotive air conditioning system", Elsevier - Science Direct, Experimental Thermal and Fluid Science, No. 30, 2005, pp. 59-66
- [1.47]** Emerson Escobar Nunez, Kyriaki Polychronopoulou, Andreas A. Polycarpou, "Lubricity effect of carbon dioxide used as an environmentally friendly refrigerant in air-conditioning and refrigeration compressors", Elsevier - Science Direct, Wear, No. 270, 2010, pp. 46 - 56
- [1.48]** Youn Cheol Park, "Transient analysis of a variable speed rotary compressor", Elsevier - Science Direct, Energy Conversion and Management, No. 51, 2010, pp. 277-287

CHAPTER 2

6 Slot/8 Pole Synchronous Machine: Analytical Design for a Surface Permanent Magnet Motor

Abstract

This chapter deals with the preliminary analytical design of a surface permanent magnet synchronous motor. Even though it follows a more or less traditional path, several adaptations are implemented in order to comply with the chosen topology's specificities. Analytical dimensioning methodology, active material weight and costs along with thermal verification will provide in the end a first motor prototype. The data will be used further, as input for the following design steps that will finally provide an optimized motor geometry.

2.1. Introduction

The electric motor that has to be designed is destined for the automotive air conditioning compressor electric drive. Some of the typical drive characteristics and requirements were presented in the previous chapter.

For the automotive industrial domain, volume, torque density, efficiency and price are equally important constraints that establish certain guidelines for the electric motor design process. And, just because all these four attributes have to be accomplished at once, the permanent magnet motors have made their way through, overpassing other candidates for these specific applications. From small power drives (that should open/close your car's window, for example) to large consumers (like the vehicle alternator, or the traction electric motor for HEV/electric cars), the permanent magnet synchronous motors, with different topologies are the most preferred solutions. [2.1 – 2.4].

This statement has narrowed our motor topology choice but did not offer a single solution. Permanent magnets may be placed both on rotor and stator. Anyway, because the permanent magnets are the most expensive out of the necessary material, in order to optimize cost from the beginning, the motor topology that will be considered, consists of an inner rotor with permanent magnets and a tooth-wound stator. The next two sections will help us decide on the exact rotor and stator type.

2.2. PM rotors variety

Different ways of arranging magnets on the rotor have created many types of PMSMs and brushless dc machines. The arrangement of the permanent magnets has impact on the air gap flux density, winding inductances, reluctance (cogging) torque amplitude and periodicity and finally influences the useful electromagnetic torque the motor has to deliver [2.5 – 2.21].

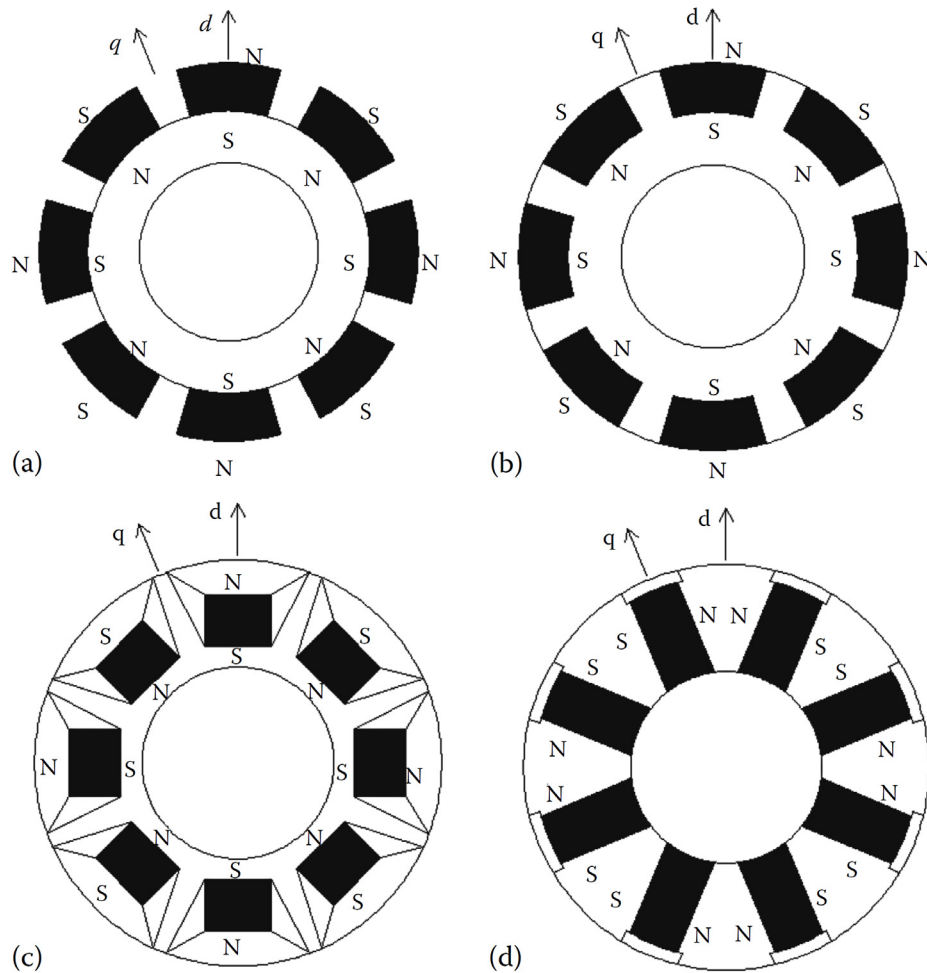


Figure 2.1 Typical PM rotor topologies: a) Surface PM (SPM) synchronous machine. (b) Surface inset PM (SIPM) synchronous machine. (c) Interior PM (IPM) synchronous machine. (d) Interior PM synchronous machine with circumferential orientation [2.6]

Typical PM rotor topologies are depicted in Figure 2.1 [2.6]. The surface mounted PM rotor configuration (see Figure 2.1a) provides the highest airgap flux density as it directly faces the air gap without the interruption of any other medium such as part of rotor laminations. Still mechanical robustness and structural integrity cannot be assured at very high speeds (a maximum speed of 3000 rpm is employed for high power motors and can even reach 50,000 rpm for very small motors). In practice the magnets are usually buried in the rotor laminations and fixed with special resins. The topology also provides a very small reluctance variation (less than 10%) between the direct and quadrature axes, so actually the motor with this kind of rotor can be considered non-salient. This particular fact has consequence on the control, operation, and characteristics of the surface mount PMSM drives.

For more mechanical robustness a variation of the surface mounted PMs is to have them totally buried, placed in the grooves of the outer periphery of the rotor laminations, providing a uniform cylindrical surface of the rotor. The so called inset

PMSM (see Figure 2.1b) is obtained this way. Now that the integrity of the rotor can be better guaranteed, it is safe to provide a higher operational speed. The ratio between the quadrature and direct axes inductances can be as high as 2–2.5 in this machine.

If the permanent magnets are buried deeper, in the middle of the rotor laminations in radial and circumferential orientations, respectively, an interior PMSM (see Figure 2.1c) configuration is obtained. The interior PM rotor construction is mechanically robust and therefore suited for high-speed applications. The manufacturing of this arrangement is more complex than the surface mount or inset magnet rotors. It is important to mention that the ratio between the quadrature and direct axes inductances can be higher than that of the inset magnet rotor and it is approximately 3, or even higher (with the emerging implications related to control possibilities). The configuration has also to consider airgaps between the magnets in order to limit the flux flow between adjacent magnets. Still, by having part of the steel removed in order to create the flux barriers, rotor weight reduction is accomplished and a lower inertia can be provided. This enables faster accelerations for drives that should contain these types of motors. Low cogging torque can be assured with this configuration, but still the total delivered torque is considerably lower than the one offered by the surface mounted PM motor.

The circumferential inset PM rotor (shown in Figure 2.1d) requires large volume of the PMs. This configuration is suitable only for low energy density permanent magnets (ferrites) due to cost implications. Still this configuration can lead to an airgap flux density enabling a higher efficiency and smaller stator excitation for the same power output. But this advantage does not come out without an expense; the rotor volume is considerably larger.

Taking into account speed and dynamic requirements for the automotive air conditioning compressor drive, along with overall volume and cost limitations, the rotor considered best suited is the surface mounted PM one.

2.3. Concentrated winding stator

The stator variations are numerous. Still, from the beginning a slotless design is eliminated. Even though this configuration provides zero cogging torque, thermal stress issues are present and generally a higher magnet length on the rotor is required [2.7].

Distributed windings have been extensively used, especially due to the resulting sinusoidal magneto-motive force (MMF) distribution and back-EMF waveform. Some disadvantages are to be mentioned. Usually a maximum slot filling factor of 0.4 is allowed, while end turns are significantly long. In order to surpass these disadvantages and reduce the cost of winding and manufacturing complexity, the slotted stator with concentrated windings was considered.

It is not only the higher airgap flux density that can be provided, but also the following favourable features [2.6]:

- simpler construction,
- no mutual inductance between phases endowing a higher fault tolerance in these machines.
- low cogging torque as it engenders high number of cogging cycles per mechanical revolution.
- no large end connections because of concentrated coil winding, contributing to savings in copper volume and its losses.

- high direct axis self-inductance which can provide a wider flux weakening operation.

So, it is more than obvious that this construction particularity is more and more adopted, especially for small to medium power electric motors([2.21]-[2.32]).

Furthermore, another design particularity has to be established. Depending on the number of slots per pole and phase (named N_{ssp} later on in this Chapter), two possibilities arise: "integer slot concentrated windings" or "fractional slot concentrated windings" stator, emerging from slot/pole number combinations. The later has impact on slot number reduction (particularly important for large pole number machines) and provides the motor prototype with the following additional advantages: high-power density, high efficiency, short end turns, high slot fill factor particularly when coupled with segmented stator structures, low cogging torque, flux-weakening capability, and fault tolerance.

However, the disadvantages of such choice should be also mentioned. Fractional slot concentrated windings produce rich m.m.f harmonics, are blamed to determine relatively high rotor eddy current loss, potentially high unbalanced magnetic force and acoustic noise and vibration.

Several slot/pole number combinations are to be found in the literature, providing in general a larger number of slots than magnet poles. Still, according to [2.6] a feasible pole and slot combinations for the class of concentrated coil-wound is:

$$\begin{aligned} N_s &= N_{PM} \pm 1 \text{ for odd slots per phase} \\ N_s &= N_{PM} \pm 2 \text{ for even slots per phase} \end{aligned} \quad (2.1)$$

where N_s is the slot number and N_{PM} is the number of rotor poles

Anyway, before taking advantages of reduced slot number provided according to equation (2.1), the unbalanced magnetic forces issue has to be considered. In [2.33] an extensive study regarding the afore mentioned slot-pole number combinations is realized. It has been proved that machines having slot/pole numbers differed by two exhibit smaller UMF than machines having slot/pole numbers differed by one, and consequently an even number of slots per phase is to be considered for the final solution. And, further on, by considering lowest possible slot number (to minimize manufacturing complexity) we end up choosing a 6 slot stator. According to (2.1), 4 or 8 magnet poles would fit the combination. But a pole number that respects the $3k+1$ formula (the case of 4, 16, etc.) can provide a reduced UMF (even to 0) only with the increase of pole number while the $3k-1$ combination (namely 8, 12, etc.) provides the decrease anyway.

Since the rated (and maximum) speed the motor will have to be capable of, in order to meet the automotive air conditioning compressor drive requirements, is in the medium range, the higher pole number valid for the "feasible" combination will be chosen.

In the end a 6 slot stator 8 pole rotor topology is prefigured. Several factors have to be considered before sketching the first topological characteristics for a motor prototype. There is no unique solution and only further design steps will approve initial selection or oblige the designer to reconsider initial data.

Table 2.1. [2,5]
Winding factors of concentrated windings

		2p-Poles														
		2	4	6	8	10	12	14	16	18	20	22	24	26	28	30
N_s	slots	**	**	*	**	*	**	*	**	*	**	*	**	*	**	*
3	*	0.86	*	*	*	*	*	*	*	*	*	*	*	*	*	*
6	*	*	0.866	*	*	0.866	*	*	0.866	*	*	*	*	*	*	*
9	*	*	0.736	0.617	0.667	0.866	0.945	0.96	0.945	0.966	0.933	0.764	0.218	0.473	0.177	0.175
12	*	*	*	*	*	*	0.866	0.866	0.866	0.933	*	*	0.966	0.933	0.866	0.866
15	*	*	*	0.247	0.481	0.383	0.621	0.866	0.866	0.808	0.906	0.957	0.951	0.951	0.957	0.951
18	*	*	*	*	*	0.473	0.543	0.676	0.647	0.866	0.866	0.844	0.902	0.960	0.931	0.931
21	*	*	*	*	*	0.248	0.468	0.397	0.565	0.622	0.521	0.866	0.866	0.793	0.851	0.851
24	*	*	*	*	*	*	*	0.930	0.463	*	*	0.561	0.76	0.866	0.866	0.866

* One layer

** Two layers

2.4. Preliminary analytical design

The analytical design methodology for a surface permanent magnet synchronous motor characterized by fractional, less than unity slot per pole ratio will be detailed.

2.4.1. Topology quality factors

Three quality factors are considered in what follows: winding factor, cogging torque factor and a global quality factor that merges both.

The winding factor can also be found from Table 2.1([2.5]), but is actually the result of the product between the distribution and coil-span factor.

First the ratio z is defined according to (2.2). For the given slot/pole combinations z equals 1. This particular value determines a unity distribution factor (k_d – see equation (2.3)), no matter which winding space harmonic order (n) is considered

$$z = \frac{N_s}{\text{GCD}(N_s, N_{PM} \times N_{ph})} = \frac{6}{\text{GCD}(6, 8 \times 3)} = 1 \quad (2.2)$$

$$k_d = \frac{\sin\left(n \frac{1}{2} \frac{2\pi}{N_s}\right)}{z \sin\left(n \frac{1}{2} \frac{2\pi}{N_s} \frac{1}{z}\right)} = 1 \quad (2.3)$$

The slot pitch angle and coil span angle are given by equations (2.4) and (2.5)

$$\theta_{se} = \frac{\pi N_{PM}}{N_s} = \frac{4\pi}{3} \quad (2.4)$$

$$\varepsilon = \pi - \theta_{se} = -\frac{\pi}{3} \quad (2.5)$$

The coil span factor is:

$$k_\varepsilon = \cos\left(n \frac{\varepsilon}{2}\right) = \cos\left(-\frac{n\pi}{6}\right) = \cos\left(\frac{n\pi}{6}\right) \quad (2.6)$$

The winding factor for the fundamental yields:

$$k_w = k_d \times k_\varepsilon = 0.866 \text{ if } n = 1 \quad (2.7)$$

The cogging torque factor is defined by the cogging cycles per revolution that characterize the slot/pole combination:

$$k_{cogg} = \text{LCM}(N_s, N_{PM}) = \text{LCM}(6, 8) = 24 \quad (2.8)$$

The global topology quality factor [2.2], may be defined with equal weighting coefficients, resulting as an arithmetic mean between the first two quality factors:

$$k_{quality} = 0.5 \times k_w + 0.5 \times k_{cogg} = 0.5 \times 0.866 + 0.5 \times 24 = 12.433 \quad (2.9)$$

2.4.2. Active material selection

In the following the selection of the materials for the active parts will be presented. Highly energy efficient utilization and economical design is aimed for the motor prototype, so material choices are made accordingly. Furthermore, since there are constraints regarding the motor volume, high energy density permanent magnets will be considered.

2.4.2.1. Stator and rotor core

The material for the stator and rotor cores was chosen to be laminated non-oriented silicon M800-50A electric steel [2.36, 2.37]. Table 2.2 presents the main material properties of the iron core laminations

Table 2.2. Material properties for iron core laminations

Parameter	Symbol	Value	Unit
Composition	v	99,95	[%] Fe
Initial relative permeability at $B=0.02$ [T]	μ_{ri}	1084	[-]
Maximum relative permeability	$\mu_{r\max}$	4032	[-]
Saturation induction	B_{sat}	1.7	[T]
Mass density	γ_{Fe}	7800	kg/m ³

The DC magnetization curve is shown in Figure 2.2. The variation of the specific total losses versus frequency at 1.5 T (peak), and versus peak flux density at 400 Hz (corresponding to rated speed) is presented in Figure 2.3, and Figure 2.4 respectively.

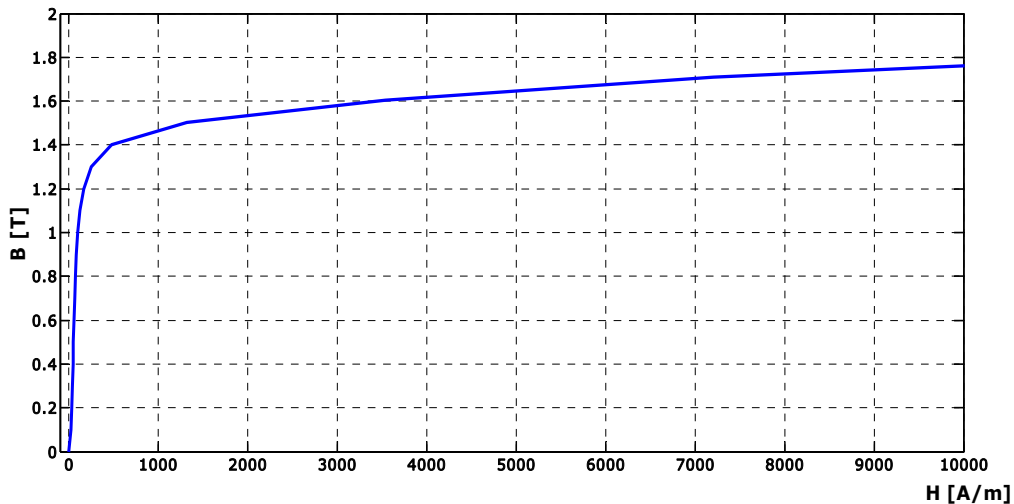


Figure 2.2. B-H curve for SURA M800-50A

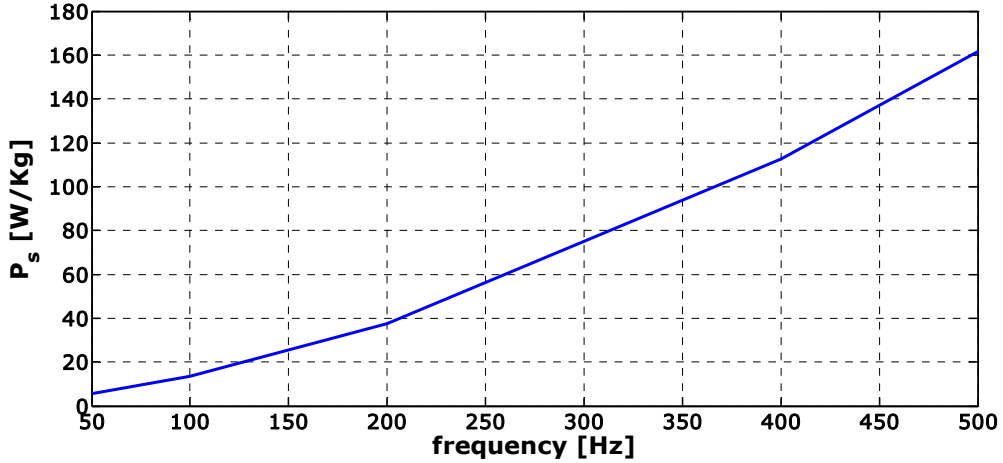


Figure 2.3. Specific total losses versus frequency at 1.5 T (peak).

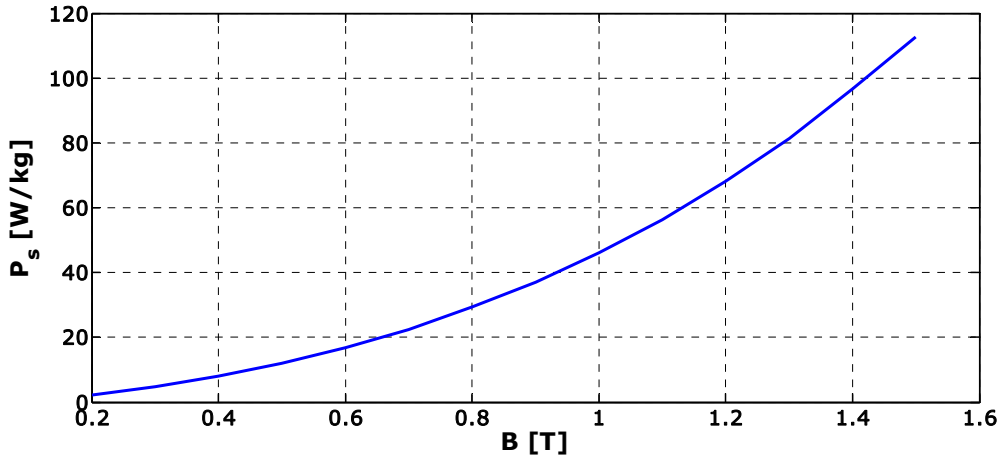







Figure 2.4. Specific total losses versus peak flux density at 400 Hz.

2.4.2.2. Permanent magnets

High energy density magnetic material is required for the prototype to fulfil both efficiency and compact size goals. The price for permanent magnets has continuously been increased in the last decade and obliged designers to reconsider "PM-less" solutions especially for large sized motors. However, to comply with the

Table 2.3 Material properties for NdFeB family

Material	$(BH)_{max}$ [kJ/m ³]	B_r [T]	H_c [A/m]	H_{cl} [A/m]
 NdFeB 31/25	246.7	1.12	875352	1989436
 NdFeB 35/19	278.5	1.23	946971	1511971
 NdFeB 38/17	302.4	1.25	962887	1352817
 NdFeB 40/14	318.3	1.26	978802	1114084
 NdFeB 44/12	350.1	1.35	875352	954929

low cost constraint and still keep our design in the compact size range, Neodymium-Iron-Boron (NdFeB) magnets will be chosen as they come along with a reasonable price on the market. Table 2.3 [2.38] offers an overview on available PM products and their characteristics, while Figure 2.5 presents the demagnetization curves.

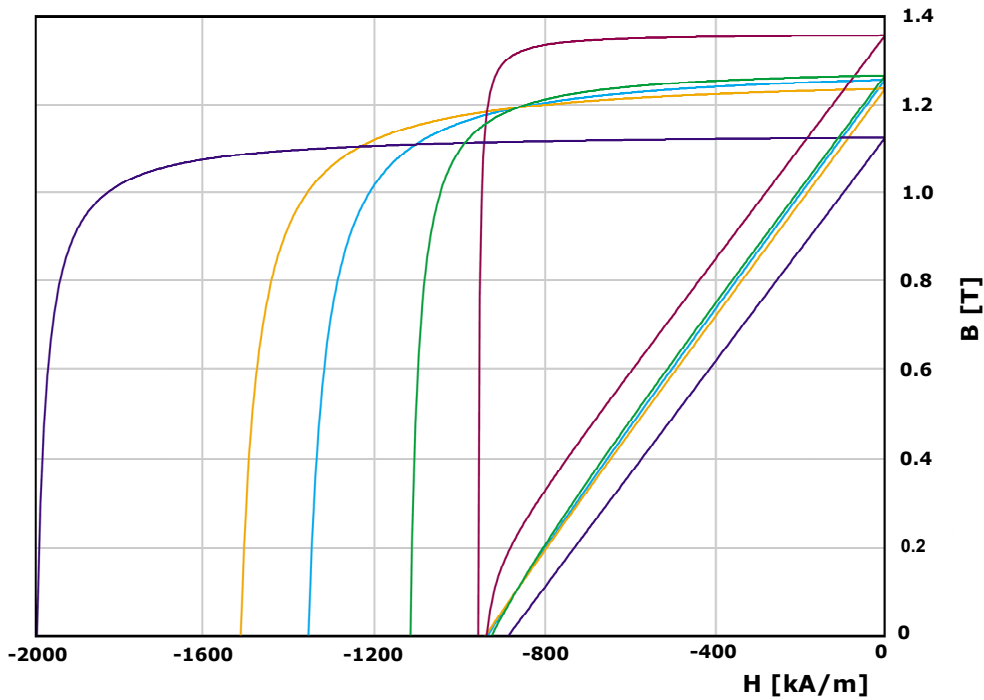


Figure 2.5. Demagnetization curves for NdFeB family

The NdFeB 31/25 product is considered suited for the application. Further details for the chosen permanent magnet product is given in table 2.4

Table 2.4 Additional material properties for NdFeB 31/25

Parameter	Symbol	Value	Unit
Remanent induction	B_r	1.12	T
Magnetic coercivity	H_c	875×10^3	A/m
Intrinsic coercivity	H_{cI}	1.99×10^6	A/m
Recoil permeability	μ_r	1.018	-
Maximal energy product	BH_{max}	246.7	kJ/m^3
Magnetizing force	H_{magn}	$2300 \cdot 10^3$	A/m
Temperature coefficient of the remanent induction	α_{br}	-0.001	$1/^\circ\text{C}$
Temperature coefficient of the intrinsic coercivity	α_{HcI}	-0.0006	$1/^\circ\text{C}$
Curie temperature	T_{Currie}	310	$^\circ\text{C}$
Mass density	γ_{PM}	7400	kg/m^3

2.4.3. Design theme

General specifications for a variable speed surface permanent magnet synchronous machine:

- Base power, $P_b = 2500$ [W]
- Base speed, $n_b = 6000$ [rpm]
- Maximum speed, $n_{\max} = 8000$ [rpm]
- Power at maximum speed: P_b
- DC voltage, $V_{dc} = 50$ [V]
- Number of poles, $N_{pM} = 8$
- Number of phases, $N_{ph} = 3$
- Supply: PWM inverter, rectangular current control,
- Star connection of stator phases
- No forced/additional cooling system

2.4.4. Electric and magnetic loadings

The following step in general design of electric machines consists in choosing the electric and magnetic loadings. For PMSMs, these loadings are described as follows [2.1, 2.5, 2.6]:

- If high torque density is aimed through design, the specific tangential force, f_{tsp} , concept is introduced. It is measured in N/cm^2 and varies from $0.1N/cm^2$ in micro-motors to $10N/cm^2$ in larger torque density.
- A second factor that impacts directly on motor volume is the PM air-gap flux density level: B_g (T). its variation starts $0.2T$ for micro-motors and reaches $1T$ in large torque density design.
- The magnetic saturation degree of the machine is specifically determined by the stator tooth flux density, B_{st} (T). For silicon laminated stator cores, this parameter varies generally from $1.2T$ to $1.8T$. Small B_{st} values lead to wider teeth and consequently reduces the slot area. Core losses are diminished this way, but due to thinner slot design, higher current density is required and copper losses increase. To lower the current density, the slot area may be increased by enlarging the slot depth, but this means that we increase the stator diameter. The impact of such topology change on copper loss reduction is not that drastic, since end-turns are also increased. Depending on rated frequency, a large B_{st} value may direct us to high core losses; still, if the airgap height is appropriate and large enough the impact is diminished.
- Especially for small pole number machines, the stator yoke flux density B_{ys} (T) level has direct and substantial impact on machine size and weight. The consequences resulted after choosing small versus large values for B_{ys} respect the same reasoning as before. Again, a compromise between magnetic saturation level and core losses limitations has to be acquired.
- Copper losses and copper volume are a consequence of the current density j_{co} (A/mm^2) we choose for the design. On one hand, small j_{co} values are desired, since they are automatically translated into small copper losses (which means higher efficiency), but if the reduced value of the current density is a result of

deeper and thinner slots, the compact size constrained might not be respected. High j_{co} values ($> 8\text{A/mm}^2$) not only increase copper losses but imply forced cooling. Appropriate current density levels should be included in the $3.5 \div 10\text{ A/mm}^2$ range

- Rotor losses are significantly reduced if PMs are considered instead of windings. Still there are some rotor core losses present, determined by the yoke flux density B_{yr} (T) value. Anyway, for surface mounted PM rotor configuration the losses are negligible.

2.4.5. Some dimensioning guidelines

- The ratio between the axial (stack) length of the machine, l_{stack} , and the stator interior diameter, D_{si} , also known as machine shape factor, λ , determines an elongated or on the contrary, a more dumpy shape for the final motor. The values for λ are typically chosen between 0.3 and 3 and should comply with application specific volume limitations.
- To avoid circulation current between current paths, due to inherent machine asymmetry, the stator winding current path count, a_1 , should be fixed to 1. However, this rule may be reconsidered for automotive applications, when a_1 should be either a divisor of number of poles (two layers winding) either a divisor of the number of pole pairs (single layers windings).
- In order to reduce skin effects, the coil turns should be made of multiple elementary conductors in parallel with same degree of transposition. This design strategy is important especially for large current drives.
- While searching for the right stator, it was already mentioned that the slotted stator configuration in combination with the permanent magnet rotor creates the so called "cogging" torque, which is considered a parasitic and undesirable characteristic. The slot opening (w_s) has direct impact on the detent torque amplitude. The slot opening (width) minimization should create same effect on cogging amplitude. Still a minimum value, that should at least allow introducing the windings "turn by turn" should be taken into consideration.

2.4.6. Technological constraints

- The stator or rotor cores are made from packed insulated laminations. The ratio of laminations height to total laminated core length is described by the laminated core filling factor, k_{st} , that varies between $0.8 \div 0.95$
- The ratio between the copper filled area and the total slot area is comprised by slot filling factor, k_{sf} . Its value may be chosen from $0.33 \div 0.7$ intervals. Higher values are allowed when open slots (large slot width) are considered and pre-made coils. However, concentrated windings configurations permits larger filling factors.
- The straight turn end connection that exits the slot.
- Mechanical reasoning should determine a minimum shaft diameter that depends on the rated torque the motor will deliver.
- The same reasoning should establish a safe difference between permanent magnet height and stack length in order to avoid axial forces on the bearings.
- Finally a minimum airgap that should limit stator MMF space harmonics impact on eddy current losses must complete the initial dimensioning stage.

2.4.7. Dimensioning methodology

Based on the general aspects regarding the sizing of electric machines this paragraph will offer a computing course that offers first geometrical dimensions, analytically predicted parameters and losses. The dimensioning procedure is applied for our case study - the 6 slots/ 8 poles SPMSM.

The calculations should respect a certain order. The algorithm must be repeated if the results are not satisfying.

The cross-section of our case study prototype, having the main geometrical dimensions depicted is presented in Figure 2.6. Detailed stator dimensions are offered in Figure 2.7, while rotor geometrical details can be found in Figure 2.8.

The first step is to determine the stator inner diameter. Its value is torque dependant, having into the consideration the so called "torque per rotor volume" key dimensioning concept.

The base speed and base power are prior fixed parameters in our design process, so the electromagnetic torque yields (equation 2.10):

$$T_e = \frac{P_b}{2\pi n_b} = \frac{2500}{2\pi 6000 / 60} = 3.97 [\text{Nm}] \quad (2.10)$$

The geometrical form factor is defined by the ratio between the stack length and stator inner diameter:

$$\lambda = \frac{l_{stack}}{D_{si}} = 0.3 \div 3 \quad (2.11)$$

A very elongated motor shape is not aimed, so the shaping factor will be chosen to be $\lambda = 0.7$. In order to comply with the compact size attribute for the power level considered, a specific tangential force of $f_{tsp} = 2 [\text{N/cm}^2]$ is considered suitable. The inner stator diameter becomes (2.12):

$$D_{si} = 3 \sqrt{\frac{2T_e}{\lambda \pi f_{tsp}}} = 3 \sqrt{\frac{2 \times 3.97}{0.7 \times \pi \times 2 \times 10^4}} = 0.057 [\text{m}] = 57 [\text{mm}] \quad (2.12)$$

Going back to (2.11) the stack length, and corresponding rotor length are found to be:

$$\begin{aligned} l_{stack} &= \lambda D_{si} = 0.7 \times 57 = 39.9 \approx 40 [\text{mm}] \\ l_{rotor} &= 1.05 \times l_{stack} = 1.05 \times 40 = 42 [\text{mm}] \end{aligned} \quad (2.13)$$

The airgap height is also included in the prior-set parameters category. It must vary from 0.3 [mm], for small power motors, to 0.9 [mm] for larger power machines. For the given motor design, the airgap, g , will be 0.5 [mm]. so, the outer rotor diameter becomes

$$R_{ro} = \frac{D_{si}}{2} - g = \frac{57}{2} - 0.5 = 28 [\text{mm}] \quad (2.14)$$

Continuing the list of prior-fixed dimensions, the value for permanent magnet height must be at least four times larger than the established airgap height. For the 0.5 [mm] airgap width, a minimum value of 2 [mm] results. Consequently, a

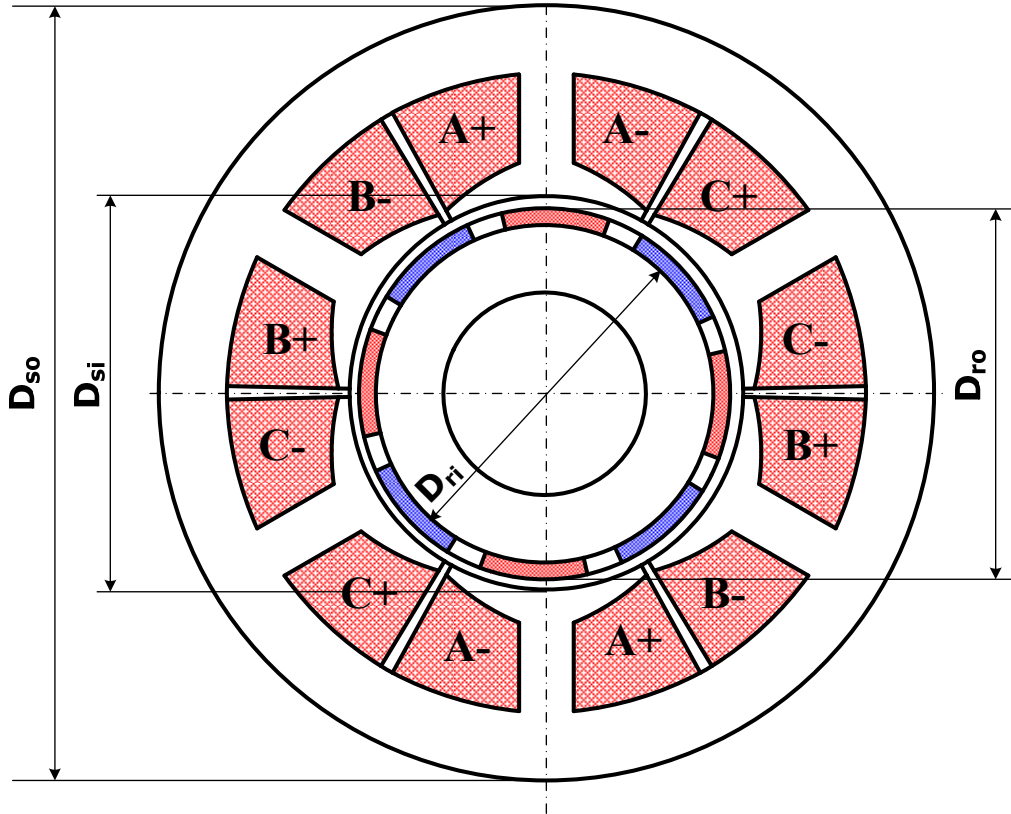


Figure 2.6. Cross-section of a surface permanent magnet synchronous motor

3[mm] value is chosen to cover the condition, but also to keep a reasonable magnet volume, and finally a reasonable cost for the prototype.

With the permanent magnet height set to $h_{PM} = 3[\text{mm}]$, the inner rotor radius becomes:

$$R_{ri} = R_{ro} - h_{PM} = 28 - 3 = 25[\text{mm}] \quad (2.15)$$

The number of stator slots and rotor poles has already been chosen and the reasoning is given in Sections 2.2 and 2.3. These values are prior fixed, too. Several ratios that characterize the topological choice are determined in what follows.

The number of slots per phase, N_{sp} , is

$$N_{sp} = \frac{N_s}{N_{ph}} = \frac{6}{3} = 2 \quad (2.16)$$

The number of slots per phase per pole, N_{ssp} , becomes:

$$N_{ssp} = \frac{N_{sp}}{N_{PM}} = \frac{2}{8} = 0.25 \quad (2.17)$$

The number of slots per pole is

$$N_{sm} = N_{spp} \times N_{ph} = 0.25 \times 3 = 0.75 \quad (2.18)$$

The coil-pole ratio is determined by the number of stator slots divided by the number of rotor poles (permanent magnets)

$$\alpha_{cp} = \frac{N_s}{N_{PM}} = \frac{6}{8} = 0.75 \quad (2.19)$$

The angular pole pitch:

$$\theta_p = 2\pi / N_{PM} = 2\pi / 8 = \pi / 4 \quad (2.20)$$

The angular slot pitch:

$$\theta_s = 2\pi / N_s = 2\pi / 6 = \pi / 3 \quad (2.21)$$

The slot-pole pitch angle is:

$$\theta_{se} = \pi / N_{sm} = \frac{4\pi}{3} \quad (2.22)$$

The pole pitch can be easily calculated with already known stator inner radius and angular pole pitch:

$$\tau_p = R_{si} \theta_p = \frac{57}{2} \times \frac{\pi}{4} = 22.384 \text{ [mm]} \quad (2.23)$$

The coil pitch:

$$\tau_c = \tau_p / \alpha_{cp} = 22.384 / 0.75 = 29.84 \text{ [mm]} \quad (2.24)$$

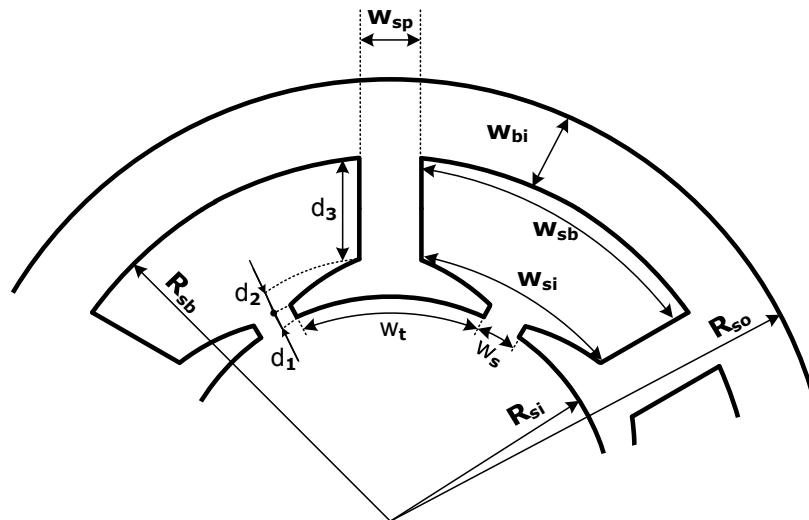


Figure 2.7 Stator slot geometry

Slot pitch at airgap

$$\tau_s = R_{sl}\theta_s = 28 \times \frac{\pi}{3} = 43.98[\text{mm}] \quad (2.25)$$

Tooth width at airgap

$$w_t = \tau_s - w_s \quad (2.26)$$

The distribution factor was already derived in Section 2.4.1, but is rewritten in (2.27) with the now defined angular slot pitch. The distribution factor is unity because z is 1.

$$k_d = \frac{\sin\left(\frac{\theta_s}{2}\right)}{z \times \sin\left(\frac{\theta_s}{z \times 2}\right)} = 1 \quad (2.27)$$

The coil span (pitch) factor is given by equation (2.28)

$$k_p = \cos\left(\frac{\pi - \theta_{se}}{2}\right) = \cos\left(\frac{\pi - 4\pi/3}{2}\right) = 0.866 \quad (2.28)$$

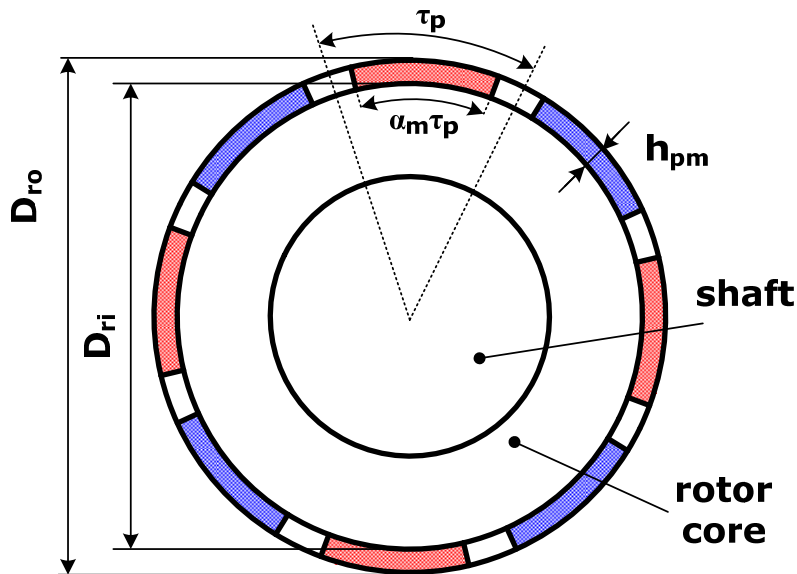


Figure 2.8. Rotor configuration

The permanent magnets will not cover the whole pole pitch. This aspect is considered by introducing the magnet fraction term α_m . Theoretically this factor may be equal to 1, but practically this value will never be true. The so called flux concentration factor is defined in order to consider further in the calculation the real airgap flux. For an established magnet fraction of 0.85, C_ϕ becomes:

$$C_{\Phi} = \frac{2\alpha_m}{1 + \alpha_m} = \frac{2 \times 0.85}{1 + 0.85} = 0.918 \quad (2.29)$$

The permeance coefficient P_c is approximated by (2.30)

$$P_c = h_{PM} / (gC_{\Phi}) = \frac{3}{0.5 \times 0.918} = 6.53 \quad (2.30)$$

This concept was first introduced by Miller and was defined as the absolute value of the slope of the magnet load line formed from the operating point to the origin, normalized by μ_0 . The higher this coefficient is, the better and should be definitely be higher than 1. A high P_c assures an operating area where the magnet will never risk losing some magnetization irreversibly.

Magnet leakage factor is given by (2.31) and must be introduced because the permanent magnet flux does not cross the air-gap entirely since flux paths are created between adjacent magnets.

$$\begin{aligned} k_{ml} &= 1 + \frac{4h_{PM}}{\pi\mu_R\alpha_m\tau_p} \ln \left[1 + \pi \frac{g}{(1 - \alpha_m)\tau_p} \right] = \\ &= 1 + \frac{4 \times 3}{\pi \times 1.018 \times 0.85 \times 22.384} \ln \left[1 + \pi \frac{0.5}{(1 - 0.85) \times 22.384} \right] = 1.075 \end{aligned} \quad (2.31)$$

The slots from the stator actually determine an irregular air-gap width over the rotor periphery. The slot area facing the airgap has low relative permeance, since the windings are non-magnetic. So the flux path is not straight-lined from the permanent magnet rotor pole to the stator core, because the airgap flux tends to avoid the low permeability area. To take count of the real field distribution, several analytical models for airgap flux were developed while making use of different simplifications. The model developed by Carter is considered to be accurate. Before defining carter coefficient (equation (2.33)) an equivalent airgap height has to be determined.(equation (2.32))

Effective air gap for Carter coefficient

$$g_c = g + h_{PM} / \mu_R = 0.5 + \frac{3}{1.018} = 3.447 [\text{mm}] \quad (2.32)$$

Carter coefficient

$$k_c = \frac{1}{1 - \frac{1}{\frac{\tau_s}{w_s} \left(5 \frac{g_c}{w_s} + 1 \right)}} = \frac{1}{1 - \frac{1}{\frac{43.98}{8} \left(5 \frac{3.447}{8} + 1 \right)}} = 1.061 \quad (2.33)$$

The airgap flux is obtained after calculating the airgap flux density (equation 2.35) and the airgap area (equation 2.34).

$$A_g = \frac{\tau_p l_{stack} (1 + \alpha_m)}{2} = \frac{22.384 \times 40 \times (1 + 0.85)}{2} = 828.208 [\text{mm}^2] \quad (2.34)$$

$$B_g = \frac{C_\Phi}{1 + \mu_R k_c k_{ml} / P_c} B_r = \frac{0.918}{1 + \frac{1.018 \times 1.061 \times 1.075}{6.53}} 1.12 = 0.873 [\text{T}] \quad (2.35)$$

The airgap flux is finally:

$$\Phi_g = B_g A_g = 0.873 \times 828.208 \times 10^{-6} = 7.23 \times 10^{-4} [\text{Wb}] \quad (2.36)$$

The stator core dimensioning process may continue once the stacking factor is considered ($k_{st}=0.9$) and the B_{st} and B_{ys} values are set. Assuming the same value, under $B_{max}=1.5$ [T], the geometrical characteristics for stator yoke and teeth may be determined. The calculation follows.

The back-iron width (yoke width) is:

$$w_{bi} = \frac{\Phi_g}{2B_{max}k_{st}l_{stack}} = \frac{7.23 \times 10^{-4}}{2 \times 1.5 \times 0.9 \times 40 \times 10^{-3}} = 0.00669 [\text{m}] = 6.69 [\text{mm}] \quad (2.37)$$

The tooth width is calculated according to (2.38), considering an streamline ratio that considers slot/pole ration (N_{sm})

$$w_{tb} = \frac{2}{N_{sm}} w_{bi} = \frac{2}{0.75} 6.69 = 17.84 [\text{mm}] \quad (2.38)$$

The stator back-iron radius yields:

$$R_{sb} = R_{so} - w_{bi} = 60 - 6.69 = 53.31 [\text{mm}] \quad (2.39)$$

The slot geometrical characteristics are determined now. The slot bottom width results:

$$w_{sb} = R_{sb}\theta_s - w_{tb} = 53.31 \times \frac{\pi}{3} - 17.84 = 37.98 [\text{mm}] \quad (2.40)$$

The slot width inside shoes has to be calculated after choosing the shoe depth fraction. Now, a very large fraction, will reduce the available area for winding placement, while a very small one leads to very thin shoes that will not only face mechanical strength issues, but will also be the high saturated areas of the machine. Making a compromise, the shoe depth is chosen $\alpha_{sd} = 0.2$ and the slot width becomes:

$$w_{si} = (R_{si} + \alpha_{sd}w_{tb})\theta_s - w_{tb} = (28 + 0.3 \times 17.84) \times \frac{\pi}{3} - 17.84 = 17.08 [\text{mm}] \quad (2.41)$$

The slot fraction inside shoes is:

$$\alpha_s = \frac{w_{si}}{w_{si} + w_{tb}} = \frac{17.08}{17.08 + 17.84} = 0.489 \quad (2.42)$$

The total slot depth results:

$$d_s = R_{sb} - R_{ro} = 53.31 - 28 = 25.31 [\text{mm}] \quad (2.43)$$

The area of the slot that may be filled with windings is obtained after eliminating the shoe area. The calculation follows.

The slot depth corresponding to conductor area is:

$$d_3 = d_s - \alpha_{sd} w_{tb} = 25.31 - 0.3 \times 17.84 = 19.95 [\text{mm}] \quad (2.44)$$

And the shoe depth ends to be:

$$d_1 + d_2 = \alpha_{sd} w_{tb} = 0.3 \times 17.84 = 5.352 [\text{mm}] \quad (2.45)$$

Finally, the conductor area A_s can be calculated according to (2.46)

$$\begin{aligned} A_s &= d_3 \left[\theta_s (R_{sb} - d_3 / 2) - w_{tb} \right] = \\ &= 19.95 \left[\frac{\pi}{3} \left(53.31 - \frac{19.95}{2} \right) - 17.84 \right] = 549.429 [\text{mm}^2] \end{aligned} \quad (2.46)$$

The number of turns per slot is obtained by imposing the maximum back-emf amplitude, E_{max} , according to (2.47)

$$\begin{aligned} n_s &= \text{int} \left(\frac{E_{max}}{N_{PM} k_d k_p B_g l_{stack} R_{ro} N_{spp} \omega_m} \right) = \\ &= \text{int} \left(\frac{20}{8 \times 1 \times 0.866 \times 0.873 \times 40 \times 10^{-3} \times 27.5 \times 10^{-3} \times 0.25 \times \frac{2\pi}{60} \times 6000} \right) \quad (2.47) \\ &= \text{int}(19.15) = 19 \end{aligned}$$

The peak back-emf, for the chosen number of turns per slot becomes:

$$\begin{aligned} e_{max} &= N_{PM} k_d k_p B_g l_{stack} R_{ro} N_{spp} n_s \omega_m = \\ &= 8 \times 1 \times 0.866 \times 0.873 \times 40 \times 10^{-3} \times 27.5 \times 10^{-3} \times 0.25 \times 19 \times \frac{2\pi}{60} \times 6000 \quad (2.48) \\ &= 20.168 [\text{V}] \end{aligned}$$

The peak slot current may be calculated with (2.49):

$$\begin{aligned} I_s &= \frac{T_e}{N_{PM} k_d k_p B_g l_{stack} R_{ro} N_{spp}} = \\ &= \frac{3.97}{8 \times 1 \times 0.866 \times 0.873 \times 40 \times 10^{-3} \times 27.5 \times 10^{-3} \times 0.25} = 2385.908 [\text{A}] \end{aligned} \quad (2.49)$$

The phase current results immediately:

$$I_{ph} = \frac{I_s}{N_{ph} n_s} = \frac{2385.908}{3 \times 19} = 41.85 [\text{A}] \quad (2.50)$$

In order to comply with the compact size criterion the current density should be high, but it should not exceed the maximum value of 10 A/mm², because this would mean not only high copper losses but also forced cooling. The peak conductor current density for a slot filling factor established to $k_{cp} = 0.5$ is:

$$j_{Co} = \frac{I_s}{k_{cp} A_s} = \frac{2385.908}{0.5 \times 549.429} = 8.68 [\text{A}/\text{mm}^2] \quad (2.51)$$

The peak slot density can be calculated in respect to equation (2.52)

$$|B_s|_{\max} = \frac{\mu_0 I_s}{w_s} = \frac{4\pi \times 10^{-7} \times 2385.908}{8 \times 10^{-3}} = 0.374 [\text{T}] \quad (2.52)$$

Resistance computation is performed taking into consideration slot resistance component and end-turn component. Copper resistivity value is considered for 100 °C, to cover resistance increase with temperature.

Slot resistance is computed with (2.53)

$$R_s = \frac{\rho_{Co} n_s^2 l_{stack}}{k_{cp} A_s} = \frac{2.3 \times 10^{-8} \times 19^2 \times 40 \times 10^{-3}}{0.5 \times 549.429 \times 10^{-6}} = 1.64 \times 10^{-3} [\Omega] \quad (2.53)$$

The end turn resistance yields:

$$R_e = \frac{\rho_{Co} n_s^2 \pi \tau_c}{2 k_{cp} A_s} = \frac{2.3 \times 10^{-8} \times 19^2 \times \pi \times 29.84 \times 10^{-3}}{2 \times 0.5 \times 549.429 \times 10^{-6}} = 1.41 \times 10^{-3} [\Omega] \quad (2.54)$$

So, finally the phase resistance results:

$$R_{ph} = N_{sp}(R_s + R_e) = 2(1.64 + 1.41) \times 10^{-3} = 6.1 \times 10^{-3} [\Omega] = 6.1 [\text{m}\Omega] \quad (2.55)$$

For inductance computation three components have to be considered, the airgap inductance, L_g (according to equation 2.56), the slot leakage inductance L_s (according to equation 2.57) and the end turn inductance, L_e (according to equation 2.58).

$$L_g = \frac{n_s^2 \mu_R \mu_0 l_{stack} \tau_c k_d}{4(h_{PM} + \mu_R k_c g)} = \frac{19^2 \times 1.018 \times 4\pi \times 10^{-7} \times 40 \times 10^{-3} \times 29.84 \times 10^{-3} \times 1}{4(3 \times 10^{-3} + 1.018 \times 1.061 \times 0.5 \times 10^{-3})} = 38.92 \times 10^{-6} [\text{H}] \quad (2.56)$$

$$L_s = n_s^2 \left[\frac{\mu_0 d_3^2 l_{stack}}{3A_s} + \frac{\mu_0 d_2 l_{stack}}{(w_s + w_{sj}) / 2} + \frac{\mu_0 d_1 l_{stack}}{w_s} \right] = 19^2 \times \left[\frac{4\pi \times 10^{-7} \times 19.95^2 \times 10^{-6} \times 40 \times 10^{-3}}{3 \times 549.429 \times 10^{-6}} + \frac{4\pi \times 10^{-7} \times 2.352 \times 10^{-3} \times 40 \times 10^{-3}}{(8 + 17.08) \times 10^{-3} / 2} + \frac{4\pi \times 10^{-7} \times 4 \times 10^{-3} \times 40 \times 10^{-3}}{8 \times 10^{-3}} \right] = 16.85 \times 10^{-6} [\text{H}] \quad (2.57)$$

$$L_e = \frac{n_s^2 \mu_0 \tau_c}{8} \ln \left(\frac{\tau_c^2 \pi}{4A_s} \right) = \frac{19^2 \times 4\pi \times 10^{-7} \times 29.84 \times 10^{-3}}{8} \ln \left(\frac{29.84^2 \times 10^{-6} \times \pi}{4 \times 549.429 \times 10^{-6}} \right) = 4.08 \times 10^{-7} [\text{H}] \quad (2.58)$$

The phase inductance results:

$$L_{ph} = N_{sp}(L_g + L_s + L_e) = 2 \times (38.92 + 16.85 + 0.408) \times 10^{-6} \approx 112 [\mu\text{H}] \quad (2.59)$$

Stator steel volume can be easily calculated according to (2.60)

$$\begin{aligned} V_{st} &= \left[\pi (R_{so}^2 - R_{si}^2) - N_s A_s \right] l_{stack} k_{st} = \\ &= \left[\pi (60^2 - 28^2) \times 10^{-6} - 6 \times 549.429 \times 10^{-6} \right] \times 40 \times 10^{-3} \times 0.9 = \\ &= 1.998 \times 10^{-4} [\text{m}^3] \end{aligned} \quad (2.60)$$

In order to determine the prototype's efficiency, losses have to be estimated. Copper losses are calculated with (2.61) and are:

$$P_r = N_{ph} I_{ph}^2 R_{ph} = 3 \times 41.85^2 \times 6.1 \times 10^{-3} = 32.05 [\text{W}] \quad (2.61)$$

Core losses are calculated for rated frequency ($f_b=400\text{Hz}$) and maximum magnetic flux level considered while dimensioning the stator and rotor teeth and yokes. More accurate calculations should discriminate between teeth and yoke losses, taking into account the maximum flux density in the region, determined by actual geometric characteristics. (2.62) leads to a higher core losses value, but it covers the "worst-case-scenario"

$$P_{cl} = \gamma_{Fe} V_{st} \Gamma(B_{max}, f_e) = 7.8 \times 10^3 \times 1.998 \times 10^{-4} \times 112.71 = 174.772 [\text{W}] \quad (2.62)$$

The supplementary losses are calculated as a fixed percentage from the base power; they are usually considered to be as large as 0.5%:

$$P_s = 0.5\% P_b = \frac{0.5}{100} \times 2500 = 12.5 [\text{W}] \quad (2.63)$$

The overall efficiency can be computed from (2.64)

$$\eta = \frac{P_b}{P_b + P_r + P_{cl} + P_s} \times 100 = \frac{2500}{2500 + 32.05 + 174.77 + 12.5} \times 100 = 91.19 [\%] \quad (2.64)$$

It has to be noted that real prototype efficiency is actually higher at rated speed. This is due to "worst-case scenario" principle that was applied.

For thermal calculations, different heat density values might be calculated, so that proper heat removal measures should be considered.

Slot heat density

$$q_s = \frac{P_r}{L(2d_3 + w_{sb})N_s} = \frac{32.05}{40 \times 10^{-3} \times (2 \times 19.95 + 37.98) \times 10^{-3} \times 6} = 19.96 [\text{W}/\text{m}^2] \quad (2.65)$$

Stator heat density

$$q_{st} = \frac{P_r + P_{cl}}{2\pi R_{so} l_{stack}} = \frac{32.05 + 174.772}{2\pi \times 60 \times 10^{-3} \times 40 \times 10^{-3}} = 13.7 [\text{kW}/\text{m}^2] \quad (2.66)$$

2.5. Active materials weights and costs

Active materials determine an important part of the final prototype weight. Calculations are made in order to determine initial weight. Furthermore, initial cost is then computed with the results from previous calculation step.

Copper mass m_{Co} is determined with (2.68), taken into account the copper filled slot area and knowing the coil turn length, l_{turn} . Calculations follow.

$$l_{turn} = 2 \left(l_{stack} + \frac{\pi}{2} (D_{si} + d_s) \sin \left(\frac{\theta_s}{2} \right) \right) = 2 \left(40 + \frac{\pi}{2} (57 + 25.31) \sin \frac{\pi}{2 \times 3} \right) = \quad (2.67)$$

$$= 209.29 [\text{mm}]$$

$$m_{Co} = N_s \frac{l_{turn}}{2} A_s k_{cp} \gamma_{Co} = 6 \frac{0.20929}{2} 549.429 \times 10^{-6} \times 0.5 \times 8.93 \times 10^3 = \quad (2.68)$$

$$= 1.544 [\text{kg}]$$

Permanent magnet weight is easily computed because of the simplified geometric characteristics.

$$m_{PM} = \alpha_m \times \frac{\pi}{4} (D_{ro}^2 - D_{ri}^2) \times l_{rotor} \times \gamma_{PM} = \quad (2.69)$$

$$= 0.85 \times \frac{\pi}{4} (56^2 - 50^2) \times 10^{-6} \times 42 \times 10^{-3} \times 7.4 \times 10^3 = 0.132 [\text{kg}]$$

Stator iron mass, m_{sFe} and rotor iron mass m_{rFe} is determined by:

$$m_{sFe} = \left(\frac{\pi}{4} (D_{so}^2 - D_{si}^2) - N_s \times A_s \right) \times l_{stack} \times \gamma_{Fe} =$$

$$= \left(\frac{\pi}{4} (120^2 - 57^2) \times 10^{-6} - 6 \times 549.429 \times 10^{-6} \right) \times 40 \times 10^{-3} \times 7.8 \times 10^3 = \quad (2.70)$$

$$= 1.704 [\text{kg}]$$

$$m_{rFe} = \frac{\pi}{4} D_{ri}^2 \times l_{stack} \times \gamma_{Fe} = \quad (2.71)$$

$$= \frac{\pi}{4} \times 50^2 \times 10^{-6} \times 40 \times 10^{-3} \times 7.8 \times 10^3 = 0.612 [\text{kg}]$$

The total mass of the motor (excluding bearings and frame) is the sum of active material weights:

$$m_{total} = m_{Co} + m_{sFe} + m_{rFe} + m_{PM} = \quad (2.72)$$

$$= 1.544 + 0.132 + 1.704 + 0.612 = 3.992 [\text{kg}]$$

As the laminations are stamped from squares, the iron mass m_{Fe} for cost calculation has to be re-computed:

$$m_{Fe} = D_{so}^2 \times l_{stack} \times k_{st} \times \gamma_{Fe} = \quad (2.73)$$

$$= 120^2 \times 10^{-6} \times 40 \times 10^{-3} \times 0.9 \times 7.8 \times 10^3 = 4.044 [\text{kg}]$$

$$\begin{aligned}
c_{mat} &= m_{Fe} \times C_{lam} + m_{PM} \times C_{PM} + m_{Co} \times C_{Co} = \\
&= 4.044 \times 5 + 0.132 \times 50 + 1.544 \times 10 = 42.26 [\text{USD}]
\end{aligned} \tag{2.74}$$

where $C_{lam} = 5$ USD/kg, $C_{Co} = 10$ USD/kg and $C_{PM} = 50$ USD/kg are the specific prices for the laminations, copper and permanent magnets respectively [2.2].

2.6. Thermal verification

To roughly verify the winding over-temperature of the machine, first the total frame area, A_{frame} , for heat transfer has to be calculated. :

$$A_{frame} = \pi D_{so} l_{frame} k_f + \frac{\pi}{2} D_{so}^2 \tag{2.75}$$

k_f is a cooling factor that characterizes the heat transfer determined by frame shape. If fins are considered for the frame, then k_f is 3.

$$\begin{aligned}
l_{frame} &= l_{stack} + (D_{si} + d_s) \times \sin\left(\frac{w_{tb}}{D_{si}} + \arcsin\frac{w_s}{D_{si}}\right) = \\
&= 40 \times 10^{-3} + (57 + 25.21) \times 10^{-3} \times \sin\left(\frac{17.83 \times 10^{-3}}{57 \times 10^{-3}} + \arcsin\frac{8 \times 10^{-3}}{57 \times 10^{-3}}\right) = \\
&= 63.738 \times 10^{-3} [\text{m}]
\end{aligned} \tag{2.76}$$

$$\text{So } A_{frame} = \pi \times 120 \times 10^{-3} \times 63.738 \times 10^{-3} \times 3 + \frac{\pi}{2} 120^2 \times 10^{-6} = 0.094 [\text{m}^2]$$

An equivalent heat transfer coefficient, α_t (in $\text{W}/\text{m}^2\text{°C}$), from 14 (for unventilated frames) to 100 (for water-cooled frame jackets), the winding over temperature, T_w , is

$$T_w = \frac{P_r + P_{cl}}{\alpha_t A_{frame}} = \frac{32.05 + 174.772}{17 \times 0.094} = 129.425 [\text{°C}] \tag{2.77}$$

The insulation class is F, so a maximum winding temperature of 155°C is allowed. The thermal calculation is verified.

If the over temperature is high, the machine design must be restarted, with a smaller f_{isp} and / or longer λ (longer stack length).

2.7. Conclusion

A synthesis of fractional slot concentrated winding permanent magnet synchronous machines was presented, emphasizing the PMSM structures with concentrated windings and fractional, less than unity slot per pole per phase ratio.

The case study was represented by a 6 slot/8 pole surface permanent magnet synchronous machine prototype.

A preliminary electromagnetic design for chosen topology was derives, taking onto account configuration specificities. Analytic calculation of some motor parameters, active material weights and cost along with thermal verification computation comes to complete the design procedure.

The resulted prototype's characteristics are presented in Tables 2.5 and 2.6.

Table 2.5 Dimensions and properties of the designed SPMSM

Parameter	Value	Measure unit
Topology		
number of phases	3	-
number of stator slots	6	-
number of rotor poles	8	-
Geometry		
stator outer diameter	120	[mm]
stator inner diameter	57	[mm]
air-gap	0.5	[mm]
rotor outer diameter	56	[mm]
rotor inner diameter	50	[mm]
stator tooth width	17.84	[mm]
stator yoke height	6.69	[mm]
stator slot bottom width	37.98	[mm]
stator slot top width	17.08	[mm]
stack length	40	[mm]
slot depth	25.31	[mm]
magnet height	3	[mm]
slot opening	8	[mm]
tooth neck height	2.352	[mm]
tooth wedge height	3	[mm]
Winding		
number of slots/pole/phase -	0.25	[-]
number of slots turns per phase	19	[-]
number of slots of parallel current paths	1	[-]
slot fill factor	0.5	[-]
no. coils/phase -	2	[-]
Materials		
core material	M800-50A	[-]
magnet type .	NdFeB 31/25	[-]
Weight & costs		
motor weight	3.992	[kg]
initial cost	42.26	[USD]

Table 2.6. Machine parameters (analytical calculation)

Parameter	Symbol	Value	Measure unit
Phase resistance (100°C operating temperature)	R_{ph}	6.1	[mΩ]
Phase inductance	L_{ph}	112	[μH]
Phase current	I_{phase}	41.85	[A]
Base output power	P_b	2500	[W]
Rated efficiency	η	91.9	[%]
Rated copper losses	P_r	32.05	[W]
Rated iron losses	P_{cl}	172.778	[W]
Rated friction losses (bearing, windage)	P_s	12.5	[W]

References

- [2.1] D. Iles, "Automotive Permanent Magnet Actuation Technologies", PhD Thesis, Politehnica University from Timisoara, 2005
- [2.2] D. Iles-Klumpner, I. Boldea, "Permanent magnet synchronous motor solutions for automotive applications including x-by-wire systems", Proceedings of PCIM, 2004, pp. 1 - 6.
- [2.3] D. Iles-Klumpner, M. Risticevic, H. W. Hartkorn, G. Lahm, I. Serban, I. Boldea, "Electric actuation technologies for automotive steering systems", SAE 2005 World Congress & Exhibition, April 2005.
- [2.4] D. Iles-Klumpner, I. Serban, M. Risticevic, "PMSM Drive Systems for Electric Active Steering (EAFS) Application: a Comparative Characterization", Proceedings of the IEEE International Vehicle Power and Propulsion Conference, (VPPC '06), 2006, pp. 1 -6
- [2.5] Ion Boldea, Lucian Tutelea, "Electric Machines – Steady State, Transients and Design with Matlab[®]", CRC Press, Taylor&Francis Group, 2010
- [2.6] R. Krishnan, "Permanent Magnet Synchronous and Brushless DC Motor Drives", CRC Press, Taylor and Francis Group, 2010
- [2.7] Duane C. Hanselman, "Brushless Permanent-Magnet Motor Design", McGraw –Hill Inc., 1994
- [2.8] Duane C. Hanselman, "Brushless Permanent-Magnet Motor Design", Second Edition, Magna Physics Publishing, 2006
- [2.9] Handbook of Electric Motors, Second Edition, CRC Press, Taylor and Francis Group, 2004, Chapter 6, pp. 328 – 364
- [2.10] Hiroshi Murakami, Yukio Honda, Hiroyuki Kiriya, Shigeo Morimoto, Yoji Takeda, "The Performance Comparison of SPMSM , IPMSM and SynRM in Use as Air-conditioning Compressor", Proceedings of the IEEE Thirty-Fourth Industry Applications (IAS) Annual Meeting, Volume: 2, 1999, pp. 840 - 845
- [2.11] Kan Akatsu, Katsuyuki Narita, Yoshiyuki Sakashita, Takashi Yamada, "Characteristics comparison between SPMSM and IPMSM under high flux density condition by both experimental and analysis results", Proceedings of the IEEE International conference on Electrical Machines and Systems (ICEMS), 2008, pp. 2848 – 2853
- [2.12] M. Chabchoub, I. Ben Salah, G. Krebs, R. Neji, C. Marchand, "PMSM cogging torque reduction: Comparison between different shapes of magnet", Proceedings of the IEEE International Conference on Renewable Energies and Vehicular Technology (REVET), 2012, pp. 206 - 211
- [2.13] Juha Pyrhonen, Tapani Jokinen, Valeria Hrabovcova, "Design of Rotating Electrical Machines", Wiley, 2008
- [2.14] Shih-Chin Yang, Takahiro Suzuki, Robert D. Lorenz, Thomas M. Jahns, "Surface Permanent Magnet Synchronous Machine Design for Saliency-Tracking Self- Sensing Position Estimation at Zero and Low Speeds", Proceedings of the IEEE Energy Conversion Congress and Exposition (ECCE), 2010, pp. 3493 - 3500
- [2.15] Luigi Alberti, Emanuele Fornasiero, Nicola Bianchi "Impact of the Rotor Yoke Geometry on Rotor Losses in Permanent-Magnet Machines", IEEE Transactions on Industry Applications, Vol. 48, no. 1, January/February 2012, pp 98 – 105
- [2.16] C. Grabner, "Idea, realization and characteristics of a novel permanent magnet motor topology with higher harmonic airgap waves in the BLDC

- mode", Proceedings of the IEEE International Symposium on Industrial Electronics (ISIE), 2007, pp. 1056 – 1061
- [2.17] Xinghua Wang, Shichao Yan, Xiaocui Zhang, Xiuhe Wang, Chenghui Zhang, "The rotor topology of slotless permanent-magnet brushless DC motor", Proceedings of the IEEE International Conference on Electrical Machines and Systems (ICEMS), 2010, pp. 1057 – 1060
- [2.18] K. I. Laskaris, A. G. Kladas, "Comparison of internal and surface permanent-magnet motor topologies for electric vehicle applications", Proceedings of the IEEE Advanced Electromechanical Motion Systems & Electric Drives Joint Symposium (ELECTROMOTION), 2009, pp. 1 – 4
- [2.19] Liu Guohai, Zhang Hongtao, "Design and analysis on permanent-magnet BLDC motor for automatic door", Proceedings of the IEEE International Conference on Electrical Machines and Systems (ICEMS), 2008, pp. 3171 – 3176
- [2.20] Jacek F. Gieras, "Permanent Magnet Motor Technology – Design and Applications", Third Edition, CRC Press, Taylor and Francis Group, 2010
- [2.21] A.M. El-Rafaie, "Fractional-Slot Concentrated-Windings Synchronous Permanent Magnet Machines: Opportunities and Challenges", IEEE Transactions On Industrial Electronics, Vol. 57, No. 1, January 2010, pp. 107-121
- [2.22] Jérôme Cros, Philippe Viarouge, "Synthesis of High Performance PM Motors With Concentrated Windings", IEEE Transactions On Energy Conversion, VOL. 17, NO. 2, June 2002, pp. 248 - 253
- [2.23] A. Soualmi, F. Dubas, A. Randria, C. Espanet, "Comparative Study of Permanent-Magnet Synchronous Machines with Concentrated Windings for Railway Application", Proceedings of the IEEE International Conference Electrical Machines and Systems (ICEMS), 2011, pp. 1 - 5
- [2.24] G. De Donato, F. Giulii Capponi, A. Rivellini and F. Caricchi, "Integer-Slot vs Fractional-Slot Concentrated-Winding Axial-Flux Permanent Magnet Machines: Comparative Design, FEA and Experimental Tests", Proceedings of the IEEE International Energy Conversion Congress and Exposition (ECCE), 2011 IEEE, pp. 3120 - 3127
- [2.25] Freddy Magnussen, Heinz Lendenmann, "Parasitic Effects in PM Machines With Concentrated Windings", IEEE Transactions On Industry Applications, Vol. 43, No. 5, September/October 2007, pp. 1223 - 1232
- [2.26] Mihail V. Cistelecan, Fernando J. T. E. Ferreira, Mihail Popescu, "Three phase tooth-concentrated multiple-layer fractional windings with low space harmonic content", Proceedings of the IEEE International Energy Conversion Congress and Exposition (ECCE), 2010, pp. 1399 - 1405
- [2.27] L. Chong, M. F. Rahman, "Saliency Ratio Optimization in an IPM Machine with Fractional-slot Concentrated Windings", Proceedings of the IEEE International Conference on Electrical Machines and Systems, (ICEMS), 2008, pp. 2921 - 2926
- [2.28] Ayman M. EL-Rafaie, Thomas M. Jahns, "Scalability of Surface PM Machines With Concentrated Windings Designed to Achieve Wide Speed Ranges of Constant-Power Operation", IEEE Transactions On Energy Conversion, Vol. 21, No. 2, June 2006, pp. 362 – 369
- [2.29] M. T. Abolhassani, "A New Concentrated Windings Surface Mounted Permanent Magnet Synchronous Machine for Wind Energy Application", Proceedings of the IEEE International Conference on Electric Machines and Drives (IEMDC), 2005, pp. 931 – 936

-
- [2.30] Manoj R. Shah, Ayman M. EL-Refaie, "End Effects in Multi-Phase Fractional-Slot Concentrated-Winding Surface Permanent Magnet Synchronous Machines", Proceedings of the IEEE International Energy Conversion Congress and Exposition (ECCE), 2009, pp. 3798 - 3805
- [2.31] H. Polinder, M.J. Hoeijmakers, M. Scuotto, "Eddy-Current Losses in the Solid Back-Iron of PM Machines for different Concentrated Fractional Pitch Windings", Proceedings of the IEEE International Electric Machines & Drives Conference (IEMDC), 2007, pp. 652 - 657
- [2.32] A. Cavagnino, M. Lazzari, A. Miotto, A. Tenconi, S. Vaschetto, "Impact of the Rotor Back-Iron Resistivity on the Rotor Eddy-Current Losses in Fractional-Slot Concentrated Windings PM Machines", Proceedings of the IEEE International Energy Conversion Congress and Exposition (ECCE), 2011, pp. 1604 - 1611
- [2.33] M. L. M. Jamil, L. J. Wu, "Influence of slot and pole number combinations on unbalanced magnetic force in permanent magnet machines", Proceedings of the IEEE International Energy Conversion Congress and Exposition (ECCE), 2011, pp 3291 - 3298
- [2.34] S. E. Skaar, Ø. Krøvel, R. Nilssen, "Distribution, coil-span and winding factors for PM machines with concentrated windings", Proceedings of the IEEE International Conference on Electrical Machines and Systems, (ICEMS), 2006, pp. 346 - 351
- [2.35] Ayman M. EL-Refaie, Z. Q. Zhu, Thomas M. Jahns, David Howe, "Winding Inductances of Fractional Slot Surface-Mounted Permanent Magnet Brushless Machines", Proceedings of the IEEE Annual Meeting of the Industry Applications Society (IAS), 2008, pp. 1 - 8
- [2.36] Power Core M800-50A NGO Electrical Steel Application Note, ThyssenGrupp Steel, 2009, pp. 1 - 9
- [2.37] Typical Data for SURA® M800-50A, Cogent Surahammars Bruks AB, 2008
- [2.38] DEXTER Magnetic Technologies, "Permanent Magnet Catalog".

CHAPTER 3

6 Slot/8 Pole Synchronous Machine: Optimal Design for a Surface Permanent Magnet Motor

Abstract

This chapter deals with the optimal design stage applied for the 6 slot/ 8pole surface permanent magnet prototype designed analytically in the previous Chapter. A modified Hooke Jeeves method is chosen in order to obtain a fast minimization of the objective function. A comparison between geometric characteristics and resulting parameters for the two dimensioning methodologies is given at the end.

3.1. Introduction

The analytical design methodology described in Chapter 2 was able to deliver a first prototype dimensioning. However, the process does not guarantee all constructive constraints we are looking for the automotive air conditioning compressor drive. It is a real art to know how to choose initial parameters, even if general guidelines are followed.

A good prototype is generally obtained after several repetitions of the design algorithm, which means that dimensioning calculus and verification calculus stages are scoured several times. The "road" to the most convenient prototype is shorter or longer, depending on the designer's experience. Anyway, new motor configurations are supporting the diligent efforts carried out to get the best out of each new topology.

Through design [3.1], a set of geometrical characteristics needs to be found so that specifications and requirements are met. However, because the relationships between the machine performance indices (p_i) and the geometrical dimensions, is nonlinear, it is impossible to produce a single variable vector (X) that satisfies p_i .

$$p_i = f_i(X), \quad i = 1, n \quad (3.1)$$

where f_i is the involved nonlinear function between motor parameters and design requirements.

It was already stated that the geometrical dimensioning is found iteratively. For the various analytical design methods, the initial selection of electric/magnetic stresses and fixed geometric parameters is done by the designer. Unless an appropriate correlation between electric/magnetic stress changes and geometrical parameter variations is established, the number of repetitions that need to be performed is very high or the restrictive conditions may actually require an impossible configuration. The general impression is that analytic design consumes a lot of time, even if it is aided by computer implementation, as it depends considerably on the designer's experience.

The optimal design, does not throw away the analytical design procedure, but improves it by adding an objective function and the implied calculation steps. Figure 3.1 presents the flowchart that describes optimal design algorithm ([3.1]).

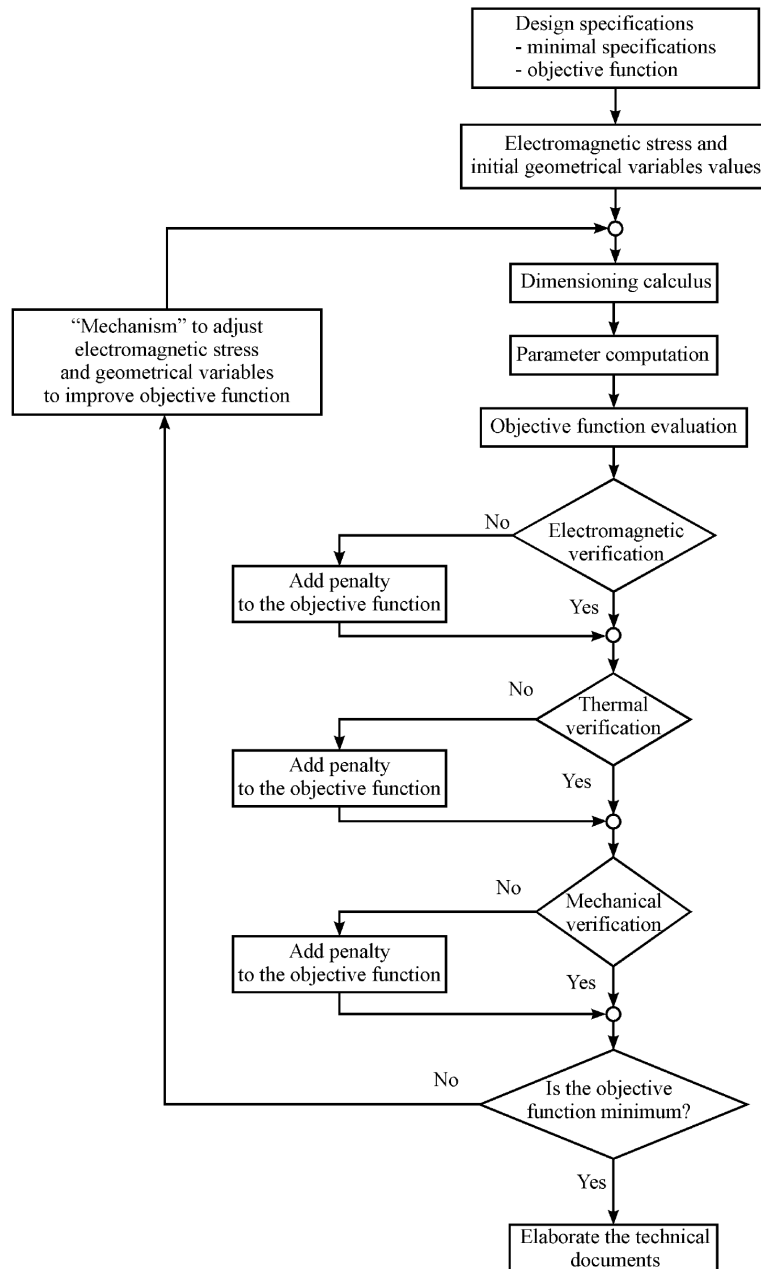


Figure 3.1. Optimal design flow chart [3.1]

The initial electromagnetic stresses and geometrical parameters are either specified by the designer or randomly generated through a dedicate routine. In parallel to performing the traditional calculus an evaluation of the objective function is realized. Penalties are added to the objective function, if electromagnetic, thermal or mechanical calculations return values that do not correspond to the performance index. The penalty coefficients that transfer non-corresponding results into correction measures determine the optimization process flow parameters.

The detection of the minimum objective function value and the selections of the new value of electromagnetic stresses and initial geometrical variables before every iteration cycle are heavily dependent on the objective function optimum search method.

The goal is to find the minimum of the objective function (defined according to the optimization criterion established). The methods that adjust electromagnetic stress and geometric variables to improve the objective function can be classified as follows ([3.1 -3.28]):

- Stochastic ([3.2, 3.3, 3.13, 3.14, 3.16]): based on genetic algorithm, evolution strategies, population based incremental learning, simulated annealing; these methodologies are inspired from bio-physics laws and are trusted to deliver the "optimum"
- Non - iterative: based on fuzzy logic, artificial neural network; the concept that lays behind the strategy is rather new, and only few convincing results are present in the literature
- Deterministic ([3.4, 3.9, 3.10-3.12]): based on conjugate gradient, quasi-Newton, Steepest-descent are not trusted to deliver the global minimum, but they do provide smaller computation time

From mathematical point of view, the optimization process consists in minimizing the desired objective function, f_{obj} , which depends on optimization variable vector, X , and a set of constrains, ($g_i(X)$ -inequality and $h_i(X)$ -equality constrains). Usually the optimization variable domain is bounded.

$$\begin{aligned} \min & (f_{obj}(\bar{X})) \\ & g_i(\bar{X}) \leq 0, \quad i = 1, m \\ & h_i(\bar{X}) = 0, \quad i = 1, k \\ & x_i \in [x_{i \min}, x_{i \max}], \quad i = 1, n \end{aligned} \quad (3.2)$$

Such constrained systems can be transformed into unconstrained ones by implementing penalty functions, G_i , by penalty coefficients, r_k . The equivalent objective function becomes:

$$f_{obj_equiv} = f_{obj}(\bar{X}) + r_k \sum_{i=1}^m G_i(g_i(\bar{X})) \quad (3.3)$$

$$G_{i_{interior}} = \begin{cases} -\frac{1}{g_i(\bar{X})} \\ \log(-g_i(\bar{X})) \end{cases} \quad G_{i_{exterior}} = \begin{cases} \max(0, g_i(\bar{X})) \\ [\max(0, g_i(\bar{X}))]^2 \end{cases} \quad (3.4)$$

For unconstrained systems, different methods that are based on search algorithms may be applied. These optimization mechanisms are easy to implement

as computer programs and come along with the advantage of a reduced computation time.

3.2. The modified Hooke Jeeves optimization method

The Hooke Jeeves optimization method is based on pattern search algorithm that uses “exploratory” and “pattern” moves to fulfil its functionality. It may be used for unconstrained systems or for systems that become this way by introducing penalty functions.

The method is chosen because it is characterized by low computational effort and time. Even though the part with computation resources might be arguable, since the “information technology” has advanced in such a manner, that devices are more performing and in the same time cheaper, the calculation time might be an issue. When differences are made from few seconds (for “search algorithms”) to some minutes/hours (for genetic algorithms, for example), the time factor has serious implications on work productivity and energy consumption, which are rigorously supervised in industry. So, the intention is not to be fashionable, but practical.

The method implementation for the motor optimization design comprises the following steps [3.1]:

Step 1. Establish the fixed parameters and constants and choose the variables vector, (\bar{X}) , and decide this way the geometrical dimensions that should undergo the optimization process. A small variable number might not accomplish the optimization process, while a large number only complicates it. For our case study, the following vector was chosen:

$$\bar{X} = (D_{si}, D_{so}, d_1, d_2, w_{tb}, w_{bi}, l_{stack}, h_{pm}, w_s)^T \quad (3.5)$$

D_{si}	stator inner diameter	w_{tb}	stator tooth width
D_{so}	stator outer diameter	w_{bi}	stator yoke width
d_1	stator tooth wedge width	l_{stack}	stack length
d_2	stator tooth neck width	h_{pm}	PM height
w_s	stator slot opening (mouth)		

Step 2. Technological limitations along with geometrical constraints must be considered and maximum and minimum limitations for the optimized variables must be set. Since a motor geometry is already available through analytical design, the initial vector will be set accordingly in *Step 4*, and limits will be chosen as in (3.6):

$$\begin{aligned} x_{\min} &= 0.7 \times x_{analytic} \\ x_{\max} &= 1.3 \times x_{analytic} \end{aligned} \quad (3.6)$$

Exception to this rule will apply for the minimum value determination for: permanent magnet height that has to be at least 4 times the airgap height, slot opening limited to at least 1.05 of conductor area, to allow at least “turn by turn” winding placement in coils and d_1 and d_2 minimum limits of 0.3mm (imposed by technological and mechanical reasoning).

Step 3. Choose the objective function. Since the requirements ask for a compact size and low cost motor, the objective function could consider the initial machine cost, the loss penalty cost and a constraint function penalty.

$$f_{obj} = c_i(\bar{X}) + c_e(\bar{X}) + c_p(\bar{X}) \quad (3.7)$$

where c_i establishes the dependence on the initial cost
 c_e establishes the dependence on the energy losses cost
 c_p establishes the dependence on the penalty cost

Each dependence is detailed in what follows.

The initial cost considers active materials cost, additional cost (for motor frame for example) and even power electronics cost (creating this way a more complete drive directed cost efficiency) – equation (3.8)

$$c_i = c_{Co}m_{Co} + c_{lam}m_{Fe} + c_{PM}m_{PM} + c_a m_{total} + c_{pe} \frac{P_b}{p_f} \quad (3.8)$$

where:

c_{Co}	copper cost, 10 [USD/kg]	m_{Co}	copper weight
c_{lam}	lamination cost, 5 [USD/kg]	m_{Fe}	iron lamination weight
c_{PM}	PM cost, 50 [USD/kg]	m_{PM}	PM weight
c_a	Additional cost, 1 [USD/kg]	m_{total}	motor total weight
c_{pe}	power electronics cost, 0.03 [USD/VA]	p_f	power factor

The observation that laminations are stamped from rectangular iron sheets remains valid, and reuse of thrown material is not taken into consideration.

The energy loss cost arises from low efficiency motor utilization. It is not only the price that you pay for acquisitioning a certain product, but also the amount of money spent for operating it that matters.

$$c_e = P_b \left(\frac{1}{\eta(\bar{X})} - 1 \right) p_e t_{operating} \quad (3.9)$$

where

P_b	rated power [W]	η	rated efficiency
p_e	energy cost – 0.1[USD/kWh]	$t_{operating}$	operating time - years of use

Constraints penalty cost, c_p is composed from penalty cost of the over-temperature (c_{p_temp}) and penalty cost of the permanent magnet demagnetization due to peak or direct start current (c_{p_demag} – (3.12)) – equation (3.10)

$$c_p = c_{p_temp} + c_{p_demag} \quad (3.10)$$

Over-temperature penalty is determined by (3.11)

$$\begin{aligned} c_{p_temp} &= c_{p_winding} + c_{p_PM} \\ c_{p_winding} &= \max(0, T_w - T_{wad}) K_{tw} c_i \\ c_{p_PM} &= \max(0, T_{PM} - T_{PMad}) K_{tPM} c_i \end{aligned} \quad (3.11)$$

where	$c_{p_winding}$	penalty cost for stator (winding) over-temperature
	c_{p_PM}	penalty cost for rotor (PM) over-temperature
	T_w	windings temperature,
	T_{wad}	maximum admissible winding temperature,
	K_{tw} or K_{tPM}	a proportional constant,
	c_i	initial cost from (3.8).
	T_{PM}	rotor temperature
	T_{PMad}	maximum admissible rotor temperature

$$\text{While } c_{p_demag} = \max \left(0, -\frac{\min(\Phi_{PM_demag})}{\Phi_{PM_0}} \right) K_{demag} c_i \quad (3.12)$$

Where	Φ_{PM_demag}	total flux trough PM at maximum demagnetization current equal to rated peak current multiplied by a demagnetization safety factor.
	Φ_{PM_0}	no load total flux trough PM
	K_{demag}	proportional constant

Step 4. The initial values of optimized variable vector, \bar{X}_0 must be chosen. These values are not randomly set, since they are the output values of the prior analytic design procedure. At the same time, the initial step vector, $d\bar{X}_0$, the minimum step vector $d\bar{X}_{min}$ and the step actualization ratio, $r \in (0,1)$, must be fixed.

Step 5. Geometrical dimensions, parameters and characteristics are determined according to motor analytical calculus. At the end the objective function is evaluated.

Step 6. Perform the "local grid search", meaning that a research movement along each optimized variable in positive and negative direction, using the initial step $d\bar{X}_0$, defined at *Step 4* will take place (see Figure 3.2 for a 2D vector). The objective function and its gradient are computed. The partial derivatives required for gradient calculations must be performed numerically with the resulted three points (corresponding to \bar{X}_0 and $\bar{X}_0 \pm d\bar{X}_0$ respectively), on the chosen direction. Gradient computation and step along gradient are determined with equations (3.13) and (3.14):

$$\bar{h} = (h_1, h_2, \dots, h_n) = \left(\frac{\partial f_{obj}}{\partial x_1}, \frac{\partial f_{obj}}{\partial x_2}, \dots, \frac{\partial f_{obj}}{\partial x_n} \right) \quad (3.13)$$

$$\bar{\Delta} = (\Delta_1, \Delta_2, \dots, \Delta_n) = \left(\frac{h_1 \times dx_1}{\|\bar{h}\|}, \frac{h_2 \times dx_2}{\|\bar{h}\|}, \dots, \frac{h_n \times dx_n}{\|\bar{h}\|} \right) \quad (3.14)$$

Step 7 The "pattern move" implies decreasing the objective function via an optimized variable vector movement with step Δ (P_i point was reached in Figure 3.2).

Step 8. Steps 6 and 7 are repeated, with new "search direction" and "pattern move" activities until $\|h\| = 0$, when no better points around the current point P_j can be found.

Step 9 Reduce the variation step by ratio r , go back to Step 5 and repeat the necessary calculation steps. The iterations stop when the minimum of the objective function is reached.

As already stated at the beginning, deterministic optimization methods are not trusted to guarantee the global minimum unlike stochastic mechanisms. They do come along with considerably reduced computation time, which permits some repetitions, with different initial variable vector, which should increase the probability to find the global minimum

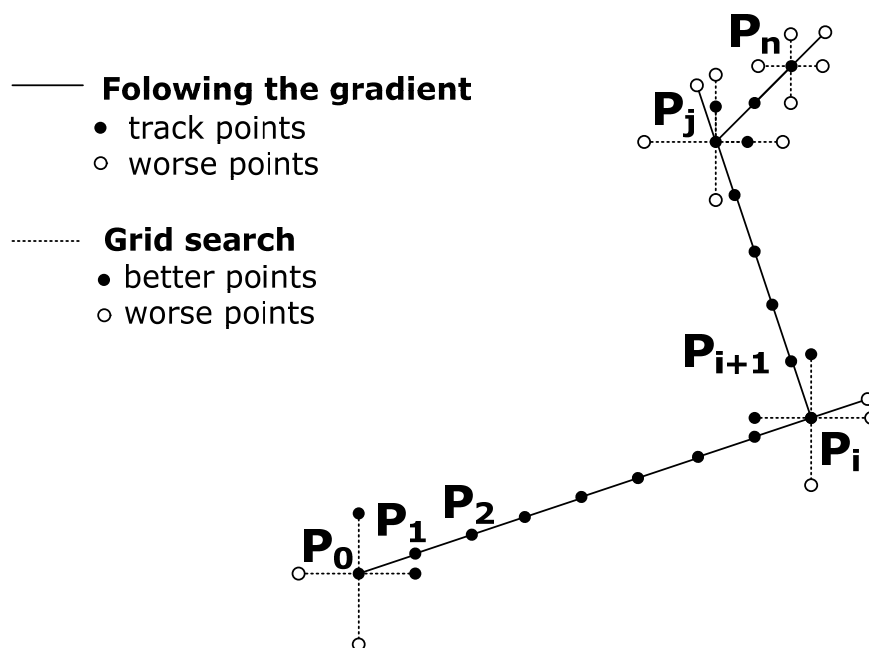


Figure 3.2 Search and gradient movement considering a 2D optimization problem [3.1]

3.3. Optimization results

Given the optimization design purpose for the 6 slots/8 poles surface permanent magnet synchronous motor, the Hooke Jeeves modified method is applied, with starting values for the variable vector chosen from analytical design process output. The process was repeated several times and the best solution accomplished is presented in what follows.

37 steps and 86 seconds are necessary in order to achieve the objective function minimum per one algorithm run. Variable variation and parameter evolution during optimization process is presented below (Figures 3.3 - 39).

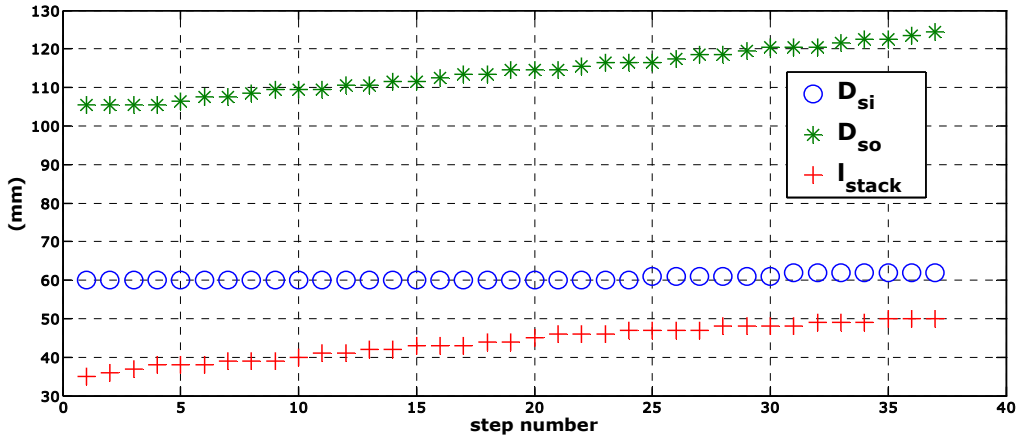


Figure 3.3. Geometrical variable variation (inner and outer stator diameter and stack length)

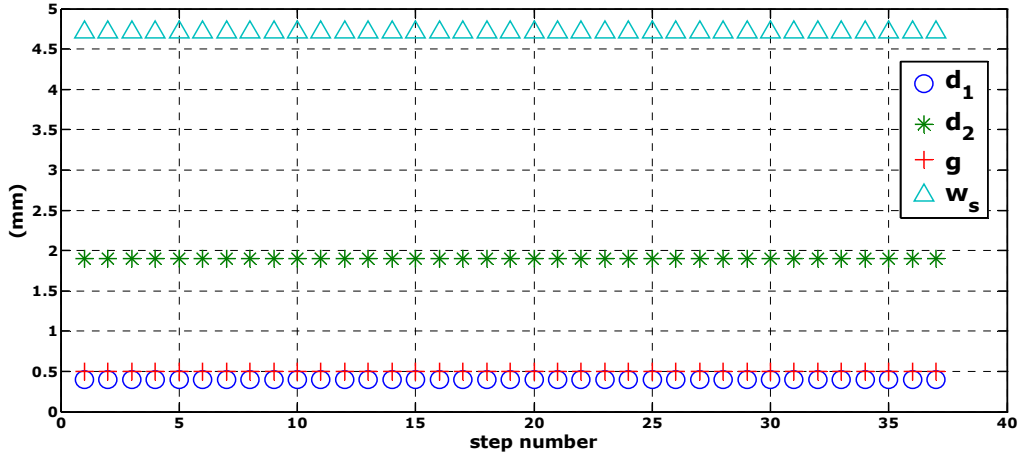


Figure 3.4. Geometrical variable variation (airgap, slot opening and tooth neck and wedge heights)

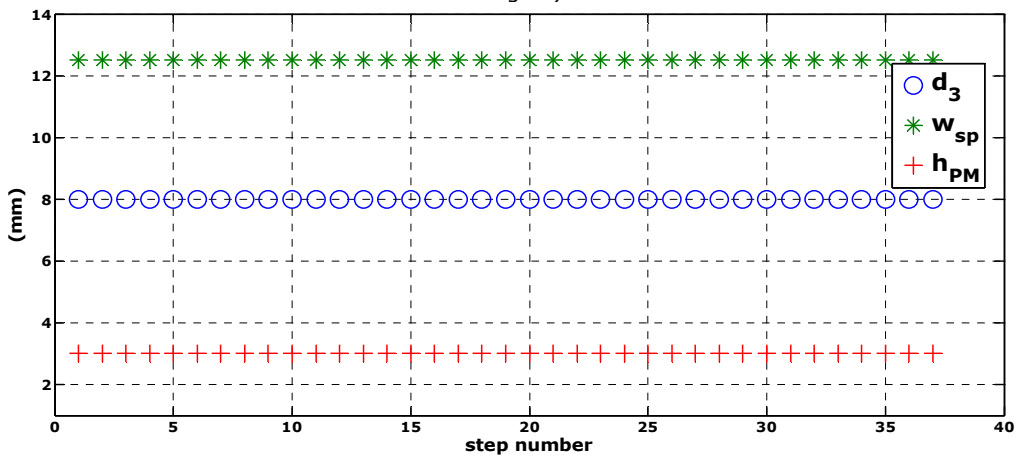


Figure 3.5. Geometrical variable variation (slot depth, slot width and PM height)

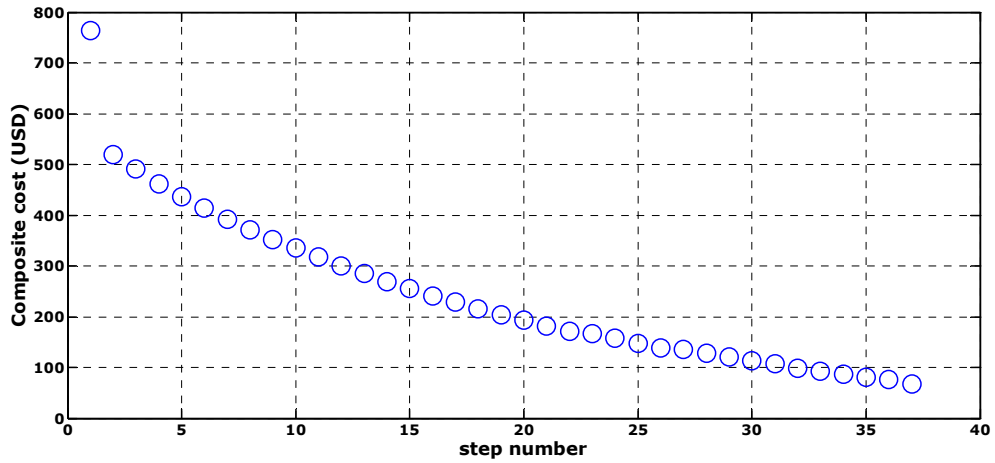


Figure 3.6. Objective function variation

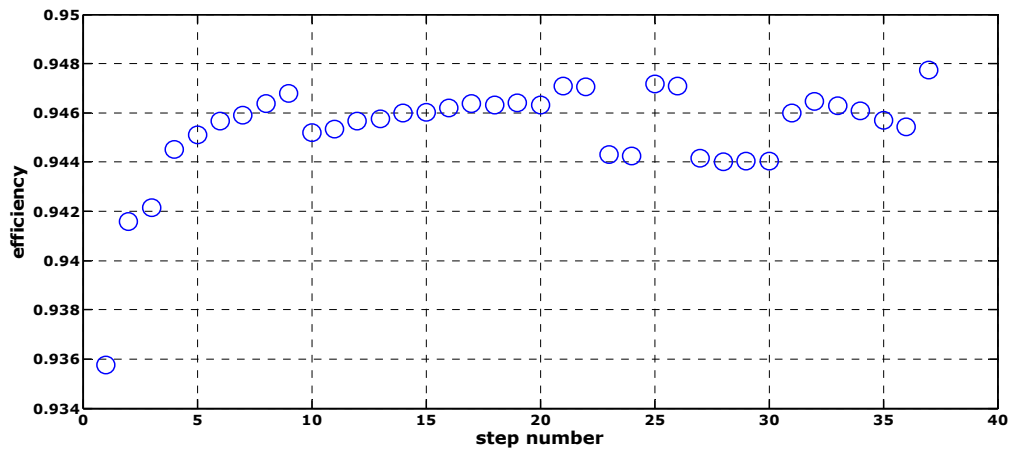


Figure 3.7. Rated efficiency variation

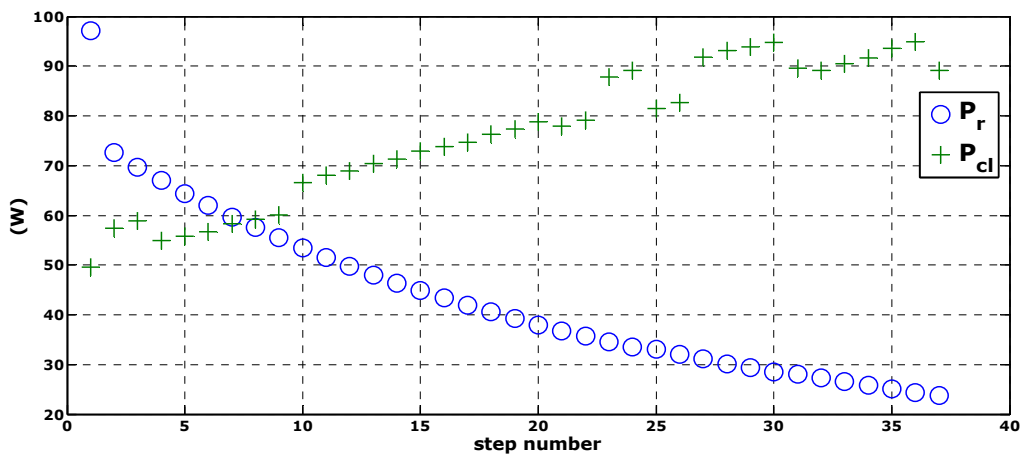


Figure 3.8. Losses (copper and iron) variation

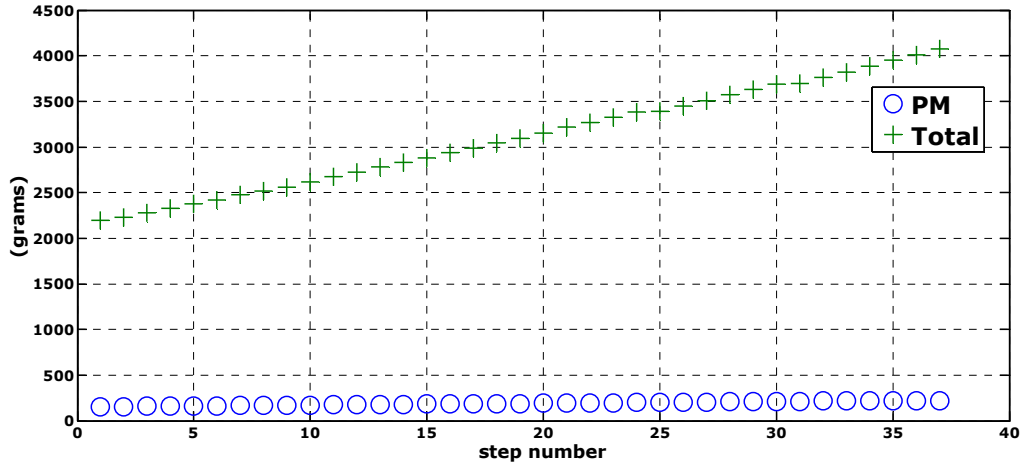


Figure 3.9. Mass evolution (PM and total)

The optimization process was repeated several times. A comparison between first motor prototype (designed only analytically, respecting the calculation algorithm presented in the previous Chapter) and repeated optimization resulted motor is performed in Tables 3.5. and 3.6.

The purpose of the optimization process is to lower motor cost and increase efficiency, since operating energy costs are considered in the objective function.

As one can see from Table 3.5 the supplementary design stage has produced an increase in motor volume and weight. The "compact size" requirement that has to be fulfilled is not affected, since we are not discussing major increase.

On the other hand, for almost the same volume, but "rearranged" topology, the motor prototype benefits from serious improvements as one can directly observe, especially in Table 3.6.

The geometrical modifications have affected the different material weight percentages out of total mass. The necessary copper was reduced significantly contributing in major active material cost minimization of almost 11 USD, given the costs level considered. This is translated into 25% cost reduction.

Furthermore, because the number of turns per slot is diminished (the main reason for copper mass reduction), end turns are also reduced, contributing this way to phase resistance decrease, from 6.1 to 4.6 [$m\Omega$].

With the new value, copper (resistive) losses are reduced, and have beneficial impact upon resulted rated efficiency.

It is also important to mention, that new geometrical configuration implies and may determine lower flux density in back-iron components. That is why the core losses are also reduced.

Supplementary losses (which take count of friction effect or bearing presence) are considered as constant percentage of the rated power.

Summing up the advantageous power loss mitigation, the rated efficiency is increased by almost 3%, from 91.9% to 95.19%. The improvement may not be considered drastic, but these are the variation levels where the "battle" is held.

Another observation is related to phase inductance reduction. The motor electrical constant is reduced this way, since inductance reduction is higher than resistance reduction.

Table 3.1 Dimensions and properties of the designed SPMSM

Parameter	Value		Measure unit
	Analytic	Optimal	
Topology			
number of phases	3	3	-
number of stator slots	6	6	-
number of rotor poles	8	8	-
Geometry			
stator outer diameter	120	124.5	[mm]
stator inner diameter	57	62	[mm]
air-gap	0.5	0.5	[mm]
rotor outer diameter	56	61	[mm]
rotor inner diameter	50	55	[mm]
stator tooth width	17.84	12.5	[mm]
stator yoke height	6.69	8	[mm]
stack length	40	50	[mm]
slot depth	25.31	21	[mm]
magnet height	3	3	[mm]
slot opening	8	4.9	[mm]
tooth neck height	2.352	0.4	[mm]
tooth wedge height	3	1.9	[mm]
Winding			
number of slots/pole/phase -	0.25	0.25	[-]
number of slots turns per phase	19	8	[-]
number of slots of parallel current paths	1	1	[-]
slot fill factor	0.5	0.5	[-]
no. coils/phase -	2	2	[-]
Materials			
core material	M800-50A		[-]
magnet type .	NdFeB 31/25		[-]
Weight & costs			
winding mass	1.544	1.11	[kg]
iron mass (before stamping)	4.044	5.44	[kg]
Permanent magnet mass	0.132	0.218	[kg]
motor weight	3.992	4.143	[kg]
initial cost	42.26	31.39	[USD]

Table 3.2. Machine parameters (analytical calculation)

Parameter	Symbol	Value		Measure unit
		Analytic	optimal	
Phase resistance	R_{ph}	6.1	4.6	[mΩ]
Phase inductance	L_{ph}	112	51.4	[μH]
Phase current	I_{phase}	41.85	44.78	[A]
Base output power	P_b	2500	2500	[W]
Rated efficiency	η	91.9	95.19	[%]
Rated copper losses	P_r	32.05	27.6	[W]
Rated iron losses	P_{cl}	172.778	86.25	[W]
Rated friction losses (bearing, windage)	P_s	12.5	12.5	[W]

3.4. Conclusions

This Chapter was focused on electric machine design optimization. A brief overview of available methods was performed. Even if deterministic optimization methods do not guarantee to bring us to the minimum of the objective function, they are appealing due to reduced computation effort and time. A modified Hooke Jeeves method is implemented with the purpose of cost reduction and efficiency improvement. The results are obtained after several algorithm repetitions, and they do accomplish the designers aim.

It should be noted that optimization design is not the last procedure before actually setting out the prototype construction. Today's engineering practice expects a third design stage – the FEM verification and validation step. This will be the subject for the next Chapter.

References

- [3.1] Ion Boldea, Lucian Tutelea, "Electric Machines – Steady State, Transients and Design with Matlab[®]", CRC Press, Taylor&Francis Group, 2010
- [3.2] G. F. Üler, O. A. Mohammed, C. S. Koh, "Utilizing Genetic Algorithms for the Optimal Design of Electromagnetic Devices", IEEE Transactions on Magnetics, Vol. 30, No. 6, November 1994, pp. 4296 - 4298
- [3.3] G. F. Üler, O. A. Mohammed, C. S. Koh, "Design Optimization of Electrical Machines using Genetic Algorithms", IEEE Transactions on Magnetics, Vol. 31, No. 3, May 1995, pp. 2008 - 2011
- [3.4] A. Krishnamoorthy, K. Dharmalingam, "Multi-objective design optimization of three phase induction motor using Hooke and Jeeves method & GA", Proceedings of the IEEE International Conference on Recent Advances in Space Technology Services and Climate Change (RSTSCC), 2010, pp. 413 - 418
- [3.5] R. Wrobel, P.H. Mellor, "The use of a genetic algorithm in the design optimisation of a brushless DC permanent magnet machine rotor", Proceedings of the IEEE International Conference on Power Electronics, Machines and Drives (PEMD), 2004, pp. 823 - 827
- [3.6] M. Balaji, V. Kamaraj, "Design optimization of Switched Reluctance Machine using Particle Swarm Optimization", Proceedings of the IEEE International Conference on Electrical Energy Systems (ICEES), 2011, pp. 164 - 169
- [3.7] Ni Youyuan, Wang Qunjing, Bao Xiaohua, Zhu Weiguo, "Optimal design of a hybrid excitation claw-pole alternator based on a 3-D MEC method", Proceedings of the IEEE International Conference on Electrical Machines and Systems (ICEMS), 2005, pp. 644 - 647.
- [3.8] M. H. Sadeghi, A. Darabi, "Optimization of a new type of hysteresis motor using genetic algorithm", Proceedings of the IEEE International Conference on Environment and Electrical Engineering (EEEIC), 2010, pp. 479 - 482
- [3.9] L. Tutelea, I. Boldea, "Induction motor electromagnetic design optimization: Hooke Jeeves method versus genetic algorithms", Proceedings of the IEEE International Conference on Optimization of Electrical and Electronic Equipment (OPTIM), 2010, pp. 485 - 492
- [3.10] X. del Toro Garcia, F. Neri, G. L. Cascella, N. Salvatore, "A Surrogate Assisted Hooke-Jeeves Algorithm to Optimize the Control System of a PMSM

- Drive", Proceedings of the IEEE International Symposium on Industrial Electronics (ISIE), 2006, pp. 347 - 352
- [3.11]** L. Tutelea, I. Boldea, "Surface permanent magnet synchronous motor optimization design: Hooke Jeeves method versus genetic algorithms", Proceedings of the IEEE International Symposium on Industrial Electronics (ISIE), 2010, pp. 1504 - 1509
- [3.12]** I. Moser, "Hooke-Jeeves revisited", Proceedings of the IEEE International Congress Evolutionary Computation (CEC), 2009, pp. 2670 - 2676
- [3.13]** N. Bianchi and S. Bolognani, "Design optimisation of electric motors by genetic algorithms", IEE Proceedings on Electric Power Applications, 1998, pp. 475 - 483
- [3.14]** H. Qi: A Genetic Algorithm with Tabu List and Sharing Scheme for Optimal Design of Electrical Machines, Electric Machines and Power Systems, 27, Taylor & Francis Inc., 1999, pp.543-552
- [3.15]** O. H. Yong-Hwan, T. K. Chung, M. K. Kim and H. K. Jung, "Optimal Design of Electric Machine using Genetic Algorithms Coupled with Direct Method", IEEE Transactions on Magnetics, Vol. 35, No. 3, May 1999, pp. 1742 - 1745
- [3.16]** D. H. Cho, H. K. Jung and C. G. Lee, "Induction Motor Design For Electric Vehicle Using A Niching Genetic Algorithm", IEEE Transactions on Industry Applications, Volume 37 , Issue 4, 2001, pp. 994 - 999
- [3.17]** V. Cingoski, K. Kaneda, H. Yamashita and N. Kowata, "Inverse Shape Optimization Using Dynamically Adjustable Genetic Algorithms", IEEE Transaction on Energy Conversion, Vol. 14, No. 3, September 1999, pp. 661 - 666
- [3.18]** B. Mirzaeian, M. Moallem, V. Tahani, C. Lucas, "Multiobjective Optimization Method Based on a Genetic Algorithm for Switched Reluctance Motor Design", IEEE Transactions on Magnetics, Vol. 30, NO. 3, May 2002, pp. 1524 - 1527
- [3.19]** K. S. Chai, C. Pollock, "Using Genetic Algorithms in Design Optimization of the Flux Switching Motor", Proceedings of the IEEE International Conference on Power Electronics, Machines and Drives (PEMDC), 2002, pp. 540 - 545
- [3.20]** L. A. Belfore II, A. Arkadan, "A Methodology for Characterizing Fault Tolerant Switched Reluctance Motors Using Neurogenetically Derived Models", IEEE Transactions on Energy Conversion, Vol. 17, No. 3, September 2002, pp. 380 - 384
- [3.21]** D-H. Cho, J-K. Kim, H-K. Jung, C-G. Lee, "Optimal Design of Permanent-Magnet Motor Using Autotuning Niching Genetic Algorithm", IEEE Transactions on Magnetics, Vol. 39, No. 3, May 2003, pp. 1265 - 1268
- [3.22]** Kondapalli Siva Rama Rao, Azrul Hisham Bin Othman, "Design optimization of a BLDC motor by genetic algorithm and simulated annealing", Proceedings of the IEEE International Conference on Intelligent and Advanced Systems, November 2007, pp.854-858
- [3.23]** S.L. Ho, S.Y. Yang, G.Z. Ni and K.F. Wong, "An efficient multiobjective optimizer based on genetic algorithm and approximation techniques for electromagnetic design", IEEE Transaction on Magnetics., vol.43, no.4, April 2007, pp.1605-1608
- [3.24]** Gregor Papa, Barbara Koroušić-Seljak, Boris Benedičič, Tomaž Kmecl, "Universal motor efficiency improvement using evolutionary optimization", IEEE Transactions on Industrial Electronics., vol.50, no.3, June 2003, pp.602-611

-
- [3.25]** S.Y. Yang et al., "A new implementation of population based incremental learning method for optimizations in electromagnetics", *IEEE Transaction on Magnetics.*, vol.43, no.4, April 2007, pp.1601-1604
 - [3.26]** Yao Duan, R.G. Harley and T.G. Habetler, "A useful multi-objective optimization design method for PM motors considering nonlinear material properties", *Proceedings of the IEEE International Congress and Exposition on Energy Conversion (ECCE)*, 2009, pp. 187 - 193.
 - [3.27]** Dušan Teodorović, Mauro Dell'Orco, "Bee colony optimization – a cooperative learning approach to complex transportation problems", *Proceedings. of 10th EWGT Meeting and 16th Mini EURO Conf.*, pp.51-60, 2005
 - [3.28]** Vlad Grădinaru, Lucian Tutelea, Ion Boldea, "Hybrid analytical/FEM optimization design of SPMSM for refrigerator compressor loads", *Proceedings of the IEEE International Aegean Conference on Electrical Machines and Power Electronics (ACEMP)*, 2011, pp. 1 – 8

CHAPTER 4

6 Slot/8 Pole Synchronous Machine: FE Analysis and Embedded FEM for direct optimization

Abstract

This chapter presents details related to FEM calculation and validation procedure, as important stage of modern electric motor design methodology. The 6slot/8 pole surface permanent magnet synchronous motor that was designed analytically in Chapter 2 and optimally in Chapter 3, undergoes a verification process and serves as case - study. Cogging torque mitigation and torque capability enlargement are achieved with the aid of a novel FEM embedded design methodology, which puts together all three design steps.

4.1. Introduction

The finite element method (FEM) is a numerical technique for finding approximate solutions to partial differential equations (PDE) and their systems, as well as integral equations. In simple terms, FEM is a method for dividing up a very complicated problem into small elements that can be solved in relation to each other. The solution approach is based on eliminating the spatial derivatives from the PDE while approximating the latter with:

- a system of algebraic equations for steady state problems,
- a system of ordinary differential equations for transient problems.

The finite element method is a good choice for solving partial differential equations over complicated domains (cars, oil pipelines), when the domain changes (as during a solid state reaction with a moving boundary), when the desired precision varies over the entire domain, or when the solution lacks smoothness. From numerical weather prediction to various field analysis, the FEM offers a wide applicability range.

It has been stated in the previous Chapters, that for given requirements, there is not a unique electric motor design solution that fulfils the specifications. Optimization design takes the resulted motor topology on a higher level of efficiency. Still, while obtaining better results for a given objective, the motor might end not fulfilling other requirements that were not subject to the optimization process. It is mandatory to predict and estimate motor characteristics/parameters that arise from different machine topologies, before stepping up to prototype construction.

Due to geometrical complexity, the analytic calculus uses various simplifications and can only offer approximate values. Sometimes the analytic parameter prediction becomes sophisticated and requires significant computation resources, since conformal/Fourier transformation must be implemented, to determine for example cogging-torque variation ([4.19]-[4.26]). Consequently, this

effort is not considered worthy, since more accurate determinations can be achieved by numerical calculus with aid from dedicated FEM software.

So, for a completely qualified solution the designer goes through analytic design, optimization process and FEM validation. Even for well experienced professionals, it is granted that the process is iterative and repetitive. The idea of process automatization appears on the horizon. Making use of advantageous Matlab interfacing, an embedded FEM procedure will deliver a hybrid design methodology that passes through all three stages and goes back if certain conditions are not verified.

4.2. FE analysis of 6/8 SPMSM with trapezoidal current control

4.2.1. FE software

There are several FEM related software packages on the market, differentiated upon the calculation accuracy. Still assuming a bit higher computation errors, the Finite Element Method Magnetics freeware, FEMM, Ver. 4.2 is chosen to implement the "validation" stage.

FEMM offers the opportunity for solving low frequency electromagnetic problems on two-dimensional planar and axisymmetric or planar domains. The program addresses linear/nonlinear magnetostatic problems, linear/nonlinear time harmonic magnetic problems, linear electrostatic problems, and steady-state heat flow problems

FEMM has three parts:

1. A pre-processor and post-processor interactive interface, where problem definition or handy field inspections are easily performed
2. A triangle-based discretization system; the discretization rate can be user defined, so that regions of interest can benefit from a higher number of elementary analysis domains.
3. Numerical computation is made by four dedicated solvers; magnetics, electrostatic, heat flow and current flow problems are targeted.

Another important feature is the LUA scripting language, that allows automated problem definition and system analysis. But LUA can be replaced by Matlab interfacing, which rises calculation performance of this free software.

4.2.2. FE model

In order to construct the FE model, the following steps must be performed [4.29]:

- *Problem definition*: Problem Type, Length Units, Frequency, Depth, Solver Precision and Minimum Angle.
- *Geometry definition*: This can be done by user, using the CAD-like features or one might make use of DXF-file importing facility.
- *Boundary definition*: an adequate number of boundary conditions has to be defined by the user, to guarantee a unique solution.
- *Materials property definition*: is used to specify the properties to be associated with each geometrical closed region. Some predefined materials

- are to be found in the dedicated library, but user defined ones are also allowed.
- *Winding system definition* – allows the user to apply constraints on the current flowing according to the winding schematic
 - *Mesh generation* – automatic or manual generation of “elementary triangles”.
 - FEM application
 - *Postprocessor* – used for extraction and analysis of the solution generate by the program
- FE-analysis of the topology can offer direct results for:
- ✓ field distribution at no-load and at load,
 - ✓ back-EMF at no-load,
 - ✓ cogging torque (zero current)
 - ✓ load torque pulsations,
 - ✓ reluctance torque pulsations,
 - ✓ torque-rotor angular position characteristics for different trapezoidal-current shapes,
 - ✓ torque-rotor angular position characteristics for different current amplitudes,
 - ✓ saturated synchronous inductances

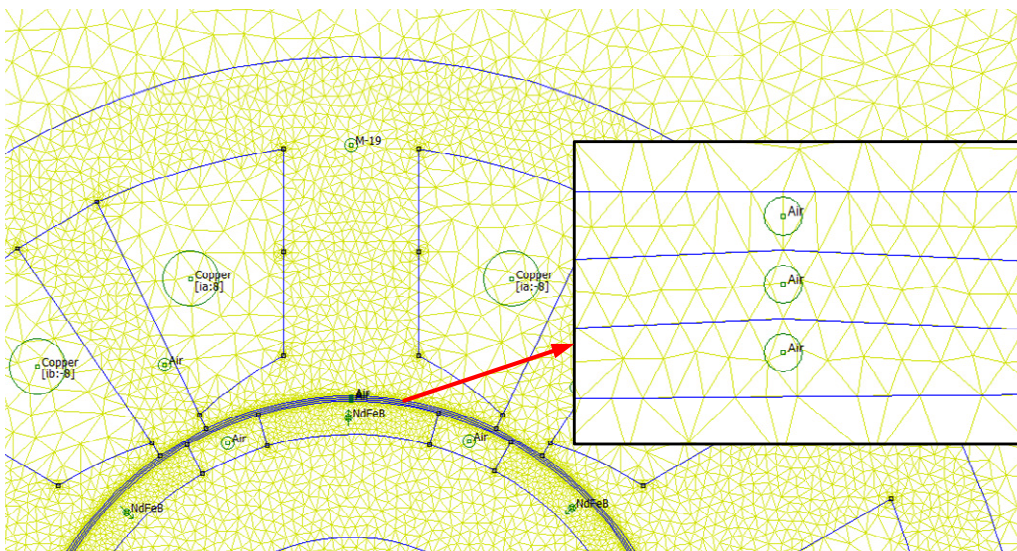


Figure 4.1. Detail on finite elements mesh and material definition

Figure 4.1. shows a detail from the motor geometry construction and material definitions. For accurate calculations, the domains of interest (the airgap, in our case) have to be divided into subdomains with fine discretization rate and calculations/evaluations have to be realized where elementary triangle corners belong all to the same “material”.

Current circulation in slots is implemented according to the winding diagram of the prototype – single-layer, concentrated fractional pitch three phase winding for 6slots/8 pole configuration, with series connected coils (see Figure 4.2).

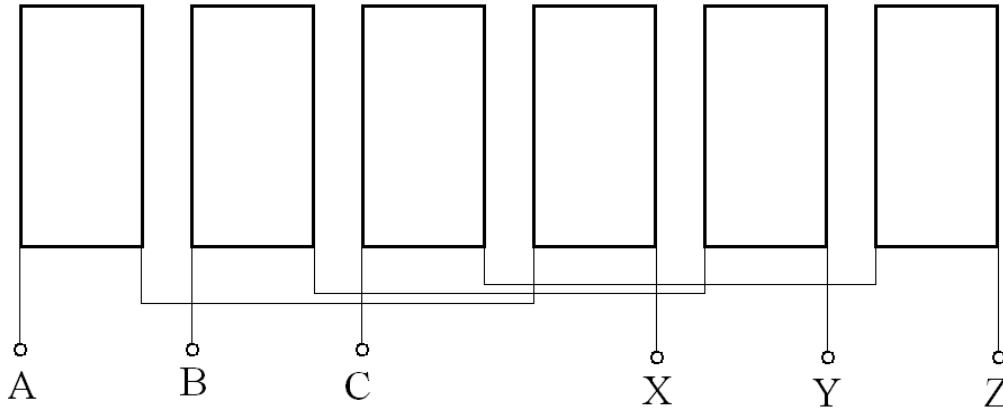


Figure 4.2. Winding schematic

4.2.3. Field distribution

Field distribution in no-load or rated-load conditions is the first to be verified by FE analysis. It offers a “plastic” characterization of the motor topology, by emphasizing the regions with high saturation levels and offering a general image upon flux density distribution.

4.2.3.1 No-load field distribution

The no-load field distribution, saturation level, and the air-gap flux density were calculated for two rotor positions. Results for d -axis aligned with phase “a” (d -axis aligned with the tooth corresponding to phase “a”) are presented in Figures 4.3, 4.4 and 4.5 respectively.

Figures 4.6, 4.7, 4.8 illustrate the results for the q -axis aligned with phase “a” (q -axis aligned with the tooth corresponding to phase “a”).

A good field distribution confirms the design and, at the same time, the correctness of the FE modelling and computation.

Some saturation regions may be identified where domains are characterised by a “sharp geometry”. Still, the maximum “localised” 2.5 [T] flux density value does not endanger the motor’s performance.

The airgap flux density is somewhere above 0.9 [T], a higher value than the analytically calculated one. The irregularities that are to be observed on both d -aligned and q -aligned cases are due to the interaction between slot opening and rotor permanent magnets. Wedges may be considered or smaller slot mouth width, to improve this aspect.

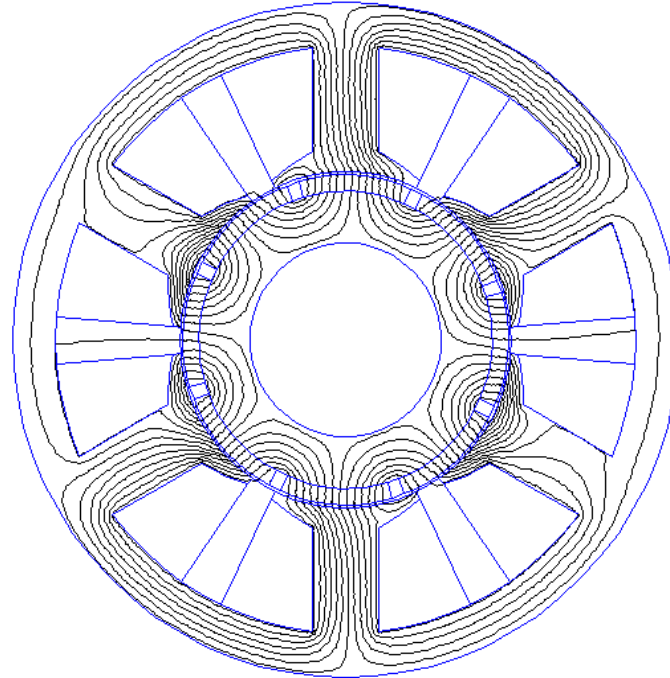


Figure 4.3. Flux line pattern for no-load, *d*-axis alignment

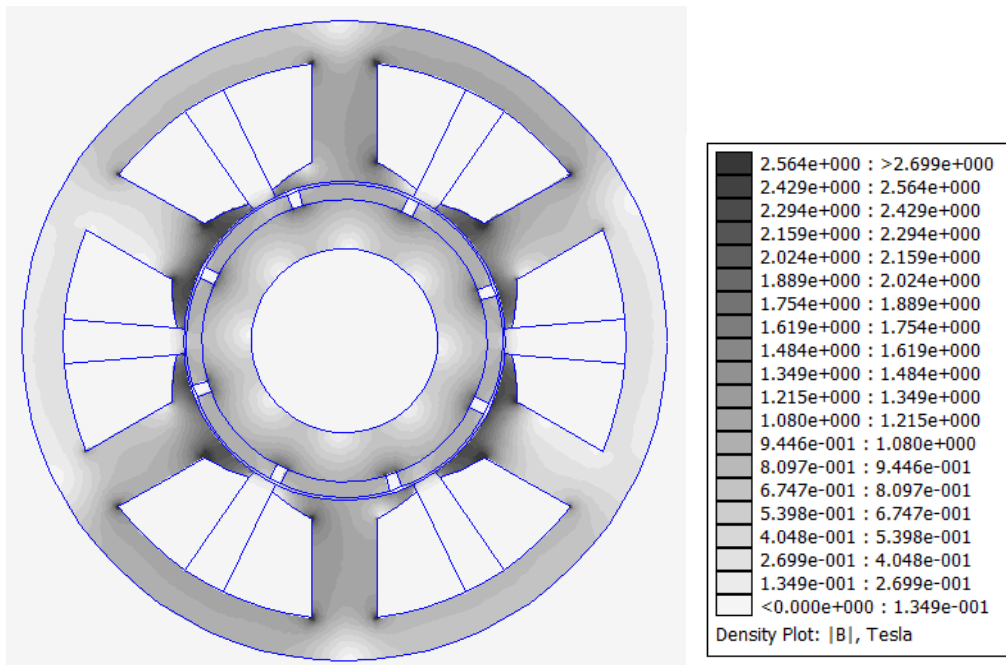


Figure 4.4. Flux density distribution for no load, *d*-axis alignment

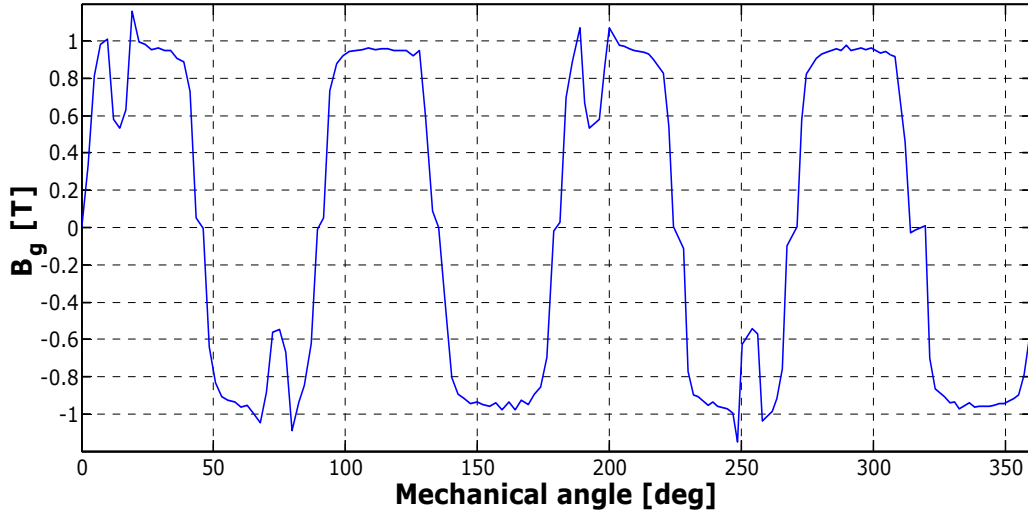


Figure 4.5. Airgap flux density for no-load , d-axis alignment

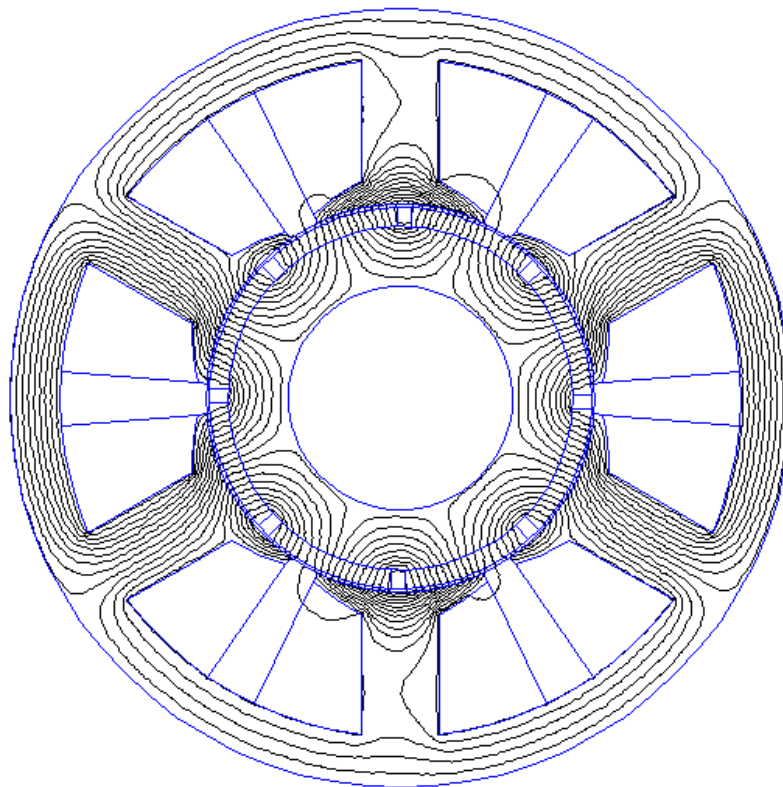


Figure 4.6. Flux line pattern for no-load, *q*-axis alignment

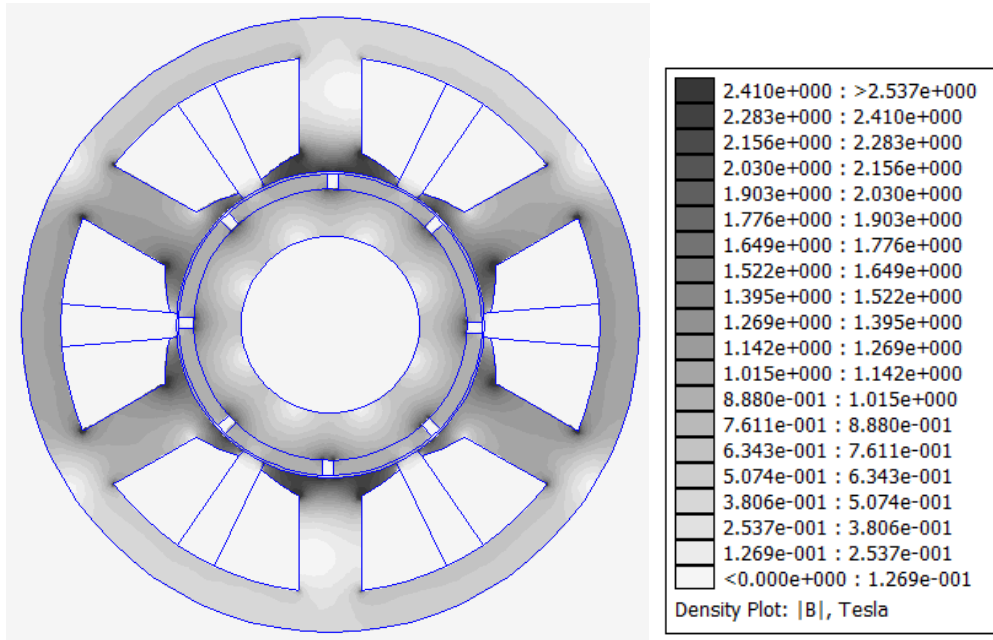


Figure 4.7. Flux density distribution for no load, q -axis alignment

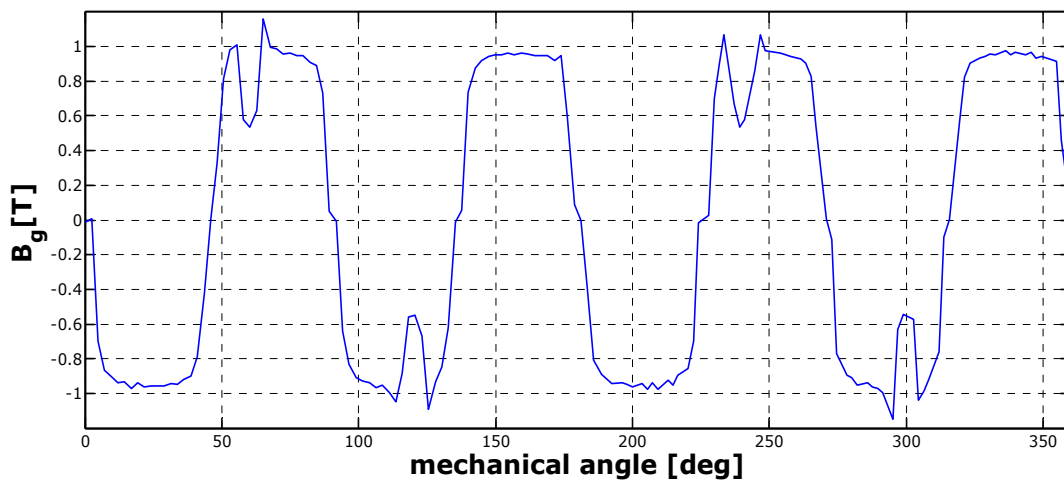


Figure 4.8. Airgap flux density for no-load, q -axis alignment

4.2.3.2 Field distribution under load

The load point is selected to be at rated conditions, i.e at rated phase current value of 45 A. The flux line pattern, flux density distribution and airgap flux density is depicted in figures 4.9, 4.10 and 4.11, respectively.

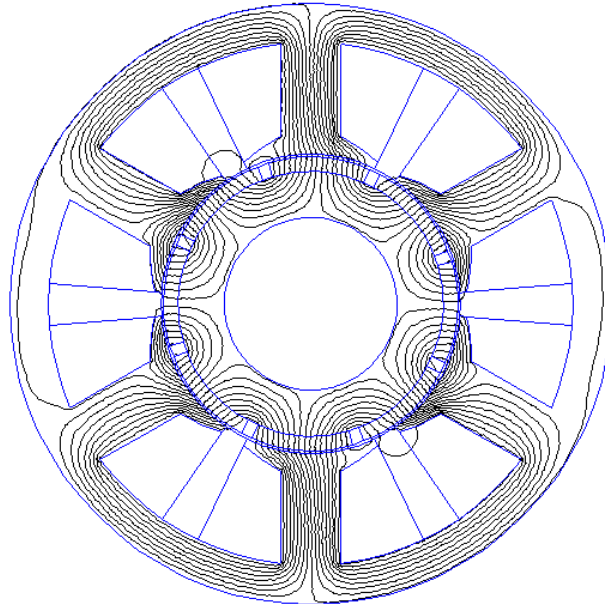


Figure 4.9. Flux line pattern for rated load condition and d -axis alignment

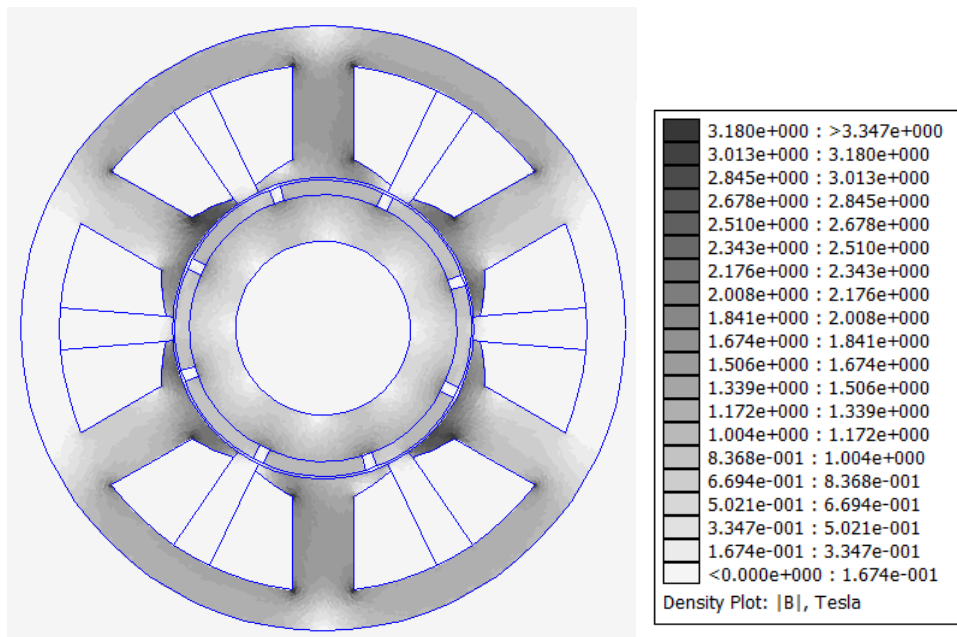


Figure 4.10. Flux density distribution for rated load condition and d -axis alignment

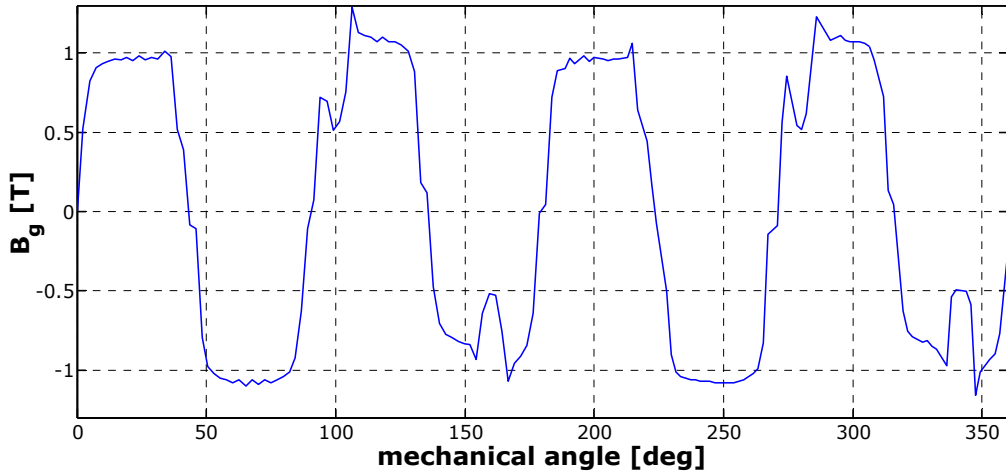


Figure 4.11. Airgap flux density distribution for rated load condition and *d*-axis alignment

4.2.4. No-load phase flux linkage and back-EMF

In FEMM the total flux in a bulk flux path can be determined using the line integral of the normal component of the flux density, B_n , along a specified contour (equation (4.1)). This integral is performed by evaluating a large number of points at evenly spaced along the contour and integrating using a simple trapezoidal-type integration scheme [20].

$$\Phi = l_{stack} \int_{\Gamma} B_n dl \tag{4.1}$$

The flux calculation contours, are chosen to correspond to middle stator tooth section, for given stack length. For each phase, the tooth “covered” by corresponding phase winding is considered. Figure 4.12 shows the no load flux linkage calculated for the given motor topology.

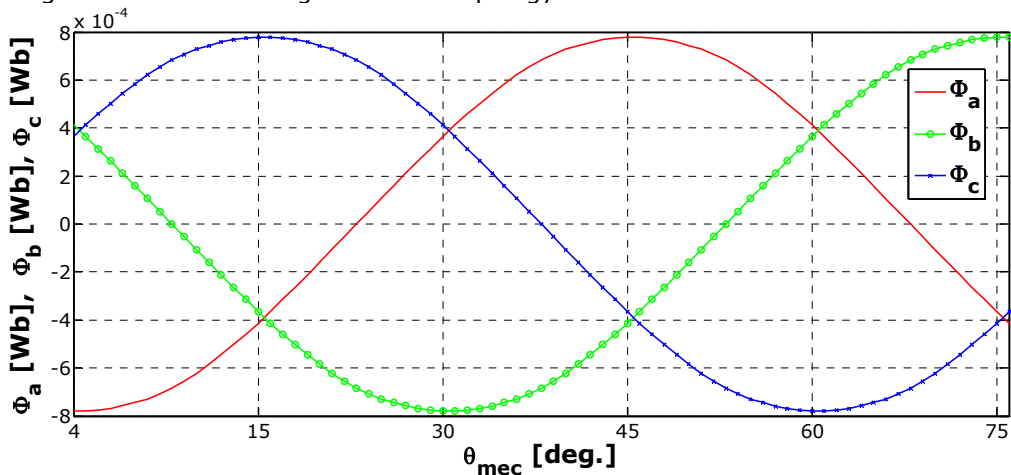


Figure 4.12. FEM-calculated no-load phase flux linkages

The back-EMF was calculated using Faraday’s Law, which describes the phenomena of electric field generation due to magnetic field variation. The induced voltage appeared due to magnetic field rotation is described by equation (4.2)

$$e_a = -\frac{d\lambda_{aPM}(\theta_m)}{dt} = -\frac{d\lambda_{aPM}(\theta_m)}{d\theta_m} \cdot \frac{d\theta_m}{dt} = -\frac{d\Phi_{aPM}(\theta_m)}{d\theta_m} \cdot n_s \cdot \frac{d\theta_m}{dt} = k_E \omega_m \quad (4.2)$$

where ω_m is the angular velocity of the rotor in mechanical rad/s,
 θ_m is the rotor position in mechanical radians and
 k_E is the back-EMF constant in Vs/rad

The phase back-EMF constant k_E versus rotor angular mechanical position, is computed according to equation (4.3), where n_s is the number of turns per phase.

$$k_e = \frac{d\Phi_{aPM}(\theta_m)}{d\theta_m} \cdot n_s \quad (4.3)$$

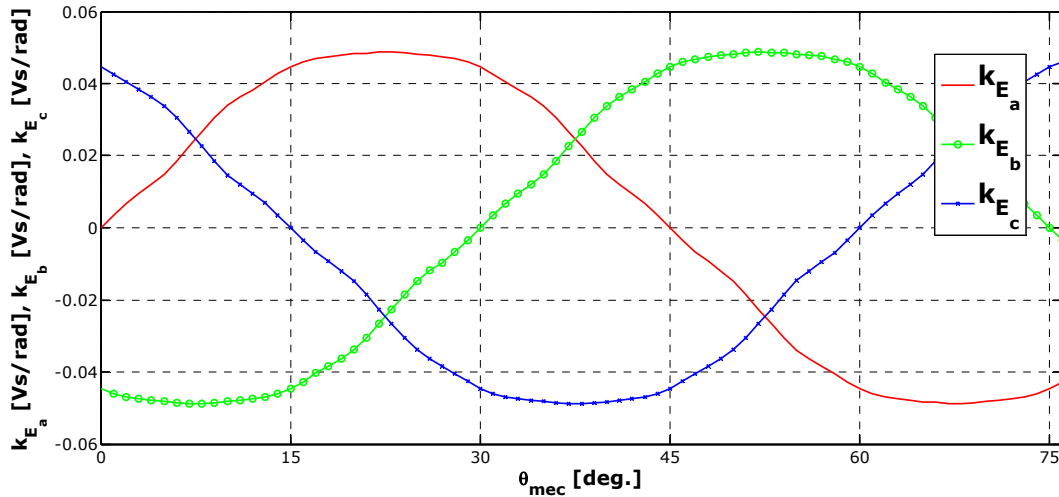


Figure 4.13. FEM-calculated phase back-EMF constant k_E versus rotor angular mechanical position

The back-EMF shape is neither sinusoidal, neither trapezoidal, but “somewhere in between”. This means that both sinusoidal current and rectangular current control strategies may apply.

Having behind economical reasoning and simplicity attribute for implementation, the common industrial practice is to have the motors characterized by such back-EMF variation controlled via rectangular or trapezoidal current strategies.

However, due to imperfect sinusoidal variation of the back-EMF, the control suited for the perfect counterpart category of motors, surely encounters difficulties and efficiency will be lower.

On the other hand, the “better-than-trapezoidal” variation, brings along torque ripple (due to commutation) unwanted effect.

The compromise that brings less harm should be chosen, especially if practical solutions are considered

4.2.5. Cogging (zero-current) torque calculation

An electromagnetic torque exists in PM machines even when there is no excitation of the stator windings. This arises due to the interaction between the rotor PM field and the stator teeth. This torque is sometimes referred as detent or cogging torque in the literature. Since the cogging torque appearance is due to reluctance variation, the term of "reluctance torque" may also apply.

This most unwanted parasitic effect may be avoided for slotless stator design, as it was mentioned in Chapter 2, but there are other issues that have to be taken care of. Strongly dependent upon design variation, the cogging torque may represent as low as 5%-10% of the rated torque, or reach as much as 25%, for improper designed machines.

Even though reluctance torque may be compensated through control, it is more desirable to have it diminished by design. Cogging torque computation is essential and its existence affect directly motor performance. Diligent research activities are carried out for this purpose.

The cogging torque variation is somehow sinusoidal, but maximum and minimum amplitude are not equidistant and symmetric in respect to the variation period. Khrishnan [4.29] has established that the number of cogging cycles $N_{cogging}$ per mechanical revolution equals:

$$N_{cogging} = LCM(N_s, N_{PM}) \quad (4.4)$$

He also determined that maximum and minimum are equal to 60° respectively 90° out of a period of 180° . In Figure 4.14 the cogging torque variation for our SPMSM prototype was computed by FEM.

The cogging cycle rule is respected, and for our 6slot/8poles configuration a number of 24 cogging periods are to be found for one mechanical complete revolution. From the 15° mechanical degrees cogging period, the corresponding maximum and minimum amplitude values, are found at 5° and 10° , respectively, confirming again Khrishnan's theory. As one can notice, the prototype may be cost efficient, but is characterized by a high cogging torque value, and this aspect must be improved.

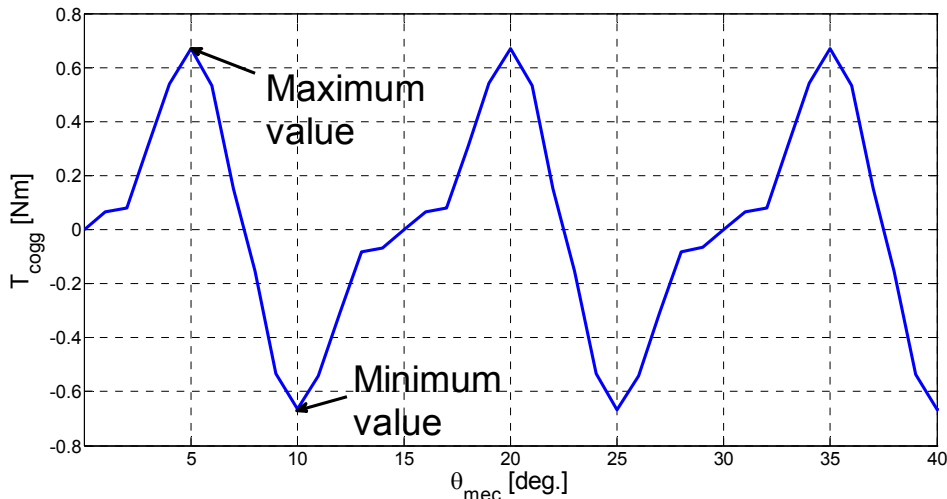


Figure 4.14. Cogging torque variation for the given SPMSM prototype

4.2.5. Electromagnetic torque calculation

From previous FEM investigations, the phase back-EMF shape for the chosen motor topology was predicted. It was appreciated that both "sinusoidal" and "rectangular" control may be suitable.

Taking into consideration the low cost requirement for the drive, the temptation is to choose the rectangular current control strategy.

For the present FE - calculations a more practical trapezoidal current waveform is considered. Even though it was proved that trapezoidal variation with no zero sequence current shape reduces torque pulsations [4.28], dead time issues for the inverter are introduced, and the solution is not considered totally suitable.

Phase current variation with rotor position is depicted in Figure 4.15. Six-step commutation pattern is considered, so the phase current and corresponding phase induced voltage should not be delayed.

The electromagnetic torque is computed for "rated" conditions, which is translated into 45 [A] current command.

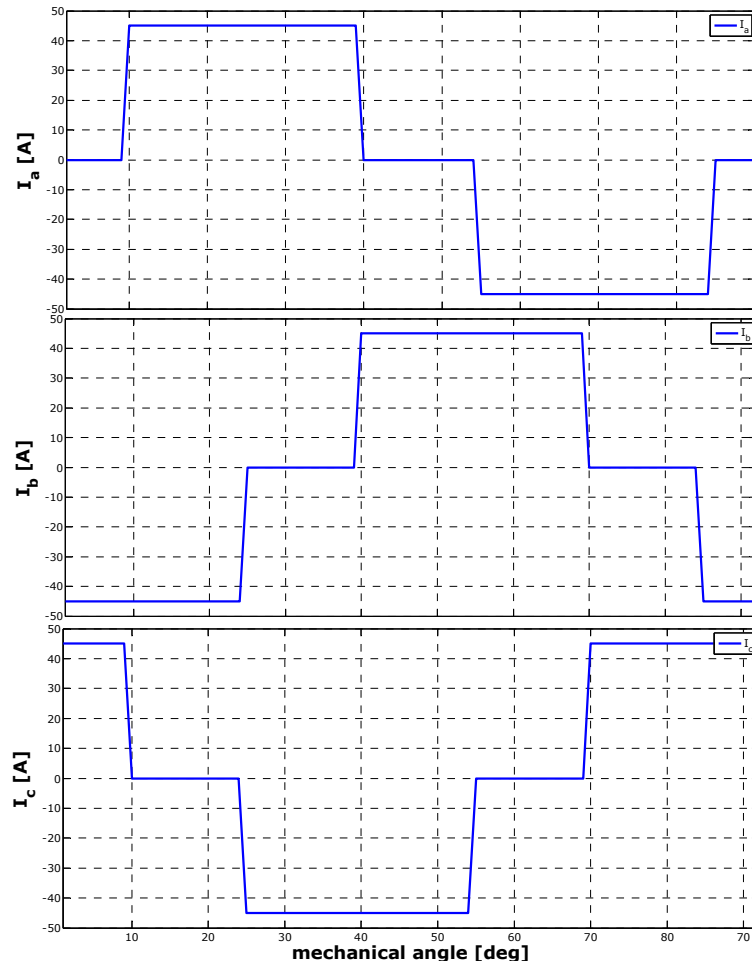


Figure 4.15. Phase current variation versus rotor mechanical position

The predicted electromagnetic torque is represented in Figure 4.16. The ripples are caused both by control and high cogging torque. A resulted average value of 3.58[Nm] is satisfactory.

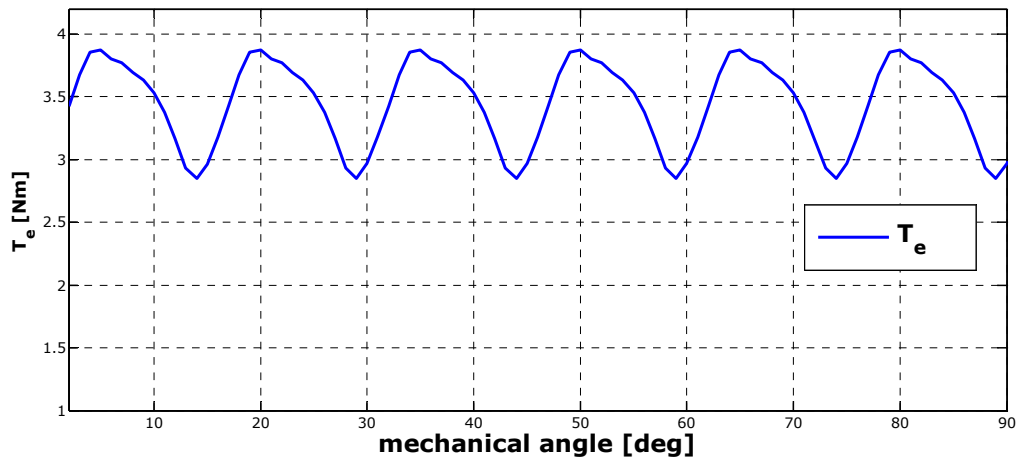


Figure 4.16. Electromagnetic torque versus rotor mechanical position

4.3. FEM embedded hybrid design methodology

The previous subsections have proved that even though a low cost and highly efficient motor prototype was obtained by applying traditional analytical design procedure followed by optimization stage, the configuration is unfortunately a high cogging torque carrier.

Usually, FEM investigation shows different drawbacks of various motor design results, even if stochastic optimization algorithms are implemented, which are trusted to lead to global objective function minimum. This is due to the fact that engineering, in general, has to fulfil requirements that are, most of the time divergent (low cost and high performance do not coexist without a compromise). It is a common practice to apply direct geometrical rectification procedures that minimize any undesirable effect. For example, tooth neck, or tooth wedge widths may be increased to obtain a lower value of the flux density localised there. Still, the corrective measures are not simply imposed; the new topology has to undergo another verification stage. Other geometrical dimensions, secondary impacted by the corrective measure might direct to a configuration that does not even satisfy initial constraints established in the analytical design stage (especially for inexperienced designers).

Individually, the design stages already benefit from automated, computer aided implementation. Would it be too much to have them together compacted in a single but more complex design algorithm? What is the price that needs to be paid for having a number of triple stage operations repeated in an automated manner, based on a judgement that we establish. The other question that arises is related to the complexity level allowed by objective limitations.

Since cogging torque presence seems to limit the designed motor's performance, the FEM embedded algorithm's main goal will be to minimize its

amplitude. Secondly, electromagnetic torque inspection is performed, and corrective measures will apply if the minimum required torque level cannot be delivered.

4.3.1. Cogging torque mitigation

The cogging torque is actually a parasitic torque produced by reluctance variation due to motor saliency. Its variation and amplitude depend on two factors: airgap flux and airgap reluctance variation as function of the rotor mechanical angle. Basically the methods [4.29 -4.31] that promise to reduce the detent torque may be split into two categories:

- methods that act basically in respect to airgap flux reduction
- methods that are based on reluctance variation minimization

It is important to mention that airgap flux reduction can be performed only in limited conditions, since the airgap flux also determines the "useful" electromagnetic torque the machine has to deliver.

The following design techniques/guidelines/measures are known to contribute to cogging torque reduction:

- Reduction of stator saliency by adding *shoes* for stator teeth; the measure also protects winding from centrifugal forces while motor general performance is not influenced, but winding inductance is increased
- For feasible slot/pole/phase combinations, a *fractional pitch winding* can reduce drastically cogging torque, while creating "positive" and "negative" effects that sum up and determine even zero cogging torque
- *Airgap lengthening* reduces both reluctance variation and airgap flux and implies permanent magnet lengthening to have an overall positive effect
- *Skewing* performs a controlled misalignment between each magnet and the corresponding stator winding to reduce the peak magnet flux linked to the coil and obtain a "sum up to zero" effect. It may be applied both for stator or rotor structure, but comes with several disadvantages. If applied for the rotor, the cost for permanent magnets is increased. If applied for the stator the turn length is increased (and higher resistive losses are determined) and slot filling allowed ratio is reduced. A small thrust load to the rotor bearings is also added by this design measure.
- *Magnet shaping* tries to remove sharp permanent magnet edges, since is considered to contribute on increased magnet-to magnet leakage flux and consequently increased cogging torque
- *Slot opening variation* has to take into account two aspects; while a slot opening equal to tooth width is considered optimal for maximum torque production, an increased reluctance variation is produced this way, and consequently a large cogging torque amplitude. The slot "mouth width" may be decreased to a minimum that should allow at least "turn by turn" coil introduction. Closing the slot opening with wedges may also be considered.
- Introducing *notches* on stator periphery, meaning creating "fake" slots, have impact on cogging frequency increase. And while the number of cogging cycles per one mechanical revolution increases (equation 4.4) due to the interaction between same number of rotor poles and "artificially" increased stator slot number, the amplitude is reduced.

The motor configuration already takes advantage of adding shoes to the stator teeth. Directly related to this topological aspect, slot opening variation is the easiest to implement for a "direct optimization" based algorithm.

So, the dimensioning procedure will pass through analytical design step, optimal design step and then FEM inspection will follow. After FE model definition, cogging torque is computed for minimum and maximum value for already known rotor angles value (see figure 4.14).

Cogging torque amplitude may be calculated:

$$T_{cogg} = T_{cogg_{max}} - T_{cogg_{min}} \tag{4.5}$$

Slot opening variation is made by:

$$w_s = \frac{D_{si} \cdot \pi}{N_s} (1 - k_1 \cdot \frac{\theta_s}{2}) \tag{4.6}$$

where D_{si} is the stator inner diameter, N_s is the slot number and θ_s is the angular slot pitch.

k_1 may be chosen

$$k_1 = (0.5 \div 0.75) \frac{0.05T_e}{T_{cogg}} \tag{4.7}$$

Shoes are already considered for the topology, so is more than evident that $k_1=1$ (corresponding to slot and tooth widths) is not possible. The correction factor intends to impose smaller slot openings if the cogging torque amplitude is more than 5% out of the rated required torque. Still, the 0.5 coefficient that accompanies the corrective measure comes to avoid the situation when a too reduced slot opening would not allow coil introduction, or may cause back-EMF deformation (see Figure 4.17) for uninspired too drastic corrective measures.

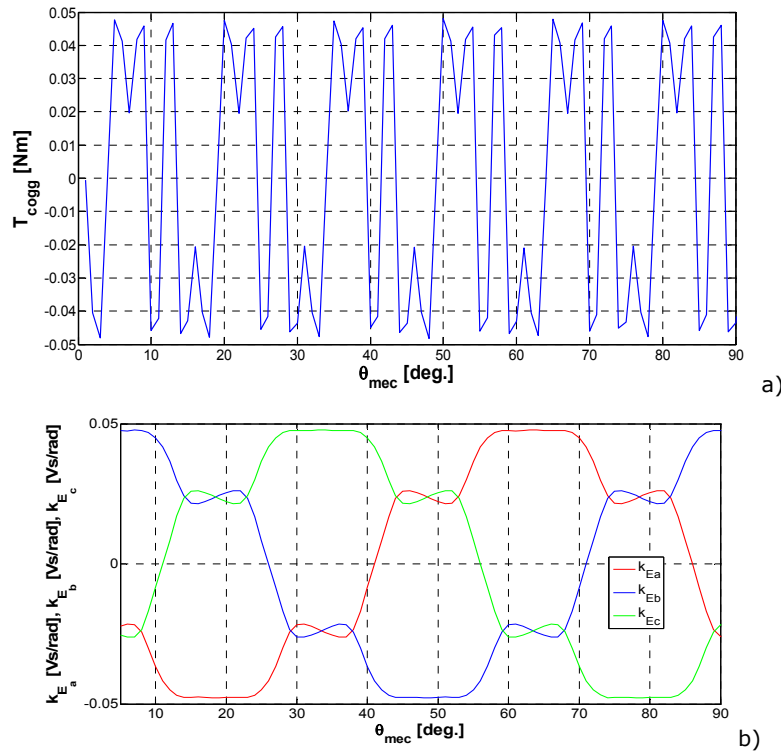


Figure 4.17. Cogging torque (a) and back-emf constant (b) for minimum slot opening

4.3.2. Electromagnetic torque optimization

In the previous subsection the measure of slot opening variation was implemented to minimize the cogging torque amplitude. But the design measure may also affect the torque capability of the motor. So, while applying corrective measures, the electromagnetic torque should also be evaluated.

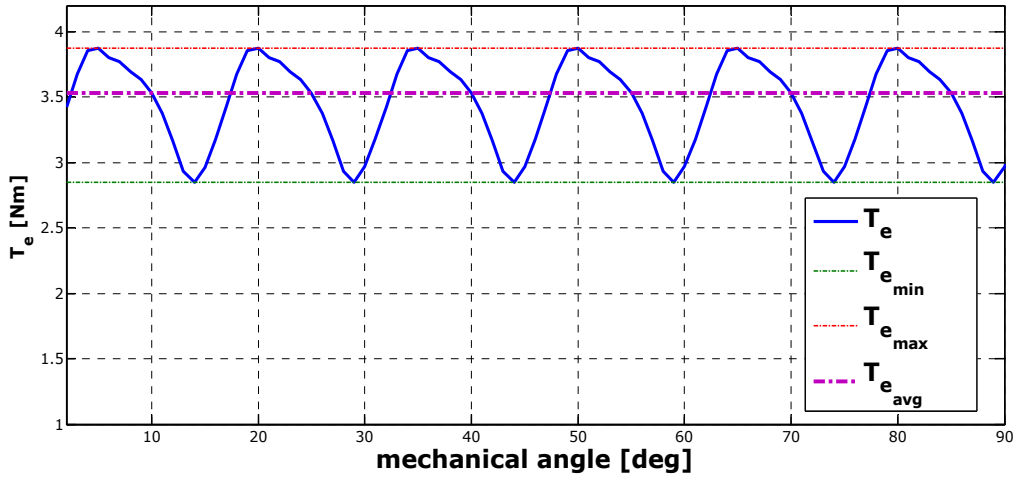


Figure 4.18. Electromagnetic torque variation versus rotor mechanical angle

Average electromagnetic torque computation is performed according to equation (4.8), which offers a rough, but satisfactory estimation based on electromagnetic torque ripples periodicity (caused by commutation and by cogging cycles)

$$T_{e_{avg}} = (3 \times T_{e_{max}} + T_{e_{min}}) / 4 \quad (4.8)$$

The corrective measure is accomplished by k_2 factor, that follows required torque achievement. Smoothing coefficients (0.3 ÷ 0.6) are again applied.

$$E_{max_{new}} = E_{max_{old}} (1 - k_2) \quad (4.9)$$

$$k_2 = (0.3 \div 0.6) \cdot \left(\frac{T_{e_{avg}}}{T_{e_{req}}} - 1 \right)$$

However, as one can see from Figure 4.19, the cogging torque reduction is only to half of the starting value. This is due to the "precautions" corrective measures that were implemented, but one cannot react in a different way, since cogging torque and electromagnetic torque do not impose 100% converging mitigation measures.

A more drastic reduction of the cogging torque is achieved by considering the inexpensive "notching" measure.

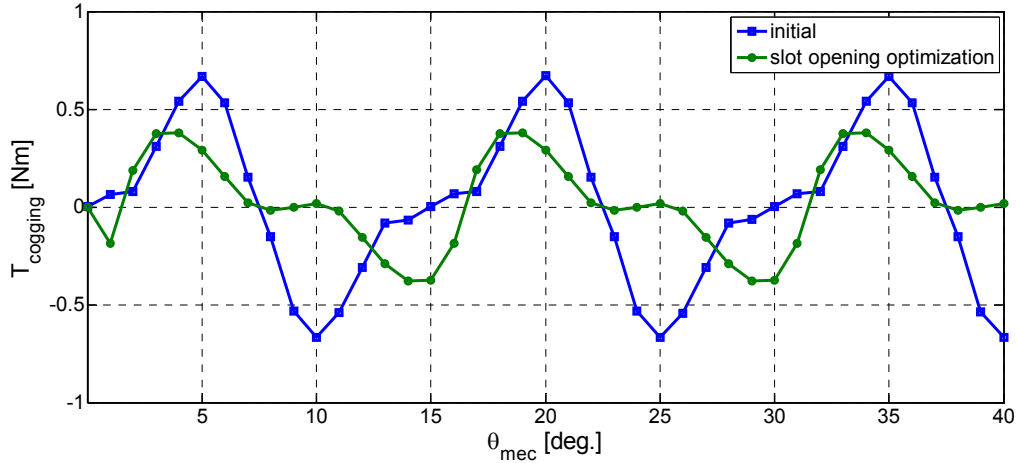


Figure 4.19. Resulted cogging torque after FEM induced corrections

4.3.3. Stator Notches

To increase the number of cogging cycles per mechanical revolution, which leads to amplitude decrease, dummy slots can be introduced by notching the teeth. This increases the number of interactions between the rotor PMs and the created mini-teeth and slots. The slots that are created on the teeth are not as deep as the regular slots having the windings but for the purpose of cogging torque mitigation they serve as slots. The notches in teeth are easy to make during punching of stator laminations. These notches introduce cogging torque cycles of their own with a phase shift given by :

$$\rho_{notch} = \frac{2\pi}{N_s(1 + N_{notch})} \quad (4.10)$$

The cogging torque generated with notches is superposed on the cogging torque of the conductor-carrying slots to obtain the resultant cogging torque. Firstly, the dummy slots have increased the cogging cycles with the attendant consequence that they can mitigate the cogging torque. The cogging torque harmonic multiples of $(N_{notch} + 1)$ of the dummy slots all add and their frequency is increased while all other higher harmonics are cancelled in the resultant torque. This enables the reduction of cogging torque magnitude. Anyway, in order for notching to be effective in reducing the cogging torque, certain guidelines need to be followed. Otherwise, the cogging torque may even increase – equation (4.11)

$$\begin{aligned} HCF[(1 + N_{notch}), N_{pp}] &= 1 \\ N_{pp} &= \frac{N_p}{HCF[N_s, N_p]} \end{aligned} \quad (4.11)$$

By analysing equation (4.11) for our case study, N_{pp} is 4, and consequently, the $(N_{notch} + 1)$ quantity has to be an odd number, for the rule to be respected. So the number of notches that can be introduced is 2 or multiples of 2. For our case study, it was discovered that 6 notches per stator tooth can indeed

reduce the cogging torque. Some saturation appears in the notches area even if circular instead of rectangular shape was chosen, but is acceptable.

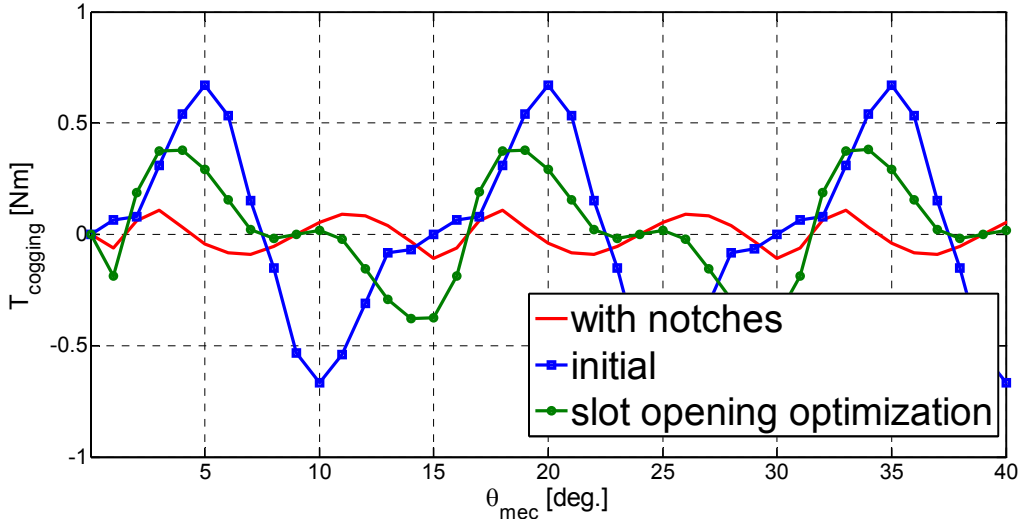


Figure 4.20. Cogging torque comparison: initial, optimized and with notches

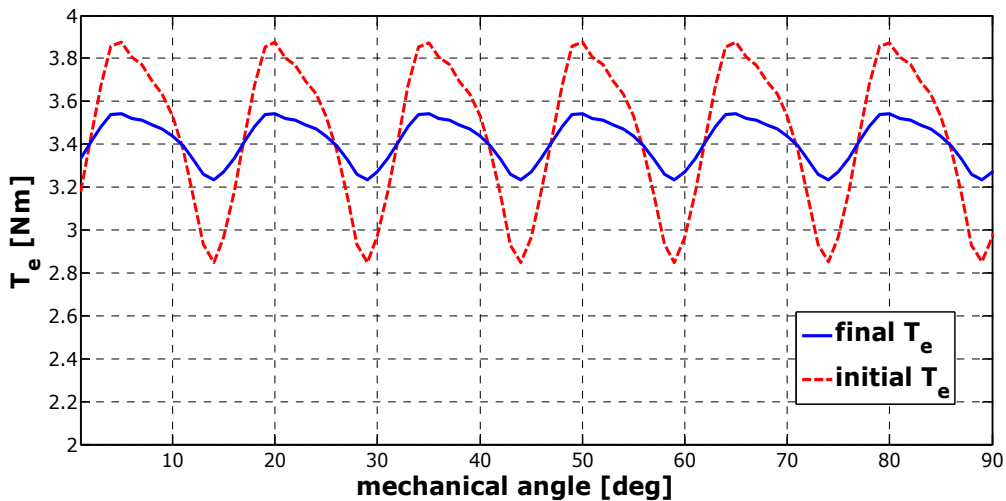


Figure 4.21. "Final" electromagnetic torque

As it can be noticed from Figures 4.20 and 4.21, respectively, the cogging torque amplitude was reduced 6 times, so that the total electromagnetic torque contains mainly only commutation effect ripples. The side effect that the medium electromagnetic torque value is decreased, induced by the smaller slot opening/stator tooth shoe width ratio. The final resulted torque is still above the 3 Nm imposed by the requirements.

The design methodology was implemented as a computer aided list of Matlab scripts taking advantage of the interfacing possibility femm4.2 has for the latter. The Matlab-femm4.2 allows us to use the Matlab high computing power for analytic calculation, optimization calculus and FE model definition and inspection.

The results, from quality point of view are satisfying, but there is a price to pay. Script running for analytic + optimized design lasts approximately 90 [s], while with the hybrid FEM embedded methodology, the one complete run time reaches almost 40 [min], even if FEM calculation are made in prior determined points. However, the motor geometry is not drastically modified and only 1.2 USD initial cost reduction is obtained with a supplementary 0.9% efficiency increase, compared to the Hooke Jeeves optimized topology.

Several observations are still required. This last time interval is very much dependent on computer resources and performance on one hand, and on the under-relaxation/correction factors (k_1 and k_2) values on the other hand. "Strong" correction factors bring faster results, while a "precautious attitude" slows the process.

The next step, to reduce this large timing, is to consider motor symmetry, and simulate through FE only a part of the motor.

The quality related improvements are not spectacular, but having in mind that the automotive industry (that should benefit after our incursion) is a high volume one, the final economic impact that yields, is rather significant.

4.4. Conclusions

This Chapter has presented the FEM inspection and verification stage, as constituting part of the modern engineering practice for electric motor design. Not all possible determinations were performed through FE model computing, but only the one that presented special interest.

The case study was again the 6 slot/8 poles motor prototype that was previously analytically designed and optimized. Because the optimization objective was only to reduce initial and exploiting/operating cost, the resulted motor topology was characterized by a high cogging torque amplitude.

Since direct geometrical correction activities are usually required iteratively after FEM validation stage, an embedded and automated algorithm based hybrid design methodology was constructed and presented. It starts from analytic design stage, passes through optimization process, verifies the resulted topology by FE model computation and imposes correction factors while the whole design process is restarted.

The improvements are paid by the increased computation time, but the algorithm is not fully optimized regarding this purpose.

Furthermore, an inexpensive design artifice is applied (directly) so that cogging torque reduction is increased even more. Notches were applied, and their optimal number was determined.

References

- [4.1] Ion Boldea, Lucian Tutelea, "Electric Machines – Steady State, Transients and Design with Matlab[®]", CRC Press, Taylor&Francis Group, 2010
- [4.2] D. Iles-Klumpner, Automotive Permanent Magnet Brushless Actuation Technologies, PhD Thesis, University Politehnica Timisoara, Romania, 2005
- [4.3] N. Bianchi, S. Bolognani, F. Luise, "Analysis and design of a brushless motor for high speed operation", IEEE Transactions on Energy Conversion, Vol. 1, June 2003, pp. 44-51.

- [4.4] D. Iles-Klumpner, I. Şerban, M. Risticevic, I. Boldea, "High-Speed Automotive Permanent Magnet Synchronous Motors", Proceedings of PCIM, Nürnberg, Germany, 2005.
- [4.5] S.-O. Kwon, S.-II. Kim, P. Zhang, J.-P. Hong, "Performance comparison of IPMSM with distributed and concentrated windings", IEEE Transactions on Industry Application, Vol. 4, Oct. 2006 pp. 1984-1988.
- [4.6] M.S. Islam, S. Mir, T. Sebastian, "Paralleling the Stator Coils in Permanent Magnet Machines", IEMDC, pp. 1479-1486, May 2005.
- [4.7] T. Noguchi, "Trends of Permanent-magnet Synchronous Machine Drives", IEEJ Trans. on Electrical and Electronic Engineering, pp. 125-142, 2007.
- [4.8] H. Jussila, P. Salminen, M. Niemelä, J. Pyrhönen, "Comparing Different Slot-Pole Combinations of a Concentrated-Winding Fractional-Slot Permanent-Magnet Machine", Norpie, Lund, Sweden, 2006.
- [4.9] J. Cros and P. Viarouge, "Synthesis of high performance PM motors with concentrated windings", IEEE Trans. on Energy Conversion, Vol. 17, No. 2, pp. 248-253, June 2002.
- [4.10] D. Iles-Klumpner, M. Risticevic, I. Serban, I. Boldea, "Sinusoidal and trapezoidal PMSM drives for automotive applications: a comparative characterization", PCIM Europe, 2006
- [4.11] B. Ackermann, J. H. H. Janssen, R. Sottek et al., "New technique for reducing cogging torque in a class of brushless DC motors", IEE Proceedings, Part B: Electric Power Applications, 139(4), 315-320, 1992.
- [4.12] Y. Kawashima and Y. Mizuno, Reduction of detent torque for permanent magnet synchronous motor by magnetic field analysis, Symposium Proceedings EVS-11. 11th International Electric Vehicle Symposium. Electric Vehicles: The Environment-Friendly Mobility, pp. 8-10, 1992.
- [4.13] Z. Q. Zhu and D. Howe, "Analytical prediction of the cogging torque in radial-field permanent-magnet brushless motors", IEEE Transactions on Magnetics, 28(2), 1371-1374, 1992.
- [4.14] E. Favre, L. Cardoletti, and M. Jufer, "Permanent-magnet synchronous motors: A comprehensive approach to cogging torque suppression", IEEE Transactions on Industry Applications, 29(6), 1141-1149, 1993.
- [4.15] T. Ishikawa and G. R. Slemon, "A method of reducing ripple torque in permanent magnet motors without skewing", Transactions on Magnetics, 29(2), 2028-2031, March 1993.
- [4.16] N. Bianchi and S. Bolognani, "Design techniques for reducing the cogging torque in surface-mounted PM motors", IEEE Transactions on Industry Applications, 38(5), pp. 1259-1265, 2002.
- [4.17] C. S. Koh and J.-S. Seol, "New cogging-torque reduction method for brushless permanent- magnet motors", IEEE Transactions on Magnetics, 39(6), 3503-3506, 2003.
- [4.18] M. S. Islam, S. Mir, and T. Sebastian, "Issues in reducing the cogging torque of mass produced permanent-magnet brushless DC motor", IEEE Transactions on Industry Applications, 40(3), 813-820, 2004.
- [4.19] J. F. Gieras, "Analytical approach to cogging torque calculation of PM brushless motors, IEEE Transactions on Industry Applications, 40(5), 1310-1316, 2004.
- [4.20] Wang Xun, Qiu Ariu, "Calculation of cogging torque in squirrel-cage induction motors", Proceedings of the IEEE International Conference on Electrical Machines and Systems (ICEMS), 2010, pp. 1347 - 1350

- [4.21]** J. F. Gieras, "Analytical approach to cogging torque calculation in PM brushless motors", Proceedings of the IEEE International Conference on Electric Machines and Drives (IEMDC), 2003, pp. 815 - 819 vol.2
- [4.22]** M.V. Ferreira da Luz, P. Dular, N. Sadowski, R. Carlson, J. P. A. Bastos, "Development of analytical equations to calculate the cogging torque in transverse flux machines", Proceedings of the IEEE International Conference on Electric Machines and Drives Conference, (IEMDC), 2009, pp. 612 – 1616
- [4.23]** Z. Liu, J. Li, Q. Jiang, C. Bi, "A Numerical Approach for Accurate Prediction of Magnetic Field in Permanent Magnet Motors", Proceedings of the IEEE International Magnetics Conference (INTERMAG), 2006, pp. 504 – 511
- [4.24]** R. P. Deodhar, D. A. Staton, T. M. Jahns, T. J. E. Miller, "2Prediction of cogging torque using the flux-MMF diagram technique", Proceedings of the IEEE International Industry Applications Conference, 1995, pp. 693 - 700
- [4.25]** Z. Q. Zhu, D. Howe, "Analytical prediction of the cogging torque in radial-field permanent magnet brushless motors", IEEE Transactions on Magnetics, Volume: 28, Issue: 2, 1992, pp. 1371 – 1374
- [4.26]** R. Islam, I. Husain, "Analytical Model for Predicting Noise and Vibration in Permanent-Magnet Synchronous Motors", IEEE Transactions on Industry Applications, Volume: 46 , Issue: 6, 2010, pp. 2346 – 2354
- [4.27]** D. Meeker, "Finite Element Method Magnetics-FEMM, Version 4.2, User's Manual", May 2009.
- [4.28]** A. N. Stirban, "Low Cogging Torque PMSM Drives with Rectangular Current Control", PhD Thesis, Politehnica University from Timisoara, 2010
- [4.29]** R. Krishnan, "Permanent Magnet Synchronous and Brushless DC Motor Drives", CRC Press, Taylor and Francis Group, 2010
- [4.30]** Duane C. Hanselman, "Brushless Permanent-Magnet Motor Design", McGraw-Hill Inc., 1994
- [4.31]** Duane C. Hanselman, "Brushless Permanent-Magnet Motor Design", Second Edition, Magna Physics Publishing, 2006

CHAPTER 5

SUITABLE CONTROL STRATEGIES

Abstract

This chapter concentrates on possible control strategies to be implemented for the prior designed motor prototype. The specific application requirements, that of the automotive air conditioning compressor should be accomplished, in an efficient but low cost manner.

An overview of existing controls comes first. Due to back-EMF shape characteristic it was appreciated that both sinusoidal control and rectangular current based methods may apply. A SVM technique will be considered as strong opponent for six-step commutation pattern based control.

Still, since the low cost factor is a priority and the drive requirements are not rigorous, a novel sensorless control strategy, based on the second control technique, that uses only DC link current and voltage measurement is proposed.

The SVM technique is used more for prototype experimental characterization purpose.

5.1. Introduction

The automotive industry relies on permanent magnet motors as heart-component for the electric drives included in the automobile-dedicated devices, as they come along with high power density, compact size and low maintenance [5.1]. It has already been established that the motor topology suited for this particular application is represented by the surface permanent magnet synchronous machine.

When it comes to control strategies, two categories can be identified: sensed and sensorless. This attributes refer to the presence or absence of "motion" (position or speed) sensors. Hall transducers or encoders become unattractive not only due to the additional cost they bring for the drive, but also due to the increase in volume they determine, along with mounting issues and operating environmental requirements (they are not reliable in "harsh" operating conditions – immersed in oil or high temperature, for example).

However, the lack of motion sensors for various drives is disputable. The industry still relies on sensed drives to fulfil certain "safety-critical" functionalities, while sensorless strategies are considered for "back-up solutions" (sensor failure). Nevertheless, there has been a constant interest to perfect these new control strategies so they could be considered reliable, at least for non-safety-critical applications.

Depending on the requirements, the control strategy may contain a single control loop, or several, in an extended configuration. A schematic representation of a full positioning system (generally used in industry) is depicted in Figure 5.1. [5.2]. The controllers that appear in the schematic may be the "traditional" PID regulators, sliding mode controllers or fuzzy-logic based (and the list might continue).

An overview of typical control strategies, applicable for PMSM follows.

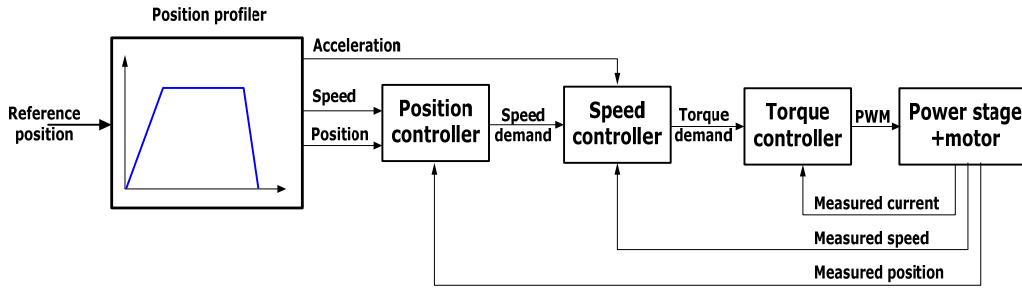


Figure 5.1. Full positioning system – control structure [5.2]

5.1.1. Scalar (V/f) control of PMSM

The scalar control only enables to supervise the magnitude of the chosen control quantities. Also known in the literature as V/f control, the technique keeps a constant ratio between voltage demand and corresponding frequency. It is easy to implement, and that is why it gained popularity for industrial purpose. Still, it cannot assure good performance for high dynamic or demanding drive systems over a wide speed range; its applicability is limited usually to fan/pump drives or other simple household devices. A typical control schematic is depicted in Figure 5.2 [5.3].

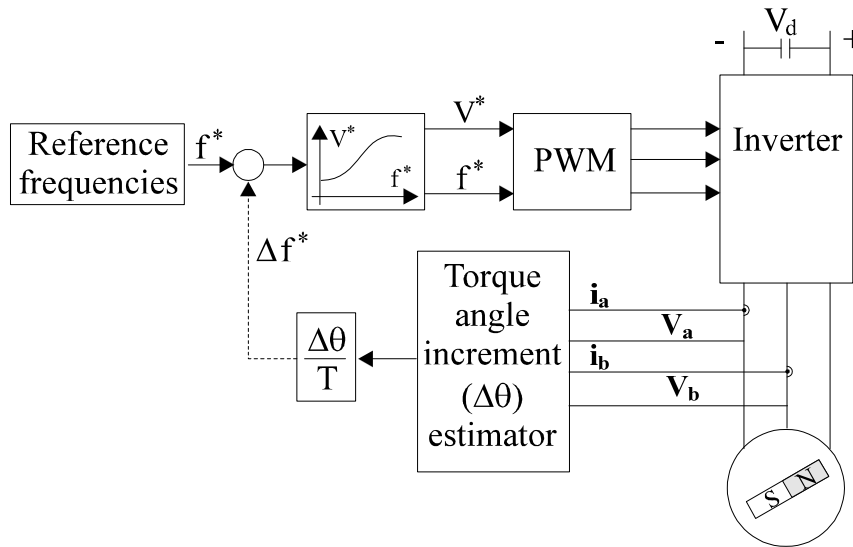


Figure 5.2. V/f (scalar) control for PM - SM with torque angle increment [5.3]

And just because it requires few resources (low cost) and it is easy to implement, several studies have been carried out, either to assure stability over a wide speed range, either to increase its dynamic capabilities.

To assure stability for the V/f control strategy, a damper cage on the rotor would be necessary; still, PMSMs rarely come with this kind of topology.

Several solutions can be identified. A damping factor can be assured from the square torque load characteristics of fans and pumps; this way a simple DC-link

peak currents based control is implemented in [5.11], that assures stability at starting and steady state.

To cope with the lack of dumping another solution is presented in [5.9, 5.10]. The magnitude of the voltage is controlled in order to maintain a constant stator flux linkage in the PMSM, while the applied frequency is modulated proportionally to the input power perturbations to stabilize the drive for a wide frequency range.

Two stabilizing loops are considered in [5.4] to increase dynamic performances and allow high speed operation. Corrections for the frequency and voltage prescriptions are introduced for zero interior reactive power (implicitly pure i_q control). The control schematic is depicted in Figure 5.3.

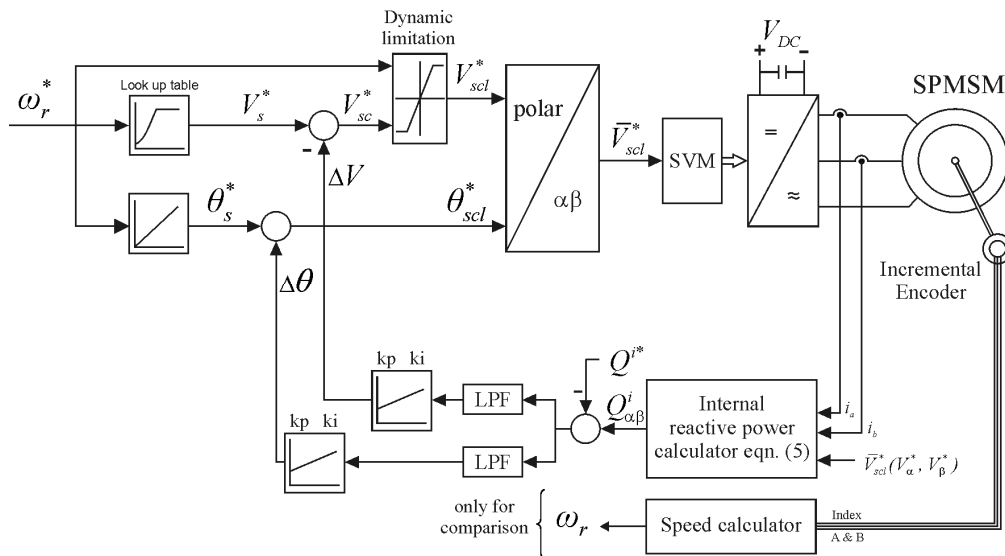


Figure 5.3. V/f control system with two stabilizing loops control [5.4]

The idea of compensating loops is considered further in [5.7] and [5.12]. The first uses oscillatory active power information to generate a load angle compensation component and adjust the load angle to stabilize the system, and the drive imaginary power regulation to correct the voltage requirement. The imaginary power controller respects MTPA performance, such that the drive can operate under the minimum copper loss condition in the steady state. The second uses a voltage-vector speed correction using active power variation (active only during transients) and a voltage amplitude correction based on unity power-factor regulation loop, employing reactive power.

[5.8] provides an optimal design of a V/f control curve with consideration of the stator resistance in order to make this type of control suitable for super high speed permanent magnet synchronous motor drives.

However, scalar control is well suited for middle-range to high speed range operation, while the low speed range cannot "be covered" properly [5.6].

5.1.2. Vector control of PMSM

Low speed operation and fast dynamics are assured if vector control is used for driving. Also known as FOC (field oriented control), this technique was pioneered by Hasse (1968, - indirect variant) and Blaschke (1970 - direct variant).

A typical vector control structure is presented in Figure 5.4 [5.3]

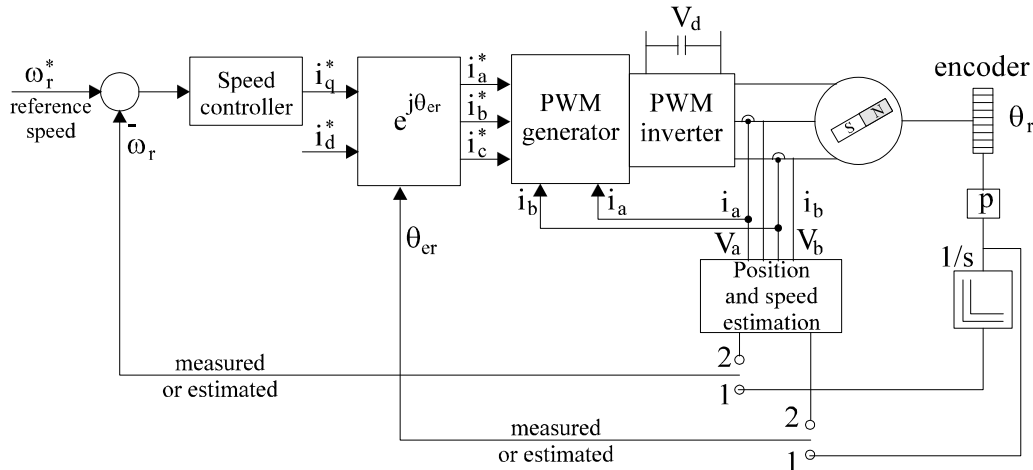


Figure 5.4. Basic speed vector control of PM – SM: 1 - with motion sensor, 2 - sensorless [5.3]

This control technique has practically propelled the A.C. motor drives in the front line. In FOC, an A.C. induction or synchronous motor is controlled under all operating conditions like a separately excited D.C. motor; this means that the AC motor behaves like a DC motor in which the field flux linkage and armature flux linkage created by the respective field and armature (or torque component) currents are orthogonally aligned such that, when torque is controlled, the field flux linkage is not affected, hence enabling dynamic torque response.

Voltage magnitude, orientation and angle are simultaneously controlled. The method implies coordinate transformations and it wasn't until the early 1980' that easy practical implementation was supported by the microprocessor's appearance. Even though it is a resource-consuming control method (sensors for data acquisition and signal processing devices), it is more than competitive over the whole operating speed range and assures fast dynamic stable operation.

Constant interest has been granted for this research subject and it may be considered mature. Still, motion sensorless control techniques that make use of FOC ([5.13]-[5.25]) keep the research flame burning, and new observer structures for various estimations are now obtained.

The general "active flux" (or "torque producing flux") based observer ([5.13], [5.14]) manages to overpass rotor position and speed estimation issues related to magnetic saturation, especially in the low speed operating range. The concept comes to give an alternative solution to signal injection based self-estimation rotor position methods ([5.22]), that are not that attractive from practical implementation point of view.

Filtering theory and methodology ([5.15], [5.16]) accompanies the necessary signal processing involved, so that vector controlled drives assure the best performances at high speed and full torque (starting and steady state).

On the other hand, the progress registered in the microprocessor and digital signal processor industry has sustained compact and commercial implementation of FOC based drives ([5.17], [5.18], [5.20], [5.21], [5.23]). This has enabled implementation of "complicated" and relative costly model reference adaptive system (MRAS), like in [5.23], or low cost variants ([5.20]) (where drive requirements allow it).

5.1.3. DTFC of PMSM

The direct stator flux and torque control is actually derives from "traditional" FOC and it leads to a table of voltage switching (voltage vector sequence). Vector rotation has been dropped but flux and torque observers are required. While speed is observed, rotor position estimation is not required in sensorless driving (see Figure 5.5).[5.3]

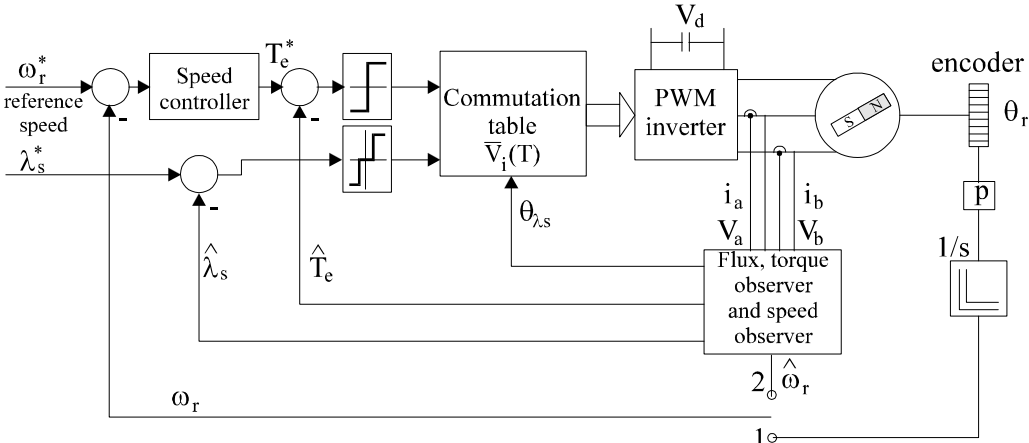


Figure 5.5. Direct torque and flux control (DTFC) of PM - SMs:
1 - with motion sensor, 2 - sensorless [5.3]

Sensorless operation and flux, torque or speed estimations are again the challenge the research teams face ([5.27] - [5.33]). DTFC is best suited for very high dynamic systems, which fall out of our interest.

5.1.4. Rectangular current control of PMSM

Rectangular current control is applied to non-sinusoidal (trapezoidal) PM-e.m.f. waveform, typical for motors with concentrated coil stator windings. The low-cost characteristic of this drive system relies on the simple control strategy that does not require any coordinate transformation but follows the maximum torque principle. On the power electronics part, only 2 switches are active for one commutation sequence determining lower commutation caused losses, less power electronic device wear and avoiding dead-time issues (that may appear only in very high speed applications). A general control schematic is depicted in Figure 5.6. Further details will be given latter on, in this chapter.

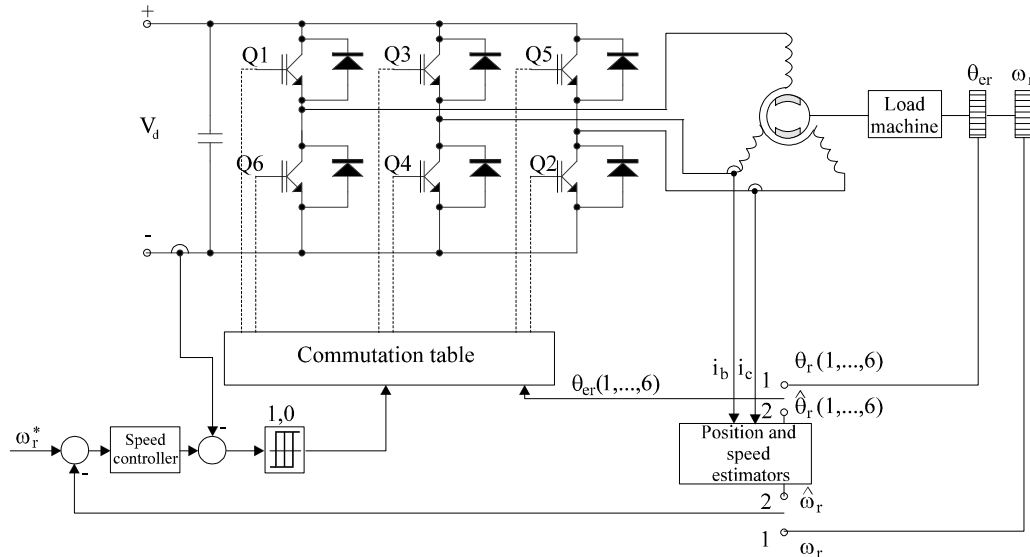


Figure 5.6. Rectangular current control of BLDC [5.3]

5.2. Sinusoidal control

This type of control strategy was considered possible and appropriate, since back-EMF shape is “almost sinusoidal”.

The chosen speed control strategy relies on vector control and max torque/current principle for the entire speed range, meaning that i_d is kept 0 (see Figure 5.7).

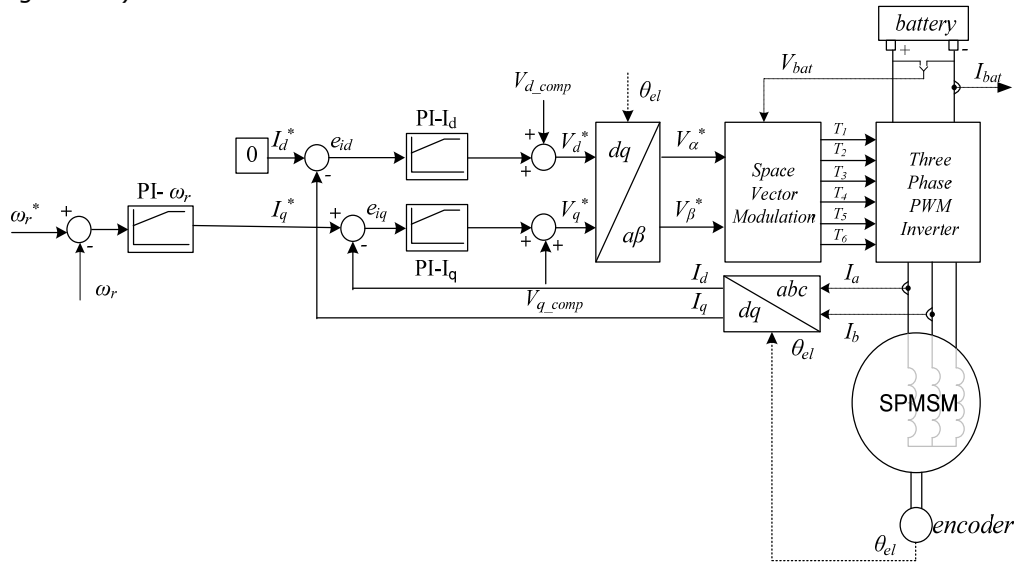


Figure 5.7. Speed vector control with encoder – general overview

The system is provided with an encoder which gives the position information used both for coordinate transformation and speed measurement.

A PI controller with anti-wind-up regulates the speed and gives the I_q^* prescription. Same controller structure is used to regulate the currents in dq coordinates. V_d and V_q compensations are introduced to ensure faster response and to reduce the control effort from the current regulators. These compensation are calculated from

$$\begin{aligned} V_{d_{comp}} &= -\omega_r L_q i_q \\ V_{q_{comp}} &= \omega_r \Phi_{PM} \end{aligned} \quad (5.1)$$

where ω_r is the rotor electrical speed in [rad/s] while Φ_{PM} is the permanent magnet flux [Wb].

Since i_d prescription is kept zero, the load torque was estimated according to equation (5.2), considering only copper losses and motor mechanical equation.

$$\begin{aligned} \hat{T}_{load} &= \frac{3}{2} (V_q i_q - R_s i_q^2) \times \frac{1}{\Omega} \\ \Omega &= 2\pi\omega_{mec} \end{aligned} \quad (5.2)$$

To verify torque capability and efficiency under control, the prototype was run as generator, being connected to an IM loading machine. Since the induction motor provided the drive system with different constant speed levels, the prototype was controlled only by I_q prescription (the speed control loop from Figure 5.17 is not active).

The tests were performed only for a maximum speed level of 3000 [rpm], which is only half the rated speed. This is due to mechanical security and reliability of the driving belt coupling.

Aquisitions for 3000 [rpm] and step torque command progressively raised till 3 [Nm] are presented in Figures 5.8, 5.9, 5.10 and 5.11, since they are considered most representative.

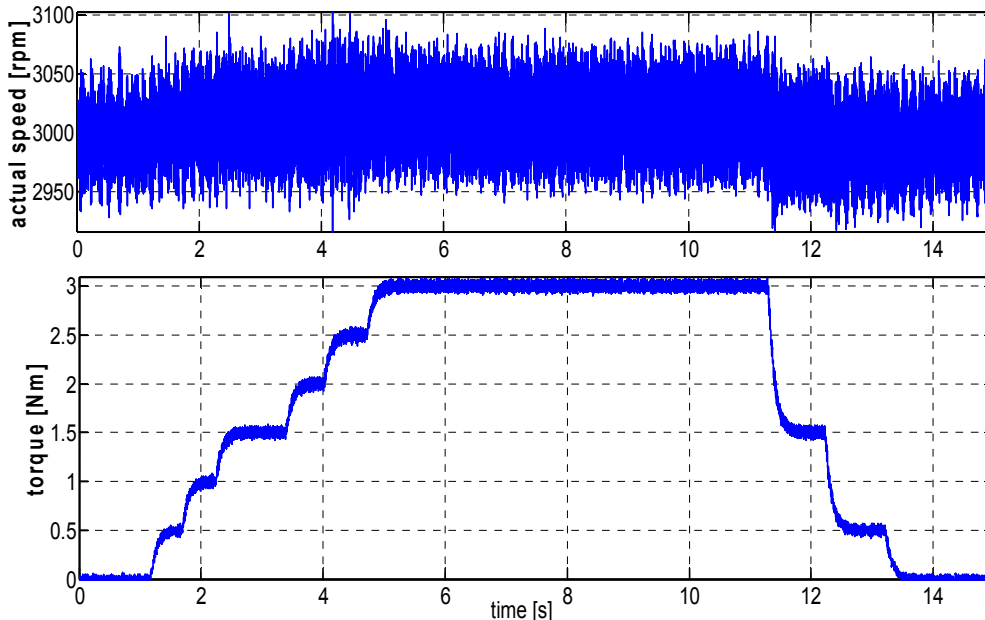


Figure 5.8. Torque command(estimated) for 3000 [rpm]

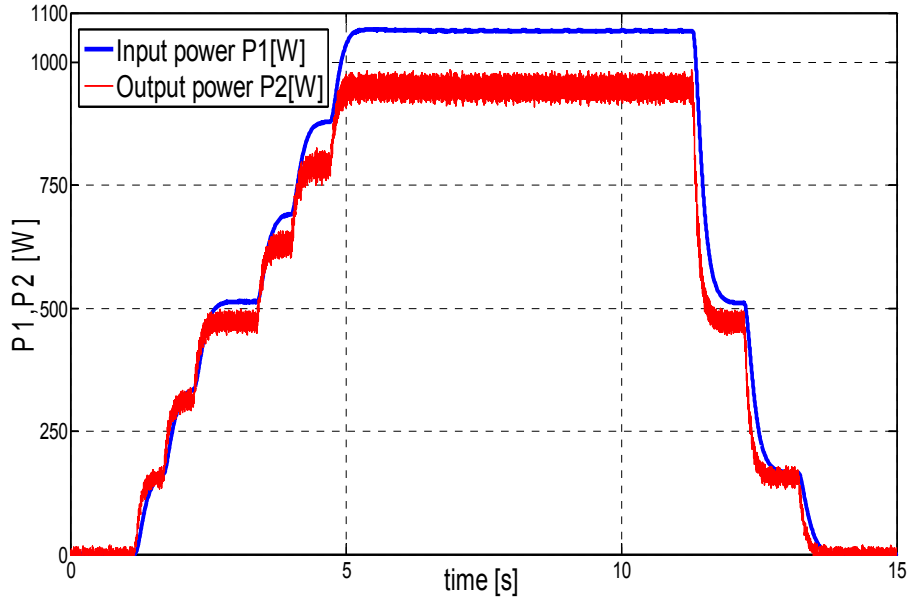


Figure 5.9. Input and output powers

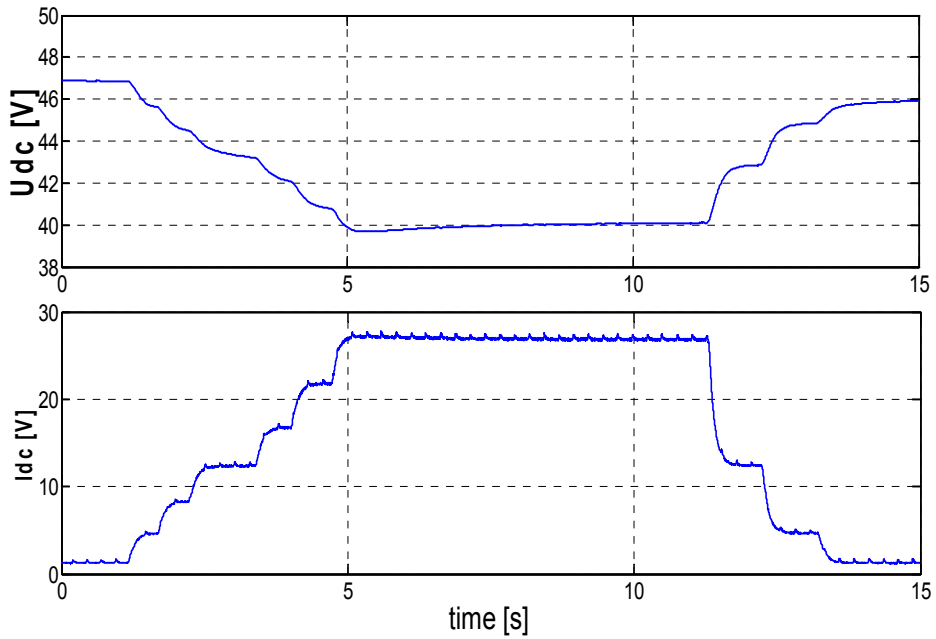
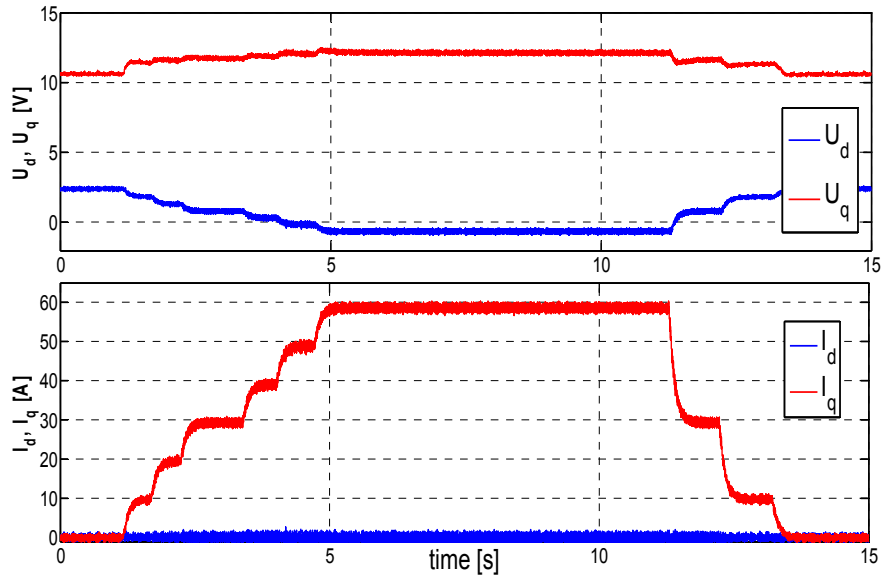


Figure 5.10. Battery current and voltage variations

Figure 5.11. dq currents and voltages

Input (from battery variables) and output power (from dq frame variables) were also estimated in order to determine the efficiency. Experiments were carried out for several speed levels and torque loadings (see table 5.1 for all the realized experiments). Efficiency variation, under given conditions is depicted in Figure 5.12.

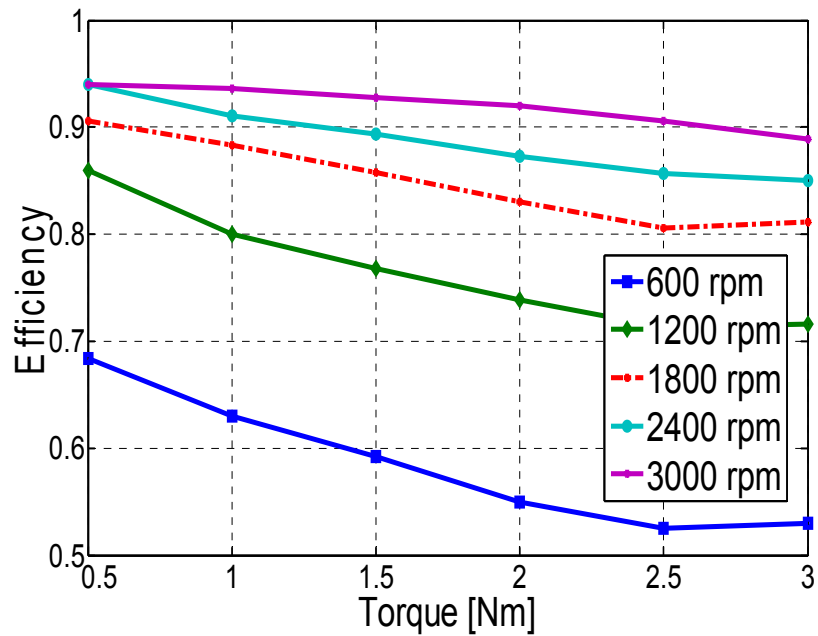


Figure 5.12. Efficiency as function of speed and torque

Table 5.1. Acquisition data for generator mode experiments

n [rpm]	T [Nm]	V_s [V]	I_s^{peak} [A]	P₁ [W]	P₂ [W]	η
600	0.5	3.25	9.8	46	31.5	0.684
600	1	3.45	19.5	100	63	0.63
600	1.5	3.7	29.25	160.5	95	0.592
600	2	3.9	39	228	126	0.55
600	2.5	4.1	49	301	158	0.525
600	3	4.25	58.5	359	190	0.53
1200	0.5	5.2	9.75	73.25	63	0.86
1200	1	5.5	19.5	157.8	126	0.80
1200	1.5	5.65	29.3	246	189	0.768
1200	2	5.85	39	341	252	0.739
1200	2.5	6.08	48.7	443	316	0.713
1200	3	6.25	58.5	530.5	380	0.716
1800	0.5	7.35	9.8	103.8	94	0.9055
1800	1	7.55	19.5	214	189	0.883
1800	1.5	7.7	29.2	331	284	0.858
1800	2	7.95	39	457	379	0.83
1800	2.5	8.2	48.8	589	475	0.806
1800	3	8.42	58.5	702	570	0.811
2400	0.5	9.44	9.8	135.2	127	0.94
2400	1	9.7	19.5	276.4	252	0.911
2400	1.5	10	29.3	423	378	0.8936
2400	2	10.25	39	578.5	505	0.873
2400	2.5	10.5	48.8	739	633	0.8565
2400	3	10.75	58.6	894	760	0.8501
3000	0.5	11.75	9.8	166	156	0.94
3000	1	11.85	19.5	336.5	315	0.936
3000	1.5	12.15	29.3	512	475	0.9277
3000	2	12.35	39	685	630	0.92
3000	2.5	12.5	48.6	866	785	0.9064
3000	3	12.7	58.5	1063	945	0.889

The following observations are valid. A high efficiency is obtained for high speed operation under load. A maximum efficiency of 94% is obtained corresponds to 3000 [rpm] and a loading of only 0.5 [Nm]. Either way, the efficiency is expected to increase once the speed level is raised. For rated speed of 6000 [rpm] operation under rated torque loading, the efficiency should be the one predicted by the motor design.

Dynamic performances for the prototype were tested for motor mode operation. The control principle is the one depicted in Figure 5.7.

The control parameters were adjusted in order to obtain fast dynamic responses. Experiments carried out for 1000 rpm, 2000 rpm and 3000 rpm, no-load starting are depicted in Figures 5.13, 5.14 and 5.15 respectively.

The high dynamic capability may be observed since the motor needs

- 50 [ms] to reach 1000rpm
- 115 [ms] to reach 2000 rpm
- 300 [ms] to reach 3000 rpm

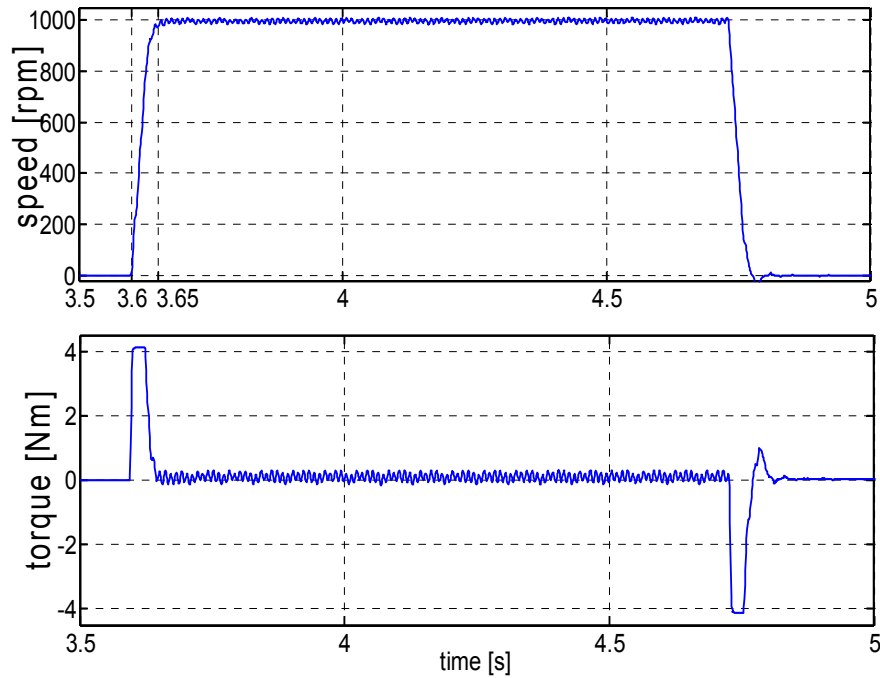


Figure 5.13. No-load start-up to 1000 [rpm] (speed and torque variation)

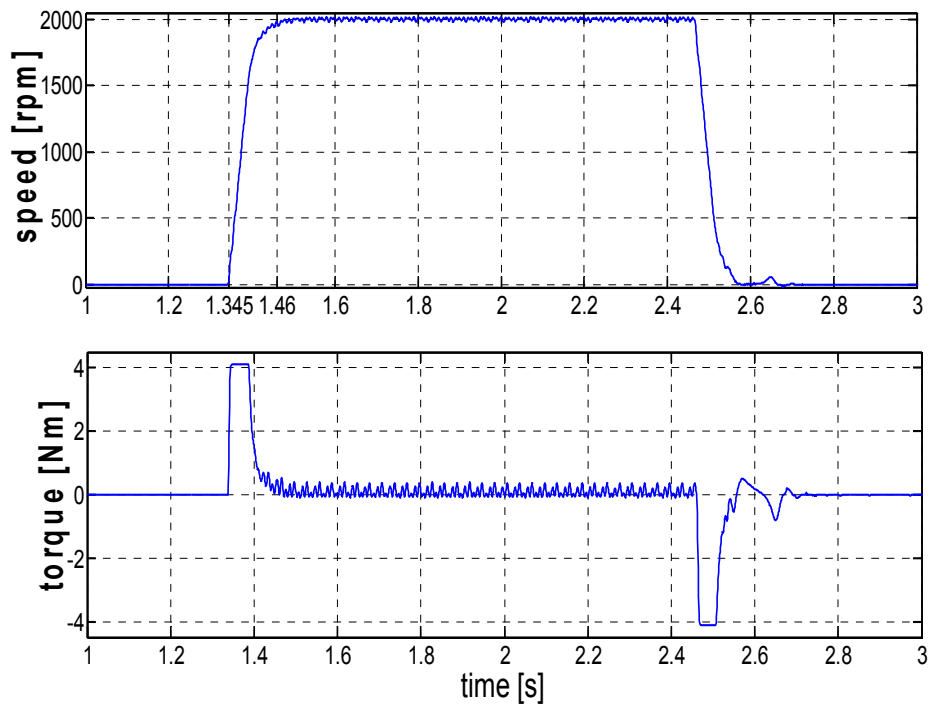


Figure 5.14. No-load start-up to 2000 [rpm] (speed and torque variation)

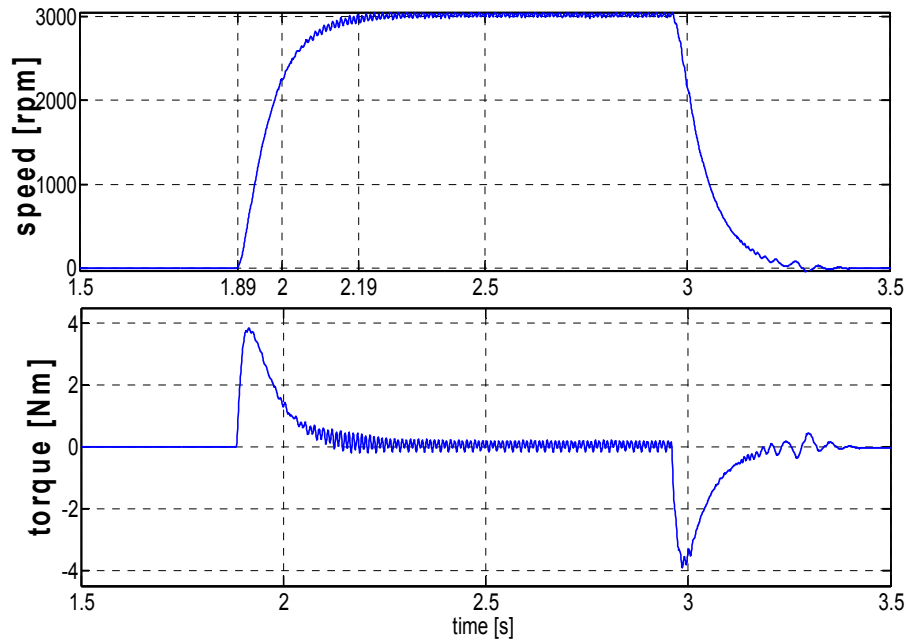


Figure 5.15. No-load start-up to 3000 [rpm] (speed and torque variation)

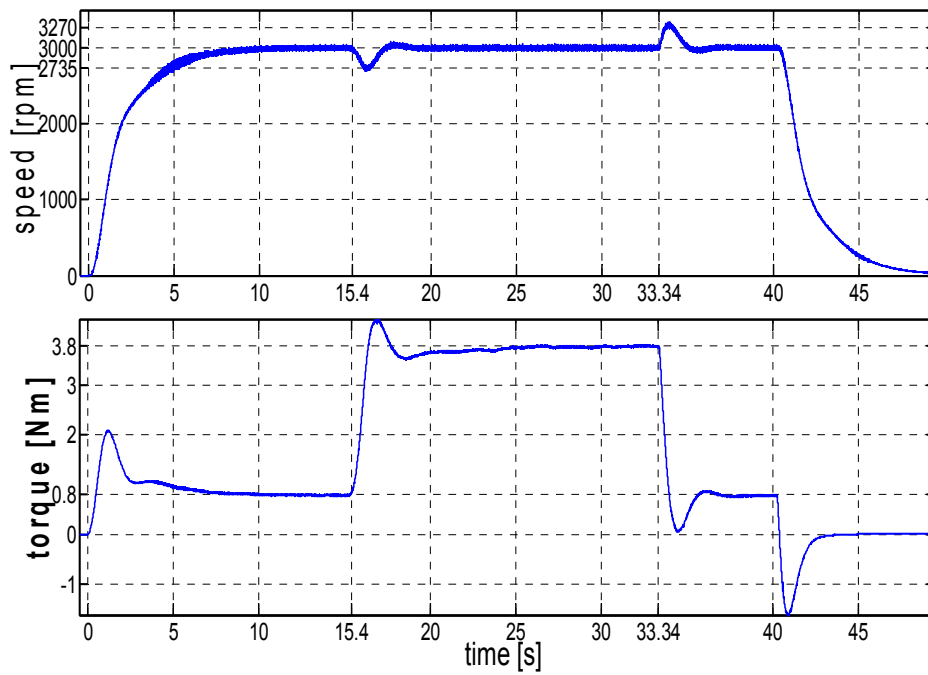


Figure 5.16. 3000 [rpm] operation with 3 [Nm] loading and unloading perturbation (speed and torque variation)

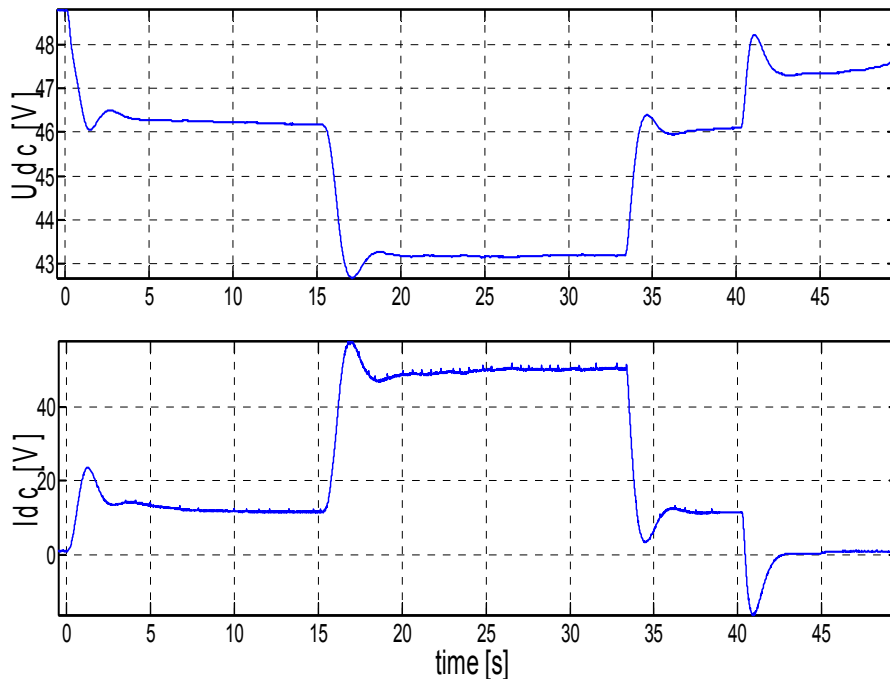


Figure 5.17. Battery current and voltage variation for 3000 rpm operation with load perturbation

Control performance for load disturbance scenario was also inspected. Tests were performed for several speed and load torque values, but the 3000 [rpm] with 3[Nm] load perturbation is considered to be the most representative. As it can be seen (Figure 5.16), the motor is loaded with 3 Nm at 15.4s and unloaded at 33.34s. The machine copes with 3Nm load torque (from 0.8 Nm to 3.8Nm) and the control assures 9% transitory speed error. As expected, further improvements in the control can lead to better performances.

It was proved that the motor prototype is capable of the performance specified/expected by design. In the same time, vector control may be suitable for the machine, even though back-EMF shape is not perfectly sinusoidal. The control was performed for motion sensor equipped drive condition. Taking into consideration the automotive air conditioning compressor drive, a sensorless variant is desirable.

However, for sensorless operation, estimation for both speed and position have to be made accurately and "continuously" (speed is required for the feedback loop, while position is needed for coordinate transformation). Accuracy of speed and position estimations must surely take into account the harmonics introduced by phase back-EMF imperfections. Considering computation effort, this kind of solution is not by far cheap. On the other hand an increased number of sensors that must measure phase quantities (consequently they need to have a large frequency band), makes this type of control even more expensive. Dynamic performance is also above the one stated in drive requirements. From practical and economic considerations, this control strategy is not the best.

5.3. Rectangular control

Rectangular control is from the beginning not only simpler to implement, but also cheaper. It addresses mainly trapezoidal back-EMF shape characterized motors, but it is known to produce torque ripples. However, if the torque ripples do not contribute to drive performance failure, a compromise should be considered. The basic principles for this kind of control strategy are presented in the subsections that follow, along with novel, original approaches.

5.3.1 Six-step commutation pattern

For this commutation pattern only two phases are energized at one time and six individual sectors can be distinguished. Each sector corresponds to one of six equal 60° portions of the electrical cycle (the sector numbering is completely arbitrary). Commutations occur at the boundary of each of the sectors. Therefore, it is the sector boundaries that need to be detected. There is a 30° offset between the BEMF zero-crossings and required commutation positions, which must be compensated for, to ensure efficient and smooth operation of the motor. The commutation pattern is explained in Table 5.2. However, if we take a closer look to the control principle, one can notice that a sort of maximum torque/current is actually implemented (which can too, assure good operating efficiency as the $I_d^* = 0$ SVM control discussed earlier).

Table 5.2. Soft switching six-step commutation table

Sector	Rotor position	Phase A	Phase B	Phase C
0	330° - 30°	0	-1	PWM
1	30° - 90°	PWM	-1	0
2	90° - 150°	PWM	0	-1
3	150° - 210°	0	PWM	-1
4	210° - 270°	-1	PWM	0
5	270° - 330°	-1	0	PWM

The soft-switching attribute implies pulse width modulation only for high-side switches (PWM) and closing (-1) the low-side switches, in the combination dictated by the sector the motor finds itself. The „0“ means that the phase is not energized (both high-side and low-side switches are opened). While PWM is not performed for low side switches, some commutation + PWM loss reduction can be granted.

We have already stated that a sensorless control strategy is more desirable, especially because space under the vehicle bonnet is limited. If Hall sensors or encoder information is not available, the position must be estimated. It is important to mention that no continuous information is required, but sequential. Anyway, the precision of detecting position information corresponding to the sector boundary, is essential. Several techniques for sensorless position information estimation are to be found in the literature and they are described in the following subsection.

5.3.2 Position information for six-step commutation

Several approaches can be made in order to acquisition the needed position information. Estimations are based on processing rotor position containing signals. The most popular are represented by so called back-EMF sensing techniques

The phase back-emf is speed and position carrier and its zero crossing corresponds to a 30° electrical degree phase shift in respect to required ideal commutation position, so commutation information is obtained straightforward. Zero Crossing Detection (ZCD) signal, that carries along the zero-crossing of the phase induced voltages may be obtain differently.

- *Motor terminal voltage sensing*: either by direct measurement or inference (knowledge of switch states and DC bus voltage).
- *Mid-point voltage sensing*: only works for Y- and delta-connected motors; certain classes of winding connections may not work
- *Bus current gradient sensing*: relies on characteristic bus current shape due to commutation changing as rotor leads or lags

It is clear that the most straightforward way to implement rectangular control strategy is to integrate in a way or another, ZCD in the system i.e obtaining the required information. This is regularly achieved by measuring phase voltages, as stated before, and signal processing techniques that follow various judgements, according to motor specific configurations.

However, the number of sensors required for a motion-sensorless control approach remains increased when phase quantities must be measured. And from the point of view of sensor cost, the strategy is not too far from the SVM strategy discussed earlier.

However, the third method mentioned earlier may lead to a practical and useful control technique.

5.3.3 Novel approach to ZCD determination

Let us consider the current circulation for sector 1 (see Figure 5.18). For 120° conduction, the current from the d.c. link may be a faithful image of the current that circulates in the machine and may capture all the important phenomena that occur there (so a way to implement a bus current gradient sensing method could apply). For supplying the inverter, in our case study, four automotive lead-acid batteries connected in series are used (the drive system takes into consideration a 42V automotive application). This means that our dc supply voltage comes actually from a giant capacitor enabling even a more emphasised effect upon current waveform.

So current ripples occur mainly because of the commutation sequences and their frequency is six times the electrical rotor frequency as one can observe from Figure 5.19.

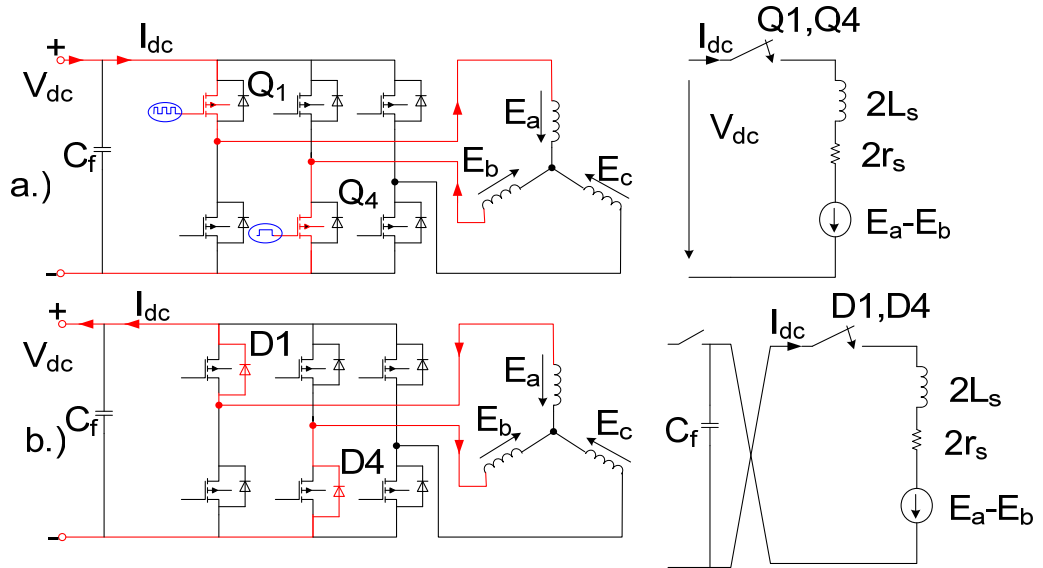


Figure 5.18. Current circulation (sector 1) and equivalent circuits for: a.) on-time; b.) off-time [5.3]

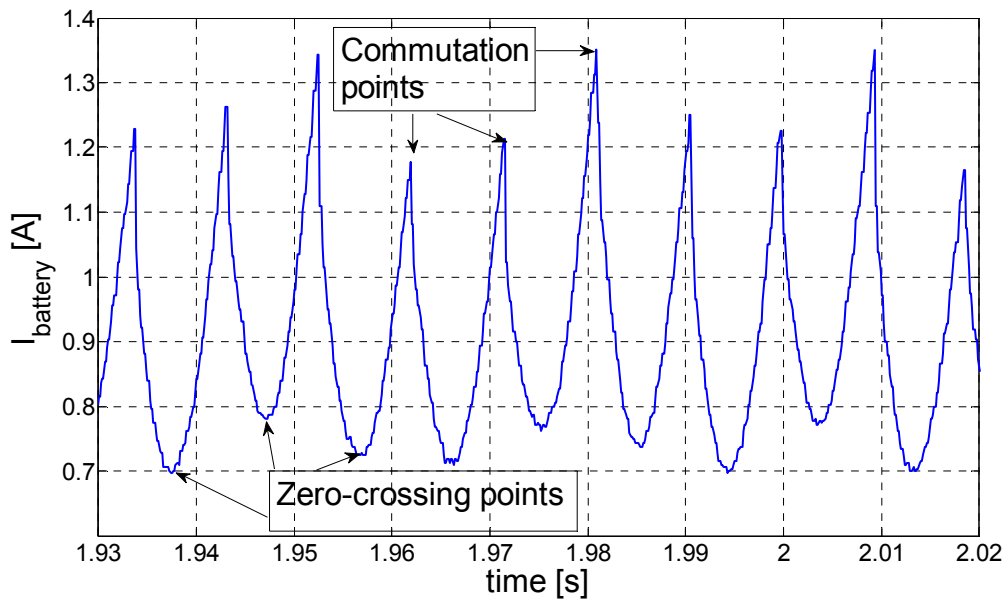


Figure 5.19. Battery (d.c.) current (experimental)

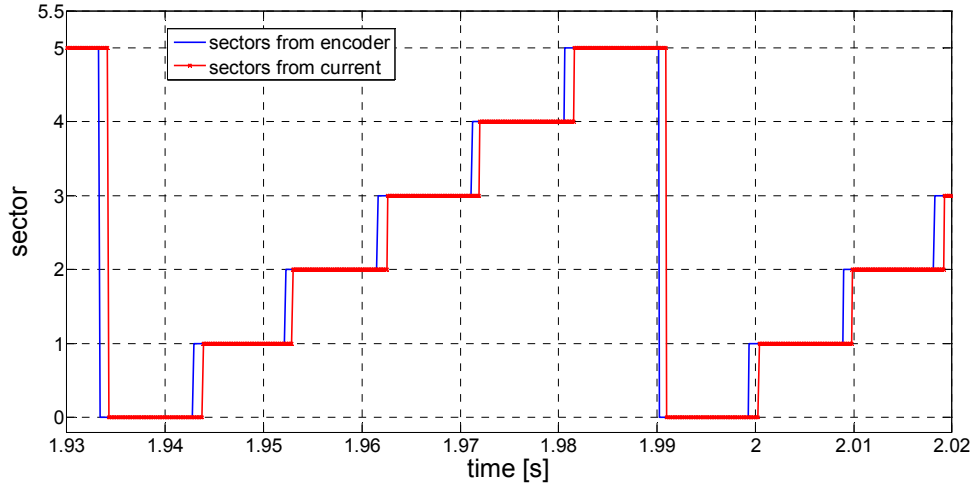


Figure 5.20. Sector variation determined from encoder and from the battery current information (experimental)

In order to verify that the current from the battery is the carrier of the above mentioned information, commutation was performed using an encoder. The points indicated in Figure 5.19 correspond to reality only if the motor is synchronized. However, independent of the motor synchronization, the "spikes" are the result of commutation. By knowing the direction and having determined the commutation points, the sector succession can be obtained. A certain delay can be noticed for the sector determined from the current waveform (see Figure 5.20). This is due to calculations and can be compensated for. The experiment was performed only to demonstrate the connection between commutation and current spikes.

If the motor is not synchronized, the zero-crossing points (when phase back-emf passes through zero, as indicated in Figure 5.19) do not illustrate what actually happens in the motor, but what is expected. Therefore, valid zero-crossing points have to be obtained. They will be used to correct bad commutation and synchronize the motor.

The identification of true zero-crossing points is a real challenge, because no direct voltage measurement from the motor is performed.

However, let us reconsider the equivalent circuit from Figure 5.18a. The following equation is true during on-time:

$$V_{dc} = 2r_s i + 2L_s \frac{di}{dt} + E_a - E_b \quad (5.3)$$

The induced phase voltage (E_a , E_b or E_c) is angle dependent (as function of rotor electrical position) (eq. 5.4), no matter if trapezoidal, sinusoidal or quasi-sinusoidal waveforms are considered

$$\begin{aligned} E_a &= f(\theta_{er}) \\ E_b &= f\left(\theta_{er} - \frac{2\pi}{3}\right) \\ E_c &= f\left(\theta_{er} + \frac{2\pi}{3}\right) \end{aligned} \quad (5.4)$$

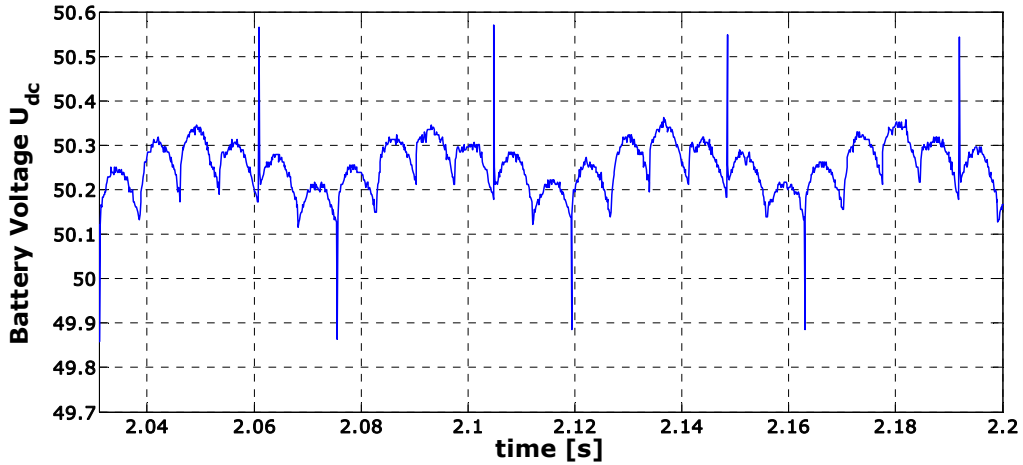


Figure 5.21. Battery voltage waveform

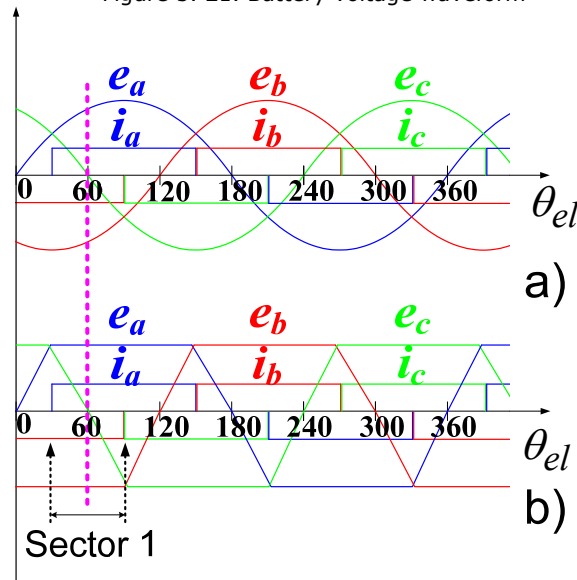


Figure 5.22 Sinusoidal (a.) and trapezoidal (b.) phase bmf variation in respect to the rotor electrical position and corresponding phase currents

In Figure 5.22. the variation of phase bmf in respect to the rotor's electrical position is represented for two ideal cases – sinusoidal and trapezoidal distribution. Some discussion is necessary. For the case in Figure 5.22a), SVM control would be suitable, since rectangular current control introduces torque pulsations (depending on drive performance requirements, still both alternatives should be considered and compared before taking a decision). The second case (Figure 5.20b) is the ideal candidate for six-step commutation based control. One can notice that for each sector (rectangular control strategy), the emf from the non-energized phase passes through zero. Going back to equation (5.3), and considering all entities as time-varying quantities for each sector, the zero-crossing of the non-energized phase back-emf could be evaluated. The difference of two induced voltages is maximum (absolute value), when the third one is zero, for non-

trapezoidal bmf variation (otherwise, the aforementioned difference would be constant for one sector and equal to twice the phase bmf amplitude). This judgment is valid in our case, since the back-emf waveform is neither pure trapezoidal, nor purely sinusoidal, but somewhere in between. So, for each sector, another possibility to determine the zero-crossing of the bmf from the non-energized phase arises.

The $(E_a - E_b)$ quantity has to be evaluated for its maximum (absolute) value for each sector. The calculations must be performed only during on-time, and one maximum value determination has to be realized between each two consecutive commutation points (determined from the battery current waveform). The current derivative is replaced by successive differences, between actual and previous aquisitioned values. These points come to correct the commutation and help the motor to get synchronized, as the time difference between expected and actual zero-crossing is used for this scope. More details regarding practical implementation will be given in the following section

5.3.4. Proposed sensorless speed control strategy

The control scheme for the SPMSM drive is presented (in principle) in Figure 5.23. The zero-cross detector (ZCD) calculator uses the measured battery current and measured battery voltage to implement the algorithm presented in Section II. It offers the input for the control block (Commutation Table), more precisely, it gives the commutation signal and speed information for the regulator, as it will be detailed further in this paragraph. The output of the current regulator is the required duty-cycle used for energizing the motor. The motor is supplied via a three-phase MOSFET PWM inverter.

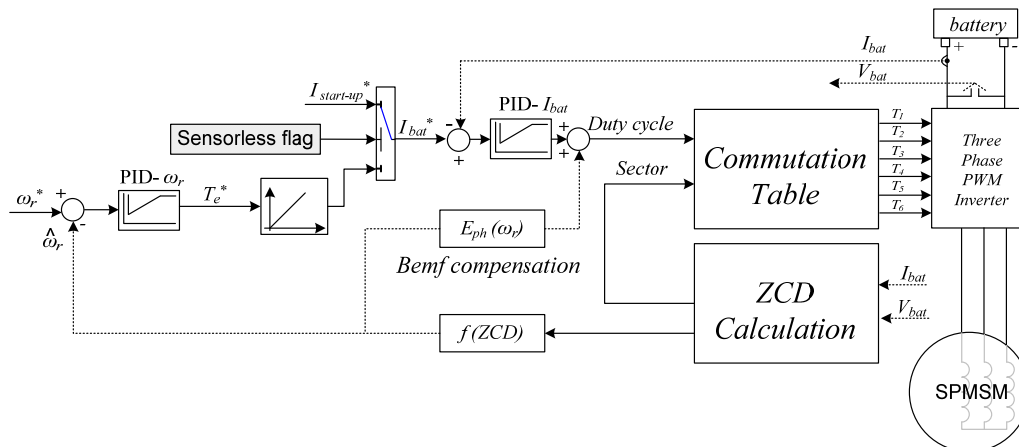


Figure 5.23. Sensorless control strategy – principle schematic

5.3.5. The alignment stage

This phase is particularly important for the success of the starting procedure. For each sector, two of the motor phases are supplied (see Figure 5.24,

where only a one-pole-pair rotor is considered, for simplicity) and the motor travels successively 60° electrical degrees. This means that no matter which single sector is chosen, it is not the best candidate for an alignment procedure. The phase shift between the stator and the rotor fields will always be 60° electrical degrees providing this way only 86% torque for starting, if we were to align with one sector and start with the consecutive one. To start successfully, in any condition, maximum starting torque should be assured. In order to achieve the 90° electrical degree phase shift (for maximum torque), the natural way is to align the motor along one phase and then choose for starting the sector which implies energizing the other two phases (there are two possibilities, but the selection should be made taking into consideration the direction in which the motor should travel).

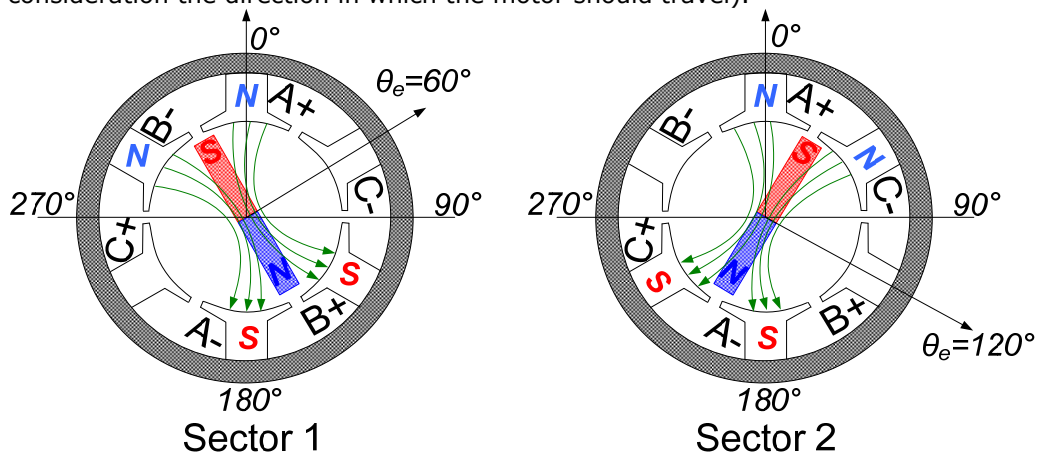


Figure 5.24. Rotor position (one pole-pair) during two sectors

The alignment procedure consists in energizing all three phases; one phase is positively energized and the other two negatively, so that the rotor will end up being aligned to the phase that was previously connected to the “+” of the dc link.

This operation mode may not be necessary with I-f starting, which, with some hesitations, can provide starting under notable load from any initial rotor position. Still, some discussion is necessary.

The motor can start with I-f method, even if the motor is not aligned (see Figure 5.25a), but it will not be able to follow closely the reference position imposed by this particular starting method. Even more, there is the possibility to start in the opposite direction and some applications are sensitive to motor reversal and do not allow it. This “blind” variant for the starting procedure leads to several consequences. The synchronization issue will be very difficult to solve (by correcting the commutation with the time difference between expected and actual zero-crossings). The large phase shift problem between actual and reference position leads to a more sophisticated “switch to sensorless” procedure, which is not desirable.

With the alignment procedure (see Figure 5.25b), the motor is capable to start with fewer hesitations and follows closely the reference position

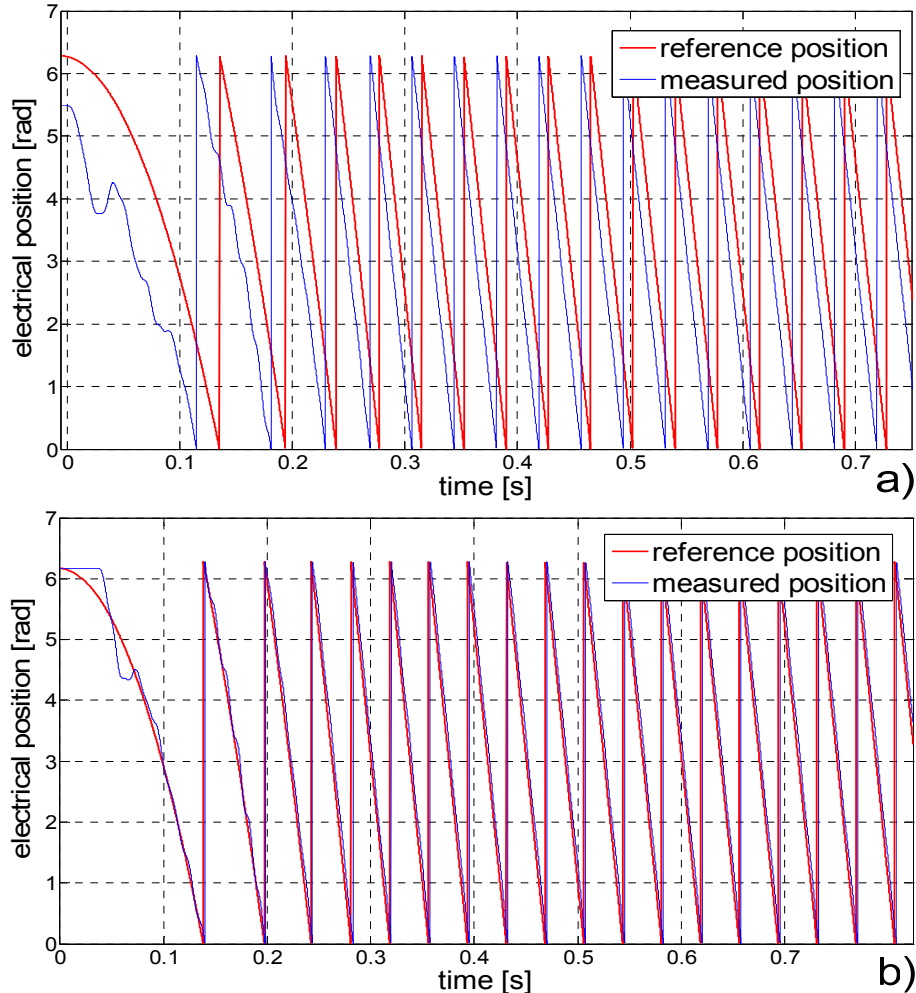


Figure 5.25. Motor start-up to -400 rpm: a). without alignment procedure and b). with alignment procedure (experimental)

5.3.6 Start-up procedure

Starting a SPMSM motor, without position sensors is the most difficult part of the whole control strategy.

With Hall sensors/Encoders, by knowing the initial position, the suitable phases are energized to obtain maximum torque, to overcome the cogging torque caused by the permanent magnets and to ensure that way a fast successful motor start.

For sensorless start-up, the proposed I-f starting strategy principle is presented in Figure 5.26. The reference position is obtained by integrating the reference speed (frequency) and the duty cycle is given by regulating the dc (battery) current.

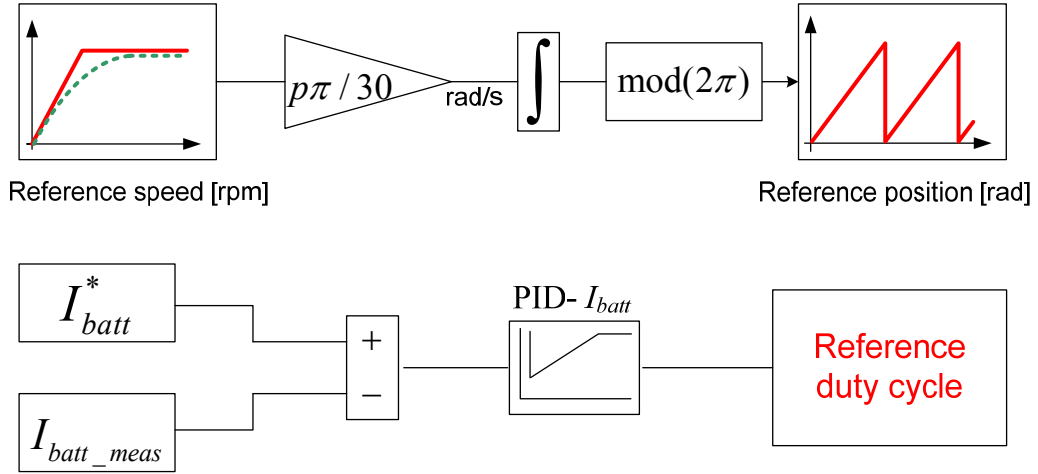


Figure 5.26. I-f starting principle

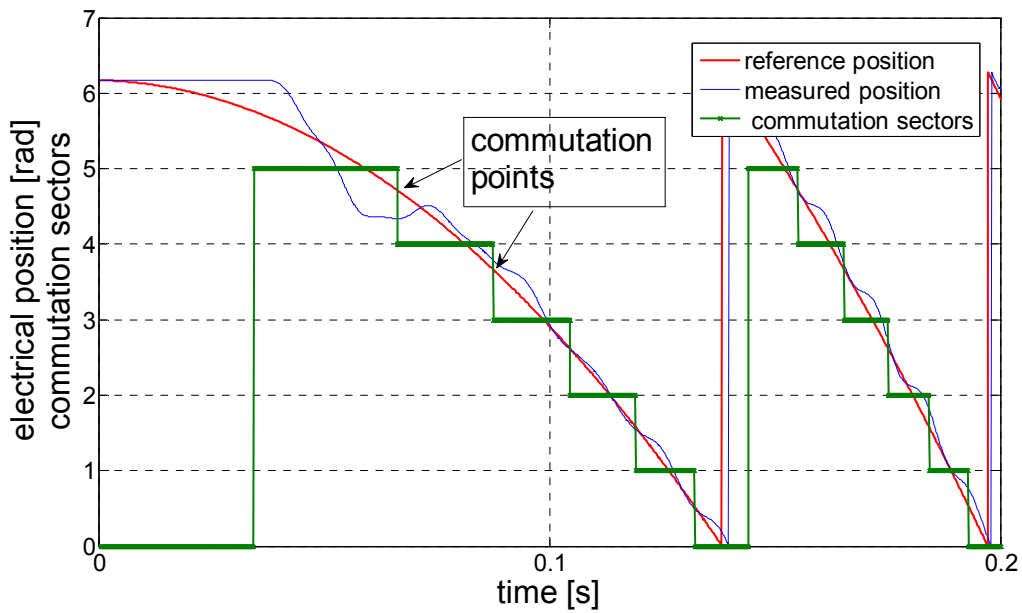


Figure 5.27. Commutation during start-up

If the motor was previously aligned, by knowing the desired direction, the correct phases of the motor will be energized (the correct sector will be chosen). Ideally the rotor follows the prescribed frequency. In reality, this is not the case due lack of any motion damping.

During start-up time, commutation is performed “artificially” taking into consideration that the frequency prescribed (the reference electrical position) – commutation occurs each 60° , starting with 30° , as it can be seen in Figure 5.27.

If the commutation is badly performed, the noisy running of the motor will be the first to manifest, and the battery current waveform and value will be

affected. So, the battery current feedback loop comes to correct (as much as possible) bad commutation.

It is important to mention that the I-f procedure has the main goal to start the motor (in a better way than traditional "align-and-go" or V/f procedures). I-f method has been proved to assure a faster and better starting, and it is not ours to claim, but the novelty relies in using the battery current (no coordinate transformations nor dq reference system are used, as in classic SVM strategies for synchronous motors – [5.5])

5.3.7. I-f to sensorless control switching

We have already established before that the I-f procedure is used solely for starting. The application considered does not require low speed operation (the typical speed range is 400-6000 rpm), so we can assume that for one operating

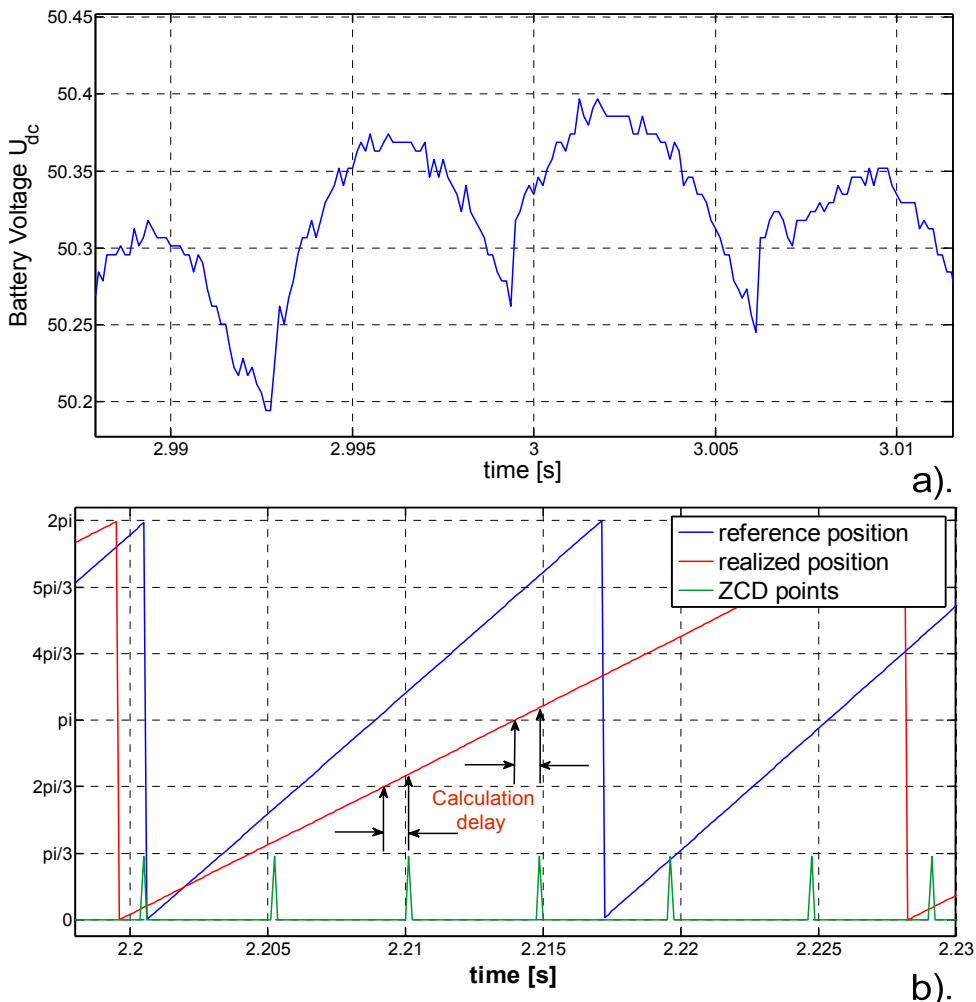


Figure 5.28. Battery voltage variation (experimental) (a) and ZCD points(b)

cycle, a single successful start-up procedure is necessary. In order to actually reach these two attributes – “single” and “successful” along with a simple method to switch from I-f to sensorless operation the alignment procedure is mandatory. The switch to sensorless operation can be made only if the motor is synchronized.

The proposed I-f starting method is rather a feed-forward procedure, even if we have some feedback assured by the battery current control loop. Still, it cannot guarantee motor synchronization. The rotor position has to be estimated for this purpose. No “continuous” information is required, so six points per one electrical revolution, image of the zero-crossings of the three phase induced voltages will do.

The idea on how to detect these points was already described briefly in the previous section and had arisen after observing the battery voltage waveform; it is not constant, as one can see in Figure 5.28a (and it is a consequence of the fact that we are using automobile lead-acid batteries for supplying the inverter). The zero-crossing points are calculated, according to equation (5.3), by evaluating $(E_x - E_y)$ quantity, where x and y are the phases that are energized for a given sector and are depicted in Figure 28b. It is true that some delays are introduced, but they are due to calculations and can be compensated for.

Ideally, if the motor is synchronized, these zero-crossing occur exactly in the middle between two consecutive commutations. So, in order to get the motor synchronized, the commutation has to be corrected with the difference between the expected and actual ZCD occurrence (see Figure 5.29), until three consecutive good zero-crossings occur. This will also be our condition to switch to sensorless operation stage and enable the speed control.

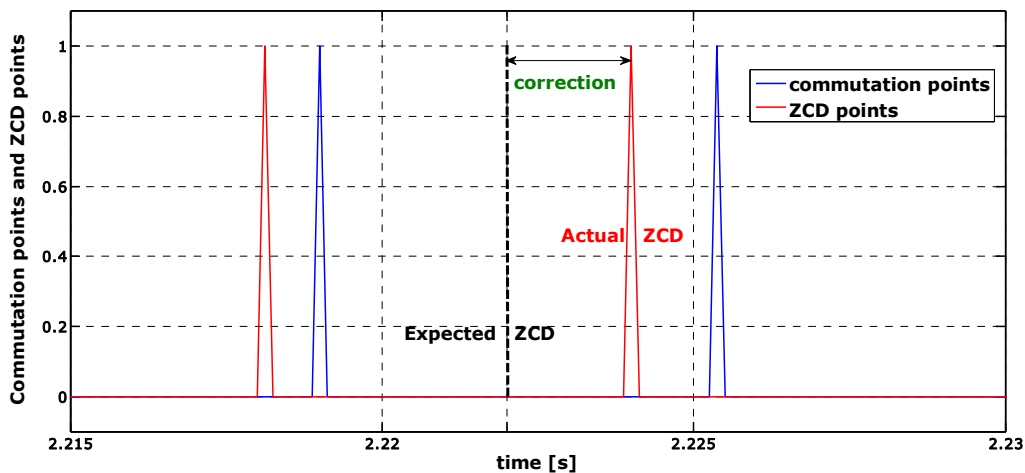


Figure 5.29 Correction algorithm

However, for a more easy solution, from practical point of view, the correction may be transformed from “time coordinates” into an “angle coordinate” variable, taking into account the speed value. As one can observe in Figure 5.30, synchronization is acquired after approximately 50ms after starting correction algorithm.

For smooth synchronization, the correction is applied gradually, through a low pass filter.

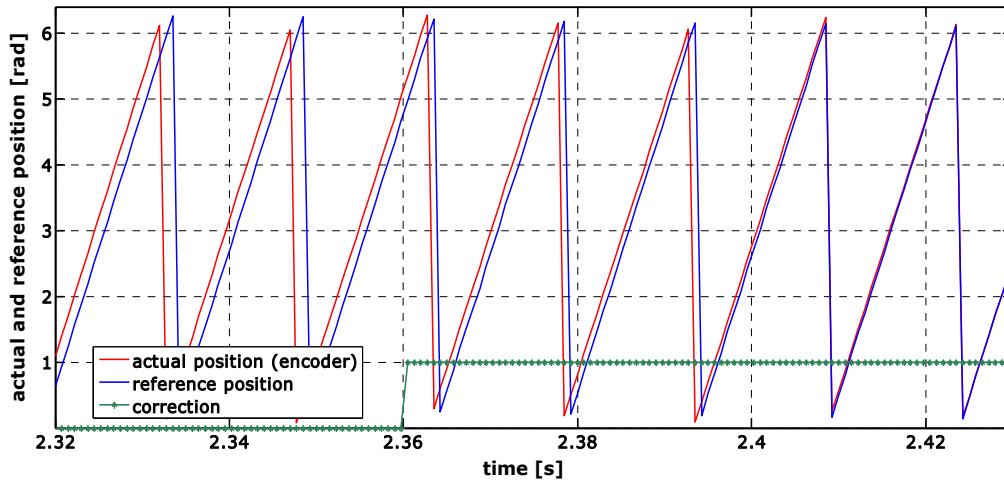


Figure 5.30. Synchronized motor after correction implementation (experimental)

5.3.8. Speed sensorless control

Let us rehearse the control steps. The motor is aligned, for a successful starting procedure (that even eliminates the possibility for the motor to go for a certain amount of the time in the opposite direction – the application does not allow motor reversal)

An I-f procedure follows in order to start the motor. During starting sequence, calculation regarding ZCD, correction and speed estimations are performed.

Speed control is enabled after synchronization (synchronization flag is enabled – from Figure 5.21). Activation of this flag, in a more resource-consuming variant, verifies the “three consecutive good ZCD” condition. Still, if the correction angle is evaluated, it is simpler to simply ask for zero correction angle for a certain amount of time

Once activated, the speed control loop receives the estimated speed for feedback. Speed estimation is performed according to equation (5.5) by knowing that ZCD or commutation has a frequency equal to 6 times the motor electric frequency:

$$n[\text{rpm}] = \frac{60 \cdot f_{el}}{p} = \frac{60}{T_{el} \cdot p} = \frac{60}{T_{ZCD(COM)} \cdot 6 \cdot p} \quad (5.5)$$

In sensorless operation, commutation is performed according to the position that results from reference speed. The correction algorithm comes to keep the motor synchronized.

Speed estimation is considered for control purpose only above 200[rpm] level. The signal processing involved does not prove reliability under this value. After the motor reaches the specified speed value, back-EMF loop is activated, assuring a better dynamic response, while contributing to a reduced control effort for the current controller. The speed errors assured by this estimation are less than

$\pm 2.5\%$, fulfilling drive requirements. See Figure 5.31, for absolute error variation while running sensorless with 800 rpm.

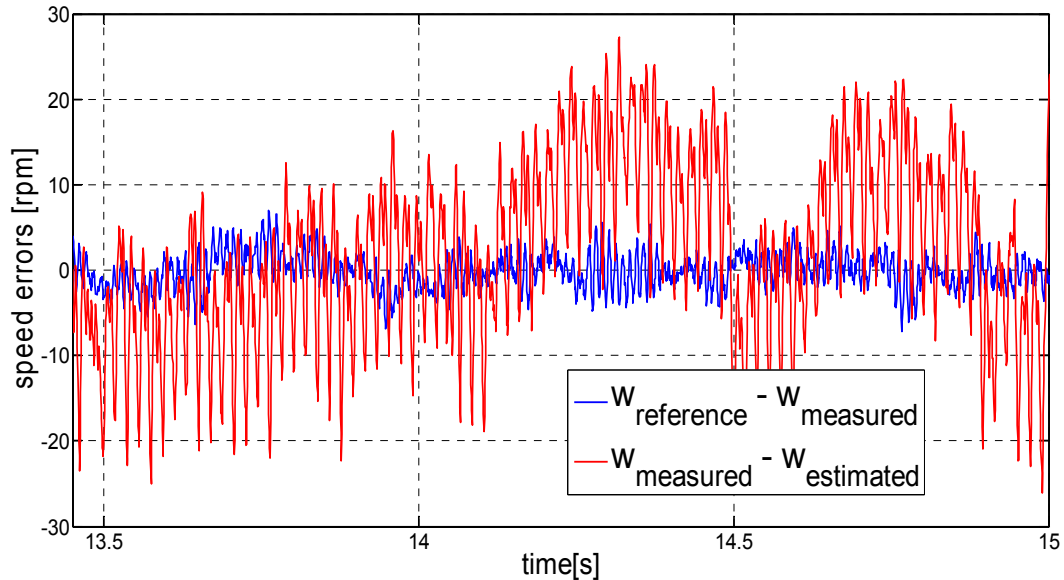


Figure 5.31. Speed errors for 800 rpm operation

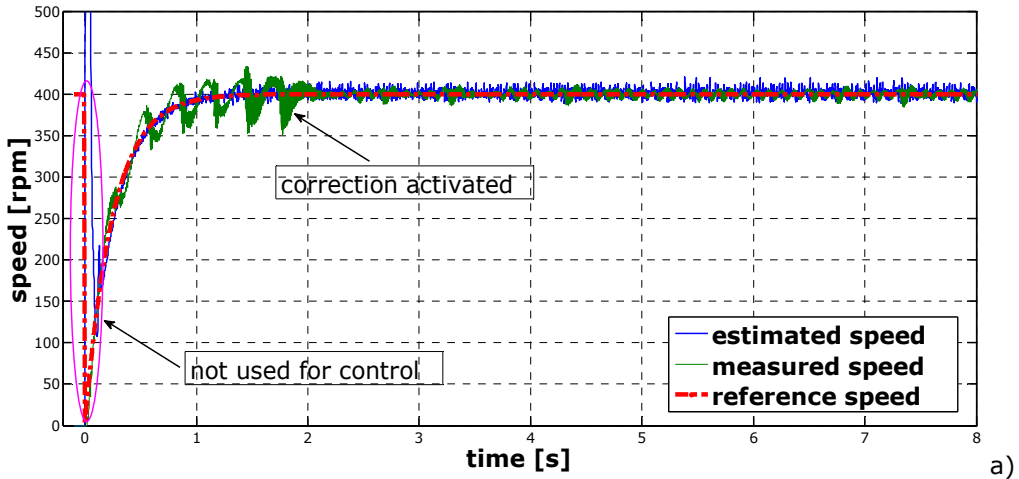
The control strategy conceived this way is based on feed-forward with correction principle. Some preliminary experimental results are presented.

5.3.9. Preliminary experimental results

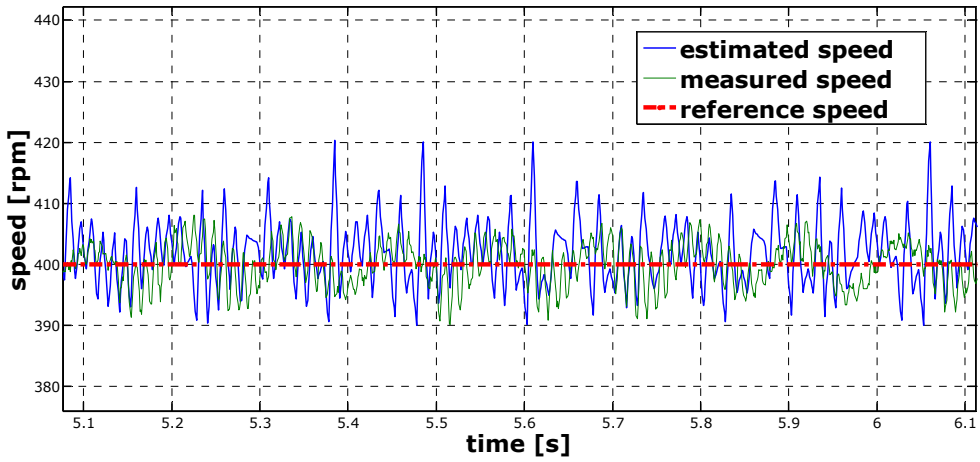
Some preliminary results for sensorless operation for the rectangular control strategy described earlier are given.

Figure 5.32 shows a start-up under 0.6 Nm load for 400 rpm required speed. The rising time (1[s]) respects the general requirement specified for this speed value. Correction was enabled after 2 seconds and its beneficial effect can be observed. The synchronization flag rises after another approximately 50[ms], and the motor runs in sensorless mode. As is was already stated, the speed estimator has problems at low speed values, for transients; that is why its output is not considered for control under 200[rpm](as one can see in Figure 5.32a). Consequently, the back-emf compensation loop is activated after 0.3 [s] to avoid bad estimation and contribute to a better dynamic response. The relative good correlation between measured and estimated speed, for steady state, can be observed in Figure 5.32b. Further improvements may be achieved if the output from the estimator is filtered carefully, without introducing too much delay in the control.

The dynamic performance in satisfactory, under given condition.



a)



b)

Figure 5.32. a)Start-up at 400 rpm, 0.6Nm load; b) zoom-in for a)

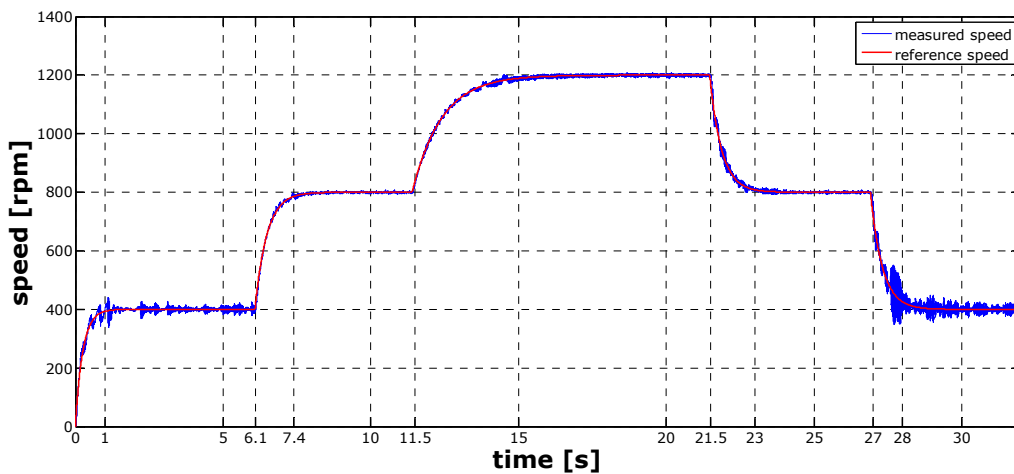


Figure 5.33. Speed step response – 400-800-1200 rpm

In Figure 5.33 the motor is started at 400 [rpm] and supplementary 400 [rpm] level speed “steps” (\pm) are required. It can be noticed that operation at 400 rpm is rather noisy compared to the motor’s operation for the other speed levels. This is not a direct consequence of the control strategy, but it is mainly due to some mechanical resonance introduced by the gear-belt coupling (the phenomena is also present under SVM control).

Rising time intervals increase once the speed required ascends. This is mainly due to the fact that the control can not assure fast dynamics. However, further improvements may be achieved for speed perturbation behaviour, if a “stronger” (though “artificial”) back-emf compensation is introduced (the back-emf constant is multiplied by a higher than one coefficient). As depicted in Figure 5.34, this measure may reduce the rising time intervals almost two times.

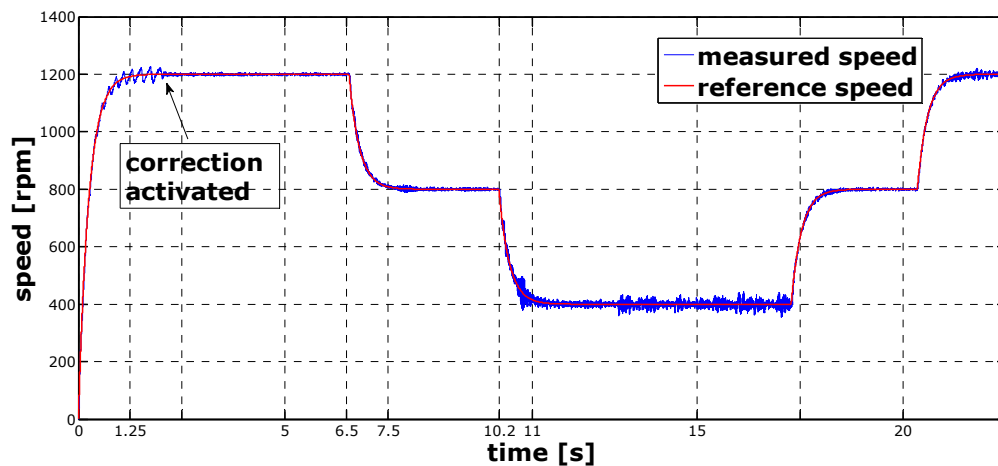


Figure 5.34. Speed response for “stronger” back-emf compensation

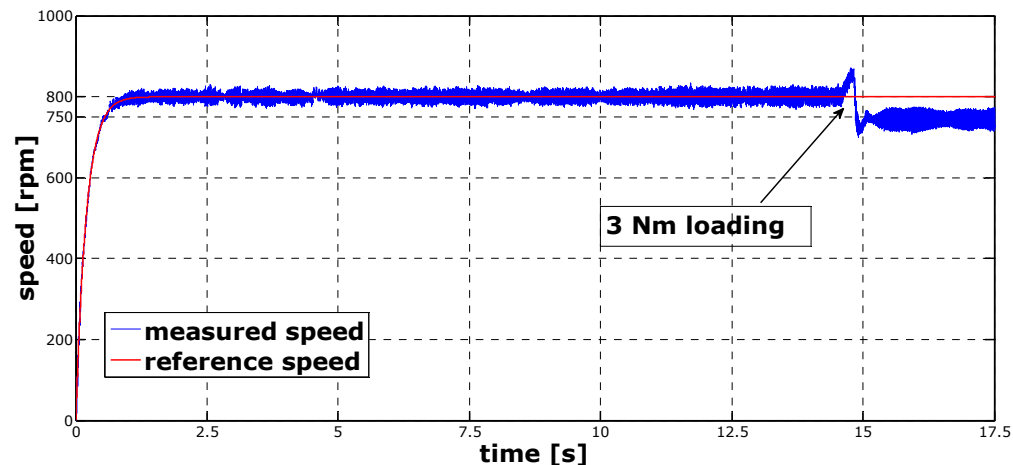


Figure 5.35. 3Nm load perturbation for 800 rpm operation

In Figure 5.35 the motor is loaded with 3Nm while running at 800 [rpm]. The current and speed controllers may be better tuned, since the motor copes with the loading (meaning that it continues running), but only with 50 rpm less than the prescribed speed. However this means only 6.25% steady state error, compared to

the 5% accepted by the application, while the experiment actually consists in a worst case scenario (maximum torque perturbation).

5.4. Conclusions

The present Chapter was focused on suitable control strategies that may be applied for the prototype designed in the first part of the thesis. Since it presented a back-EMF shape that allowed both sinusoidal and rectangular control strategies, both techniques were experimented.

The speed vector control was implemented in a sensed variant (with encoder) and was mainly used to determine experimentally the torque capability and motor efficiency. Due to limitation imposed by the driving belt coupling, the maximum speed level was set to half the rated speed (3000[rpm] out of 6000[rpm]). However, because a motion-sensorless and low cost control strategy is desired, the vector control was appreciated not to meet requirements.

On the other hand, allowed rectangular control may seem suitable. It is capable to reduce drastically drive cost since only two dc-link sensors are required. Since they are measuring non-“pulse width modulated” quantities the cost reduction is straightforward. Furthermore, it may be possible that no additional sensors for this purpose should be required. The idea of having some additional consumers on the car, supplied by a separate battery mounted on the vehicle has already overpassed the concept stage on hybrid cars. Lexus GS 4500H is equipped with such a supplementary battery, whose energy might be used either to offer more traction power, either to supply automotive consumers. The battery is also recovering energy during braking. This means that the battery status has to be monitored, since the charging while braking is intermittent.

So it may be that we could be able to utilize something that is already in the main system. However, the control strategy is applicable to restraint drive system configurations. Some preliminary experiments promise to validate the control. So far, the control performances are satisfactory for low dynamic systems (i.e the automotive air conditioning compressor drive, or similar.)

Future work is needed to fully validate the novel control concept.

References

- [5.1] D. Iles, “Automotive Permanent Magnet Actuation Technologies”, PhD Thesis, Politehnica University from Timisoara, 2005
- [5.2] Baldor – “MintDriveII Servo & Position Control”, Installation Manual, MN1901, 2010
- [5.3] Ion Boldea, S.A. Nassar, “Electric Drives – Second Edition”
- [5.4] Razvan Ancuti, Ion Boldea, Gheorghe-Daniel Andreescu, “Sensorless V/f Control of High-Speed SPMSM Drives with Two Novel Stabilizing Loops for Fast Dynamics and Robustness”, IET, 2009
- [5.5] A. Piipo, K. Suomela, M. Hinkkanen, J. Luomi,, “Sensorless PMSM Drive with DC-Link Current Measurement” IEEE Transactions on Industry Applications, 2007, pp 2371-2377
- [5.6] J. I. Itoh, N. Nomura, H. Ohsawa, “A comparison between V/f control and position-sensorless vector control for the permanent magnet synchronous

- motor", Proceedings of the IEEE International Conference on Power Conversion (PCC), 2002, pp. 1310 - 1315
- [5.7]** Shinn-Ming Sue, Tsai-Wang Hung, Jenn-Horng Liaw, Yen-Fang Li, Chen-Yu Sun, "A new MTPA control strategy for sensorless V/f controlled PMSM drives", Proceedings of the IEEE International Conference on Industrial Electronics and Applications (ICIEA), 2011, pp. 1840 - 1844
- [5.8]** L. Zhao, C. H. Ham, Q. Han, T. X. Wu, L. Zheng, K. B. Sundaram, J. Kapat, L. Chow, "Design of an optimal V/f control for a super high speed permanent magnet synchronous motor", Proceedings of the IEEE International 30th Annual Conference of Industrial Electronics Society (IECON), 2004, pp. 2260 - 2263
- [5.9]** P. D. Chandana Perera, Frede Blaabjerg, John K. Pedersen, Paul Thøgersen, "A Sensorless, Stable V/f Control Method for Permanent-Magnet Synchronous Motor Drives", Proceedings of the Seventeenth Annual IEEE Applied Power Electronics Conference and Exposition (APEC), 2002, pp. 83 - 89
- [5.10]** P. D. Chandana Perera, Frede Blaabjerg, John K. Pedersen, Paul Thøgersen, "A Sensorless, Stable V/f Control Method for Permanent-Magnet Synchronous Motor Drives", IEEE Transactions on Industry Applications, Vol. 39, No. 3, May/June 2003, pp. 783 - 791
- [5.11]** M. Kiuchi, T. Ohnishi, H. Hagiwara, Y. Yasuda, "V/f Control of Permanent Magnet Synchronous Motors suitable for Home Appliances by DCLink Peak Current Control Method", Proceedings of the IEEE International Conference on Power Electronics (IPEC), 2010, pp. 567 - 573
- [5.12]** Gheorghe-Daniel Andreescu, Cristina-Elena Coman, Ana Moldovan, Ion Boldea, "Stable V/f Control System with Unity Power Factor for PMSM Drives", Proceedings of the IEEE International Conference on Optimization of Electrical and Electronic Equipment (OPTIM), 2012, pp. 432 - 438
- [5.13]** Ion Boldea, Mihaela Codruta Paicu, Gheorghe-Daniel Andreescu, "Active Flux Concept for Motion-Sensorless Unified AC Drives", IEEE Transactions on Power Electronics, Vol. 23, No. 5, September 2008, pp. 2612 -2618
- [5.14]** Ion Boldea, Mihaela Codruta Paicu, Gheorghe Daniel Andreescu, Frede Blaabjerg, ""Active Flux" Orientation Vector Sensorless Control of IPMSM", Proceedings of the IEEE International Conference on Optimization of Electrical and Electronic Equipment (OPTIM), 2008, pp. 161 - 168
- [5.15]** Silverio Bolognani, Mauro Zigliotto, Marco Zordan, "Extended-Range PMSM Sensorless Speed Drive Based on Stochastic Filtering", IEEE transactions on Power Electronics, Vol. 16, No. 1, January 2001, pp. 110-118
- [5.16]** Janne Salomaki, Marko Hinkkanen, Jorma Luomi, "Influence of Inverter Output Filter on Maximum Torque and Speed of PMSM Drives", Proceedings of the IEEE International Power Conversion Conference (PCC), 2007, pp. 852 - 859
- [5.17]** Wang Song, Shi Shuang-shuang, Chen Chao, "Simulation of PMSM vector control system based on non-linear PID and its easy DSP realization", Proceedings of the IEEE International Control and Decision Conference (CCDC), 2009, pp. 949 - 953
- [5.18]** Tiecheng Sun, Ce Liu, Ningbo Lu, Deyan Gao, Sanling Xu, "Design of PMSM Vector Control System Based on TMS320F2812 DSP", Proceedings of the IEEE 7th International Power Electronics and Motion Control Conference (ECCE), 2012, pp. 2602 - 2606

- [5.19] Bon-Ho Bae, Seung-Ki Sul, Jeong-Hyeck Kwon, Jong-Sub Shin, "Implementation of Sensorless Vector Control for Super-High Speed PMSM of Turbo-Compressor", IEEE Transactions on Industry Applications, Volume: 39, Issue: 3, 2003, pp. 811 – 818
- [5.20] Jinbo Yang, Guijie Yang, Tiejai Li, "Low Cost Sensorless Vector Control for PMSM Compressors", Proceedings of the IEEE International Conference on Electrical Machines and Systems (ICEMS), 2008, pp. 1456 - 1459
- [5.21] Zhao Kaiqi, "The Study of Improved PI Method for PMSM Vector Control System Based On SVPWM" Proceedings of the IEEE Industry Applications Society Annual Meeting (IAS), 2011, pp. 1 – 4
- [5.22] Xiaodong Xiang, Yikang He, "Sensorless Vector Control Operation of a PMSM By Rotating High-Frequency Voltage Injection Approach", Proceeding of IEEE International Conference on Electrical Machines and Systems (ICEMS), 2007, pp. 752 – 756
- [5.23] Zhang Bingyi, Chen Xiangjun, Sun Guanggui, Feng Guihong, "A Position Sensorless Vector-control System Based on MRAS for Low Speed and High Torque PMSM Drive", Proceedings of the IEEE Eighth International Conference on Electrical Machines and Systems (ICEMS), 2005, pp. 1682 - 1686
- [5.24] Kwang-Woon Lee, Sang Bin Lee, "MTPA Operating Point Tracking Control Scheme for Vector Controlled PMSM Drives", Proceedings of the IEEE International Symposium on Power Electronics, Electrical Drives, Automation and Motion (SPEEDAM), 2010, pp. 24 – 28
- [5.25] T. Weng, Y. Inoue, S. Morimoto, M. Sanada, "Expansion of Operating Range of Sensorless PMSM Drive by Square-wave Operation at High-speed", Proceedings of the IEEE International Power Conversion Conference, (PCC), 2007, pp. 308 – 313
- [5.26] Shigeo Morimoto, Yukinori Inoue, Ting-Fei Weng, Masayuki Sanada, "Position Sensorless PMSM Drive System Including Square-wave Operation at High-speed", Proceedings of the IEEE 42nd IAS Annual Meeting Industry Applications Conference, 2007, pp. 676 - 682
- [5.27] Yan Ying, Zhu Jianguo, Guo Youguang, Lu Haiwei, "Modeling and Simulation of Direct Torque Controlled PMSM Drive System Incorporating Structural and Saturation Saliencies", Proceedings of the IEEE 41st IAS Annual Meeting Conference, 2006, pp. 76 – 83
- [5.28] Cui Jiefan, Wang Hemin, Wang Chengyuan, Wan Junzhu, Mu Gang, "Research on high performance direct torque control system based on DSP", Proceedings of the IEEE 7th World Congress on Intelligent Control and Automation, (WCICA), 2008, pp. 1494 – 1497
- [5.29] H. Soliman, M. E. Elbuluk, "Improving the Torque Ripple in DTC of PMSM Using Fuzzy Logic", Proceedings of the IEEE 43rd IAS Annual Meeting Conference, 2008, pp. 1 - 8
- [5.30] Yan Ying, Zhu Jianguo, Guo Youguang, "A Direct Torque Controlled Surface Mounted PMSM Drive with Initial Rotor Position Estimation Based on Structural and Saturation Saliencies", Proceedings of the IEEE 42nd IAS Annual Meeting Conference, 2007, pp. 683 – 689
- [5.31] M.N. Abdul Kadir, S. Mekhilef, S.; Ping Hew Wooi, "Direct Torque Control Permanent Magnet Synchronous Motor drive with asymmetrical multilevel inverter supply", Proceedings of the IEEE International Conference on Power Electronics (ICPE), 2007, pp. 1196 - 1201

- [5.32] M. Zordan, P. Vas, M. Rashed, S. Bolognani, M. Zigliotto, "Field-weakening in vector controlled and DTC PMSM drives, a comparative analysis", Proceedings of the IEEE International Conference on Power Electronics and Variable Speed Drives, 2000, pp. 493 - 499
- [5.33] C. Lascu, I. Boldea, F. Blaabjerg, "Direct torque control via feedback linearization for permanent magnet synchronous motor drives", Proceedings of the IEEE International Conference on Optimization of Electrical and Electronic Equipment (OPTIM), 2012, pp. 338 - 343
- [5.34] T.-H. Kim and M. Ehsani, "Sensorless Control of the BLDC Motors From Near- Zero to High Speeds", IEEE Transactions on Power Electronics, Vol. 19, No. 6, November 2004, pp. 1635-1645.
- [5.35] T.-H. Kim, H. W. Lee, M. Ehsani, "State of the Art and Future Trends in Position Sensorless Brushless DC Motor/Generator Drives", Proceedings of the IEEE Industrial Electronics Society Conference, 2005, pp. 1718-1725,
- [5.36] N. Muruganantham and S. Palani, "Sensorless Methods for Brushless DC Motor With Trapezoidal Back-EMF – A Survey", International Journal of Applied Engineering Research, Vol. 4, 2009.
- [5.37] D. Montesinos, S. Galceran, F. Blaabjerg, A. Sudria, O. Gomis, "Sensorless Control of PM Synchronous Motors and Brushless DC Motors - An Overview and Evaluation", Proceedings of the European Conference on. Power Electronics and Applications, 2005, pp. 1- 10.
- [5.38] J. Shao, "Direct Back EMF Detection Method for Sensorless Brushless DC (BLDC) Motor Drives", Master Thesis, Blacksburg, Virginia, 2003.
- [5.39] J. X. Shen, Z. Q. Zhu, D. Howe, "Sensorless Flux-Weakening Control of Permanent Magnet Brushless Machines Using Third-Harmonic Back-EMF", Proceedings of the IEEE International Electric Machines and Drives Conference IEMDC, 2003, Vol. 2, pp.1229-1235
- [5.40] S. Ogasawara and H. Akagi, "An Approach to Position Sensorless Drive for Brushless DC Motors," IEEE Transactions on Industrial Applications, Vol. 27, Sept./Oct. 1991, pp. 928- 933
- [5.41] G.H. Jang, J.H. Park, J.H. Chang, "Position Detection and Start-up Algorithm of A Rotor in A Sensorless BLDC Motor Utilizing Inductance Variation", Proceedings of the IEE Electric Power Applications, Vol. 149, No. 2, pp. 137-142, March 2002.
- [5.42] O. Wallmark, "Control of Permanent-Magnet Synchronous Machines in Automotive Applications", PhD Thesis, Göteborg, Sweden, 2006.
- [5.43] Z. Wu, J. Wang, J. Ying, J. Zeng, "Sensorless Brushless DC Motor Drive for Air- Conditioner Compressor", Proceedings of the IEEE Fifth International Conference on Electrical Machines and Systems (IEMDC),2001, Vol. 2, pp. 968-971
- [5.44] A. Lelkes, and M. Bufe, "BLDC Motor for Fan Application with Automatically Optimized Commutation Angle", Proceedings of the IEEE International Postsecondary Electronic Standards Council (PESC), , 2004, Vol. 3, pp. 2277-2281,2004.
- [5.45] Yen-Shin Lai, Yong-Kai Lin, "Back-EMF Detection Technique of Brushless DC Motor Drives for Wide Range Control", IEEE Transactions on Power Electronics, 2006, No. 6, pp 1006-1011
- [5.46] Yen-Shin Lai, Yong-Kai Lin, "A Unified Approach to Back-EMF Detection for Brushless DC Motor Drives without Current and Hall Sensors", IEEE Transactions on Power Electronics, 2006, No. 6, pp 1293-1298

-
- [5.47]** Y. S. Lai, F. S. Shyu, and Y. H. Chang, "Novel loss reduction pulse-width modulation technique for brushless DC motor drives fed by MOSFET inverter," *IEEE Transactions on Power Electronics*, 2004, Vol. 19, No. 6, pp. 1646-1652
- [5.48]** Genfu Zhou; Zhigan Wu; Jianping Ying, "Unattenuated BEMF detection for sensorless brushless DC (BLDC) motor drives", *Proceedings of the IEEE International 4th Power Electronics and Motion Control Conference (IPEMC)*, 2004, Volume 3, pp. 1292 – 1297
- [5.49]** A. Știrban, I. Boldea, G.-D. Andreescu, D. Iles, F. Blaabjerg "FEM Assisted Position and Speed Observer for BLDC PM Motor Drive Sensorless Control, With Experiments", *Proceedings of the IEEE EPE-PEMC Conference*, 2010, pp. 34-40

CHAPTER 6

The Experimental Test Platform

Abstract

This chapter presents the laboratory setup used for the carried out tests. The experiments were performed in the Power Electronics and Motion Control Laboratory (PEMC), Faculty of Electrical Engineering, "Politehnica" University from Timisoara.

The experimental rig wishes to test the prototype's performance and capability under the newly proposed sensorless control strategy. The loading machine delivers different load torque profiles according to the characteristic of the automotive compressor operating cycle, assuring this way appropriate laboratory testing conditions that match the final objective.

6.1. SPMSM prototype

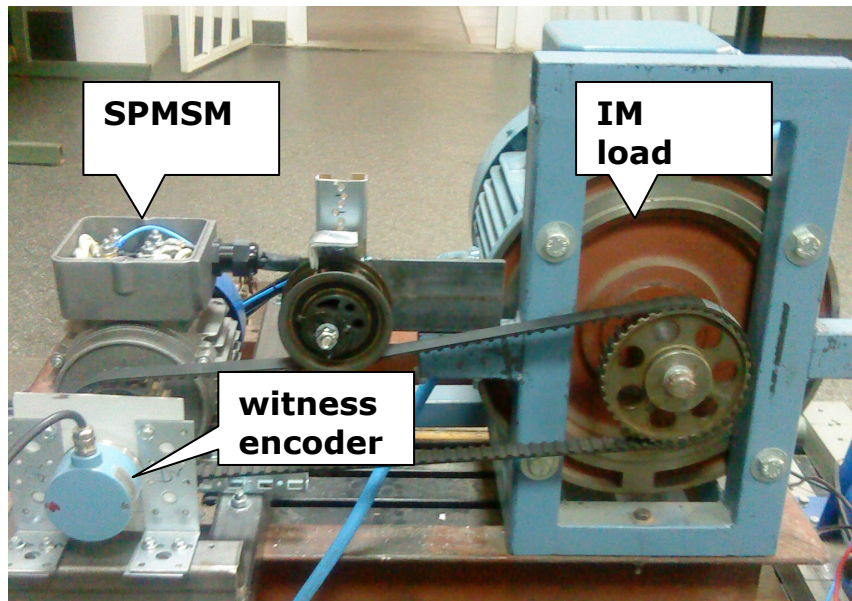


Figure 6.1. SPMSM prototype and IM loading machine on the testbench

The 6 slot/ 8 poles three phase SPMSM prototype that was designed and tested is presented in Figure 6.1 . The coupling with the loading machine was performed by a automotive gear belt and a pressure pulley. Its main parameters are listed in table 6.1.

Table 6.1. Some SPMSM parameters

Parameter	Symbol	Value	Measure unit
DC voltage	V_{dc}	50	[V]
Phase resistance	R_{ph}	4.6	[m Ω]
Phase inductance	L_{ph}	51.4	[μ H]
Phase current	I_{phase}	44.78	[A]
Base output power	P_b	2500	[W]
Rated efficiency	η	95.19	[%]
Rated copper losses	P_r	27.6	[W]
Rated iron losses	P_{cl}	86.25	[W]
Rated friction losses (bearing, windage)	P_s	12.5	[W]

6.2. IM loading machine

The induction machine used for loading purpose and speed control while the SPMSM was operating in generator mode can be observed in Figure 6.1, while its basic parameters are presented in Table 6.3

Table 6.2. IM parameters

Motor parameters	
Rated Power	5.5 [KW]
Rated Speed	2950 [rpm]
Number of pole pairs	1
Rated torque	17.5 [Nm]
Inertia	$3 e^{-4}$ [kgm ²]
Line voltage	380 [V]

6.3. ABB ACS 600

The ACS 600 frequency converter (see Figure 6.2) from ABB is used to control the loading machine presented in the previous subsection. The system was originally designed for fan and pump application; for our purpose, it serves to have a torque-controlled loading induction motor on the test bench.

The device is capable of self-tuning, if the parameters of the motor that needs to be controlled are offered. Torque profiles can be requested from the machine by easily defining the torque value and rise time.

The torque profiles that can be defined are step-torque and ramped-torque, with different dynamical constraints. These profiles match loading requirements for the compressor operating cycle application.

All these activities can be accomplished with the control panel the ACS 600 is provided with.

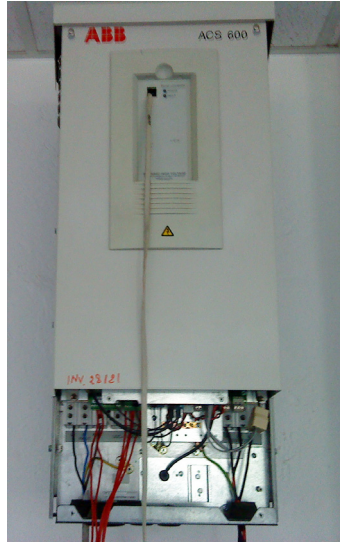



Figure 6.2. ABB ACS 600 frequency converter

6.4. Incremental encoder

A witness incremental encoder is provided for the test rig in order to have actual position and speed information. It is necessary to validate speed and sequential position observers' output, for the sensorless control. Some important characteristics for the Telemecanique XCC 1510PR50R encoder are presented in Table 6.3.

Table 6.3. Incremental encoder characteristics [2]

 XCC 1510 PR50R	Resolution	Connection method	Output stage type	Weight
	5000 points	Pre-cabled, radial	5 V, RS 422, 4.5...5.5 V	0.500 kg
Supply voltage	Maximum ripple	No-load current consumption	Protection	
5 V \pm 10 %	200 mV	100 mA	Short-circuit protection, 1 second on 1 channel	

6.5. The Supply system

The surface permanent magnet synchronous motor is powered by four automotive lead-acid batteries via a three phase inverter.

6.5.1. Lead-acid automotive batteries

For the proposed air conditioning compressor electric drive, a 42V dc bus is considered. In order to comply with this requirement, and to be as close as possible to real conditions, eventhough tests are performed on a laboratory test-rig, four automotive lead-acid batteries connected in series are used in the system (see Figure 6.3). Their characteristics are presented in Table 6.4.

Table 6.4. Battery characteristics

Manufacturer	Bosch
Voltage (100% soc)	12.75 [V]
Maximum current	420 [A]
Capacity	100 [Ah]



Figure 6.3. Series connected lead-acid Bosch automotive batteries

6.5.1. Three phase inverter

A Sauer Danfoss BPI 5818 three phase battery powered inverter is used in the system. Its interface and control board is removed and a custom-made interface board is used instead. This way, the gate driver receives the individual commands for all the six transistors in accordance to our control strategy timings and requirements. Further more optical is ensured by a specially designed PCB to ensure DS1103 safe interfacing. Figure 6.4 presents the 2 devices.

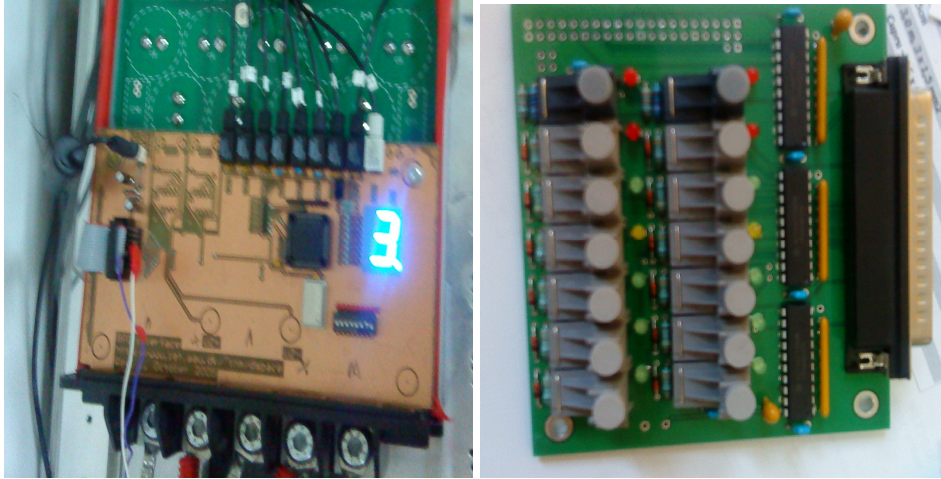


Figure 6.4. BPI inverter with custom build interface board and optic connection PCB

6.6. Sensor box

Current and voltage measurement is realized through a custom built sensor box (see Figure 6.5)

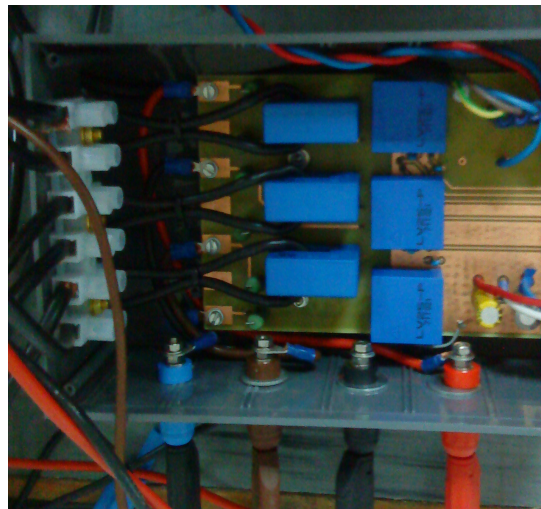


Figure 6.5. Sensors box

6.7. DS1103

The Dspace 1103 controller board is designed to meet the requirements of modern rapid control prototyping and is highly suitable for a large variety of applications. It is a very flexible and powerful tool, featuring both high

computational capability and comprehensive I/O periphery, built for real-time control system with just one controller board (Fig.6.6). DSpace 1103 has been used in all experiments in this thesis.

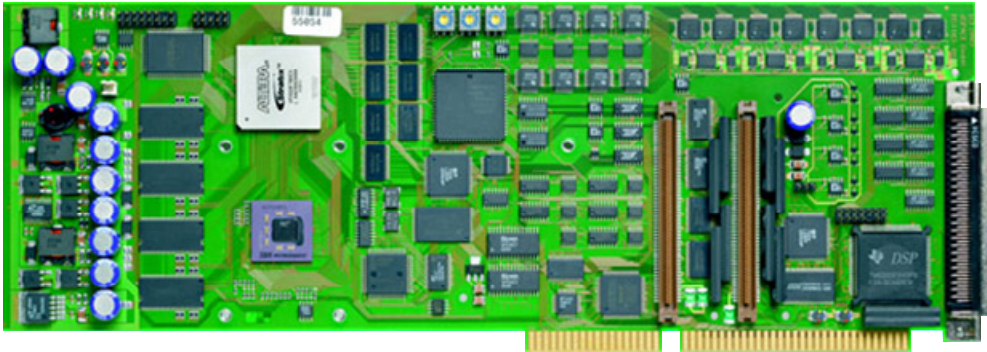


Figure 6.6. DS1103 PPC Controller Board [6.4]

Used with Real-Time Interface (RTI), the controller board is fully programmable from the Simulink® block diagram environment. The user can configure all I/O graphically by dragging RTI blocks from Matlab® libraries. This is a quick and easy way to implement your control functions on the board and also reduces the implementation time to minimum.

Some of the important features are presented below:

- Single-board system with comprehensive I/O;
- CAN interface and serial interfaces;
- Interfaces for connecting incremental encoders;
- High I/O speed and accuracy;
- PWM-synchronous or externally triggered I/O strobe;
- 32 MB application memory;
- PLL-driven UART for accurate baud rate selection.

6.8. Software

Matlab /Simulink was used for control algorithm implementation. Control Desk interface (Figure 6.7) was used because enabled on-time visualisation as well as real-time control parameter modifications.

146 CHAPTER 6 The Experimental Test Platform

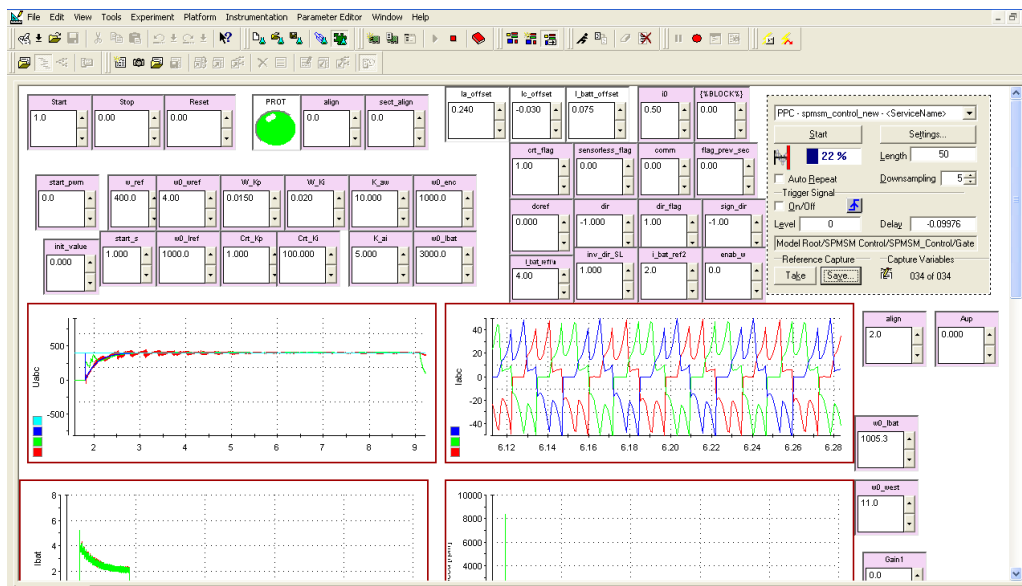


Figure 6.7. Control Desk interface

6.9. Conclusions

The experimental test platform used during torque capability and efficiency determination, as well as for sensorless control technique (based only on DC link current and voltage measurement) implementation and testing was presented in this chapter. Both hardware and software components were included

References

- [6.1] ABB ACS 600, Firmware manual
- [6.2] Schneider Electric, Telemecanique products, incremental encoders, 30502
- [6.3] R. Teodorescu, "Getting Started with dSpace System", Flexible Drives System Laboratory (FDSL) Reference Manual, Version 1.0, Institute of Energy Technology, Aalborg University, Denmark.
- [6.4] www.dspace.com.

CHAPTER 7

Conclusions and Contributions

7.1. Conclusions

The present work is dedicated to a possible solution for the electrically driven automotive air conditioning compressor. Consequently, two problems have to be solved, the electric motor design and the control strategy that should fulfil dynamic speed and torque demands under specific working cycles

The thesis focused on the following major topics:

- automotive air conditioning system description
- compressor types, operating cycles and specific requirements
- analytic electromagnetic design for a fractional, concentrated winding and less than unity slot per pole ratio SPMSM motor
- optimization design for permanent magnet synchronous machines;
- FEM inspection and validation procedure for modern electric machinery design;
- cogging torque reduction;
- existing and novel control solutions for SPMSM;

The main conclusions are:

- The automotive industry equips the modern car with a large and increasing number of electric devices. New practical and low cost solution for dedicated electric drives is intensively demanded
- For safety-critical applications, sensorless control solutions are considered only for back-up.
- Modern electric machinery design contains three stages: analytical, optimal and FEM inspection +validation stage
- Modern electric machinery design contains three stages: analytical, optimal and FEM inspection +validation stage
- There is no standard motor topology.
- The use of windings concentrated around the teeth, offer obvious advantages for the electric machines with radial air-gap. The motor configurations that implement such feature benefit from copper loss reduction due to shorter end turns and to constructive simplification. Furthermore a less than unity slot/pole ratio may structures allow further advantages related to cost and volume reduction.
- Motor design may be radically improved according to a specified objective if optimization design methods are applied
- FEM software enables us to accurately determine parameters and characteristics of any motor configuration
- Control strategies should take into account practical requirements

7.2. Contributions

The present thesis includes, from the author point of view, the following original contributions:

- An overview of automotive air conditioning system components, characteristics and requirements
- The electromagnetic design for a fractional slot concentrated winding permanent magnet synchronous machine case study: a surface permanent magnet synchronous motor with 8 rotor poles and 6 stator slots and concentrated windings fed with trapezoidal currents;
- An optimization design for the same motor topology, whose objective is to reduce initial cost and increase efficiency
- A numerical calculation of the magnetic field distribution, using a 2D Finite Element Method (FEM), was used. FEM is used to validate and to analyse the topology, determining most relevant characteristics of the machine: field distribution at no-load and at load, back-EMF at no-load, cogging torque (zero current), load torque pulsations, reluctance torque.
- A hybrid design methodology that combines all three design stages and intends to further improve motor performance by reducing cogging torque
- A novel sensorless control strategy for SPMSM topologies that present almost sinusoidal back-emf shape.
- Preliminary validation for the proposed solution

7.3. Future work

The thesis has left open the following research subjects:

- Improved hybrid design structure
- Full experimental validation for the proposed control strategy
- Stability study for the proposed control structure

APPENDIX

% This script is performing the analytic design – “analytic_calc.m”

```
error_status=0; % error status - 0 means no error
Ns=6; % no. of stator slots
Nph=3; % no. of phases
N_PM=8; % no. of rotor poles
aa=1; % no. of parallel current paths
Pb=2500; %base power [W]
fb=400; %base frequency [Hz]
csp=Np/(aa*Nph); % number of coil in series per phase
w_e=2*pi*fb; % rated angular frequency
w_m=2*pi*fn/(N_PM/2); % mechanical speed
Tb=Pb/w_m; % mechanical torque
eval(stcore); % loading the stator core features in the work space
rt_Fe=load(rtcore); % loading the rotor core features in the rt_Fe object
Hc=Hc_20*(1+(Tpm-20)*Tcbr1/100); % computing the PM coercitive field at
working temperature
mur_pm=Br_20/Hc_20/mu_0; % computing the PM relative permeability
rho1=rho_copper*(1+alpha_copper*Tw1)/(1+20*alpha_copper); % copper
resistivity at working temp.

lambda=0.7; % geometrical shape factor
f_tsp=2*e-4; % specific tangential force
Dsi_3=(2*Tb)/(lambda*pi*f_tsp); % stator inner diameter ^3
Dsi=nthroot(Dsi_3, 3)*1000; % stator inner diameter in mm
Dso=2*Dsi; % stator outer diameter
Rsi=Dsi/2; % stator inner radius
Rso=Dso/2; % stator outer radius
lstack=round(Dsi*lambda); % stack length
Nsp=Np/Nph; % no. of slots per phase
Nssp=Nsp/N_PM; % no. of slots per phase per pole
Nsm=Nssp*Nph; % no. of slots per pole
alfa_cp=Np/N_PM; % coil pole ratio
teta_p=2*pi/N_PM; % angular pole pitch
teta_s=2*pi/Np; % angular slot pitch
teta_se=pi/Nsm; % slot-pole pitch angle
tau_p=Rsi*teta_p; % pole pitch
tau_c=alfa_cp*tau_p; % coil pitch
tau_s=Rsi*teta_s; % slot pitch
ws=4; %slot opening width (mouth)
wt=tau_s-ws; % tooth width at airgap (shoe width)
kd=sin(Nssp*teta_se/2)/(Nssp*sin(teta_se/2)); % distribution factor
kp=alfa_cp; % coil-span factor
alfa_m=0.85; %magnet fraction
h_PM=3; % permanent magnet height
g=0.5; %airgap height
```

```

C_fi=2*alfa_m/(1+alfa_m); % flux concentration factor
Pc=h_PM/(g*C_fi); % permeance factor
kml=1+(4*h_PM/(pi*mu_r*alfa_m*tau_p))*log(1+pi*g/((1-alfa_m)*tau_p));
% magnet leakage factor
gc=g+h_PM/mu_r; % effective airgap for Carter coefficient calculation
kc=1/(1-1/((5*gc/ws+1)*tau_s/ws)); % Carter coefficient
Ag=tau_p*Istack*(1+alfa_m)/2; % airgap area
Bg=C_fi*Br/(1+mu_r*kc*kml/Pc); % airgap flux density
Fi_g=Bg*Ag; % airgap flux
kst=0.9; %stack filling factor
wbi=Fi_g/(2*Bmax*kst*Istack); % back-iron width (stator yoke width)
wtb=2*wbi*Nsm; %tooth width
Rsb=Rso-wbi; % slot back-iron radius
Rro=Rsi-g; % rotor outer radius
Rri=Rro-h_PM; % rotor inner radius
wsb=Rsb*teta_s-wtb; % slot bottom width
wsi=(Rsi+alfa_sd*wtb)*teta_s-wtb; % slot top width
alfa_s=wsi/(wsi+wtb); % slot fraction
ds=Rsb-Rro-g; % total slot depth
d3=ds-alfa_sd*wtb; % slot depth corresponding to conductor area
d1=alfa_sd*3*wtb/5; % tooth neck depth
d2=2*alfa_sd*wtb/5; % tooth wedge depth
As=d3*(teta_s*(Rsb-d3/2)-wtb); % conductor area
lturn=2*Istack+4*lc1+(Dso-2*wbi-2*d3/3)*pi/Nsc*asp*pi/2+(2-pi/2)*wtb; % one
turn length
alpha2=asp*pi/Ns; % radian - Geometric span angle of the stator pole
alpha1=asin(wtb/Dsi); % radian - Span angle of the body of stator pole
Rpm=Rsi-hag; % mm - Outer rotor (PM) radius
Az1=(d1+d2)*wtb/2; % mm^2 Tooth tip - partial area
Az2=(d1*(Rsi+d1/2)+d2*(Rsi+d1))*(alpha2-alpha1); % mm^2 Tooth tip - partial
area
Az3=d3*wtb/2; % mm^2 - Main tooth area
Asy=(Dso-wbi)*wbi*pi/(2*Nsc); % mm^2 - stator yoke area - corresponding to
one tooth
Acore=2*Ns*(Az1+Az2+Az3+Asy); %mm^2 - total cross core area
ksf=0.5; %slot filling factor;
mcu1=lturn*As*ksf*copper_density*1e-9; % kg - mass of one coil
mcu=Ns*mcu1; % kg - Total copper mass
mstiron=lstack*Acore*iron_density*1e-9; % kg - Stator core mass
lpm=lstack+dlpm; % mm - Total PM length
mpm=pi*hpm*(Dsi-2*g-h_PM)*h_PM*pm_density*1e-9; %kg - PM mass
mriron=pm*pi*Rr^2*iron_density*1e-9; %kg - Rotor core mass
(partial shaft mass)
mr=mpm+mriron; %kg - Rotor total mass
mst=mstiron+mcu; % kg - Active stator mass
mmotor=mst+mr; % kg - Active motor mass
lframe=lstack+2*sw1; % mm - Length of the motor frame
Aframe=pi*Dso*lframe*kff+pi/2*Dso^2; % mm^2 - Thermal equivalent frame area
Rc_1turn=rho1*lturn/(Acoil*kfill*1e-3); % Ohm - Resistance of Equivalent one turn
coil

```

```

alpha3=pi/(Ns*kc); %radian - Magnetic span angle of the stator pole
lfsy=(Dso-4*wbi/3)*0.001*pi/(2*N_PM); % m - length of magnetic field line in the
stator yoke
hry=2*Rri*sin(pi/(2*N_PM))*0.001; % m - height of magnetic rotor core
lfry=pi/2*hry; % m - length of the magnetic field line in the rotor core
lfz1=(d1+d2)*0.001; % m - length of the magnetic field line in stator tooth tip -
central part
lfz2=(alpha2-alpha1)*(Dsi/2+d1+d2)*0.001; %m - length of the mag. line in the
edge of tooth tip
lfz3=((Dso-Dsi)/2-d1-d2-2/3*wbi)*0.001; %m - length of the mag. line in the st.
tooth
Rma0=(log(Rro/Rr)+mur_pm*log(Rsi/Rro))/(mu_0*mur_pm); % PM and air-gap
reluctance
Rma1=Rma0/alpha1; % PM and air-gap partial permeance
Gma2=(min(alpha3,pi/N_PM)-alpha1)/Rma0; % PM and air-gap partial permeance
Gma3=max((alpha3-pi/N_PM),0)/Rma0; % PM and air-gap partial permeance
Gma2e=Gma2+Gma3; %equivalent
Gmsig1=mu_0*(d1/ws+d2*log(wsb/ws))/(wsb-ws); % slot leakage permeance -
top part
Gmsig2=mu_0*d3*log(wsi/wsb)/(3*(wsi-wsb)); % slot linkage permeance - main
part
Gmsig3=mu_0/pi*log(1+pi*(h_PM+g)/ws); % air-gap linkage permeance
Vpm=Hc*h_PM*0.001; % A - PM mmf

if(d3<d3_min) error_status=error_status+1; end % setting the error code
if(2*Rro<Dro_min) error_status=error_status+2; end
if(wsb<ws) error_status=error_status+4; end

% This script is performing flux and emf calculations - "flux_calc.m" - adaptation
after L. Tutelea's flux.m

fipmz=[Vpm/Rma1 Vpm*Gma2 Vpm/Rma1+Vpm*Gma2
Vpm/Rma1+Vpm*Gma2+Vpm*Gma3];
mmfn=0;
eps=1;
dfipr=[0 0 0 0];
it=20;
while((eps>0.005)& it)
    Bz11=fipmz(1)/(0.0005*wtb);
    Bz12=(fipmz(1)+0.5*fipmz(2))/(0.0005*wtb);
    Bz13=fipmz(3)/(0.0005*wtb);
    Bsy=fipmz(3)/(0.001*wbi);
    Bz23=fipmz(2)/(d1+d2)*1000;
    Bry=fipmz(4)/hry;
    Hsx=getHx(Bref,Href,[Bz11,Bz12,Bz13,Bz23,Bsy]);
    Hrx=getHx(rt_Fe(:,1),rt_Fe(:,2),Bry);
    Rmz1=(Hsx(1)+4*Hsx(2)+Hsx(3))*lfz1/(6*fipmz(1));
    Gmz2=fipmz(2)/(Hsx(4)*lfz2);
    Rmz3=Hsx(3)*lfz3/fipmz(3);
    Rmsy=Hsx(5)*lfsy/fipmz(3);
    Gmry=(fipmz(1)+fipmz(2))/(Hrx*lfry);

```

```

Gm13=1/(Rma1+Rmz1);
Gm30=1/(Rmz3+Rmsy);
Am=[Gmry+Gma2e+Gm13 -Gma2e -Gm13;
-Gma2e Gma2e+Gmsig1+Gmz2 -Gmz2;
-Gm13 -Gmz2 Gm13+Gmz2+Gm30+Gmsig2;];
Bm=[-Gm13 -Gma2 -Gma3 0; 0 Gma2 Gma3 0;Gm13 0 0 Gm30];
Em=[Vpm Vpm -Vpm mmfn]';
Vm=Am\(Bm*Em);
fipmold=fipmz;
fipmz=[(Vm(1)-Vm(3)+Vpm)*Gm13 (Vm(2)-Vm(3))*Gmz2 (Vm(3)-
Em(4))*Gm30 -Vm(1)*Gmry];
dfipr_old=dfipr;
dfipr=(fipmz-fipmold)./fipmz;
iv=find(dfipr.*dfipr_old<0);
fipmz(iv)=0.7*fipmold(iv)+0.3*fipmz(iv);
eps=norm(dfipr);
it=it-1;
end
fipm=2*fipmz(3)*lstack*0.001;
E_1turn=2*pi*fn*fipm;
mmfn=2*Pem_n/(3*csp*E_1turn)/ktav;
Bst(1,:)=[Bz11 Bz12 Bz13 Bz23 Bsy];
eps=1;
dfipr=[0 0 0 0];
it=20;
while((eps>0.005)&it)
Bz11=fipmz(1)/(0.0005*wtb);
Bz12=(fipmz(1)+0.5*fipmz(2))/(0.0005*wtb);
Bz13=fipmz(3)/(0.0005*wtb);
Bsy=fipmz(3)/(0.001*d3);
Bz23=fipmz(2)/(d1+d2)*1000;
Bry=fipmz(4)/hry;
Hsx=getHx(Bref,Href,[Bz11,Bz12,Bz13,Bz23,Bsy]);
Hrx=getHx(rt_Fe(:,1),rt_Fe(:,2),Bry);
Rmz1=(Hsx(1)+4*Hsx(2)+Hsx(3))*lfz1/(6*fipmz(1));
Gmz2=fipmz(2)/(Hsx(4)*lfz2);
Rmz3=Hsx(3)*lfz3/fipmz(3);
Rmsy=Hsx(5)*lfy/fipmz(3);
Gmry=(fipmz(1)+fipmz(2))/(Hrx*lfry);
Gm13=1/(Rma1+Rmz1);
Gm30=1/(Rmz3+Rmsy);
Am=[Gmry+Gma2+Gm13+Gma3 -Gma2 -Gm13;
-Gma2 Gma2+Gmsig1+Gmz2 -Gmz2;
-Gm13 -Gmz2 Gm13+Gmz2+Gm30+Gmsig2;];
Bm=[-Gm13 -Gma2 -Gma3 0; Gma2 0 0 0;Gm13 0 0 Gm30];
Em=[Vpm Vpm Vpm mmfn]';
Vm=Am\(Bm*Em);
fipmold=fipmz;
fipmz=[(Vm(1)-Vm(3)+Vpm)*Gm13 (Vm(2)-Vm(3))*Gmz2 (Vm(3)-
Em(4))*Gm30 -Vm(1)*Gmry];
dfipr_old=dfipr;

```



```

dfipr=(fipmz-fipmold)./fipmz;
iv=find(dfipr.*dfipr_old<0);
fipmz(iv)=0.7*fipmold(iv)+0.3*fipmz(iv);
eps=norm(dfipr);
it=it-1;
end
fipp=2*fipmz(3)*lstack*0.001;
mmfn=-mmfn;
eps=1;
Bst(2,:)=[Bz11 Bz12 Bz13 Bz23 Bsy];
dfipr=[0 0 0 0];
it=20;
while((eps>0.005)&it)
    Bz11=fipmz(1)/(0.0005*wtb);
    Bz12=(fipmz(1)+0.5*fipmz(2))/(0.0005*wtb);
    Bz13=fipmz(3)/(0.0005*wtb);
    Bsy=fipmz(3)/(0.001*wsy);
    Bz23=fipmz(2)/(d1+d2)*1000;
    Bry=fipmz(4)/hry;
    Hsx=getHx(Bref,Href,[Bz11,Bz12,Bz13,Bz23,Bsy]);
    Hrx=getHx(rt_Fe(:,1),rt_Fe(:,2),Bry);
    Rmz1=(Hsx(1)+4*Hsx(2)+Hsx(3))*lfz1/(6*fipmz(1));
    Gmz2=fipmz(2)/(Hsx(4)*lfz2);
    Rmz3=Hsx(3)*lfz3/fipmz(3);
    Rmsy=Hsx(5)*lfsy/fipmz(3);
    Gmry=(fipmz(1)+fipmz(2))/(Hrx*lfry);
    Gm13=1/(Rma1+Rmz1);
    Gm30=1/(Rmz3+Rmsy);
    Am=[Gmry+Gma2+Gm13+Gma3 -Gma2 -Gm13;
        -Gma2 Gma2+Gmsig1+Gmz2 -Gmz2;
        -Gm13 -Gmz2 Gm13+Gmz2+Gm30+Gmsig2;];
    Bm=[-Gm13 -Gma2 -Gma3 0; Gma2 0 0 0;Gm13 0 0 Gm30];
    Em=[Vpm Vpm Vpm mmfn]';
    Vm=Am\(Bm*Em);
    fipmold=fipmz;
    fipmz=[(Vm(1)-Vm(3)+Vpm)*Gm13 (Vm(2)-Vm(3))*Gmz2 (Vm(3)-
Em(4))*Gm30 -Vm(1)*Gmry];
    dfipr_old=dfipr;
    dfipr=(fipmz-fipmold)./fipmz;
    iv=find(dfipr.*dfipr_old<0);
    fipmz(iv)=0.7*fipmold(iv)+0.3*fipmz(iv);
    eps=norm(dfipr);
    it=it-1;
end
fipn=2*fipmz(3)*lstack*0.001;
ktrsat=(fipn+fipp)/(2*fipm);
Lc1turn=(fipp-fipn)/(2*mmfn)+2*lstack*0.001*(Gmsig1+Gmsig2+Gmsig3);
mmfn=Pem_n/(pi*fipm*fn*Nsc)/(ktav);
Bst(3,:)=[Bz11 Bz12 Bz13 Bz23 Bsy];
Bstm=max(Bst);
Pcu=0.5*Ns*Rc_1turn*mmfn^2;

```

```

N1=round(2/pi*Vdc/(csp*sqrt((E_1turn+Rc_1turn*mmfn)^2+(w_e*Lc1turn*mmfn)^2)));
B1med=sqrt(((Bstm(1)^2+4*Bstm(2)^2+Bstm(3)^2)*Az1/6+Bstm(4)^2*Az2+...
Bstm(3)^2*Az3+Bstm(5)^2*Asy)/(Az1+Az2+Az3+Asy));
Pfe=kpfe*pfe1t400Hz*((B1med*fn/400)^2)*mstiron;
In=mmfn/(N1*sqrt(2))*aa;
etan=Pn/(Pn+Pcu+Pfe+Pmec)
eta1=Pn*n1_pu/(Pn*n1_pu+Pcu/n1_pu^2+Pfe*n1_pu^2+Pmec);
Rs=Rc_1turn*N1^2*csp/aa;
Ls=Lc1turn*N1^2*csp/aa;
qw=Acoil*kfill/N1; dcu=2*sqrt(qw/pi);
Tw=(Pcu+Pfe)/(alpha_t*Aframe*1e-6)+Tamb;

```

% This script is performing the cost calculation – “cost_calc.m” – L. Tutelea

```
f(error_status~=0)
```

```

t_cost=2*fob(1); % Unusual geometry (negative dimension) are not eligible solutions.

```

```
else
```

```
cu_c=cu_pr*mcu; %USD copper cost
```

```
lam_c=lam_pr*mstiron; %USD lamination cost
```

```
PM_c=PM_pr*mpm; %USD PM cost
```

```
rotIron_c=mr*rotIron_pr; %Usd Rotor iron cost
```

```
pmw_c=pmw_pr*mmotor; %USD passive material cost
```

```
i_cost=cu_c+lam_c+PM_c+rotIron_c+pmw_c; %USD initial cost
```

```
if(exist('eta_min','var'))
```

```
energy_c=energy_pr*Pn*(n1_pu*kn1*max(0,(1/eta1-1/eta_min))+...
```

```
(1-kn1)*max(0,(1/etan-1/eta_min)))/1000*hpy*ny; %USD/kWh only over
```

```
energy cost
```

```
else
```

```
energy_c=energy_pr*Pn*(1/etan-1)/1000*hpy*ny; %USD/kWh energy price
```

```
end
```

```
temp_cost=max(0,(Tw-Tw_max)*kct*i_cost);
```

```
t_cost=i_cost+energy_c+temp_cost; %USD total cost
```

```
end
```

% This script is performing the optimization design design – “optim_calc.m” – adaptation after L.Tutelea’s optim_eval.m

```
Var0=[Dsi Dso d1 d2 wbi wtb g h_PM lstack ws]; % initial optimization variable set
```

```
%down bounded of optimization variable
```

```
Var_low=[Dsi_min Dso_min d1_min d2_min wbi_min wtb_min g_min h_PM_min
```

```
lstack_min ws_min];
```

```
%up boundet of optimization variable
```

```
Var_up=[Dsi_max Dso_max d1_max d2_max wbi_max wtb_max g_max h_PM_max
```

```
lstack_max ws_max];
```

```
dVar=dd1; % variable variation
```

```
nVar=length(Var0); % number of optimisation variable
```

```

fob(1)=t_cost;    % objective function
i_trace=1;
opt_trace=[Var0,fob(1),Pcu,Pfe,etan,mpm,mmotor];
sdf=1;
while sdf>0
    for ii=1:nVar    % evaluate objective function in 2*nVar direction
        Varo=Var0;
        Varo(ii)=Var0(ii)+dVar;
        iup=find(Varo>Var_up);
        Varo(iup)=Var_up(iup);
        [Dsi Dso d1 d2 wbi wtb g h_PM lstack ws]=alias(Varo,Ns);
        secDims;
        flux;
        cost_eval;
        fob(2*ii)=t_cost;
        sr_trace(2*ii,:)= [Pcu, Pfe, etan, mpm, mmotor];
        dpf(ii)=fob(1)-fob(2*ii);
        Varo=Var0;
        Varo(ii)=Var0(ii)-dVar;
        ilow=find(Varo<Var_low);
        Varo(ilow)=Var_low(ilow);
        [Dsi Dso d1 d2 wbi wtb g h_PM lstack ws]=alias(Varo,Ns);
        secDims;
        flux;
        cost_eval;
        fob(2*ii+1)=t_cost;
        sr_trace(2*ii+1,:)= [Pcu, Pfe, etan, mpm, mmotor];
        dnf(ii)=fob(1)-fob(2*ii+1);
    end
    df=max(dpf,dnf); % chose the maximum variation of obj. func.
    df=max(df,0);    % keep the element of obj. func. variation at minimum zero
level
    sdf=sum(df);    % sum of partial derivative obj. func =0 are stopping the
search
    if sdf>0
        sdV=ones(size(df));
        in=find(df==dnf); % find the negative variation which produces desired obj.
func.
        sdV(in)=-1;
        dVar2=sdV.*df.*dVar/norm(df);%through direction in the optimization variable
space
        [dfm im]=max(df);
        Vars=Var0;
        Vars(im)=min(max(Var0(im)+sdV(im)*dVar,Var_low(im)),Var_up(im)); % a
better value of optimization variable set
        i_trace=i_trace+1;
        opt_trace(i_trace,:)= [Vars,fob(1)-dfm,sr_trace((2*im-min(0,sdV(im))),:));

        fobmin=fob(1)-dfm; %minimum obj. func. for optimisation search in the
through
        dds=1

```

```

while dds==1      % search loop in the through direction
    Varo=Var0+dVar2;
    ilow=find(Varo<Var_low);
    Varo(ilow)=Var_low(ilow);
    iup=find(Varo>Var_up);
    Varo(iup)=Var_up(iup);
    [Dsi Dso d1 d2 wbi wtb g h_PM lstack ws]=alias(Varo,Nsc);
    secDims;
    flux;
    fob2=t_cost;
    if(fob2<fobmin)
        fobmin=fob2
        fob(1)=fob2;
        Vars=Varo;
        i_trace=i_trace+1;
        opt_trace(i_trace,:)=[Vars,fob(1),Pcu,Pfe,etan,mpm,mmotor];
    else
        dds=0; %the obj. func. through direction is changed
    end
    Var0=Vars;
end
fob(1)=fobmin;
else
    if(dVar-d2)
        dVar=max(dVar/ropt,dd2); % update the variable variation step
        sdf=1; %let the main loop to continue objective serch with small step
    end
end
end
Varst=dd2*round(opt_trace(end,1:10)/dd2); %round the optimised variable at
technological tolerance
[Dsi Dso d1 d2 wbi wtb g h_PM lstack ws]=alias(Varst,Nsc);

analytic_calc;
flux_calc;
cost_calc;

%evaluate the geometry with FEM

openfemm;
newdocument(0);
mi_probdef(0,'millimeters','planar',1e-008,lstack,22);

% mi_addmaterial('matname', mu_x, mu_y, H_c, J, Cduct, Lam_d, Phi_hmax,
lam_fill, LamType, Phi_hx, Phi_hy, nstr, dwire)
mi_addmaterial('Air',1,1,0,0,0,0,1,0,0,0,0);
mi_addmaterial('Copper',1,1,0,0,58,0,0,1,3,0,0,1,10.32);
mi_addmaterial('NdFeB',1.018,1.018,880000,0,0.667,0,0,1,0,0,0,0);
mi_addmaterial('M800-50A',4400,4400,0,0,4.35,0.35,20,1,0,0,0,0);

```

```

Im=45;
I=Im;
iaf=0;
ibf=0; % -I;
icf=0; % I;
% mi_addcircprop('circuitname', i, circuittype)
mi_addcircprop('ia',iaf,1);
mi_addcircprop('ib',ibf,1);
mi_addcircprop('ic',icf,1);
% mi_addboundprop('propname', A0, A1, A2, Phi, Mu, Sig, c0, c1, BdryFormat)
mi_addboundprop('zero',0,0,0,0,0,0,0,0,0);
% Draw stator-geometry

mi_hidegrid;

% ALL GEOMETRICAL DIMENSIONS ARE IN MILLIMETERS %

N_PM=8;      % number of poles
p=N_PM/2;    % number of pole pairs
nslot=Ns;

rad=pi/180;

% Stator geometry

fid=fopen('SPMSM_eval.txt','wt');

alfnp=2*pi/N_PM; % angle due to the pole number
alfrg=(pi-alfnp)/2; % half angle between 2 consecutive sides of an 2p-gon
tPM=(pi*Dri)/(2*p); %
nc=N1; % number of turns per coil

% boundary

a=3*Dso/5;
mi_zoom(-a,-a,a,a);

mi_addnode(-a,a);
mi_selectnode(-a,a);
mi_setnodeprop('None',20);
mi_clearselected();

mi_addnode(-a,-a);
mi_selectnode(-a,-a);
mi_setnodeprop('None',20);
mi_clearselected();

mi_addnode(a,-a);
mi_selectnode(a,-a);

```

```
mi_setnodeprop('None',20);
mi_clearselected();

mi_addnode(a,a);
mi_selectnode(a,a);
mi_setnodeprop('None',20);
mi_clearselected();

mi_addsegment(-a,a,-a,-a);
mi_selectsegment(-a,0);
mi_setsegmentprop('zero',0,1,0,20);
% mi_setsegmentprop('proprname', elementsize, automesh, hide, group)
mi_clearselected();

mi_addsegment(-a,a,a,a);
mi_selectsegment(0,a);
mi_setsegmentprop('zero',0,1,0,20);
mi_clearselected();

mi_addsegment(a,a,a,-a);
mi_selectsegment(a,0);
mi_setsegmentprop('zero',0,1,0,20);
mi_clearselected();

mi_addsegment(a,-a,-a,-a);
mi_selectsegment(0,-a);
mi_setsegmentprop('zero',0,1,0,20);
mi_clearselected();

% end boundary
mi_addnode(-Dso/2,0);
mi_selectnode(-Dso/2,0);
mi_setnodeprop('None',1);
mi_clearselected();

mi_addnode(Dso/2,0);
mi_selectnode(Dso/2,0);
mi_setnodeprop('None',1);
mi_clearselected();

mi_addarc(-Dso/2,0,Dso/2,0,180,5);
mi_selectarcsegment(0,-Dso/2);
mi_setarcsegmentprop(5,'None',0,1);
mi_selectarcsegment(0,-Dso/2);
mi_setarcsegmentprop(5,'None',0,1);

mi_clearselected();

mi_addarc(Dso/2,0,-Dso/2,0,180,5);
mi_selectarcsegment(0,Dso);
mi_setarcsegmentprop(5,'None',0,1);
```

```

mi_clearselected();

alfsp=2*pi*asp/Ns;
alfbso=asin(ws/Dsi);
alfgo=alfsp+alfbso;
alfbt=asin((wtb/2)/(d1+d2+Dsi/2));
alfup=asin((wtb/2)/(Dso/2-wbi));

Rsi=Dsi/2;
Rs_bottom=Dsi/2+d1+d2;
Rys=Dso/2-wbi;
Rs=Dso/2;
alf=pi/2;

for i=1:ns

    alfst(1)=alf-alfsp/2;           % against x-axis

    xst(1,i)=Rsi*cos(alfst(1));
    yst(1,i)=Rsi*sin(alfst(1));
    mi_addnode(xst(1,i),yst(1,i)); % node: xst(1,i),yst(1,i)
    mi_selectnode(xst(1,i),yst(1,i));
    mi_setnodeprop('None',1);
    mi_clearselected();

    alfst(2)=alf+alfsp/2;

    xst(2,i)=Rsi*cos(alfst(2));
    yst(2,i)=Rsi*sin(alfst(2));
    mi_addnode(xst(2,i),yst(2,i)); % node: xst(2,i),yst(2,i)
    mi_selectnode(xst(2,i),yst(2,i));
    mi_setnodeprop('None',1);
    mi_clearselected();

    mi_addarc(xst(1,i),yst(1,i),xst(2,i),yst(2,i),rad2deg(alfsp),5);
    mi_selectarcsegment((xst(1,i)+xst(2,i))/2,(yst(1,i)+yst(2,i))/2);
    mi_setarcsegmentprop(5,'None',0,1);
    mi_clearselected();

    alfst(3)=alfst(2);

    xst(3,i)=(Rsi+sh4)*cos(alfst(3));
    yst(3,i)=(Rsi+sh4)*sin(alfst(3));
    mi_addnode(xst(3,i),yst(3,i)); % node: xst(3,i),yst(3,i)
    mi_selectnode(xst(3,i),yst(3,i));
    mi_setnodeprop('None',1);
    mi_clearselected();

    mi_addsegment(xst(2,i),yst(2,i),xst(3,i),yst(3,i));
    mi_selectsegment((xst(2,i)+xst(3,i))/2,(yst(2,i)+yst(3,i))/2);

```

```
mi_setsegmentprop('None',0,1,0,1);
mi_clearselected();

alfst(4)=alf+alfbt;

xst(4,i)=Rs_bottom*cos(alfst(4));
yst(4,i)=Rs_bottom*sin(alfst(4));
mi_addnode(xst(4,i),yst(4,i));    % node: xst(4,i),yst(4,i)
mi_selectnode(xst(4,i),yst(4,i));
mi_setnodeprop('None',1);
mi_clearselected();

mi_addarc(xst(4,i),yst(4,i),xst(3,i),yst(3,i),rad2deg(alfsp/2-alfbt),5);
mi_selectarcsegment((xst(4,i)+xst(3,i))/2,(yst(4,i)+yst(3,i))/2);
mi_setarcsegmentprop(5,'None',0,1);
mi_clearselected();

alfst(5)=alf+alfup;

xst(5,i)=Rys*cos(alfst(5));
yst(5,i)=Rys*sin(alfst(5));
mi_addnode(xst(5,i),yst(5,i));    % node: xst(5,i),yst(5,i)
mi_selectnode(xst(5,i),yst(5,i));
mi_setnodeprop('None',1);
mi_clearselected();

mi_addsegment(xst(4,i),yst(4,i),xst(5,i),yst(5,i));
mi_selectsegment((xst(4,i)+xst(5,i))/2,(yst(4,i)+yst(5,i))/2);
mi_setsegmentprop('None',0,1,0,1);
mi_clearselected();

alfst(6)=alf+alfsp/2;

xst(6,i)=Rys*cos(alfst(6));
yst(6,i)=Rys*sin(alfst(6));
mi_addnode(xst(6,i),yst(6,i));    % node: xst(6,i),yst(6,i)
mi_selectnode(xst(6,i),yst(6,i));
mi_setnodeprop('None',1);
mi_clearselected();

mi_addarc(xst(5,i),yst(5,i),xst(6,i),yst(6,i),rad2deg(alfsp/2-alfbt),5);
mi_selectarcsegment((xst(5,i)+xst(6,i))/2,(yst(5,i)+yst(6,i))/2);
mi_setarcsegmentprop(5,'None',0,1);
mi_clearselected();

mi_addsegment(xst(3,i),yst(3,i),xst(6,i),yst(6,i));
mi_selectsegment((xst(3,i)+xst(6,i))/2,(yst(3,i)+yst(6,i))/2);
mi_setsegmentprop('None',0,1,0,1);
mi_clearselected();
```



```
alfst(8)=alf-alfsp/2;

xst(8,i)=(Rsi+sh4)*cos(alfst(8));
yst(8,i)=(Rsi+sh4)*sin(alfst(8));
mi_addnode(xst(8,i),yst(8,i));    % node: xst(8,i),yst(8,i)
mi_selectnode(xst(8,i),yst(8,i));
mi_setnodeprop('None',1);
mi_clearselected();

mi_addsegment(xst(1,i),yst(1,i),xst(8,i),yst(8,i));
mi_selectsegment((xst(1,i)+xst(8,i))/2,(yst(1,i)+yst(8,i))/2);
mi_setsegmentprop('None',0,1,0,1);
mi_clearselected();

alfst(9)=alf-alfbt;

xst(9,i)=Rs_bottom*cos(alfst(9));
yst(9,i)=Rs_bottom*sin(alfst(9));
mi_addnode(xst(9,i),yst(9,i));    % node: xst(9,i),yst(9,i)
mi_selectnode(xst(9,i),yst(9,i));
mi_setnodeprop('None',1);
mi_clearselected();

mi_addarc(xst(8,i),yst(8,i),xst(9,i),yst(9,i),rad2deg(alfsp/2-alfbt),5);
mi_selectarcsegment((xst(8,i)+xst(9,i))/2,(yst(8,i)+yst(9,i))/2);
mi_setarcsegmentprop(5,'None',0,1);
mi_clearselected();

alfst(10)=alf-alfup;

xst(10,i)=Rys*cos(alfst(10));
yst(10,i)=Rys*sin(alfst(10));
mi_addnode(xst(10,i),yst(10,i));    % node: xst(10,i),yst(10,i)
mi_selectnode(xst(10,i),yst(10,i));
mi_setnodeprop('None',1);
mi_clearselected();

mi_addsegment(xst(9,i),yst(9,i),xst(10,i),yst(10,i));
mi_selectsegment((xst(9,i)+xst(10,i))/2,(yst(9,i)+yst(10,i))/2);
mi_setsegmentprop('None',0,1,0,1);
mi_clearselected();

alfst(11)=alf-alfsp/2;

xst(11,i)=Rys*cos(alfst(11));
yst(11,i)=Rys*sin(alfst(11));
mi_addnode(xst(11,i),yst(11,i));    % node: xst(11,i),yst(11,i)
mi_selectnode(xst(11,i),yst(11,i));
```

```

mi_setnodeprop('None',1);
mi_clearselected();

mi_addarc(xst(11,i),yst(11,i),xst(10,i),yst(10,i),rad2deg(alfsp/2-alfbt),5);
mi_selectarcsegment((xst(10,i)+xst(11,i))/2,(yst(10,i)+yst(11,i))/2);
mi_setarcsegmentprop(5,'None',0,1);
mi_clearselected();

mi_addsegment(xst(8,i),yst(8,i),xst(11,i),yst(11,i));
mi_selectsegment((xst(8,i)+xst(11,i))/2,(yst(8,i)+yst(11,i))/2);
mi_setsegmentprop('None',0,1,0,1);
mi_clearselected();

if (i==1)

mi_addblocklabel(Rys*cos((alfst(5)+alfst(10))/2),Rys*sin((alfst(5)+alfst(10))/2));

mi_selectlabel(Rys*cos((alfst(5)+alfst(10))/2),Rys*sin((alfst(5)+alfst(10))/2));
    mi_setblockprop('M800-50A',0,1,0,0,1,0);
    mi_clearselected();
end

    alf=alf+pi/3;

end

alfss=2*asin(ws/(2*Rys));

for j=1:11
    xst(j,ns+1)=xst(j,1);
    yst(j,ns+1)=yst(j,1);
end

for i=1:ns
    mi_addarc(xst(6,i),yst(6,i),xst(11,i+1),yst(11,i+1),rad2deg(alfss),5);
    mi_selectarcsegment((xst(6,i)+xst(11,i+1))/2,(yst(6,i)+yst(11,i+1))/2);
    mi_setarcsegmentprop(5,'None',0,1);
    mi_clearselected();

    mi_addarc(xst(2,i),yst(2,i),xst(1,i+1),yst(1,i+1),rad2deg(alfss),5);
    mi_selectarcsegment((xst(2,i)+xst(1,i+1))/2,(yst(2,i)+yst(1,i+1))/2);
    mi_setarcsegmentprop(5,'None',0,1);
    mi_clearselected();
end

Rss=Dsi/2+sh1/3;
alfss=pi/2+alfsp/2+alfbso/2;

for i=1:ns
xsts(i)=Rss*cos(alfss);
ysts(i)=Rss*sin(alfss);

```

```

mi_addblocklabel(xsts(i),ysts(i));
mi_selectlabel(xsts(i),ysts(i));
mi_setblockprop('Air',0,1,0,0,7,0);
mi_clearselected();
alfss=alfss+pi/3;
end

% winding definition
j=1;
while (j<=ns)
  for i=0:(2*m-1)
    mi_addblocklabel((xst(4,j)+xst(6,j))/2,(yst(4,j)+yst(6,j))/2);
    mi_selectlabel((xst(4,j)+xst(6,j))/2,(yst(4,j)+yst(6,j))/2);

    if (mod(i,2*m)==0||mod(i,2*m)==3)
      mi_setblockprop('Copper',0,5,'ia' ,0,2,nc);
      %
mi_setblockprop("blockname",automesh,meshsize,"incircuit",magdirection,group,
turns)
    end
    if (mod(i,2*m)==1||mod(i,2*m)==4)
      mi_setblockprop('Copper',0,5,'ib',0,3,nc);
    end
    if (mod(i,2*m)==2||mod(i,2*m)==5)
      mi_setblockprop('Copper',0,5,'ic',0,4,nc);
    end
    mi_clearselected();

    j=j+1;
  end
end

j=1;
while (j<=ns)

  for i=0:(2*m-1)
    mi_addblocklabel((xst(9,j)+xst(11,j))/2,(yst(9,j)+yst(11,j))/2);
    mi_selectlabel((xst(9,j)+xst(11,j))/2,(yst(9,j)+yst(11,j))/2);

    if (mod(i,2*m)==0||mod(i,2*m)==3)
      mi_setblockprop('Copper',0,5,'ia' ,0,12,-nc);
      %
mi_setblockprop("blockname",automesh,meshsize,"incircuit",magdirection,group,
turns)
    end
    if (mod(i,2*m)==1||mod(i,2*m)==4)
      mi_setblockprop('Copper',0,5,'ib',0,13,-nc);
    end
    if (mod(i,2*m)==2||mod(i,2*m)==5)
      mi_setblockprop('Copper',0,5,'ic',0,14,-nc);
    end
  end
end

```

```

mi_clearselected();

j=j+1;
end
end

%draw nodes for flux linkage
for i=1:(2*m)
if mod(i,2*m)==1
xPsia1=(xst(4,i)+xst(5,i))/2;
yPsia1=(yst(4,i)+yst(5,i))/2;
mi_addnode(xPsia1,yPsia1); % xPsia1yPsia1
mi_selectnode(xPsia1,yPsia1);
mi_setnodeprop('None',1);
mi_clearselected();

xPsia2=(xst(9,i)+xst(10,i))/2;
yPsia2=(yst(9,i)+yst(10,i))/2;
mi_addnode(xPsia2,yPsia2); % xPsia2yPsia2
mi_selectnode(xPsia2,yPsia2);
mi_setnodeprop('None',1);
mi_clearselected();
end
if mod(i,2*m)==3
xPsib1=(xst(4,i)+xst(5,i))/2;
yPsib1=(yst(4,i)+yst(5,i))/2;
mi_addnode(xPsib1,yPsib1); % xPsib1yPsib1
mi_selectnode(xPsib1,yPsib1);
mi_setnodeprop('None',1);
mi_clearselected();

xPsib2=(xst(9,i)+xst(10,i))/2;
yPsib2=(yst(9,i)+yst(10,i))/2;
mi_addnode(xPsib2,yPsib2); % xPsib2yPsib2
mi_selectnode(xPsib2,yPsib2);
mi_setnodeprop('None',1);
mi_clearselected();
% mi_addsegment(xPsib1,yPsib1,xPsib2,yPsib2)
end
if mod(i,2*m)==5
xPsic1=(xst(4,i)+xst(5,i))/2;
yPsic1=(yst(4,i)+yst(5,i))/2;
mi_addnode(xPsic1,yPsic1); % xPsic1yPsic1
mi_selectnode(xPsic1,yPsic1);
mi_setnodeprop('None',1);
mi_clearselected();

```

```

    xPsic2=(xst(9,i)+xst(10,i))/2;
    yPsic2=(yst(9,i)+yst(10,i))/2;
    mi_addnode(xPsic2,yPsic2);    % xPsic2yPsic2
    mi_selectnode(xPsic2,yPsic2);
    mi_setnodeprop('None',1);
    mi_clearselected();
end

end

% outside the stator

mi_addblocklabel((-a+Dso/2*cosd(135))/2,(a+Dso/2*sind(135))/2);
mi_selectlabel((-a+Dso/2*cosd(135))/2,(a+Dso/2*sind(135))/2);
mi_setblockprop('Air',1,0,0,0,20,0);
mi_clearselected();

%draw rotor topology

mi_addnode(-Dro/2-hag/3,0);
mi_selectnode(-Dro/2-hag/3,0);
mi_setnodeprop('None',8);
mi_clearselected();

mi_addnode(Dro/2+hag/3,0);
mi_selectnode(Dro/2+hag/3,0);
mi_setnodeprop('None',8);
mi_clearselected();

mi_addarc(-Dro/2-hag/3,0,Dro/2+hag/3,0,180,5);
mi_selectarcsegment(0,-Dro/2-hag/3);
mi_setarcsegmentprop(5,'None',1,8);
mi_clearselected();

mi_addarc(Dro/2+hag/3,0,-Dro/2-hag/3,0,180,5);
mi_selectarcsegment(0,Dro/2+hag/3);
mi_setarcsegmentprop(5,'None',1,8);
mi_clearselected();

mi_addblocklabel(0,Dro/2+hag/6);
mi_selectlabel(0,(Dro/2+hag/6)/2);
mi_setblockprop('Air',0,0.09,0,0,8,0);
mi_clearselected();

mi_addnode(-Dro/2-2*hag/3,0);
mi_selectnode(-Dro/2-2*hag/3,0);

```

```
mi_setnodeprop('None',8);
mi_clearselected();

mi_addnode(Dro/2+2*hag/3,0);
mi_selectnode(Dro/2+2*hag/3,0);
mi_setnodeprop('None',8);
mi_clearselected();

mi_addarc(-Dro/2-2*hag/3,0,Dro/2+2*hag/3,0,180,5);
mi_selectarcsegment(0,-Dro/2-2*hag/3);
mi_setarcsegmentprop(5,'None',1,8);
mi_clearselected();

mi_addarc(Dro/2+2*hag/3,0,-Dro/2-2*hag/3,0,180,5);
mi_selectarcsegment(0,Dro/2+2*hag/3);
mi_setarcsegmentprop(5,'None',1,8);
mi_clearselected();

mi_addblocklabel(0,Dro/2+hag/2);
mi_selectlabel(0,Dro/2+hag/2);
mi_setblockprop('Air',0,0.09,0,0,8,0);
mi_clearselected();

mi_addblocklabel(0,Dro/2+5*hag/6);
mi_selectlabel(0,Dro/2+5*hag/6);
mi_setblockprop('Air',0,0.09,0,0,7,0);
mi_clearselected();

mi_addnode(-Dro/2,0);
mi_selectnode(-Dro/2,0);
mi_setnodeprop('None',9);
mi_clearselected();

mi_addnode(Dro/2,0);
mi_selectnode(Dro/2,0);
mi_setnodeprop('None',9);
mi_clearselected();

mi_addarc(-Dro/2,0,Dro/2,0,180,5);
mi_selectarcsegment(0,-Dro/2);
mi_setarcsegmentprop(5,'None',0,9);
mi_clearselected();

mi_addarc(Dro/2,0,-Dro/2,0,180,5);
mi_selectarcsegment(0,Dro/2);
mi_setarcsegmentprop(5,'None',0,9);
mi_clearselected();

mi_addblocklabel(0,-Dro/2+0.25*Dri/2);
mi_selectlabel(0,-Dro/2+0.25*Dri/2);
```

```
mi_setblockprop('M-19',0,1,0,0,9,0);
mi_clearselected();

mi_addnode(-Drshaft/2,0);
mi_selectnode(-Drshaft/2,0);
mi_setnodeprop('None',9);
mi_clearselected();

mi_addnode(Drshaft/2,0);
mi_selectnode(Drshaft/2,0);
mi_setnodeprop('None',9);
mi_clearselected();

mi_addarc(-Drshaft/2,0,Drshaft/2,0,180,5);
mi_selectarcsegment(0,-Drshaft/2);
mi_setarcsegmentprop(5,'None',0,9);
mi_clearselected();

mi_addarc(Drshaft/2,0,-Drshaft/2,0,180,5);
mi_selectarcsegment(0,Drshaft/2);
mi_setarcsegmentprop(5,'None',0,9);
mi_clearselected();

mi_addblocklabel(0,-Drshaft/4);
mi_selectlabel(0,-Drshaft/4);
mi_setblockprop('Air',0,1,0,0,9,0);
mi_clearselected();

Rri=Dri/2;
Rro=Dro/2;
alfpm= pi/poles-alfapm*pi/poles;
alfr=pi/2;
aalfa_pm= 2*pi/poles;
Rpm1=Rri+0.5*hpm;

mi_addnode(-Rri,0);
mi_selectnode(-Rri,0);
mi_setnodeprop('None',9);
mi_clearselected();

mi_addnode(Rri,0);
mi_selectnode(Rri,0);
mi_setnodeprop('None',9);
mi_clearselected();

mi_addarc(-Rri,0,Rri,0,180,5);
mi_selectarcsegment(0,-Rri);
mi_setarcsegmentprop(5,'None',0,9);
mi_clearselected();

mi_addarc(Rri,0,-Rri,0,180,5);
```

```
mi_selectarcsegment(0,Rri);
mi_setarcsegmentprop(5,'None',0,9);
mi_clearselected();

for i=1:poles

    alfrt(1)=alfr-alfpm;           % against x-axis

    xrt(1,i)=Rri*cos(alfrt(1));
    yrt(1,i)=Rri*sin(alfrt(1));
    mi_addnode(xrt(1,i),yrt(1,i)); % node: xrt(1,i),yrt(1,i)
    mi_selectnode(xrt(1,i),yrt(1,i));
    mi_setnodeprop('None',9);
    mi_clearselected();

    alfrt(2)=alfr+alfpm;

    xrt(2,i)=Rri*cos(alfrt(2));
    yrt(2,i)=Rri*sin(alfrt(2));
    mi_addnode(xrt(2,i),yrt(2,i)); % node: xrt(2,i),yrt(2,i)
    mi_selectnode(xrt(2,i),yrt(2,i));
    mi_setnodeprop('None',9);
    mi_clearselected();

    alfrt(3)=alfr-alfpm;

    xrt(3,i)=Rro*cos(alfrt(3));
    yrt(3,i)=Rro*sin(alfrt(3));
    mi_addnode(xrt(3,i),yrt(3,i)); % node: xrt(3,i),yrt(3,i)
    mi_selectnode(xrt(3,i),yrt(3,i));
    mi_setnodeprop('None',9);
    mi_clearselected();

    alfrt(4)=alfr+alfpm;

    xrt(4,i)=Rro*cos(alfrt(4));
    yrt(4,i)=Rro*sin(alfrt(4));
    mi_addnode(xrt(4,i),yrt(4,i)); % node: xrt(4,i),yrt(4,i)
    mi_selectnode(xrt(4,i),yrt(4,i));
    mi_setnodeprop('None',9);
    mi_clearselected();

    alfrt(5)= i*aalfa_pm;
    xrt(5,i)=Rpm1*cos(alfrt(5));
    yrt(5,i)=Rpm1*sin(alfrt(5));

    alfrt(6)=i*aalfa_pm+aalfa_pm/2;
    xrt(6,i)=Rpm1*cos(alfrt(6));
    yrt(6,i)=Rpm1*sin(alfrt(6));
```



```
mi_addblocklabel(xrt(5,i),yrt(5,i));
mi_selectlabel(xrt(5,i),yrt(5,i));
mi_setblockprop('Air',0,1,0,0,9,0);
% mi_setblockprop('M-19',0,1,0,0,9,0);
mi_clearselected();

mi_addblocklabel(xrt(6,i),yrt(6,i));
mi_selectlabel(xrt(6,i),yrt(6,i));

a(i)=mod(i,2);
if a(i)==0
    alfPM(i)=alfrt(6);
else
    alfPM(i)=alfrt(6)+pi;
end

mi_setblockprop('NdFeB',0,0.5,0,rad2deg(alfPM(i)),6,1);
mi_clearselected();

mi_addsegment(xrt(1,i),yrt(1,i),xrt(3,i),yrt(3,i));
mi_selectsegment((xrt(1,i)+xrt(3,i))/2,(yrt(1,i)+yrt(3,i))/2);
mi_setsegmentprop('None',0,1,0,9);
mi_setsegmentprop('None',0,1,0,9);
mi_clearselected();

mi_addsegment(xrt(2,i),yrt(2,i),xrt(4,i),yrt(4,i));
mi_selectsegment(xrt(2,i),yrt(2,i));
mi_setsegmentprop('None',0,1,0,9);
mi_setsegmentprop('None',0,1,0,9);
mi_clearselected();
alfr=alfr+2*pi/poles;

end

fclose(fid);

mi_saveas('SPMSM_eval3.fem');

mi_createmesh;

% EMF and cogging torque calculation
mi_analyse(1);
mi_loadsolution;
mo_hidepoints;
```

```
mi_seteditmode('group')
mi_selectgroup(6);
mi_selectgroup(9);
mi_moverotate(0,0,-24);
mi_clearselected();

k=1;

I=Im; mo_seteditmode('contour');
mo_addcontour(xPsia1,yPsia1);
mo_addcontour(xPsia2,yPsia2);
li=mo_lineintegral(0);
Phi_a(1)=li(1);
mo_clearcontour;

mo_seteditmode('contour');
mo_addcontour(xPsib1,yPsib1);
mo_addcontour(xPsib2,yPsib2);
li=mo_lineintegral(0);
Phi_b(1)=li(1);
mo_clearcontour;

mo_seteditmode('contour');
mo_addcontour(xPsic1,yPsic1);
mo_addcontour(xPsic2,yPsic2);
li=mo_lineintegral(0);
Phi_c(1)=li(1);
mo_clearcontour;

mo_seteditmode('block');
mo_groupselectblock(6);
mo_groupselectblock(8);
mo_groupselectblock(9);
Tcogg(1)=mo_blockintegral(22);
mo_clearblock;
mo_close;

alfel(1)=0;
i=1;
for alfmec=0:1:90

    i=i+1;
    alfel(i)=alfmec*4;

    mi_seteditmode('group');
    mi_selectgroup(6);
    mi_selectgroup(9);
    mi_moverotate(0,0,1);
    mi_clearselected;
```

```
mi_analyse(1);
mi_loadsolution;

mo_seteditmode('contour');
mo_addcontour(xPsia1,yPsia1);
mo_addcontour(xPsia2,yPsia2);
li=mo_lineintegral(0);
Phi_a(i)=li(1);
mo_clearcontour;

mo_seteditmode('contour');
mo_addcontour(xPsib1,yPsib1);
mo_addcontour(xPsib2,yPsib2);
li=mo_lineintegral(0);
Phi_b(i)=li(1);
mo_clearcontour;

mo_seteditmode('contour');
mo_addcontour(xPsic1,yPsic1);
mo_addcontour(xPsic2,yPsic2);
li=mo_lineintegral(0);
Phi_c(i)=li(1);
mo_clearcontour;

mo_seteditmode('block');
mo_groupselectblock(6);
mo_groupselectblock(8);
mo_groupselectblock(9);
Tcogg(i)=mo_blockintegral(22);
mo_clearblock;
mo_close;
end

mi_seteditmode('group');
mi_selectgroup(6);
%mi_selectgroup(8);
mi_selectgroup(9);
mi_moverotate(0,0,-90);
mi_clearselected;

    mi_modifycircprop('ia',1,0);

    mi_modifycircprop('ib',1,(-I));

    mi_modifycircprop('ic',1,(I));

mi_analyse(1);
mi_loadsolution;
fid=fopen('ia.txt','wt');
```

```
mo_seteditmode('block')
mo_groupselectblock(2);
w1=mo_blockintegral(7);
fprintf(fid, '%d ',w1/2,'\n');
fclose(fid);
mo_clearblock;
```

```
fid=fopen('ib.txt','wt');
mo_seteditmode('block')
mo_groupselectblock(3);
w2=mo_blockintegral(7);
fprintf(fid, '%d',w2/2,'\n' );
fclose(fid);
mo_clearblock;
```

```
fid=fopen('ic.txt','wt');
mo_seteditmode('block')
mo_groupselectblock(4);
w3=mo_blockintegral(7);
fprintf(fid, '%d', w3/2,'\n');
fclose(fid);
mo_clearblock;
```

```
fid=fopen('tload.txt','wt');
mo_seteditmode('block')
mo_groupselectblock(6);
mo_groupselectblock(8);
mo_groupselectblock(9);
w=mo_blockintegral(22);
fprintf(fid, '%d', w,'\n');
fclose(fid);
mo_clearblock;
```

```
alfel(1)=0;
i=1;
```

```
for alfmec=0:1:90
    i=i+1;
```

```
    alfel(i) = alfmec*4;
```

```
    if (alfel(i)<(30-2*k))
        iaf=0;
        ibf=-I;
        icf=I;
```

```
    end
```

```
    if ((alfel(i)>=(30-2*k)) && (alfel(i)<(30+2*k)))
```

```
        a1=-I/(4*k);
        b1=-a1*(30-2*k);
        a2=I/(4*k);
        b2=-a2*(30+2*k);
```

```
    iaf=a1*alfel(i)+b1;
    ibf=a2*alfel(i)+b2;
    icf=I;
end
if ((alfel(i)>=30+2*k) && (alfel(i)<90-2*k))
    iaf=-I;
    ibf=0;
    icf=I;
end
if ((alfel(i)>=90-2*k) && (alfel(i)<=90+2*k))
    a1=I/(4*k);
    b1=-a1*(90-2*k);
    a2=-I/(4*k);
    b2=-a2*(90+2*k);
    iaf=-I;
    ibf=a1*alfel(i)+b1;
    icf=a2*alfel(i)+b2;
end
if ((alfel(i)>90+2*k) && (alfel(i)<150-2*k))
    iaf=-I;
    ibf=I;
    icf=0;
end
if ((alfel(i)>=150-2*k) && (alfel(i)<=150+2*k))
    a1=I/(4*k);
    b1=-a1*(150+2*k);
    a2=-I/(4*k);
    b2=-a2*(150-2*k);
    iaf=a1*alfel(i)+b1;
    ibf=I;
    icf=a2*alfel(i)+b2;
end
if ((alfel(i)>150+2*k) && (alfel(i)<210-2*k))
    iaf=0;
    ibf=I;
    icf=-I;
end
if ((alfel(i)>=210-2*k) && (alfel(i)<=210+2*k))
    a1=I/(4*k);
    b1=-a1*(210-2*k);
    a2=-I/(4*k);
    b2=-a2*(210+2*k);
    iaf=a1*alfel(i)+b1;
    ibf=a2*alfel(i)+b2;
    icf=-I;
end
if ((alfel(i)>210+2*k) && (alfel(i)<270-2*k))
    iaf=I;
    ibf=0;
    icf=-I;
end
```

```
if ((alfel(i)>=270-2*k) && (alfel(i)<=270+2*k))
    a1=-I/(4*k);
    b1=-a1*(270-2*k);
    a2=I/(4*k);
    b2=-a2*(270+2*k);
    iaf=I;
    ibf=a1*alfel(i)+b1;
    icf=a2*alfel(i)+b2;
end
if ((alfel(i)>270+2*k) && (alfel(i)<330-2*k))
    iaf=I;
    ibf=-I;
    icf=0;
end
if ((alfel(i)>=330-2*k) && (alfel(i)<=330+2*k))
    a1=-I/(4*k);
    b1=-a1*(330+2*k);
    a2=I/(4*k);
    b2=-a2*(330-2*k);
    iaf=a1*alfel(i)+b1;
    ibf=-I;
    icf=a2*alfel(i)+b2;
end
if alfel(i)>(330+2*k)
    iaf=0;
    ibf=-I;
    icf=I;
end

mi_modifycircprop('ia',1,iaf)

mi_modifycircprop('ib',1,ibf)

mi_modifycircprop('ic',1,icf)

mi_seteditmode('group');
mi_selectgroup(6);
    mi_selectgroup(9);
mi_moverotate(0,0,1);
mi_clearselected;

mi_analyse(1)
mi_loadsolution;

fid=fopen('ia.txt','wt');
mo_seteditmode('block')
mo_groupselectblock(2);
w1(i)=mo_blockintegral(7);
fprintf(fid,'%d', w1,'\n');
```

```
fclose(fid);
mo_clearblock;

fid=fopen('ib.txt','wt');
mo_seteditmode('block');
mo_groupselectblock(3);
w2(i)=mo_blockintegral(7);
fprintf(fid, '%d',w2,'\n');
fclose(fid);
mo_clearblock;

fid=fopen('ic.txt','wt');
mo_seteditmode('block');
mo_groupselectblock(4);
w3(i)=mo_blockintegral(7);
fprintf(fid, '%d', w3,'\n');
fclose(fid);
mo_clearblock;

fid=fopen('tload.txt','wt');
mo_seteditmode('block');
mo_groupselectblock(6);
mo_groupselectblock(8);
mo_groupselectblock(9);
w(i)=mo_blockintegral(22);
fprintf(fid, '%d',w,'\n');
fclose(fid);
mo_clearblock;

mo_close;

end

mi_seteditmode('group');
mi_selectgroup(6);
mi_selectgroup(9);
mi_moverotate(0,0,-90);
mi_clearselected();

mi_analyse(1);
mi_loadsolution;

n=length(w);
%
for i=1:n-1
    kE_a(i)=nc*(Phi_a(i)-Phi_a(i+1))/(-0.5*pi/180);
    kE_b(i)=nc*(Phi_b(i)-Phi_b(i+1))/(-0.5*pi/180);
    kE_c(i)=nc*(Phi_c(i)-Phi_c(i+1))/(-0.5*pi/180);
```

```
end
```

```
kE_a(n)=nc*(Phi_a(n)-Phi_a(1))/(-0.5*pi/180);  
kE_b(n)=nc*(Phi_b(n)-Phi_b(1))/(-0.5*pi/180);  
kE_c(n)=nc*(Phi_c(n)-Phi_c(1))/(-0.5*pi/180);
```

```
%Tcogg
```

```
figure;  
plot(Tcogg);  
xlabel('\theta_{mec} [deg.]');  
ylabel('T_{cogg} [Nm]');  
title('Plot of T_{cogg}(\theta_{mec})');  
grid on;  
figure;  
plot(w);  
xlabel('\theta_{mec} [deg.]');  
ylabel('T_{elm} [Nm]');  
title('Plot of T_{elm}(\theta_{mec})');  
grid on;
```

```
%Back EMF
```

```
figure;  
plot(kE_a, '-r');  
hold on;  
plot(kE_b, '-b');  
hold on;  
plot(kE_c, '-g');  
xlabel('\theta_{mec} [deg.]');  
ylabel('k_{E_a} [Vs/rad], k_{E_b} [Vs/rad], k_{E_c} [Vs/rad]');  
title('Plot of k_{E_{abc}}(\theta_{mec})');  
grid on;
```


% determine commutation sector from measured/estimated position

```

#define S_FUNCTION_NAME sector
#define S_FUNCTION_LEVEL 2

#include "simstruc.h"

#include "math.h"

static void mdlInitializeSizes(SimStruct *S)
{
    ssSetNumSFcnParams(S, 0); /* Number of expected parameters */
    if (ssGetNumSFcnParams(S) != ssGetSFcnParamsCount(S)) {
        /* Return if number of expected != number of actual parameters */
        return;
    }

    ssSetNumContStates(S, 0);
    ssSetNumDiscStates(S, 0);

    if (!ssSetNumInputPorts(S, 1)) return;
    ssSetInputPortWidth(S, 0, 1);
    ssSetInputPortDirectFeedThrough(S, 0, 1);

    if (!ssSetNumOutputPorts(S, 1)) return;
    ssSetOutputPortWidth(S, 0, 1);

    ssSetNumSampleTimes(S, 1);

    /* Take care when specifying exception free code - see sfuntmpl.doc */
    ssSetOptions(S, SS_OPTION_EXCEPTION_FREE_CODE);
    // ssSetOptions(S, 0);
}

static void mdlInitializeSampleTimes(SimStruct *S)
{
    // ssSetSampleTime(S, 0, CONTINUOUS_SAMPLE_TIME);
    ssSetSampleTime(S, 0, INHERITED_SAMPLE_TIME);
    ssSetOffsetTime(S, 0, 0);
}

#define MDL_INITIALIZE_CONDITIONS
static void mdlInitializeConditions(SimStruct *S)
{
    real_T *sect = ssGetOutputPortRealSignal(S, 0);
    //enable[0]=1.0;
}

```

178 % determine commutation sector from measured/estimated position

```
}

static void mdlOutputs(SimStruct *S, int_T tid)
{
    InputRealPtrsType theta= ssGetInputPortRealSignalPtrs(S,0);
    real_T          *sector = ssGetOutputPortRealSignal(S,0);

    if ((*theta[0]>=30)&&(*theta[0]<90)) sector[0]=1;
        else if ((*theta[0]>=90)&&(*theta[0]<150)) sector[0]=2;
            else if ((*theta[0]>=150)&&(*theta[0]<210)) sector[0]=3;
                else if ((*theta[0]>=210)&&(*theta[0]<270)) sector[0]=4;
                    else if ((*theta[0]>=270)&&(*theta[0]<330)) sector[0]=5;
                        else if ((*theta[0]>=330)||(*theta[0]<30))
sector[0]=0;
}

static void mdlTerminate(SimStruct *S)
{
}

#ifdef MATLAB_MEX_FILE /* Is this file being compiled as a MEX-file? */
#include "simulink.c" /* MEX-file interface mechanism */
#else
#include "cg_sfun.h" /* Code generation registration function */
#endif
```

Summary in Romanian

Sumar

Industria automotivă echipează mașina modernă cu un număr mare și în continuă creștere de dispozitive electrice și electronice. Aceasta se datorează atât necesității de a implementa noi funcționalități pe vehicul, dar și nevoii de a se alinia noilor reglementări în domeniu. Pentru că o putere tot mai mare instalată pe mașină presupune și probleme legate de generarea energiei de pe vehicul și utilizarea ei în mod dinamic și eficient, termenul de "management energetic dedicat automotive" vine să sintetizeze totalitatea activităților de interes care rezultă. Se urmărește reducerea consumului de combustibil, îmbunătățirea performanțelor, creșterea randamentului anumitor subsisteme și reducerea emisiilor poluante.

Introducerea acționărilor electrice pentru îndeplinirea variatelor funcționalități este una dintre măsurile adoptate; avantajele ce rezultă printr-o astfel de măsură sunt legate de funcționare cu randament crescut, funcționare independentă de cea a motorului cu combustie internă (la vehicule clasice și hibride), control mai bun și scăderea consumului de carburant. Îmbunătățirea unei asemenea acționări devine scopul tezei de față. Constrângerile impuse de industria automotivă sunt legate de dimensiune compactă, cost redus, randament ridicat și aplicabilitate practică. Prin urmare proiectarea motoarelor de acționare și conceperea strategiilor de control (cele două activități principale de cercetare pentru realizarea unei acționări electrice) trebuie să respecte aceste cerințe.

Ca studiu de caz se alege acționarea electrică a compresorului de aer condiționat de pe automobil, motivată de faptul că este unul dintre cei mai mari consumatori auxiliari de pe vehicul.

În ceea ce privește motorul de acționare, se consideră o topologie care să implice costuri reduse de manufacturare, dar și dimensiune compactă și densitate de cuplu ridicată. Se alege un motor sincron cu magneți permanenți de suprafață, cu șase creștături statorice și opt poli rotorici, cu înfășurare concentrată, fracționară. Proiectarea motorului se realizează parcurgând toate etapele impuse de practica inginerescă modernă – proiectare analitică, optimizare, verificare FEM. Se trece și la o metodă hibridă de proiectare, printr-un algoritm în care etapele se parcurg

succesiv și iterativ până când prototipul îndeplinește satisfăcător toate cerințele aplicației.

Strategia de control trebuie în esență să asigure funcționarea motorului la diferite viteze, în condiții de încărcare (cuplu proporțional cu viteza), pentru cerințe dinamice moderate, respectând timpii de ciclu (de ordinul secundelor) impuși de aplicație. Capacitatea prototipului de a livra cuplul cerut și randamentul acestuia se determină experimental prin implementarea unei strategii de control de tip vectorial, cu encoder. Această strategie nu este considerată ca și soluție finală, pentru că asigură performanțe peste cele cerute și implică costuri ridicate (mai ales dacă se dorește o configurație fără senzor/traductor de poziție). Se propune o nouă strategie de control, cu curent trapezoidal. Se aplică principiul comutației în șase trepte și măsurarea doar a curentului și tensiunii din baterie pentru obținerea informațiilor necesare și estimarea vitezei, pentru o soluție de tip "sensorless". Se validează preliminar, prin experimente strategia propusă.

Se conturează astfel o posibilă soluție pentru acționarea electrică a compresorului auto de aer condiționat.

Obiectivele tezei

Principale obiective ale tezei au fost:

- Să ofere o descriere comprehensivă a sistemului de aer condiționat de pe vehicule, cu evidențierea caracteristicilor principale;
- Să se identifice avantajele și cerințele acționării electrice dedicate pentru compresorul de aer conditionat de pe automobil;
- Să se aleagă topologia corespunzătoare pentru motorul de acționare;
- Să se implementeze etapa de proiectare analitică pentru un motor sincron cu magneți permanenți de suprafață și înfășurări concentrate, fracționare, cu exemplificare pentru cazul unui MSMP cu 6 crestături statorice și 8 poli rotorici, cu înfășurări concentrate, fracționare;
- Implementarea unei etape de proiectare optimală, cu scopul de a reduce costul inițial al prototipului;
- Etapa de verificare și calcul FEM pentru motorul rezultat;
- Metode de reducere a cuplului la curent zero ("cogging"), cu menținerea în limite rezonabile a capacității motorului de a livra cuplul util cerut;

- Să se propună o nouă strategie de tip "sensorless" pentru acționarea cu MSMP, cu respectarea cerințelor impuse de aplicație;
- Utilizarea unei metode de pornire care să asigure plecarea de pe loc a mașinii chiar și în condiții de încărcare, numită I-f, cu tranziție lină la controlul efectiv de viteză de tip "sensorless";
- Validări experimentale utilizând echipamentul dedicat din laborator;

Organizarea tezei

Lucrarea se întinde pe șapte capitole după cum urmează:

Capitolul *întâi* pornește cercetarea prin evidențierea direcțiilor de acțiune pentru a asigura un management eficient al generării și utilizării energiei de pe automobil. Utilizarea acționărilor electrice pentru îndeplinirea diverselor funcționalități este una dintre căi, iar sistemul de aer condiționat este ales ca punct de interes, având în vedere că este cel mai mare consumator auxiliar de pe vehicul. Se realizează o scurtă descriere a sistemului, după care se evidențiază principale caracteristici și cerințe pentru compresorul acționat electric.

Al *doilea* capitolul prezintă o metodă de proiectare analitică, "clasică" pentru motoarele sincrone cu magneti permanenți de suprafață și înfășurări fracționare. Topologia corectă este dedusă logic, iar studiul de caz prezentat este cel al unui motor sincron cu 6 creștături statorice și 8 poli rotorici, cu înfășurare concentrată fracționară.

Capitolul *trei* prezintă o etapă de proiectare optimală, bazată pe o metodă modificată Hooke-Jeeves, al cărui scop este să minimizeze costul inițial al prototipului realizat în capitolul anterior.

Capitolul *patru* prezintă etapa de verificare și calcul cu metoda elementului finit (FEM), parte integrantă a practicii ingineresti moderne de proiectare a mașinilor electrice. Prin intermediul acestei etape s-au estimat diverși parametri și caracteristici pentru motorul proiectat. Amplitudinea cupului la curent zero ("cogging") calculată prin FEM este semnificativă, iar necesitatea de a o reduce este imediată. Capitolul propune o metodă hibridă de proiectare, în care valori calculate prin FEM se reîntorc în etapele de proiectare optimală/analitică prin intermediul unor

coeficienți de subrelaxare, modificând acele dimensiuni geometrice care influențează direct și pregnant amplitudinea cuplului cogging. În același timp, se monitorizează și cuplul util pe care mașina trebuie să îl genereze, mecanismul aplicându-se asemanator și în acest caz.

Capitolul *cinci* investighează posibile soluții de control pentru prototipul considerat, având în vedere că forma tensiunii induse nu este nici sinusoidală, dar nici trapezoidală. În primă fază se implementează un control de viteză vectorial, cu encoder. Acesta este utilizat pentru determinarea capabilității motorului de a livra cuplul cerut de datele de proiectare, dar și radamentul mașinii la funcționare cu încărcare nominală. Se concluzionează că acest tip de control asigură performanțe peste cele cerute de aplicație, iar o variantă fără senzori de poziție este cu siguranță una costisitoare. Se trece la implementarea unui control cu curent trapezoidal, dezvoltându-se o strategie de control de viteză "sensorless" bazată pe comutația în 6 trepte și măsurarea exclusivă a curentului și tensiunii din baterie, pentru a obține informațiile necesare pentru comutație și estimarea vitezei. Experimentele realizate, constituie o validare preliminară a strategiei de control.

Capitolul *șase* prezintă pe scurt echipamentul utilizat pentru experimentare (din cadrul laboratorului UPT).

Principalele concluzii, contribuții și piste de cercetare viitoare sunt enunțate în capitolul *șapte*.

Principalele contribuții

Principalele contribuții ale tezei sunt:

- O descriere generală a sistemului de aer condiționat de pe mașină;
- Determinarea principalelor caracteristici și cerințe ale acționării electrice a compresorului auto de aer condiționat;
- Descrierea etapei de proiectare analitică "clasică" a motoarelor sincrone cu magneți permanenți de suprafață și înfășurări concentrate fracționare, cu exemplificare pentru o topologie "6 creștături statorice/8 poli rotorici";
- Implementarea unei metode de optimizare pentru minimizarea costului inițial al prototipului;
- Verificarea și validarea FEM prin interfațare Matlab-femm4.2, pentru tipul de motor considerat;
- Implementarea unei metode hibride de proiectare, care combină succesiv și iterativ cele 3 etape de proiectare pentru o soluție completă și cât mai performantă;

- Implementarea unei strategii de control de tip vectorial (pe standul experimental de laborator cu sistem DSpace), pentru evaluarea capacității motorului de a livra cuplul cerut și pentru a determina experimental randamentul mașinii;
- Implementarea unei strategii de control cu curent trapezoidal (pe standul experimental de laborator cu sistem DSpace), fără senzori de mișcare, utilizând doar măsurarea curentului și tensiunii de baterie pentru a obține informațiile necesare comutației și estimării vitezei;
- Reducerea semnificativă a senzorilor necesari (curent/tensiune) în implementarea strategiei de control, cu reducerea drastică a costului întregii acționări.

Author's papers related to the Ph.D. thesis

- [1] A. Ungurean, V. Coroban-Schramel, I. Boldea, "Sensorless control of a BLDC PM motor based on I-f starting and back-EMF zero-crossing detection", Proceedings of the 12th International Conference on Optimization of Electrical and Electronic Equipment (OPTIM), pp. 377 - 382, May 2010, ISSN 1842-0133, Print ISBN 978-1-4244-7019-8
- [2] A. Munteanu (Ungurean), S. C. AGARLIȚĂ, I. BOLDEA, "Experimental Characterization of Surface Permanent Magnet Synchronous Motor Drive", Proceedings of the International Conference "Zilele ASTR - 2011", Editia a VI-a PRO - PROSPERITAS Industrie, energie, mediu, Timisoara, ISSN: 2066-6586, pp. 87 - 92, 22 - 23 September 2011.
- [3] A. Munteanu (Ungurean), S. C. Agarlita, F. Blaabjerg, I. Boldea, C. Lascu, " Novel sensorless six-step commutation strategy for a surface permanent magnet synchronous motor with DC link measurement", Proceedings of the 13th International Conference on Optimization of Electrical and Electronic Equipment (OPTIM), pp. 521 - 528, May 2012, ISSN 1842-0133, E-ISBN 978-1-4673-1652-1 (pending for ISI indexing)
- [4] A. Munteanu (Ungurean), I. Boldea, L. Tutelea, " Novel hybrid design methodology for a surface permanent magnet synchronous motor", Proceedings of the International Symposium on Power Electronics, Electrical Drives, Automation and Motion (SPEEDAM), pp. 603 - 608, June 2012, Print ISBN: 978-1-4673-1299-8, (pending for ISI indexing)

Author's CV

Anamaria Ungurean (Munteanu)

Office: University Politehnica of Timisoara, Romania

Blvd. Vasile Parvan, no. 2, room D108

Tel: +40 256403463

Email: ungurean_am@yahoo.com

Home Address: 1D, Lacului Street

Timisoara, Timis, Romania

Mobile: +40 742663339

EDUCATION

- 2009-2012 Ph.D. student at University "Politehnica" of Timisoara,
Faculty of Electrical and Power Engineering,
Dept. of Electrical Machines and Drives, Timisoara, Romania
- 2009 Dipl. degree in Electrical Engineering
- 2004-2009 University "Politehnica" of Timisoara, Timisoara, Romania
Faculty of Electrical Engineering
- 2000-2004 High School "Kőrösi Csoma Sándor", Covasna, Romania

PROFESSIONAL EXPERIENCE

July-Oct. 2011 Guest Researcher at Institute of Energy Technology,
Aalborg University Denmark,

July 2007 - Dec. 2009 Function Developer at S.C. Continental Automotive
Romania, Powertrain Division, Timisoara, Romania

PERSONAL INFORMATION

Born: August 19th, 1985

Family: Married